Biophysical Modelling of Rat Cardiac Electrophysiology and Calcium Handling

Harley Jacob Stevenson-Cocks

Submitted in accordance with the requirements for the degree of
Doctor of Philosophy

The University of Leeds
Faculty of Biological Sciences
School of Biomedical Sciences
Multidisciplinary Cardiovascular Research Centre

September, 2019

Acknowledgements

I would like to extend thanks to my supervisors, Dr Al Benson, Professor Ed White, and Dr Michael Colman, for their support throughout the past 4 years. Al, your relaxed and informal approach to supervision at times made you seem more like a fellow student than a supervisor, but I am thankful for your help and guidance nonetheless! Ed, thank you for your patience in allowing a computational student to use the optical mapping rig, and for your feedback throughout the project. Mike, thanks in particular for your assistance in computing and programming matters, not forgetting that this project would probably be completely different without your calcium handling framework!

Thanks also to members of the cellular cardiology research group in Leeds: Tom and Maxx (the other members of the 'Tenacious 3') for broadening my musical horizons and your shared appreciations of all things beer; Ashlea, for showing me all the free parking spots near campus and sharing my appreciation for 'no science talk' lunches; Dr Kaarjel Narayanasamy, for finding enjoyment in my programming-related frustrations and laughing profusely at everything I said for 2 years; and Dr Dominic Whittaker, for sharing mixed success in the lab with me, and for bringing 'high-brow' humour to the office for a (short) year.

I am extremely grateful for the University of Leeds demonstrating studentship that has funded my time on this project. I am very thankful to have had the opportunity to engage so much with teaching and demonstrating within the Faculty over the years, enabling me to attain Associate Fellowship of the Higher Education Academy along the way. Thanks in particular to Dr Charlotte Haigh for her invaluable help on that front, and to the other academics who have provided me with opportunities to teach.

Thank you to my family, for supporting me through my various educational endeavours (of which there have been a fair few), as well as to my friends, for not berating me too much that I've essentially been avoiding income tax and student loan repayments for 4 more years.

Mostly, I would like to thank my girlfriend, Abi, whose love and support have remained constant over the years (as has, more recently, our dog Nessie's). I don't think I would have made it this far without you!

Declarations

Some parts of the work presented in this thesis have been published, or submitted for publication, in the following articles:

Benson, A.P., **Stevenson-Cocks, H. J.**, Whittaker, D. G., White, E. & Colman, M. A. (2020). Multi-scale approaches for the simulation of cardiac electrophysiology: II - tissue-level structure and function. *Methods*.

Stevenson-Cocks, H. J., Colman, M. A., White, E. & Benson, A. P. (2018). Inward rectifier current downregulation promotes spontaneous calcium release in a novel model of rat ventricular electrophysiology. *Computing in Cardiology*, **45**.

The candidate confirms that the work submitted is his own and that appropriate credit has been given where reference has been made to the work of others.

Communications

Oral

Towards detailed biophysical modelling of rat cardiac tissue electrophysiology and calcium handling. March 2017. *Multidisciplinary Cardiovascular Research Centre Retreat*, Ullswater, UK.

A novel model of rat ventricular electrophysiology reveals mechanisms of spontaneous Ca^{2+} release in heart failure. June 2017. *44th International Congress on Electrocardiology*, Portland, Oregon, USA.

Mechanisms of arrhythmia triggers in heart failure predicted by a novel model of rat ventricular electrophysiology. May 2018. *Leeds Institute of Cardiovascular and Metabolic Medicine Early Careers Science Day*, Leeds, UK. **Oral communication prize**.

Inward rectifier current (I_{K1}) downregulation in heart failure promotes triggered activity in a novel computational model of rat ventricular electrophysiology and calcium handling. September 2018. *Europhysiology*, London, UK.

Inward rectifier current downregulation promotes spontaneous calcium release in a novel model of rat ventricular electrophysiology. September 2018. *Computing in Cardiology*, Maastricht, Netherlands.

Poster

25th Northern Cardiovascular Research Group meeting. Manchester, UK. April 2017.

Physiological Society: Future Physiology. Leeds, UK, December 2017.

Multidisciplinary Cardiovascular Research Centre Retreat. Ullswater, UK. March 2018.

The Heart by Numbers: Integrating Theory, Computation and Experiment to Advance Cardiology. Berlin, Germany, September 2018.

Multidisciplinary Cardiovascular Research Centre Retreat. Ullswater, UK, March 2019.

Abstract

The primary purpose of the heart is to act as a regular, rhythmic pump in order to maintain the circulation of blood throughout the body. This mechanical activity is driven by electrical activity at the cell-level, through the intricate processes comprising excitation-contraction coupling. Disruption to these processes can result in rhythm disturbances (arrhythmias), which are potentially fatal, but the underlying mechanisms are complex, dynamic and multi-scale. Thus, they are difficult to experimentally dissect, and have been a major focus in the field of computational biology. Detailed quantitative descriptions of cardiac electrophysiology have been developed over the past 60 years that allow the simulation of healthy and pathophysiological excitation, permitting detailed computational investigation of the complex processes that result in pro-arrhythmic behaviour.

However, despite the rat being the most widely used animal model in cardiovascular research, existing computational models of rat ventricular electrophysiology are unable to account for stochastic subcellular calcium dynamics, which are known to trigger arrhythmias. The aims of this thesis were to: (i) develop a new computational model of rat ventricular electrophysiology including stochastic spatio-temporal calcium cycling dynamics; and (ii) use this model to explore how ion channel remodelling observed in heart failure results in pro-arrhythmic activity at the single cell level, and the mechanisms underlying the unique restitution characteristics of the rat ventricular action potential.

A recent rat ventricular electrophysiology model was coupled to a stochastic, spatio-temporal calcium cycling model. The new model reproduced various experimental action potential and calcium handling dynamics from the literature for rat ventricular myocytes, and revealed that electrical remodelling in heart failure increases the propensity for spontaneous calcium release events and lowers the threshold for generation of delayed afterdepolarisations, both of which are pro-arrhythmic. In addition, the restitution properties of rat ventricular myocytes are the result of a complex balance between altered repolarising potassium current kinetics and calcium handling properties, including the sodium-calcium exchanger.

The model developed in this thesis has provided insight into pro-arrhythmic and rate-dependent phenomena in rat ventricular myocytes, and is suitable for future single cell and tissue simulations.

Contents

List of Figures

List of Tables

Abbreviations and Acronyms

0D	Zero-dimensional
1D	One-dimensional
2D	Two-dimensional
3D	Three-dimensional
AE	Anion exchanger
AP	Action potential
APA	Action potential amplitude
$\mathrm{APD}_{\mathrm{x}}$	Action potential duration/at x percentage repolarisation
AVN	Atrioventricular node
BCL	Basic cycle length
Ca^{2+}	Calcium ion
CaMK(CaMKII)	Calcium/calmodulin-dependent protein kinase (II)
CF	Cumulative frequency
CHE	Chloride-hydrogen ion (proton) exchanger
CICR	Calcium-induced calcium release
CL	Cycle length
Cl^{-}	Chloride ion
C_{m}	Membrane capacitance
CRU	Calcium release unit
CT	Computed topography
DAD	Delayed afterdepolarisation
DI	Diastolic interval
ds	Dyadic space
DTI	Diffusion tensor imaging
E	Nernst potential
EAD	Early afterdepolarisation
EC	Excitation-contraction
ECG	Electrocardiogram
E_{eq}	Equilibrium potential
ERP	Effective refractory period
E_{x}	Reversal potential for ion x
FFR	Force-frequency relationship
g_{x}	Maximum conductance of current x

hERG	Human ether-a-go-go-related gene
HF	Heart failure
I_{b}	Total background current
I_{Cab}	Background calcium current
I_{CaL}	L-type calcium current
I_{CaP}	Sarcolemmal calcium pump current
I_{CaT}	T-type calcium current
I_{f}	Hyperpolarisation-activated (funny) current
I_{ion}	Total ionic current
I_{K1}	Inward rectifier potassium current
$I_{\mathrm{K,ACh}}$	Acetylcholine-activated potassium current
I_{KATP}	ATP-sensitive potassium current
I_{Kb}	Background potassium current
I_{Kr}	Rapid delayed rectifier potassium current
I_{Ks}	Slow delayed rectifier potassium current
I_{Kur}	Ultra-rapid delayed rectifier potassium current
$I_{\mathrm{Kv1.1}}$	Kv1.1-mediated potassium current
I_{Na}	Fast sodium current
I_{Nab}	Background sodium current
I_{NaCa}	Sodium-calcium exchanger current
I_{NaK}	Sodium-potassium pump current
I_{NaL}	Late sodium current
I_{SK}	Small conductance calcium-activated potassium current
ISO	Isoprenaline/isopreterenol
I_{ss}	Steady-state outward potassium current
I_{to}	Transient outward potassium current
jSR	Junctional sarcoplasmic reticulum
J_{x}	Flux for process x
K^+	Potassium ion
LTCC	L-type calcium channel
MD	Median duration
MRI	Magnetic resonance imaging
mRNA	Messenger ribonucleic acid
MUV	Maximum upstroke velocity

Na^+	Sodium ion
NBC	Sodium-bicarbonate cotransporter
NCX	Sodium-calcium exchanger
NHE	Sodium-hydrogen exchanger
NO	Nitric oxide
$N_{\mathrm{RyR\_O}}$	Number of open ryanodine receptors
nSR	Network sarcoplasmic reticulum
OS	Overshoot potential
P_{x}	Permeability to ion x
RMP	Resting membrane potential
RyR	Ryanodine receptor
SAC	Stretch-activated channel
SAN	Sinoatrial node
SCRE	Spontaneous calcium release events
SERCA	Sarco(endo)plasmic reticulum calcium ATPase
SFR	Slow-force response to stretch
SR	Sarcoplasmic reticulum
SRF	Spontaneous release functions
ss	Subspace
t_{f}	Final time of spontaneous calcium release
t_{i}	Initiation time of spontaneous calcium release
t_{p}	Peak time of spontaneous calcium release
T_{peak}	Time to peak
T-tubule/TT	Transverse tubule
VF	Ventricular fibrillation
V_{m}	Membrane potential
VT	Ventricular tachycardia
VW	Vulnerable window
WT	Wild-type

Chapter 1

Introduction

1.1 The heart

The human heart beats approximately 3 billion times in the average lifetime [264], a task it does continuously without break. In doing so, the heart is responsible for circulating 8,000 litres of blood each day to the body's cells, supplying essential nutrients, hormones and oxygen, and removing metabolic waste. Normal cardiac function is compromised in cardiovascular diseases such as cardiac arrythmias, heart failure, cardiomyopathy, and ischaemic heart disease, all of which can be fatal if untreated [372, 389]. Accordingly, cardiovascular diseases present a significant economic and healthcare burden [206, 224, 419].

Cardiovascular diseases have been the leading cause of global mortality since 1980, and were the second main cause of death in the UK in 2014 [47, 206]. Despite the high prevalance and considerable health, social, and economic impact of cardiovascular disease, our understanding of the complicated underlying processes remains limited, and so there is a pressing need to improve understanding in order to drive the development of novel therapeutic and surgical interventions, as well as to maximise prevention where possible. The mechanical beating of the heart is driven by electrical activity, so the heart can be considered an electro-mechanical pump, and it is at this interface of biology, physics and mathematics where efforts are increasingly being made to understand the complex pathogenesis of cardiac disorders [312].

Since the development of the voltage clamp in 1947 and patch clamp technology in the 1970s, considerable advances have been made in experimental methods used to understand both the normal and abnormal functioning of the heart [87], with a move from single channel and single cell studies towards the tissue and organ scales. Optical mapping, for example, provides a platform to investigate changes in both voltage and calcium (simultaneously, or in isolation) across the whole heart [185,335], and so the influence of exercise training, obesity, diabetes, or pharmacological modulation on electrophysiological parameters can be explored [262]. However, it remains difficult to explore experimentally how pathological changes across the scales interact - for example, how subcellular alterations in ion homeostasis manifest at the tissue-level and result in arrhythmias. Integrating experimental findings at the subcellular level to the tissue level therefore remains a major research challenge [329].

1.2 Cardiac modelling

Over the past 70 years, there have been considerable advances in the field of computational physiology [93], stemming largely from seminal work by Hodgkin and Huxley [170] and later, specific to cardiac physiology, Noble [280]. Computational models have since become increasingly complex, integrating biophysical descriptions of subcellular calcium cycling dynamics [69, 166, 360], ion current formulations [151, 289], and contraction mechanics [208, 276]. Such models have been developed for a variety of species, e.g. mouse [56], rat [293], rabbit [18], canine [36], and human [289], and from the subcellular level [104, 166] through to the cell [235, 293] and tissue levels [18, 387]. With the development of more recent techniques such as diffusion tensor imaging and micro-computed tomography, anatomically-detailed geometries of the heart can now be coupled with mathematical models of electrophysiology to produce powerful research and patient-specific clinical models [20, 37, 307]. As a result, cardiac modelling now plays a critical role in applications such as drug safety testing [110] and optimising surgical interventions [221,307], while still being used to explore the fundamental mechanisms underlying cardiac arrhythmogenesis and pathogenesis [99,258].

Computational modelling holds many advantages over traditional experimental methodologies, not least financially given that the only required equipment is a computer. Computational modelling also confers an unrivalled degree of control to the researcher, as each parameter can be both recorded and controlled to any degree of precision. In addition, model outputs can be dissected in time and by parameter, providing unparalleled analytical opportunities. Computational modelling also is a non-invasive research technique, so ethical considerations are, at worst, minimal. However, models by definition are simplifications of reality and so it is only possible to capture a small fraction of the complexity of the heart, hence they require thorough validation against experimental data in order for their outputs to be considered useful. It is essential that a model's functionality is properly understood, so that they can be used effectively [103], and they are most effectively employed simultaneously alongside experimental or clinical research, creating the so-called 'Virtual Heart' – a multi-disciplinary effort to create a functional, *in silico* heart that can be used for all aspects of the prevention, diagnosis, assessment and treatment of cardiac disease [19,281,447]. Thus, cardiac modelling plays a considerable (and increasing) role in the interdisciplinary research effort to understand the normal and pathological functioning of the heart.

1.3 Thesis overview

Despite the common use of the rat as an animal model of cardiovascular disease, existing computational models of rat ventricular electrophysiology implement deterministic descriptions for the L-type Ca^{2+} channel and ryanodine receptor (RyR), so are unable to account for the stochastic nature of spontaneous calcium release events, which are a known trigger for arrhythmias [74, 202]. As excitation-contraction coupling encompasses an intricately balanced set of processes linking membrane currents to intracellular Ca^{2+} handling, it has so far not been possible to explore how ion channel remodelling as observed in a variety of pathophysiologies including heart failure [175, 186] results in pro-arrhythmic behaviour resulting from spontaneous Ca^{2+} release. The aims of this work were to develop a novel model, validated against experimental data, of rat ventricular electrophysiology, including descriptions for stochastic spatio-temporal Ca^{2+} cycling, and to use this model to investigate how ion channel remodelling as observed in heart failure can promote spontaneous Ca^{2+} release events and pro-arrhythmic behaviour at the cell level. In addition, the mechanisms underlying the unique restitution characteristics of the rat ventricular action potential were investigated in simulations informed by experimental observations.

In Chapter 2, the biological, mathematical and computational background of the works presented in this thesis is discussed. The general structure and function of the heart is introduced, followed by the sub-cellular events underlying electrical excitation and mechanical contraction. Experimental and clinical measurements of cardiac features are described, and the transition from normal heart rhythms to pathophysiological arrhythmias is explained. Finally, the mathematical and computational basis of biophysical modelling of cardiac electrophysiology is described.

Existing computational models of rat ventricular electrophysiology are extensively reviewed in Chapter 3. Firstly, important differences in cardiac electrophysiology between species are reviewed, highlighting the importance of translating findings from rodents. Existing models are then reviewed, and the two principal models (the Pandit and Gattoni models) are incorporated into a framework to allow direct comparison between each model under identical simulation conditions and protocols. The ability of these models to reproduce experimental observations for action potential and calcium handling dynamics is assessed, as well as their utility for recreating APD restitution characteristics. Finally, their utility for exploring the effects of ion channel remodelling is investigated.

In Chapter 4, a novel model of rat ventricular electrophysiology is described. This model (the SC model) is formed by the incorporation of the Gattoni rat electrophysiology model, into the Colman [97] stochastic spatio-temporal Ca^{2+} cycling framework. The Ca^{2+} framework is described alongside the new model development process, before validation of the model is undertaken against various experimental sources from the literature.

The SC model is then used in Chapter 5 to explore the influence of remodelling of the inward rectifier K^+ current, I_{K1}, as observed in heart failure [34, 139], on the dynamics of spontaneous Ca^{2+} release events. The results suggest that the prolonged action potential duration observed in HF-associated I_{K1} downregulation promotes greater loading of the sarcoplasmic reticulum (SR) with Ca^{2+}, which favours spontaneous Ca^{2+} release events. These events are shown to be initiated sooner, and of larger magnitude, than in control simulations. Independently of SR Ca^{2+} load, the action potential changes from

I_{K1} remodelling *alone* are able to account for a greater propensity for delayed afterdepolarisations, resulting in triggered activity. These effects are likely to be attenuated *in vivo* given that I_{K1} downregulation also destabilises the resting membrane potential.

In Chapter 6, the SC model is used to explore the mechanisms posited to cause the inverse rate-dependence of the rat ventricular action potential duration (which prolongs at shorter cycle lengths) as observed experimentally. Simulations show that the contribution of reduced repolarising K^+ currents to inverse rate-dependence outweighs that of reduced I_{CaL}, and suggest that downregulation of Na^+-Ca^{2+} exchanger current may reduce APD prolongation at faster pacing frequencies.

Finally, Chapter 7 discusses the major findings from the work presented in this thesis, as well as their associated limitations. Directions for future works are also discussed.

Chapter 2

Cardiac Electrophysiology and Computational Modelling

2.1 Introduction

In this chapter, the basic anatomy and physiology of the heart and circulatory system will be described. The electrical conduction system of the heart will be introduced, which determines how the electrical impulse (leading to contraction of the myocardium) spreads across the heart. This electrical impulse, the cardiac action potential, results from the interaction of many ion channels and currents operating at the sub-cellular level, with contraction resulting from a rise in the intracellular calcium concentration (the calcium transient). Together, the cardiac action potential and calcium transient comprise the process of excitation-contraction coupling, which is the summation of the intracellular processes that result in excitation of cardiac tissue and synchronous contraction (which is perturbed in diseased states). How the electrical activity of the heart can be measured experimentally and clinically will then be discussed, leading to an explanation of rhythm disorders (arrhythmias) and their associated treatments.

The second half of this chapter is dedicated to introducing the underlying concepts involved in mathematical modelling of cardiac electrophysiology. Cell biophysics and electrical circuit theory will be introduced, before descriptions of different types of cardiac modelling (Hodgkin-Huxley, Markov formulations and stochastic modelling) will be detailed. Finally, a summary of the mathematical models and methods of integration used in this thesis will be provided.

2.2 The heart

2.2.1 The heart and circulatory system

The heart (Figure 2.1) is a muscular, four-chambered organ responsible for pumping blood containing oxygen, nutrients and hormones throughout the body. The heart pumps approximately 8,000 litres of blood per day [264] throughout the circulation, which comprises two circuits: the pulmonary circuit (right side of the heart), where blood travels to the lungs to be oxygenated and to release waste carbon dioxide, and the systemic circuit (left side of the heart), where oxygen-saturated blood is delivered to the body's organs, tissues and cells. Oxygenated blood is carried away from the heart via vessels called arteries, and deoxygenated blood is delivered back to the heart via veins (the exception to this rule being the pulmonary artery, which carries deoxygenated blood from the right side of the heart to the lungs to be oxygenated, and the pulmonary vein, which returns this oxygenated blood to the left side of the heart). The four chambers of the heart are the left and right atria (located superiorly) and the left and right ventricles (located inferiorly). The function of the atria is to receive blood from the systemic (right atria) or pulmonary (left atria) circulations, which then flows into the corresponding ventricle (passively, predominantly, though atrial contraction becomes important in diseased states and old age), which then contracts to eject blood from the heart. The thickness of each ventricular wall is an indicator of their respective workloads – the left ventricle has to pump blood a greater distance than the right, against a larger systemic pressure ($\sim$120 mmHg), and its wall is therefore much thicker. The atria, by comparison, are thin-walled as they develop much smaller pressures when pumping blood. These wall thicknesses can be seen in Figure 2.1 along with the direction of blood flow (depicted by the dashed arrows).

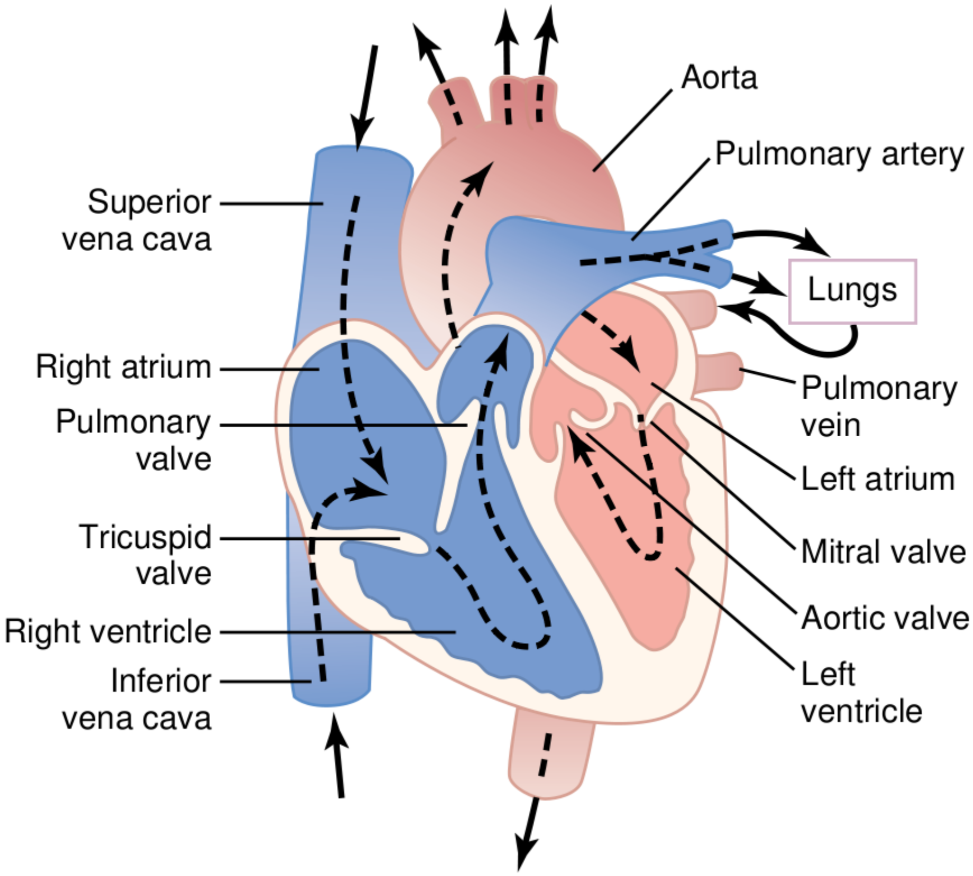

Figure 2.1. Structural anatomy of the human heart. Arrows indicate the direction of blood flow. From [157].

2.2.2 Electrical conduction in the heart

The cardiac conduction system (Figure 2.2) is a specialised network of cardiac muscle cells (cardiac myocytes) arranged in such a way that the electrical impulse, originating in the sinoatrial node (SAN), is quickly conducted throughout the heart in a systematic, coordinated manner. The sinoatrial node (SAN), located just laterally to the junction of the superior vena cava and right atrium, is responsible for cardiac pacemaking in healthy subjects. The SAN generates spontaneous electrical impulses which are conducted quickly (1 $m.s^{-1}$) across the atria (via Bachmann's bundle, for the left atrium) towards the atrioventricular node (AVN) located at the interatrial septum. Here, conduction velocity slows to roughly 0.05 $m.s^{-1}$, which allows time for atrial contraction (i.e. time for ventricular filling to occur). From the AVN, electrical impulses are rapidly conducted (4 $m.s^{-1}$) down the left and right bundle branches in the septum to the Purkinje fibres – as the major blood vessels exiting the heart are located superiorly, fast conduction down the bundle branches

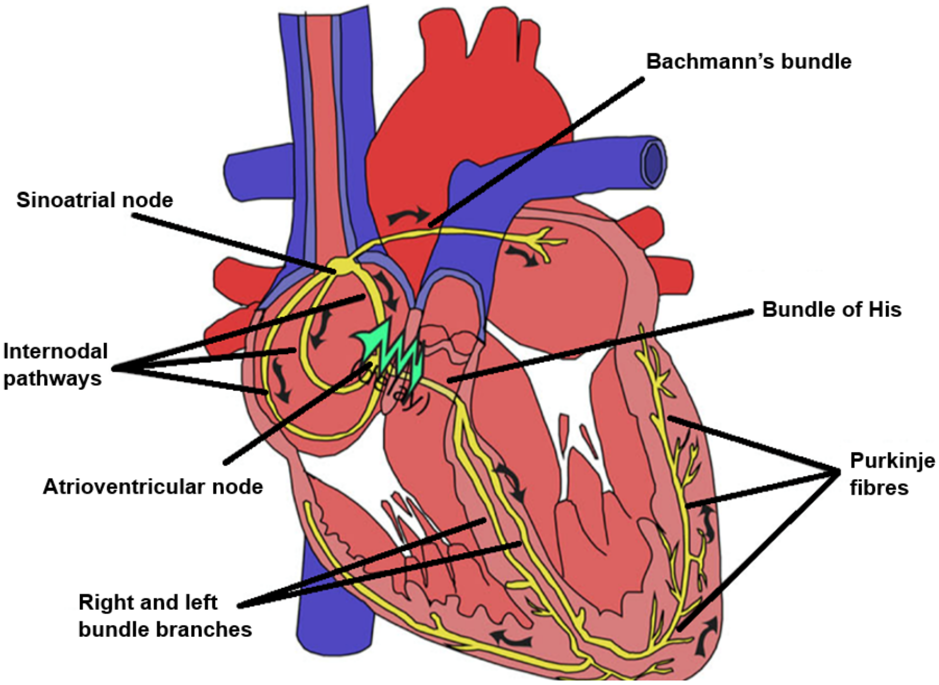

Figure 2.2. Electrical conduction system of the heart. Electrical impulses originating from the sinoatrial node pass to the atrioventricular node (and Bachmann's bundle, in the right atrium), then through the Bundle of His and bundle branches to the Purkinje fibres which extend superiorly through the ventricles. Adapted from [255].

to the apex of the heart ensures that blood is forced upwards and out of the ventricles into the pulmonary and systemic circulations. The Purkinje fibres, muscle fibres specialised for fast conduction, then distribute the electrical excitation quickly over the ventricular walls from endocardium to epicardium (i.e. inner to outer) so that ventricular contraction occurs in a coordinated manner [264]. The SAN is the primary pacemaker of the heart, however other cells can act as subsidiary pacemakers in the event of SAN failure; AVN cells generate electrical excitation at rates between 40 and 60 bpm, or 20 to 40 bpm for Purkinje cells [243].

2.2.3 The cardiac myocyte

The muscle cells that make up the heart are known as cardiac myocytes, or cardiomyocytes. Cardiac myocytes are cylindrical in shape and typically range from 50 to 200 μm in length and 10 to 20 μm in radius [243], although their size is variable depending on the region of the heart they occupy. As the cells comprising the cardiac conduction system are specialised for fast electrical conduction, they typically have fewer contractile proteins than those of the atrial or ventricular myocardium [196], and they also tend to be smaller. For example, SAN cells are approximately 5 to 10 μm in diameter and 25 to 30 μm in length. Purkinje cells have a large diameter which contributes towards their fast conduction velocities [291]. Cardiac cells are coupled to adjacent cells both electrically and mechanically.

2.3 Cardiac electrophysiology

2.3.1 The cell membrane

Cardiac myocytes are ensheathed by a phospholipid bilayer, which forms a semi-permeable membrane around each cell. Embedded within the cell membrane are specialised proteins called ion channels, which are selectively permeable to specific ion species and permit their entry into or exit out of the cell. These ion channels are heterogeneously distributed across the cell membrane, and undergo conformational changes to either open, close, or become inactive in response to different stimuli, such as voltage, stress, stretch, and neurotransmission [264]. The majority of ion channels are responsive to changes in voltage, so are referred to as voltage-gated channels. Ion channels that respond to chemical messengers (such as hormones) are referred to as ligand-gated ion channels.

Figure 2.3 shows a voltage-gated sodium (Na^+) channel in 3 different configurations. At resting membrane potential, the channel is closed (Figure 2.3A). In response to electrical excitation, the channel undergoes a conformational change, opening and permitting an influx of Na^+ ions due to the electrochemical gradient for Na^+ (Figure 2.3B). Shortly after activation, the channel transiently inactivates and is no longer responsive to electrical stimuli (Figure 2.3C). Opening, closing and inactivation kinetics for different ion channels play a pivotal role in the morphology of the cardiac action potential [329].

2.3.2 Ion channels and currents

Ion channels are complex proteins that span cell membranes to form pores that permit the flow of ions. Ion currents in the heart are typically carried by Na^+, potassium (K^+),

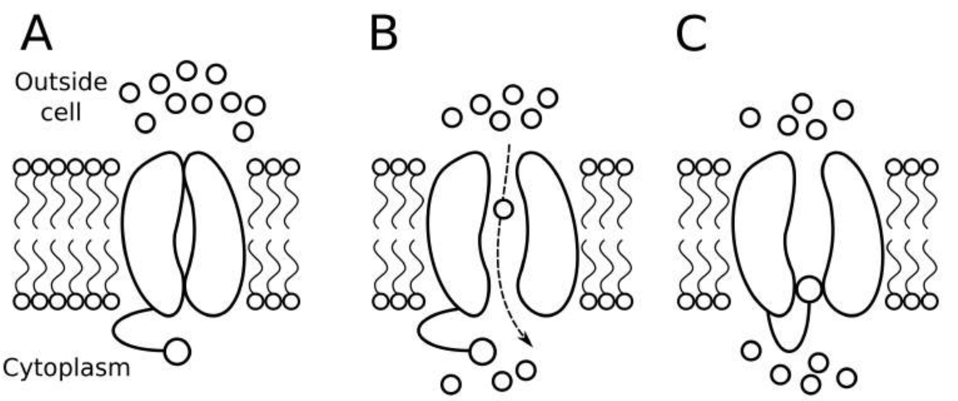

Figure 2.3. Idealised schematic for a voltage-gated Na^+ channel. (A) At rest, the channel is closed. (B) Electrical stimulation results in channel opening and an influx of Na^+ ions. (C) Following activation, the channel inactivates briefly and no longer responds to electrical excitation. Note that the gate-like structure represents the activation gate, and the ball-and-chain structure represents the inactivation gate.

and calcium (Ca^{2+}), with chloride (Cl^-) currents less prevalant. By convention, an inward current refers to the movement of positively-charged ions into the cell (influx), whereas positively-charged ions leaving the cell (efflux) result in an outward current. Inward currents, therefore, raise the cell's membrane potential to more positive values (termed depolarisation), whereas outward currents result in more negative membrane potentials (hyperpolarisation). In cardiac myocytes, inward currents result from the flow of Na^{2+} and Ca^{2+}, whereas outward currents are predominantly carried by K^+ ions.

However, multiple ion channels exist which can be permeable to the same ion species, but with different kinetic properties. Total ionic current is therefore determined by the net flow of ions through all ion channels, exchangers and pumps. Ion channels typically comprise one or more α subunit(s), which can be modulated through accessory subunits [329]. A summary of the main ion channel currents and their corresponding α subunits is given in Table 2.1.

2.3.3 The cardiac action potential

The action potential (AP) is a fast, transient rise and fall in membrane potential of excitable cardiac myocytes, resulting from the movement of ions through a suite of ion channels, exchangers, and pumps. Atrial and ventricular myocytes are excitable, thus

Table 2.1. Summary of the primary cardiac ion currents, their names, corresponding ion permeabilities, and α subunits.

Symbol	Name	Permeability	α-subunit
I_{Na}	Fast Na^+ current	Na^+	$Na_v1.5$
I_{NaL}	Late Na^+ current	Na^+	$Na_v1.5$
I_{CaL}	L-type Ca^{2+} current	Ca^{2+}	$Ca_v1.2/1.3$
I_{CaT}	T-type Ca^{2+} current	Ca^{2+}	$Ca_v3.1$
I_{to}	Transient outward K^+ current	K^+	$K_v4.3/4.2$
I_{Kur}	Ultra-rapid delayed rectifier K^+ current	K^+	$K_v1.5$
I_{Kr}	Rapid delayed rectifier K^+ current	K^+	$K_v11.1$
I_{Ks}	Slow delayed rectifier K^+ current	K^+	$K_v7.1$
I_{K1}	Inward rectifier K^+ current	K^+	Kir2.1/2.3
I_{SK}	Small conductance Ca^{2+}-activated K^+ current	K^+	KCa2.2
$I_{\mathrm{Kv1.1}}$	Kv1.1-mediated K^+ current	K^+	$K_v1.1$
I_{KATP}	ATP-sensitive K^+ current	K^+	Kir6.2
$I_{\mathrm{K,ACh}}$	Acetylcholine-activated K^+ current	K^+	Kir3.1
I_{f}	Hyperpolarisation-activated (‘funny’) current	Na^+,K^+	HCN1/4
I_{NaCa}	Na^+-Ca^{2+} exchanger current	Na^+,Ca^{2+}	NCX1
I_{NaK}	Na^+-K^+ pump current	Na^+,K^+	NaKα1/2/3
I_{CaP}	Ca^{2+} pump current	Ca^{2+}	Ca^{2+}

normally only generate APs when stimulated electrically. Conversely, pacemaking cells, such as those found in the SAN, are autorhythmic and spontaneously generate oscillatory APs [242]. For excitable cells, the AP is generated only when the membrane potential reaches a certain threshold value, and it then propagates between electrically-coupled cells like a wave.

Though there is heterogeneity in AP morphology between different heart regions and across different species [135], a typical cardiac action potential can be divided into five distinct phases (four for the pacemaking cells, such as in the SAN). The overall morphology of the AP is determined by the summation of each ionic species and associated currents. Figure 2.4 illustrates the AP waveforms of ventricular and atrial myocytes, as well as the underlying currents. Phase 0, the upstroke of the action potential, is the initial rapid depolarisation of the membrane to a positive potential, resulting from a supra-threshold

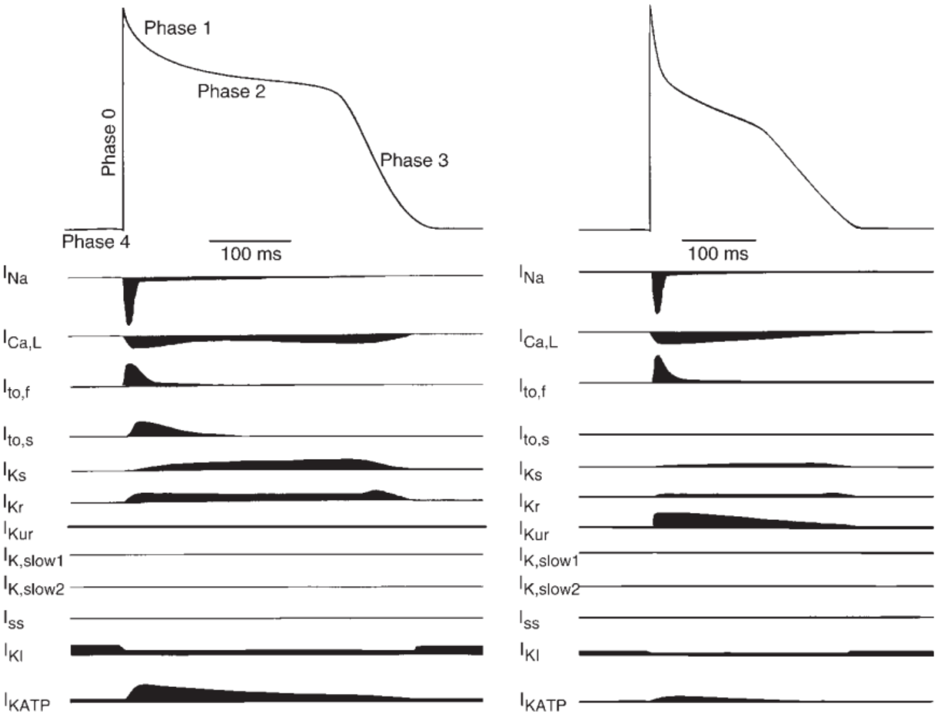

Figure 2.4. Comparison of inward and outward currents underlying the ventricular (left) and atrial (right) myocyte action potentials. Fast and slow components of I_{to} are illustrated, as well as other K$^+$ currents ($I_{\mathrm{K,slow}}$, I_{ss}) which may be present only in certain species. I_{NaCa} also plays an important role in determining AP morphology but is not shown. From [270].

electrical stimulus triggering rapid influx of Na$^+$ ions via the fast sodium current, I_{Na}. I_{Na} quickly inactivates as the membrane potential reaches the equilibrium potential for Na$^+$. Phase 1 then follows, which is an initial rapid repolarisation underlain by the transient outward potassium current, I_{to}, which represents K$^+$ efflux. A plateau phase (phase 2) then follows, which is maintained by the inward movement of Ca^{2+} through the L-type calcium current, I_{CaL}. This coincides with the activation of outward K$^+$ currents carried by I_{Kr} and I_{Ks}. The final stage of repolarisation, phase 3, occurs as I_{CaL} inactivates and K$^+$ currents predominate, largely driven by the inward rectifier current, I_{K1}. I_{Kr} and I_{Ks} inactivation results in phase 4 of the AP, leading to the resting membrane potential (RMP). The RMP is mainly determined by I_{K1}, but also various background currents ($I_{\mathrm{b_{Na,K,Ca}}}$) and the sodium-calcium exchanger current, I_{NaCa}. Together, these currents result in a stable membrane potential during diastole. In pacemaking cells, the RMP is not stable, and instead the presence of the 'funny' current, I_{f}, and T-type calcium current, I_{CaT}, result in slow diastolic depolarisation of the membrane potential between APs [173].

The action potential is an all-or-nothing phenomenon, as a threshold potential exists under which electrical stimuli do not result in an action potential, but at or above which an action potential will be triggered through phase 0 depolarisation. This phenomenon, termed excitability, is prevalent throughout many biological systems and is critical for the normal functioning of nerve and muscle cells. As the action potential is determined by the various currents crossing the cell membrane through multiple channels that open, close, and inactivate, or *via* pumps and exchangers, the factors that determine ion flow beyond ion channel open/closed states are crucially important. These factors will be discussed in Section 2.6.3.

As well as heterogeneity in AP morphology between different regions of the heart, there exist species differences in ion channel expression throughout the heart. As a result, even different mammalian myocytes from the same region have markedly different AP morphologies [342]. In larger mammalian myocytes, such as human and canine, the action potential is described as having a ‘spike and dome’ morphology (illustrated in Figure 2.4), caused by a reduced repolarising I_{to} current and a larger, and longer-lasting, inward I_{CaL}. Conversely, in smaller mammals such as the mouse and rat, the action potential is described as having a more ‘triangular’ shape, with I_{to} being the main repolarising current [111]. This diversity in AP configuration means that, as smaller-mammalian species are commonly used in the laboratory in cardiovascular research, research findings and, importantly, drug effects, can not necessarily be extrapolated between species [408]. Nevertheless, smaller-mammalian species, particularly rats, are a common animal model used experimentally (see Chapter 4).

2.3.4 Calcium cycling and excitation-contraction coupling

Contraction of cardiac muscle is the result of Ca^{2+} ions binding to contractile myofilaments in the cytoplasm, and relaxation comprises the dissociation of Ca^{2+} from these myofilaments. As contraction occurs 60 to 100 times per minute at rest, this cycle of Ca^{2+} binding and unbinding to myofilaments must happen very quickly, and be tightly regulated so that there are no aberrations or disturbances to the normal cycle. Ca^{2+} ions, however, do not simply enter and then leave the cell via one, or several, ion channels or pumps, unlike other ions such as Na^{+} and K^{+}. Cardiac myocytes have an intracellular structure known as the sarcoplasmic reticulum (SR), which is an internal store of Ca^{2+} and

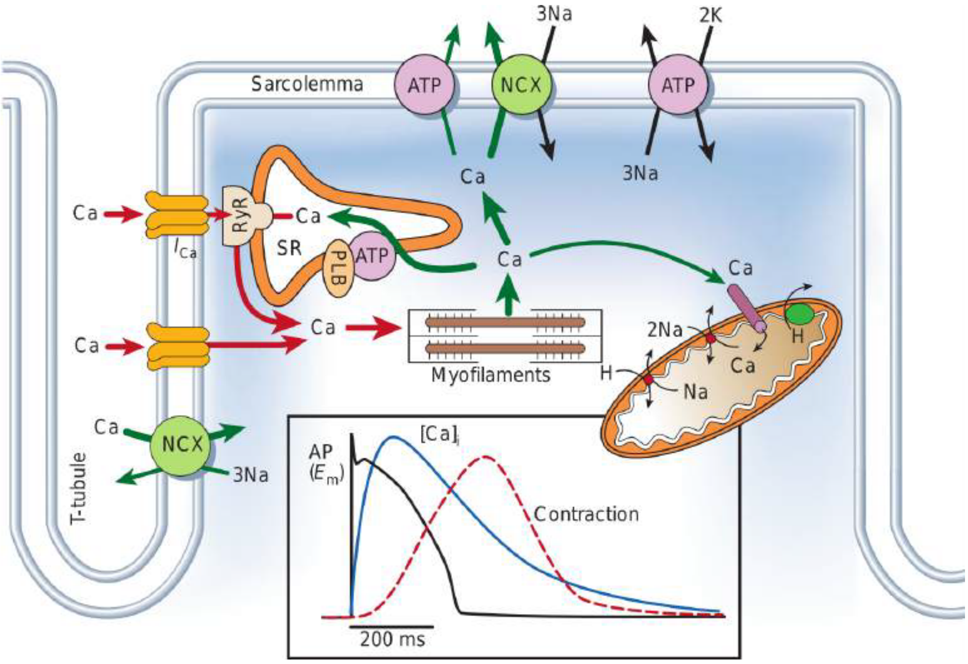

Figure 2.5. Schematic of excitation-contraction coupling in cardiac myocytes. Ca^{2+} entry through the L-type Ca^{2+} channel (I_{CaL}) results in further release of Ca^{2+} from the sarcoplasmic reticulum (SR) through ryanodine receptors (RyRs). Ca^{2+} then binds with myofilament proteins to initiate contraction. $[Ca^{2+}]_i$ is then restored by the SR Ca^{2+}-ATPase on the SR membrane, and the Na^+-Ca^{2+} exchanger (I_{NaCa}) and Ca^{2+}-ATPase (I_{CaP}) on the sarcolemmal membrane. Inset shows the time course of the AP, the resulting calcium transient and developed tension. From [42].

plays a pivotal role in the process of excitation-contraction coupling (Figure 2.5). During the plateau phase of the AP, Ca^{2+} ion influx through I_{CaL} causes the SR to release further Ca^{2+} into the cytoplasm through ryanodine receptors (RyRs, which are Ca^{2+}-sensitive channels embedded within the SR membrane) through the process of calcium-induced calcium release (CICR). RyR proteins are located proximal to the L-type Ca^{2+} channels forming a segment known as a dyad, or calcium release unit (CRU). Specifically, it is the junctional portion of the SR (jSR) that forms the dyad with the L-type Ca^{2+} channel [209] (the remainder is termed the 'network' SR, nSR, and spans the bulk cytoplasm). The diffusion of Ca^{2+} through the cytoplasm raises the intracellular Ca^{2+} concentration, $[Ca^{2+}]_i$, to form the Ca^{2+} transient, and binding of Ca^{2+} to myofilaments then occurs to result in contraction [42]. $[Ca^{2+}]_i$ is restored to normal resting levels by the SR Ca^{2+}-ATPase [55] (SERCA, $\sim 80\%$), which pumps Ca^{2+} back into the SR, the Na^+-Ca^{2+} exchanger, which exchanges intracellular Ca^{2+} for extracellular Na^+ in normal conditions (I_{NaCa}, $\sim$ 18-

19%), the sarcolemmal Ca^{2+}-ATPase [3] (I_{CaP}, $\sim$ 1-2%), and the mitochondrial Ca^{2+} uniporter [28] ($<$1%).

In Figure 2.5, a structure known as the T-tubule can be seen. Transverse (T)-tubules are invaginations of the sarcolemmal membrane that penetrate deep into cardiac cells, along which L-type Ca^{2+} channels are positioned so that they are in close coupling with RyRs. This ensures a rapid and near-synchronous rise in $[Ca^{2+}]_i$ following excitation, triggering CICR and resultant contraction, collectively referred to as excitation-contraction (EC) coupling. Many other proteins involved in EC-coupling are concentrated along the T-tubules [64] and they play a critical role in cardiac ventricular function. Though previously thought to be absent from atrial myocytes, it was recently shown that T-tubules are present in atrial myocytes of larger mammals, including human [324]. T-tubule remodelling, in diseases such as heart failure and ischaemia, is now known to result in abnormal Ca^{2+} handling and dyssynchrony between electrical excitation and contraction [232].

Grossly, cardiac muscle consists of muscle fibres, each of which comprises thousands of myofibrils which can actively shorten to produce contraction. Each myofibril contains thousands of thick (myosin) and thin (actin) filaments (collectively called myofilaments) which are adjacent to each other. At the end of each muscle fibre, the myofibrils are anchored to the inner surface of the muscle cell membrane, called the sarcolemma, thus contraction of the myofibrils results in cell shortening. The functional unit of the muscle is called the sarcomere, which is the portion of the myofibril lying between two successive Z-lines, which are the sections to which actin filaments are bound. The existence of the Z-lines gives muscle a striated appearance. It is the interaction of myosin heads, which protrude from the thick filament at regular intervals, with the actin filaments, that causes contraction – these interactions are known as ‘cross-bridges’ [243].

Three protein complexes make up the actin filaments: actin, tropomyosin, and the calcium-dependent troponins (troponin I, C and T, Figure 2.6). Tropomyosin wraps around actin, obscuring myosin binding sites during the relaxed phase. Troponin I secures the actin-tropomyosin complex, troponin T binds to tropomyosin to form the troponin-tropomyosin complex, and troponin C binds Ca^{2+} ions [250]. A rise in $[Ca^{2+}]_i$ following SR Ca^{2+} release results in conformational changes in the binding of the troponins to tropomyosin, ultimately uncovering the myosin binding site on actin, permitting the formation of actin-myosin cross-bridges [287]. The cross-bridge cycle then follows. Briefly, the initial binding of myosin to actin to form a cross-bridge is weak and results in the release of

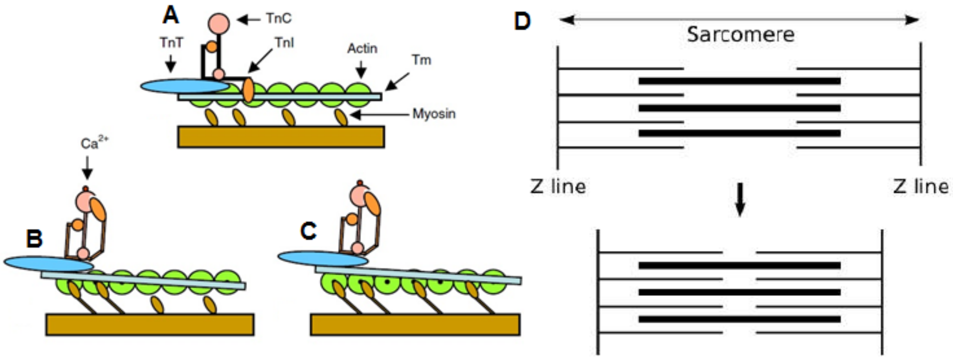

Figure 2.6. Schematic of contraction at the thin filament. (A) In the absence of Ca^{2+} the myosin binding site is blocked by tropomyosin. (B) Binding of Ca^{2+} to troponin C alters the troponin C-I interactions, relieving inhibition by tropomyosin and allowing myosin to bind weakly and cross-bridges to form. (C) Stronger myosin binding exposes further myosin binding sites, allowing more cross-bridge formation. (D) The sarcomere goes from a relaxed to a contracted state. TnT, troponin T; TnC, troponin C; TnI, troponin I; Tm, tropomyosin. Figure adapted from [287] and [67].

inorganic phosphate (P_i), leading to a strongly-bound state which precedes the force-generating powerstroke phase, in which ADP is released [107, 287]. An ATP molecule then binds to the myosin head, weakening the actin-myosin link such that the myosin head detaches [245]. The myosin head then hydrolyses ATP, utilising the energy to return to the pre-powerstroke position [174]. As this cycle continues, the thin filaments move closer to the centre of the thick filaments, so the sarcomere contracts. This process is known as sliding filament theory of muscle contraction [102].

2.3.5 Action potential propagation

Cardiac myocytes are coupled adjacently via intercalated discs; specialised junctions which allow the entire myocardium to function as a single organ [264] (cardiac myocytes are often described as acting as a functional syncytium). Intercalated discs allow cell-to-cell electrical coupling through gap junctions, which are clusters of intracellular channels formed by connexin proteins that directly couple the cytoplasm of neighbouring myocytes [178]. This electrical coupling permits AP propagation throughout the heart. It has been shown that conduction slowing, as a result of gap junction uncoupling, could underline arrhythmogenesis in various conditions, such as ischaemia or heart failure [161,304,359]. Action potentials, however, do not propagate isotropically throughout the myocardium; as cardiac myocytes are arranged in fibres longitudinally, with gap junctions found principally at the ends of myocytes, APs propagate considerably faster parallel to fibres than perpendicular to them [405].

2.4 Experimental/clinical cardiology

2.4.1 Action potential characteristics

In order to compare APs between different species, regions, and disease states, it is important to have a consistent method of characterising various aspects of the cardiac AP. The most widely used biomarkers of the cardiac AP for cardiomyocytes are illustrated in Figure 2.7 and described below (typical values provided in humans):

- **Action potential duration (APD):** a measure of repolarisation, typically defined as the time interval between the maximal upstroke velocity and a given percentage of repolarisation of membrane potential, e.g. 90% (APD_{90}) or 50% (APD_{50}). Typically between 200 and 400 ms.
- **Resting membrane potential (RMP):** the stable (resting) diastolic membrane potential of a non-pacemaking myocyte. Typically between -90 and -60 mV.
- **Overshoot (OS):** the maximum membrane potential reached during the AP upstroke. Typically between 10 and 50 mV.
- **Action potential amplitude (APA):** the total size of the transmembrane potential, equal to the difference between the RMP and OS. Typically between 90 and 120 mV.
- **Maximum upstroke velocity (MUV):** the maximum rate of change of membrane potential during the AP, commonly referred to as $\mathrm{d}V/\mathrm{d}t_{\mathrm{max}}$. Typically between 100 and 300 V/s.
- **Cycle length (CL, or basic cycle length, BCL):** the time interval between successive APs. Typically 700 to 1000 ms.

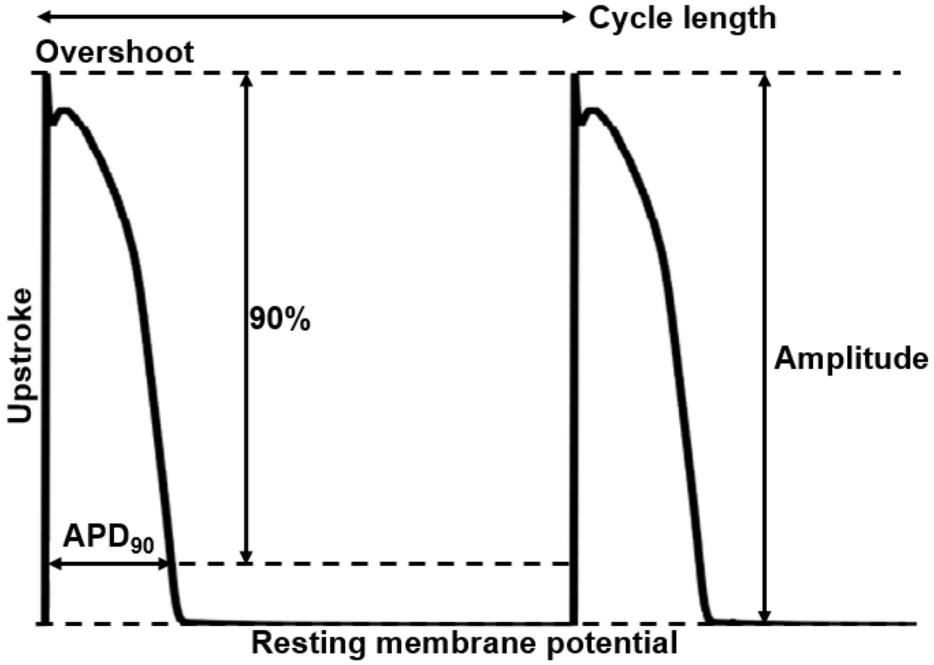

Figure 2.7. Schematic showing biomarkers used to characterise cardiac action potentials. Diagram shows biomarkers as applied to two typical human action potentials.

2.4.2 Refractoriness and re-entry

An important property of cardiac action potentials is refractoriness. The absolute refractory period in cardiac myocytes is the period during which a subsequent AP cannot be elicited, irrespective of stimulus strength. The relative refractory period follows, during which a small AP can be elicited given certain conditions. Collectively, these periods are termed the effective refractory period (ERP), which is generally defined as the duration over which a stimulus applied after AP initiation will fail to produce a propagating AP. The ERP protects against premature stimuli in the heart, which can be pro-arrhythmic [436]. The ERP prevents sustained tetanic contraction of cardiac muscle, allowing for diastole and a normal pumping action.

Re-entry describes a self-perpetuating propagating wave of electrical excitation in the heart in a rapid circuitous movement. Re-entry is typically caused by heterogeneity in refractoriness, and requires unidirectional block in cardiac tissue. Consider a 2D patch of cardiac tissue as shown in Figure 2.8, the bottom edge of which has an electrical stimulus applied. This results in a uniformly-propagating planar wave of excitation across the tissue, travelling from the bottom to the top of the tissue and therefore creating a gradient

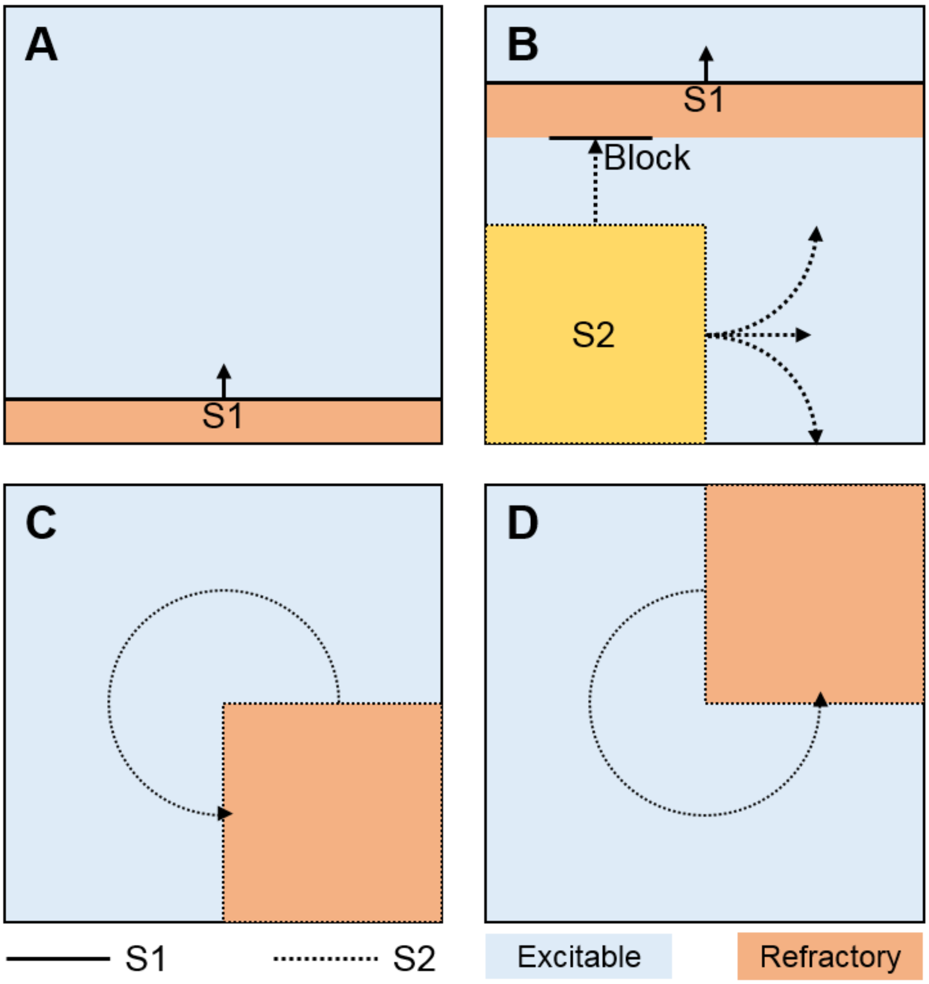

Figure 2.8. Illustration of re-entry initiation in a 2D patch of tissue. (A) A stimulus (S1) is applied to one edge of the tissue to initiate a normal wave of propagating electrical excitation. (B) A second stimulus (S2, yellow) applied to the lower left quadrant of the tissue induces unidirectional conduction block as the area behind the S1 wavefront (red) is still refractory. The S2 wavefront propagates laterally and begins to travel vertically. (C) The excitation wave re-excites the upper half of the tissue as it has now recovered from S1 excitation. The site of origin of the S2 stimulus has also recovered, generating a re-entrant circuit as the wave continues to loop back on itself (D). S1 and S2 denote 1st and 2nd stimulus, respectively.

in ERP parallel to the direction of activation. A second, premature stimulus applied to a localised region of the tissue in the wake of the excitation wave results in conduction block in the direction parallel to wave propagation if applied when the lower half of the tissue is excitable again but the upper half of the tissue is still refractory. Propagation is therefore only permitted in the perpendicular direction, and the initiated wave of excitation spreads outwards to re-excite the upper half of the tissue patch once it has repolarised. As the region in which the second stimulus was applied is now recovered, the wave circles back on itself to form a self-sustaining spiral wave re-entry. Unidirectional conduction blocks such as this may also result from structural abnormalities, in which an infarcted region of tissue, for example, forms an anatomical circuit around which electrical excitation may propagate.

2.4.3 Action potential restitution

Action potential duration restitution is an inherent property of cardiac tissue that describes the adaptation to changes in heart rate of APD, which is thought to preserve diastole at faster heart rates such as during exercise [433]. At rest, the APD of a cardiac myocyte can be longer than the cycle length at the fastest heart rate, therefore if the resting APD was maintained at fast heart rates (i.e. there was no adaptation to rate), block of the heartbeat would occur. Adaptation of APD to pacing rate maintains proper contraction and pumping of blood under varying physiological conditions. From a functional perspective, restitution is a reflection of the inability to fully recover from inactivation of some ion channels before the subsequent action potential, resulting in a decreased current if the next stimulus occurs before full recovery.

The APD restitution curve (Figure 2.9), first described in [285], details the time-dependent recovery of APD as a function of the diastolic interval (DI) [142]. Many studies have shown that a steep APD restitution curve can give rise to pro-arrhythmic alternans (beat-to-beat oscillations in APD), as changes in DI have a larger effect on the subsequent APD [145,261]. For a steep restitution curve and a constant CL (CL = APD + DI), shortening of DI leads to a consequently short APD during the next cycle, resulting in a long DI (as CL is constant). A long APD and short DI then follows, giving a stable alternation. Conversely, variations in APD rapidly diminish for a shallow restitution curve.

There are two main protocols used to generate restitution curves. In the more common S1-S2 restitution protocol, the cell/tissue preparation is paced at a fixed CL (S1) until steady-state is achieved, but is then perturbed by a subsequent stimulus (S2) after a variable-length interval. The preparation is then paced to steady-state at S1 again, before being perturbed by a different S2 stimulus. The restitution curve is then formed

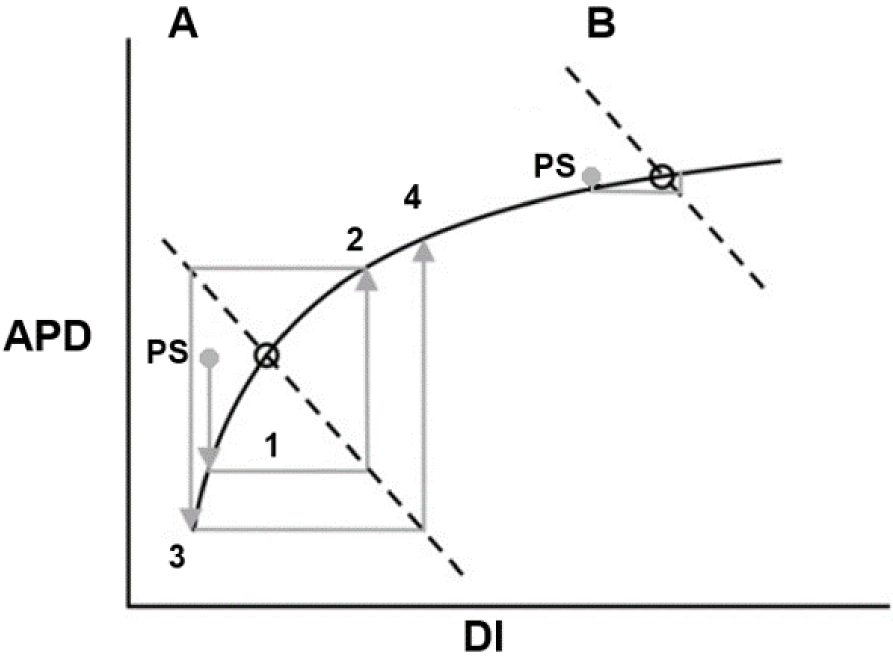

Figure 2.9. Principles of APD restitution. (A) indicates a system operating on a steep part of the APD restitution curve. Application of a premature stimulus (PS, filled circle) results in a short DI and thus short APD (1), resulting in a subsequently long DI (2) that dictates a shorter APD (3) and finally a longer DI (4). Because the curve is steep, the resultant fourth beat is likely to be skipped as conduction block occurs when the DI becomes so short that the stimulus arrives in the absolute refractory period. (B) Indicates a system operating on a flat part of the APD restitution curve. The same premature stimulus (filled circle) has a negligible effect on APD and does not result in alternans. Dashed line satisfies the condition cycle length (CL) = APD + DI. Adapted from [261].

by plotting the relevant APDs and DIs as determined by the application of S2 stimuli. Using this protocol, it is possible to obtain a number of restitution curves over a range of S1 cycle lengths, to quantify short-term cardiac memory [313]. In the dynamic (also known as steady-state) protocol, the preparation is paced at a given CL until steady-state is achieved, and the resulting APD and preceding DI are recorded. This process is then repeated with other cycle lengths [203]. While the S1-S2 protocol is a measure of the immediate response of APD to changes in cycle length, the dynamic protocol is a steady-state response measurement and can be used to detect alternans [203, 400].

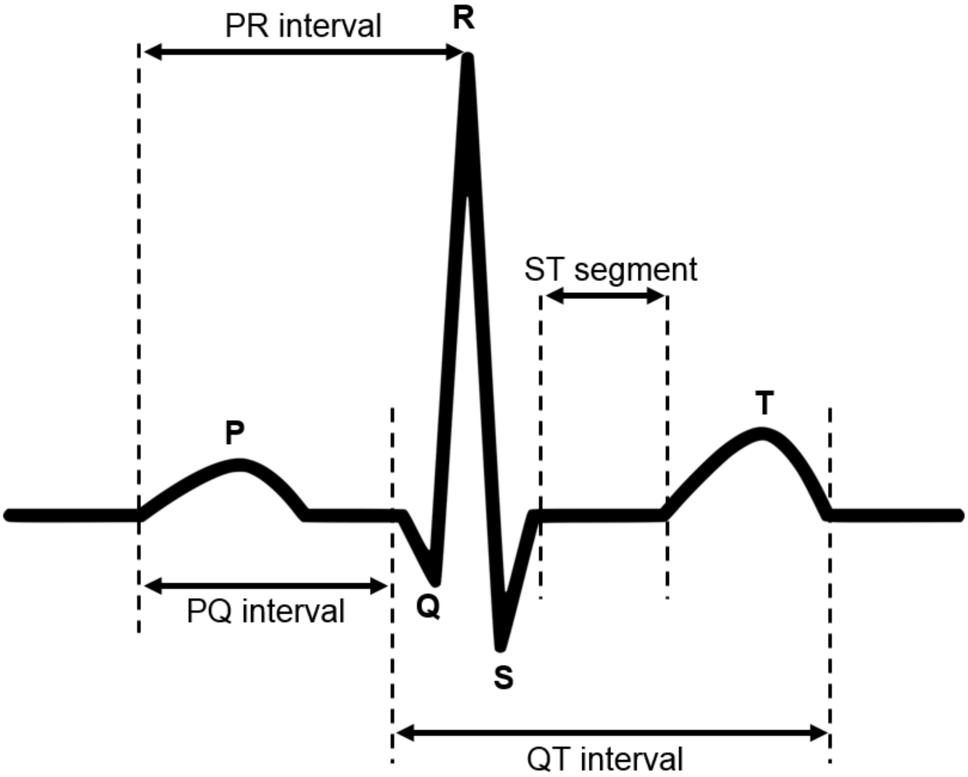

Figure 2.10. Diagram showing the clinical ECG and associated intervals. The PR interval (typically between 120 and 200 ms) represents conduction time through the AVN. The QRS complex (typically between 60 and 100 ms) represents ventricular depolarisation. The ST segment (typically between 5 to 150 ms) represents the isoelectric period between ventricular depolarisation and repolarisation. The QT interval (typically between 350 and 450 ms) represents the full duration of ventricular depolarisation and repolarisation.

2.4.4 The ECG

Electrocardiography is an extremely important tool in the clinical cardiology field, as the interpretation of the electrocardiogram (ECG) forms the basis of many diagnoses and treatments of electrical disorders of the heart. The ECG is an external measure of the internal electrical activity of the heart, so is a painless and non-invasive routine procedure in the clinic. The ECG waveform is illustrated in Figure 2.10 and is comprised of distinct phases, representing activation and recovery of different regions of the heart. The first region, the P wave, represents atrial depolarisation, with the early part of the P wave representing the AP of the SAN. Then follows the QRS complex, which is triphasic and corresponds to activation of the ventricles. Atrial repolarisation also happens at this time, but the larger mass (and therefore larger signal) of the QRS complex dominates and atrial repolarisation cannot be visualised. The final region of the ECG is the T wave, representing ventricular repolarisation.

Because of the distinct regions of the ECG waveform, various intervals can be measured which can be useful in clinical diagnoses of heart problems. The PQ interval, measured from the start of the P wave to the first deflection of the QRS complex, represents atrial depolarisation and AV node conduction, thus the total conduction time of excitation waves before reaching the ventricles. A prolonged PR interval is therefore indicative of AVN dysfunction. The duration of the QRS complex is also an important biomarker; as prolonged QRS duration may indicate conduction defects or the presence/origin of arrhythmias. Lastly, the QT interval is defined as the period between onset of the QRS complex and the end of the T wave, therefore represents the total time of electrical activation and recovery of the ventricles. Abbreviation or prolongation of the QT interval results in the short or long QT syndromes, respectively, which are associated with increased incidence of lethal ventricular arrhythmias, and so the QT interval is a crucial biomarker for the risk of sudden cardiac death [109, 160].

2.5 Cardiac arrhythmias

In health, electrical impulses in the heart propagate in a regular manner, ensuring rhythmic, coordinated contraction of the myocardium. Normal variations in rhythm are common, such as due to inspiration and expiration, or during exercise, however serious aberrations in heart rhythm, known as arrhythmias, are a major cause of morbidity and mortality.

2.5.1 Bradycardia and tachycardia

Bradycardia refers to an abnormally low heart rate, typically less than 50 bpm [7]. Bradycardic patients may experience weakness, dizziness, fatigue, and syncope. Severe or chronic forms of bradycardia may lead to heart failure, as the heart is unable to pump sufficient blood to the body, cardiac arrest and sudden cardiac death. Bradycardia is typically treated with pacemaker therapy [243].

Tachycardia refers to an abnormaly fast heart rate, typically defined as greater than 100 bpm at rest [243]. Tachycardic patients may experience chest pain (resulting from the increased workload placed on the heart), palpitations, hypotension, dyspnoea, and syncope. Persistent tachycardias may result in electrical and structural remodelling, which may predispose to the development of fibrillation, and sustained ventricular tachycardias are the commonest cause of sudden cardiac death [343]. Re-entrant activity may result in the development of tachycardias.

2.5.2 Ectopic beats and AV node block

Another common variation in normal heart rhythm is the presence of extra beats (termed ectopic beats or extrasystoles), which may be produced by the aberrant firing of groups of cells in the ventricles prior to the SAN [264]. These ectopic beats may mean that the subsequent SAN-generated heart beat is skipped, as cardiac tissue is still refractory, so there is a compensatory pause observed in the ECG, and the following heart beat may be felt as a palpitation as the heart has had longer time to fill and so contracts more forcefully. Ectopic beats are typically harmless, but under certain conditions may preclude more serious arrhythmias.

Problems in the pacemaking regions of the heart can result in different types of heart block, leading to abnormal heart rhythms. First-degree AV block occurs when conduction through the AVN is slowed, extending the PR interval and exerting a bradycardic effect. Second-degree AV block occurs when not all P waves result in QRS complexes, which may occur at regular intervals (e.g. 2:1 if the ventricles are excited by every second P wave). Type 1 second-degree AV block (also known as Wenckebach periodicity or Mobitz I) results from AVN disease, whereas type 2 second-degree AV block (Mobitz II) typically results from His-Purkinje system disease [253, 254]. Finally, third-degree AV block occurs when the atria and ventricles are excited separately and beat independently. In third-degree AV block, the atria will beat faster than the ventricles, which will only beat at the fastest ventricular pacemaker rate (usually about 30 bpm, set by cells in the Purkinje fibres) [264].

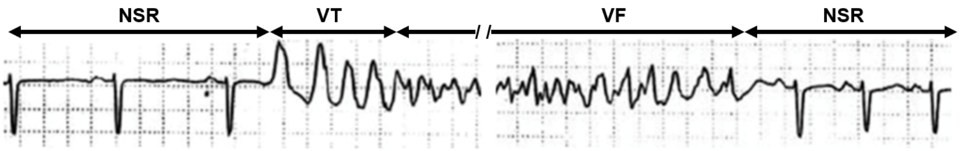

Figure 2.11. ECG showing transition from sinus rhythm to ventricular tachycardia and fibrillation. An ECG showing the transition of a patient from normal sinus rhythm to ventricular tachycardia, then into a self-terminating ventricular fibrillation back to sinus rhythm. NSR, normal sinus rhythm; VT, ventricular tachycardia, VF; ventricular fibrillation. Adapted from [312].

2.5.3 Fibrillation

Fibrillation (Figure 2.11) refers to the rapid and chaotic electrical activation of the heart, resulting in contractile dysfunction. Fibrillatory activity is typically driven by either local ectopic foci or re-entrant circuits. Local ectopic foci result in rapid activation of the surrounding tissue, driving fibrillatory activity, whereas re-entrant circuits (either one single, or multiple circuits) maintain fibrillatory activity [10,85]. Fibrillation can be distinguished from tachycardia on the ECG by the lack of organised ECG waveforms. Atrial fibrillation is the commonest cardiac arrhythmia, resulting in increased morbidity, and can persist for many months or years [266]. Atrial fibrillation also results in increased mortality, although indirectly by increasing, for example, the risk of stroke. Ventricular fibrillation, conversely, results in loss of cardiac output, and is lethal unless treated immediately [85].

2.5.4 Anti-arrhythmic therapies

A wide range of drugs are able to influence heart rate and rhythm in order to treat arrhythmias. Many act by blocking ion channels responsible for the cardiac AP, or by affecting receptors which regulate the hormonal or nervous control of the heart rate and the force of contraction. Thus, the choice of anti-arrhythmic drug must be tailored to the underlying arrhythmogenic mechanism, i.e. whether to target impulse generation, propagation, or both [271]. The Vaughan-Williams classification of anti-arrhyhtmic drugs is the most common system [264], with the main classes detailed below:

- **Class Ia:** Na^+ (open) channel blockers which lengthen the action potential, such as quinidine and disopyramide.

- **Class Ib:** Na^+ (inactivated) channel blockers which shorten the action potential, such as lidocaine and mexiletine.
- **Class Ic:** Na^+ (open) channel blockers which slow conduction speed and the upstroke of the action potential, such as flecainide.
- **Class II:** β-adrenoceptor antagonists which reduce the slope of the pacemaker potential in the SAN, such as propranolol and atenolol.
- **Class III:** K^+ channel blockers which prolong the action potential by slowing repolarisation, such as amiodarone.
- **Class IV:** Ca^{2+} channel blockers which reduce AVN conduction, such as verapamil and diltiazem.

2.6 Modelling ventricular electrophysiology

2.6.1 Cell biophysics

The cell membrane, composed of a phospholipid bilayer, separates the interior of a cell from its exterior, and is selectively permeable to ions and molecules. If the concentration of an ion inside the cell is different to that outside, an electrical potential develops, termed the Nernst potential. It is possible to calculate this potential across a membrane using the Nernst equation:

$$E = -\frac{RT}{zF}\ln\frac{[X]_\mathrm{o}}{[X]_\mathrm{i}} \tag{2.1}$$

where E is the Nernst potential, R is the universal gas constant (8.314 $\mathrm{J.K^{-1}.mol^{-1}}$), T is the absolute temperature (K), z is the valency of the ion species, F is the Faraday constant (96,485 $\mathrm{C.mol^{-1}}$), and $[X]_\mathrm{o}$ and $[X]_\mathrm{i}$ are the extracellular and intracellular concentrations of the ion species X, respectively. The Nernst potential (E) gives the membrane potential at which the ionic species is in equilibrium, i.e. there is no net movement of the ion across the membrane, and can also be called the reversal potential (E_rev) – a change in membrane potential on either side of this reverses the overall direction of ion flux. For a single ion system, the Nernst (and so also the reversal) potential is synonymous with the equilibrium potential (E_{eq}), as there is no net ion flux at this potential, so $E = E_{\text{eq}} = E_{\text{rev}}$.

For a given ionic species, the electrochemical gradient is the difference between the membrane potential and the equilibrium potential, $V - E_{\text{eq}}$, with the direction of flow determined by the sign of this gradient. Assuming only one ionic species can traverse the membrane, the electrochemical gradient causes V to move towards E_{eq}. There is no net flow when $V = E_{\text{eq}}$, and the electrochemical gradient (and so the flow of ions) will reverse if V exceeds E_{eq}.

Table 2.2. Ionic species and their Nernst potentials in cardiac myocytes.

Ion	Intracellular concentration (mM)	Extracellular concentration (mM)	Nernst potential (mV)
K^+	~ 140	~ 4	-95
Na^+	~ 10	~ 145	+70
Ca^{2+}	~ 0.0001	1.5	+128

Because $[K^+]_i$ is high at rest and so E_K is negative, K^+ ions leave the cell through K^+ channels during an action potential, generating an outward current. Conversely, low $[Na^+]_i$ and $[Ca^{2+}]_i$ results in inward currents as a result of their positive Nernst potentials. These ion gradients are maintained by a suite of ion pumps, such as the Na^+-Ca^{2+} exchanger and the Na^+/K^+-ATPase, keeping the cell polarised and maintaining excitability. The resting membrane potential in ventricular myocytes ($\sim$ -80 mV) lies close to E_K as Na^+ and Ca^{2+} channels are almost completely closed at very negative potentials.

Equilibrium potentials are not, however, properties of single ion channels. Channels are often permeable to more than one ionic species – the L-type Ca^{2+} channel, for example, is permeable to Na^+ and K^+ alongside Ca^{2+}. The reversal potential of a current, therefore, is the result of several equilibrium potentials interacting. For a single channel permeable to only one ion species, though, the reversal potential of that channel will be the same as the corresponding ion species' equilibrium potential. The Goldman-Hodgkin-Katz (GHK) equation is used to calculate the reversal potential where multiple ionic species exist:

$$E_{\text{rev}} = \frac{RT}{F} \ln \left(\frac{P_{\text{Na}}[\text{Na}^+]_o + P_K[K^+]_o + P_{\text{Cl}}[\text{Cl}^-]_i}{P_{\text{Na}}[\text{Na}^+]_i + P_K[K^+]_i + P_{\text{Cl}}[\text{Cl}^-]_o} \right) \tag{2.2}$$

where P_X is the permeability of the channel to ion X.

The GHK equation can also be utilised to calculate the resting membrane potential and the direction in which membrane potential will move if permeabilities of the ion species are altered. Membrane potential will tend to move towards the equilibrium potential of the ionic species with the greatest permeability, as the equilibrium potential of that ion will dominate E_{rev}. For a resting cardiac myocyte, $P_{\mathrm{K}} > P_{\mathrm{Na}}$ and so membrane potential will move towards E_{K} ($\sim$-90 mV), though not all the way. When the cell is depolarised beyond the threshold and Na^{+} channels open, $P_{\mathrm{Na}} > P_{\mathrm{K}}$ and so membrane potential moves from this resting value to a more positive potential, towards E_{Na} ($\sim$+80 mV). This results in phase 0 depolarisation, and an AP follows.

2.6.2 Electrical circuit theory

The first mathematical model of the AP was developed by Hodgkin and Huxley in the early 1950s, in a series of five papers [167–169, 171, 172]. Using space clamping (which removes spatial gradients in membrane potential by the insertion of a thin metallic conductor along the axon in order to provide low axial resistance) and voltage clamping (keeping membrane potential at a fixed 'command' potential by applying feedback currents to the cell) they detailed the dynamics of the ionic conductances underlying the AP of the squid giant axon. The proposed model consisted of a set of nonlinear ordinary differential equations (ODEs) that treat the cell membrane as an electrical circuit to describe the movement of ions through voltage-gated channels that underlie the AP. The Hodgkin-Huxley electrical circuit model remains widely used to this day as, despite being based on the squid giant axon, the underlying electrophysiological and biophysical principles are similar to those in cardiac electrophysiology.

The basic framework for electrical circuit models of cardiac myocytes is illustrated in Figure 2.12. Here, the cell membrane is represented as an equivalent circuit. The lipid bilayer forming the cell membrane is represented as a capacitor, as it acts to separate charge over a minute distance, and is therefore assigned a capacitance value, C_{m}. Voltage-gated ion channels are arranged in parallel and represented by nonlinear conductance values, g_{n}, which are time- and voltage-dependent. Leak channels are represented by a linear conductance, g_{L}. The arrangement of these ions in parallel assumes that they are independent of one another. Ions flow through ion channels as a result of their electrochemical gradient, represented by batteries, E. The model developed by Hodgkin-Huxley (Figure 2.12)

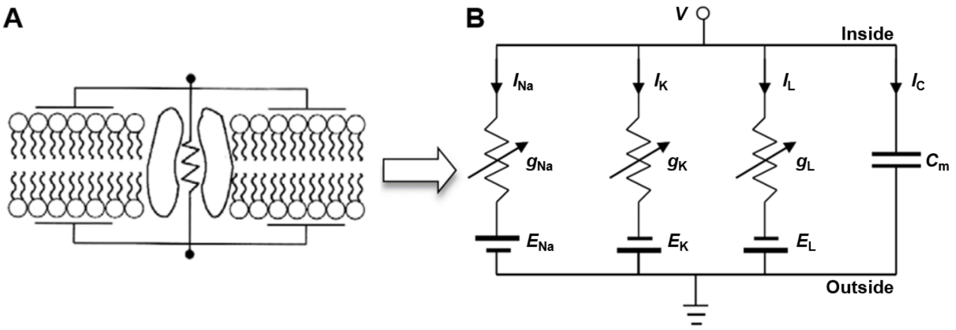

Figure 2.12. Electrical circuit model of a cell membrane. (A) Representation of the cell membrane as a capacitor and ion channel as a conductor. (B) Electrical circuit model of the squid giant axon. The lipid bilayer has a capacitance, C_m, and the Na^+- and K^+-permeable ion channels are modelled with voltage- and time-dependent nonlinear conductances, $g_{\mathrm{Na/K}}$. The leak current, I_L, has a linear voltage- and time-independent conductance, g_L. Ion flow is driven by electrochemical gradients represented as Nernst potentials, E. I_C, capacitive current. Adapted from [312].

includes a depolarising Na^+ current, I_Na, a repolarising K^+ current, I_K, and a time- and voltage-independent leakage current, I_L [171].

The cell membrane is viewed as a capacitor, and capacitance is defined as the ratio of charge across the capacitor (Q) to the voltage necessary to hold that charge, thus

$$C_\mathrm{m} = \frac{Q}{V}. \tag{2.3}$$

It follows that the current (measured in charge per unit time) is $\mathrm{d}Q/\mathrm{d}t$. In addition, cardiac cell membrane capacitance is typically a constant, 1.0 μF/cm^2. Thus, differentiating with respect to time gives

$$\frac{\mathrm{d}Q}{\mathrm{d}t} = C_\mathrm{m}\frac{\mathrm{d}V}{\mathrm{d}t}, \tag{2.4}$$

and it can be seen that the capacitive current, $\mathrm{d}Q/\mathrm{d}t$, can be expressed as $C_\mathrm{m}\mathrm{d}V/\mathrm{d}t$. As the flow of charge between the inside and outside of the membrane must be conserved, the sum of the capacitive and ionic currents must equal zero according to Kirchoff's current law [25]:

$$C_{\mathrm{m}}\frac{\mathrm{d}V}{\mathrm{d}t}+I_{\mathrm{ion}}=0 \tag{2.5}$$

more commonly represented as

$$C_{\mathrm{m}}\frac{\mathrm{d}V}{\mathrm{d}t}=-I_{\mathrm{ion}}. \tag{2.6}$$

It can therefore be seen that $\mathrm{d}V/\mathrm{d}t$, the rate of change of membrane potential, is determined by the sum of the ionic currents, I_{ion}.

Current flowing through ion channels is calculated using Ohm's law, $V = IR$, and so for a channel permeable to ion x:

$$I_{\mathrm{x}} = g_{\mathrm{x}}\left(V_{\mathrm{m}}-E_{\mathrm{x}}\right), \tag{2.7}$$

where g_{x} is the current's conductance and E_{x} is the equilibrium potential at which net ion flux equals zero. It can therefore be said that flow of current through an ion channel is a product of the ion channel's conductance and the driving force for the ion species (driving force = $V - E_{\mathrm{x}}$).

2.6.3 Hodgkin-Huxley formulation

As mentioned previously, in the Hodgkin-Huxley model, I_{ion} (total ionic current) comprised I_{Na}, I_{K} and I_{L}. Furthermore, an external stimulus current was required in order to elicit an action potential – I_{ext}. Thus, the evolution of membrane potential with respect to time is given by

$$\frac{\mathrm{d}V}{\mathrm{d}t}=\frac{-I_{\mathrm{ion}}+I_{\mathrm{ext}}}{C_{\mathrm{m}}} \tag{2.8}$$

where $I_{\mathrm{ion}} = I_{\mathrm{Na}} + I_{\mathrm{K}} + I_{\mathrm{L}} + I_{\mathrm{ext}}$ in the Hodgkin-Huxley model. Because the single channel instantaneous $I - V$ curves for open Na^{+} and K^{+} channels in the squid giant axon are approximately linear, it is possible to write each current as the product of a conductance and driving force, as in Equation 2.7. It is important to note that Hodgkin and Huxley assumed that the channels were selective for only one ionic species, hence used the equilibrium potentials for the respective channel reversal potentials. They also assumed that the leak current conductance, g_{L}, was constant, such that $g_{\mathrm{L}} = \bar{g}_{\mathrm{L}}$, where $\bar{g}_{\mathrm{L}}$ is the maximal leakage current conductance. Thus, we can write Equation 2.8 as:

$$C_{\mathrm{m}}\frac{\mathrm{d}V}{\mathrm{d}t} = -g_{\mathrm{Na}}(V - E_{\mathrm{Na}}) - g_{\mathrm{K}}(V - E_{\mathrm{K}}) - \bar{g}_{\mathrm{L}}(V - E_{\mathrm{L}}) - I_{\mathrm{stim}}. \tag{2.9}$$

To solve Equation 2.9 it is necessary to calculate the voltage- and time-dependent conductances g_{Na} and g_{K}. Hodgkin and Huxley declared that, for a unit area of membrane (1 cm^2 in their model), a conductance can be given as the product of single channel conductance, γ, the number of channels per unit area of membrane, N, and the single channel open probability, P_{open} which must be between 0 and 1 (which is the same as the fraction of channels in open state). Thus

$$g = \gamma N P_{\mathrm{open}}, \tag{2.10}$$

and as maximal conductance, $\bar{g}$, is determined by the constants γ and N:

$$\bar{g} = \gamma N, \tag{2.11}$$

we can re-write Equation 2.10 as

$$g = \bar{g} P_{\mathrm{open}}. \tag{2.12}$$

Conductance is therefore a product of the maximal conductance, $\bar{g}$, which is constant, and the probability of a channel being in the open state, P_{open}, which is determined by gating variables as described below.

For a simple channel controlled by a single voltage-dependent gate that can either be in the open or closed state (Figure 2.13), the channel moves between the two states with the rate constants α (opening) and β (closing):

$$\text{Closed} \underset{\beta(V)}{\overset{\alpha(V)}{\rightleftharpoons}} \text{Open.} \tag{2.13}$$

Note, however, that a channel can be controlled by multiple gating processes (described later), and these gating processes may not necessarily be voltage-dependent. The L-type calcium channel, for example, exhibits Ca^{2+}-dependent inactivation, and some channels may be gated by mechanical stimuli, such as stretch-activated channels. The probability of a channel being open, P_{open}, is the same as the fraction of total channels (N) in the open state, f, thus $P_{\text{open}} = f$, and $f = 1$ if all channels are open or $f = 0$ is all channels are closed. The rates of opening and closing are therefore

$$\text{Rate of opening} = \alpha_f(1-f), \tag{2.14}$$

$$\text{Rate of closing} = \beta_f f. \tag{2.15}$$

The rate of change of the fraction of channels in the open state is therefore governed by the differential equation

$$\frac{\mathrm{d}f}{\mathrm{d}t} = \alpha_f(1-f) - \beta_f f \tag{2.16}$$

which is the Hodgkin-Huxley formalism for describing a simple gating mechanism. When $\frac{\mathrm{d}f}{\mathrm{d}t} = 0$, the gating variable is said to be in steady-state (f_∞) which is given by

$$f_\infty = \frac{\alpha_\mathrm{f}}{\alpha_\mathrm{f} + \beta_\mathrm{f}}. \tag{2.17}$$

Hodgkin-Huxley type gating variables evolve according to the differential equation

$$\frac{\mathrm{d}f}{\mathrm{d}t} = \frac{f_\infty - f}{\tau_\mathrm{f}} \tag{2.18}$$

where τ_f is the time constant for gate f, i.e. a voltage-dependent time constant which is a measure of the time duration for a gate to reach steady-state following an instantaneous change in voltage. The opening and closing rate coefficients α_f and β_f determine how quickly f reaches its new value; if α_f and β_f are large then τ_f will be small and the rate of change will be fast, and *vice versa*. τ_f is related to α_f and β_f by

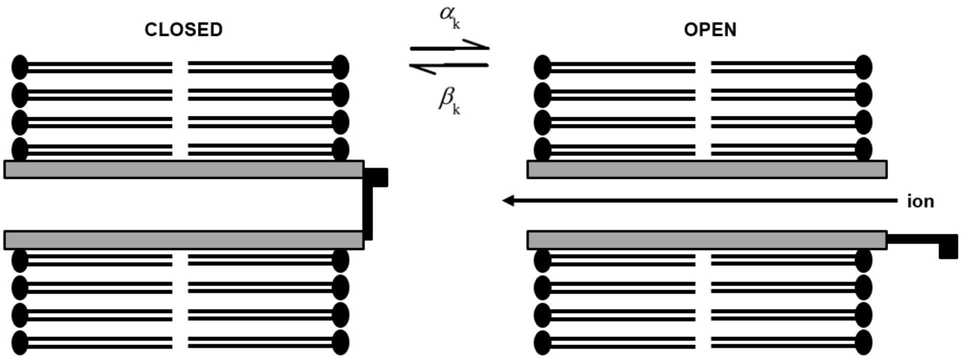

Figure 2.13. Diagram of a simple gating scheme. The channel alternates between open and closed states with rate constants α and β. The gating scheme is not physiological, but provides a useful model for mathematical reconstruction of ion channel gating kinetics.

$$\tau_f = \frac{1}{\alpha_f + \beta_f}. \tag{2.19}$$

To determine the experimental values for α_f and β_f, Hodgkin and Huxley employed a voltage-clamp protocol such that values for α_f and β_f could be determined at particular voltages. When V is clamped to a new voltage, f_∞ and τ_f can be determined, then α_f and β_f calculated as solutions to

$$\alpha_f = \frac{f_\infty}{\tau_f}, \tag{2.20}$$

and

$$\beta_f = \frac{1 - f_\infty}{\tau_f}, \tag{2.21}$$

which are derivations of Equation 2.17 and 2.19. Hodgkin and Huxley then plotted these values as functions of membrane potential and fitted an equation to these data to obtain continuous functions of α_f and β_f. They then used this protocol to determine the time course of the conductances during an action potential, as follows.

It is perhaps easier to start with the K^+ conductance, g_K, as only a single process is involved. From their voltage clamp experiments, Hodgkin and Huxley found that g_K follows a sigmoidal increase upon membrane depolarisation, then follows an exponential decrease to its original value. To model this, they raised a single gating process, as described above, to the fourth power, such that

$$g_{\mathrm{K}} = \bar{g}_{\mathrm{K}} n^4, \tag{2.22}$$

where $\bar{g}_{\mathrm{K}}$ is the experimentally-determined maximal K^+ conductance, and n is the fraction of K^+ channels in the open state (n is also referred to as the K^+ channel gating variable). The fourth power of n gave the best fit to the experimental data, rather than serving a physiological purpose. The rate of change of n is therefore

$$\frac{\mathrm{d}n}{\mathrm{d}t} = \alpha_{\mathrm{n}}(1-n) - \beta_{\mathrm{n}n} \tag{2.23}$$

the solution to which is given by

$$n = n_\infty - (n_\infty - n_0)\exp(-t/\tau_{\mathrm{n}}), \tag{2.24}$$

where n_0 is a steady-state value of n appropriate for the voltage, and the steady-state value of n is

$$n_\infty = \frac{\alpha_{\mathrm{n}}}{\alpha_{\mathrm{n}} + \beta_{\mathrm{n}}}, \tag{2.25}$$

and the time constant as

$$\tau_{\mathrm{n}} = \frac{1}{\alpha_{\mathrm{n}} + \beta_{\mathrm{f}}}. \tag{2.26}$$

For continuous functions of α_{n} and β_{n}, Hodgkin and Huxley determined values for n_∞ and τ_{n} at specific voltages from their experimental results, using forms of Equations 2.24 and 2.22 suitable for fitting to their experimental recordings;

$$g_{\mathrm{K}} = \left\{(g_{\mathrm{K}\infty})^{1/4} - [(g_{\mathrm{K}\infty})^{1/4} - (g_{\mathrm{K}0})^{1/4}]\exp(-t/\tau_{\mathrm{n}})\right\}^4, \tag{2.27}$$

where $g_{\mathrm{K}0}$ is the initial conductance at $t = 0$ and $g_{\mathrm{K}\infty}$ the conductance at the end of the voltage pulse. n_∞ was then given by $g_{\mathrm{K}\infty}$, as a fraction of the maximal $g_{\mathrm{K}\infty}$ attained during the voltage clamp experiments. Values for τ_{n} at particular voltages were chosen to give the best fit to experimental data. α_{n} and β_{n} were then calculated at each voltage using Equations 2.20 and 2.21 and plotted against voltage to generate best fit functions. These voltage-dependent functions are shown in Figure 2.14 and are as follows:

$$\alpha_{\mathrm{n}} = 0.01 \frac{10 - v}{\exp \frac{10 - v}{10} - 1}, \tag{2.28}$$

and

$$\beta_{\mathrm{n}} = 0.125 \exp \left(\frac{-v}{80} \right), \tag{2.29}$$

where v is the devitation of membrane potential, V, from rest in mV, i.e. $V = V_{\mathrm{rest}} + v$.

For modelling the experimentally recorded Na^{+} conductance, Hodgkin and Huxley deduced that two processes were at work; the first being responsible for an increase in conductance, and the second causing conductance to decrease, such that during a change in voltage clamp, the current activates and then inactivates at the same membrane potential. They therefore proposed that Na^{+} conductance takes the form:

$$g_{\mathrm{Na}} = \bar{g}_{\mathrm{Na}} m^3 h, \tag{2.30}$$

where $\bar{g}_{\mathrm{Na}}$ is the maximal Na^{+} conductance, m is the activation gating variable, and h is the inactivation gating variable. The Na^{+} gating variables were modelled using the same differential equation as for the K^{+} gating variable (Equation 2.16), with functions for $\alpha_{\mathrm{m/h}}$ and $\beta_{\mathrm{m/h}}$ (Figure 2.15) determined similarly to those for the K^{+} conductance:

$$\alpha_{\mathrm{m}} = 0.1 \frac{25 - v}{\exp \left(\frac{25 - v}{10} \right) - 1}, \tag{2.31}$$

$$\beta_{\mathrm{m}} = 4 \exp \left(\frac{-v}{18} \right), \tag{2.32}$$

$$\alpha_{\mathrm{h}} = 0.07 \exp \left(\frac{-v}{20} \right), \tag{2.33}$$

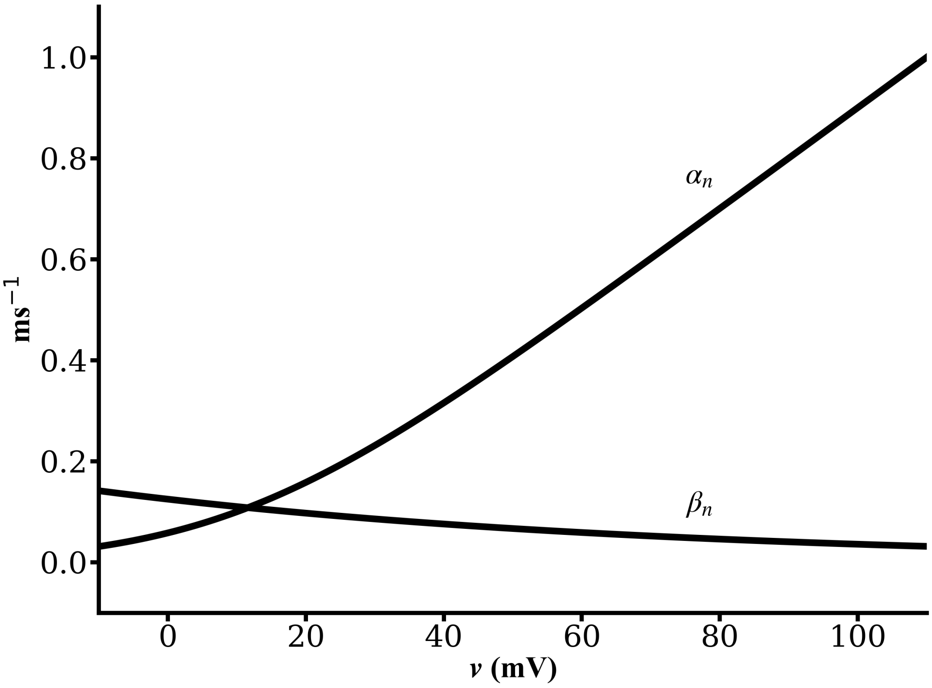

Figure 2.14. K$^+$ gating variable coefficients in the Hodgkin-Huxley model. Opening, α, and closing, β, rate coefficients of the K$^+$ gating variable n are plotted as functions of v.

$$\beta_{\text{h}} = \frac{1}{\exp\left(\frac{30-v}{10}\right)+1}. \tag{2.34}$$

The descriptions for the time- and voltage-dependence of the Na$^+$ and K$^+$ conductances, Equations 2.30 and 2.22, can be substituted into Equation 2.9 to complete the model, giving the final Hodgkin-Huxley model equations:

$$C_{\text{m}}\frac{\text{d}V}{\text{d}t} = -\bar{g}_{\text{Na}}m^3h(v-v_{\text{Na}}) - \bar{g}_{\text{K}}n^4(v-v_{\text{K}}) - \bar{g}_{\text{L}}(v-v_{\text{L}}) - I_{\text{stim}}, \tag{2.35}$$

$$\frac{\text{d}m}{\text{d}t} = \alpha_m(1-m) - \beta_m m, \tag{2.36}$$

$$\frac{\text{d}h}{\text{d}t} = \alpha_h(1-h) - \beta_h h, \tag{2.37}$$

$$\frac{\text{d}n}{\text{d}t} = \alpha_n(1-n) - \beta_n n, \tag{2.38}$$

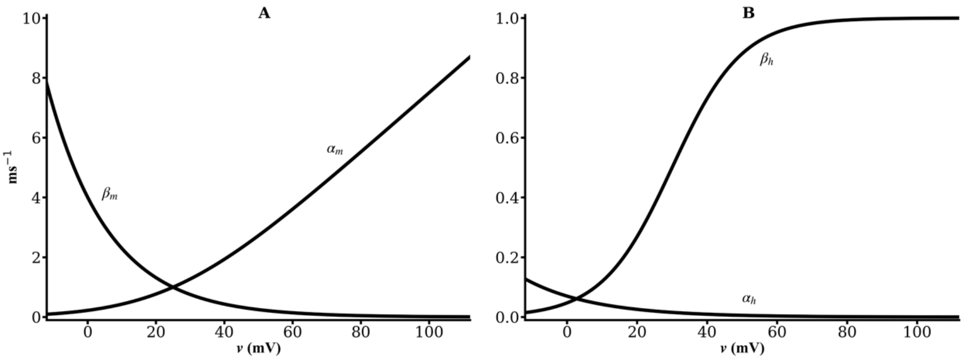

Figure 2.15. Na$^+$ gating variable coefficients in the Hodgkin-Huxley model. Opening, α, and closing, β, rate coefficients of the Na$^+$ activation, m, and inactivation, h, gating variables are plotted as functions of v.

$$\alpha_m = 0.1\frac{25-v}{\exp\left(\frac{25-v}{10}\right)-1}, \tag{2.39}$$

$$\beta_m = 4\exp\left(\frac{-v}{18}\right), \tag{2.40}$$

$$\alpha_h = 0.07\exp\left(\frac{-v}{20}\right), \tag{2.41}$$

$$\beta_h = \frac{1}{\exp\left(\frac{30-v}{10}\right)+1}, \tag{2.42}$$

$$\alpha_n = 0.01\frac{10-v}{\exp\left(\frac{10-v}{10}\right)-1}, \tag{2.43}$$

$$\beta_n = 0.125\exp\left(\frac{-v}{80}\right), \tag{2.44}$$

The dynamics of the gates m, h and n determine the time course of V during the action potential. When the cell is at rest ($v = V - V_{\text{rest}} = 0$ mV), the K$^+$ gating variable n dominates over the Na$^+$ gating variables, m^3h, so v tends towards the K$^+$ reversal potential of -12 mV. Applying a small current to the cell results in a small depolarisation, but v returns to the equilibrium resting value v = 0 mV. However, a sufficiently large stimulus will raise v beyond threshold. Then, m, which is approaching m_∞ with a small time

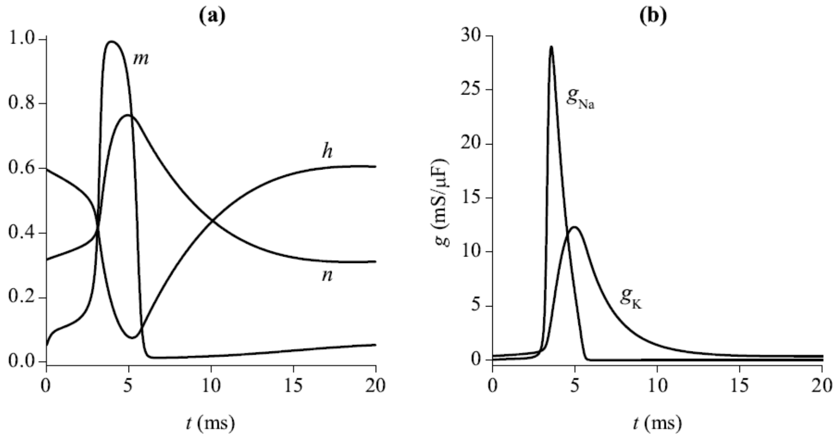

Figure 2.16. (A) Activation (*m* and *n*) and inactivation (*h*) gating variables during an action potential. The Na$^+$ activation gate *m* quickly opens and closes, whereas *h* and *n* change over a longer time course. (B) Na$^+$ and K$^+$ conductances during the action potential.

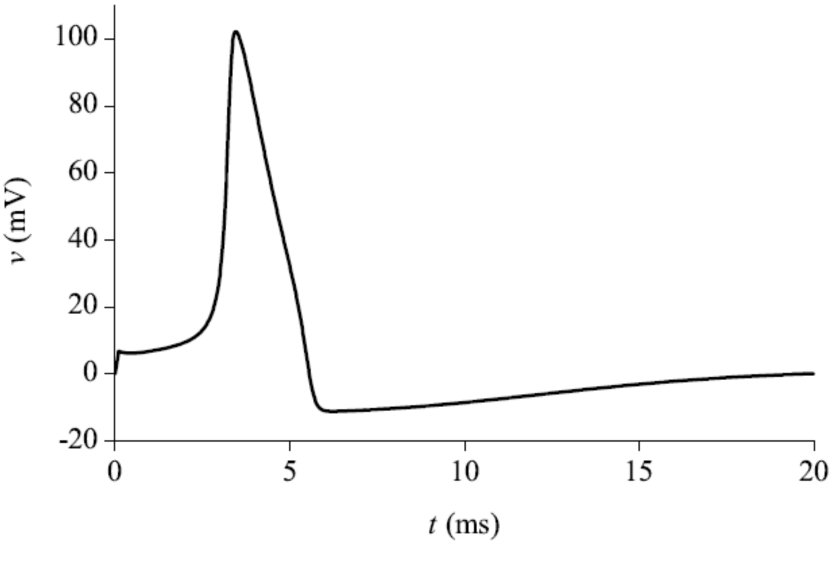

Figure 2.17. Time course of the Hodgkin-Huxley action potential in response to a 0.1 ms, -70 μA/μF stimulus current applied at t = 0 ms.

constant (i.e. the process is fast), causes an increase in g_{Na}, so the inward Na$^+$ current increases and there is further depolarisation. The Na$^+$ conductance then dominates, so v tends towards the Na$^+$ reversal potential of 115 mV. The gates h and n have begun moving towards their new values, h_∞ and n_∞, though with slower time constants. h eventually takes on its new, low value, so g_{Na} falls and I_{Na} inactivates. Meanwhile, K$^+$ activation increases as n approaches its new, high value, so g_{K} dominates and I_{K} activates to repolarise v back towards -12 mV (E_{K}). A refractory period then follows where further stimuli do not result in increases in g_{Na} (so no action potential), as the time constant for the Na$^+$ inactivation gate is large, so there is a lengthy delay before h opens at v = 0 mV. The time courses of m, h and n are shown in Figure 2.16 alongside the Na$^+$ and K$^+$ conductances – all of which result membrane depolarisation and subsequent repolarisation, forming the Hodgkin-Huxley action potential (Figure 2.17).

2.6.4 Markov modelling

Markov chain formulations differ from Hodgkin-Huxley type models of ion channels as, in place of gating variables which are not representative of kinetic states, Markov models comprise a series of states determined experimentally (e.g. closed, open, fast/slow inactivated). Markov formulations (Figure 2.18) are useful for modelling channelopathies resulting from genetic mutations, for instance, or for modelling pharmacological aspects, such as drug applications. In a Markov model formulation, state transitions are not independent (unlike Hodgkin-Huxley type models) and the occupancy of a particular state determines the probability of transition to another state. Na$^+$ channel inactivation, for example, is more likely when the channel is open, but this is not considered in the Hodgkin-Huxley model [46]. Markov models therefore more accurately recreate ion channel kinetics, so are superior to Hodgkin-Huxley models in this regard.

For the example in Figure 2.18, the states evolve according to the following differential equations:

$$\frac{\mathrm{d}C}{\mathrm{d}t} = \beta_{\mathrm{f}} IC + \beta_{\mathrm{d}} O - (\alpha_{\mathrm{d}} + \alpha_{\mathrm{f}})C, \tag{2.45}$$

$$\frac{\mathrm{d}O}{\mathrm{d}t} = \beta_{\mathrm{f}} I + \alpha_{\mathrm{d}} C - (\alpha_{\mathrm{f}} + \beta_{\mathrm{d}})O, \tag{2.46}$$

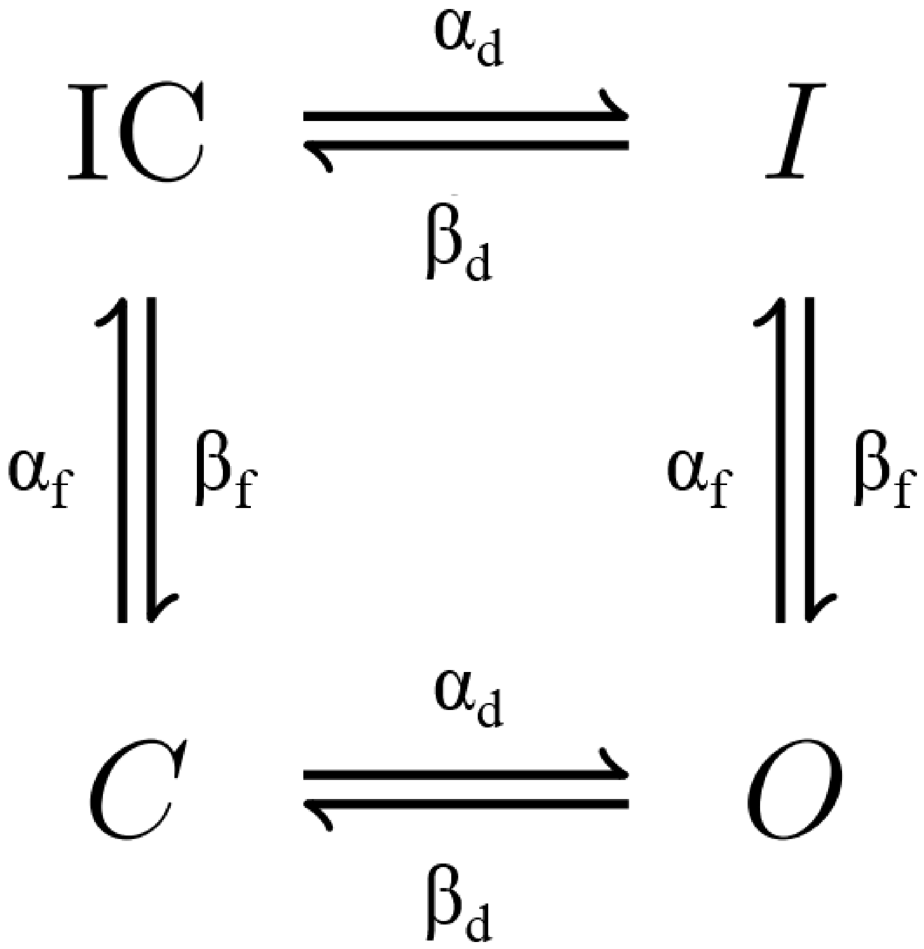

Figure 2.18. Schematic of a simple four-state Markov chain model. Four states are possible: C, closed state; O, open state; I, inactivated state; IC, inactivated closed state. Transiton rates are denoted by α and β. Adapted from [256].

$$\frac{\mathrm{d}I}{\mathrm{d}t} = \alpha_{\mathrm{d}} IC + \alpha_{\mathrm{f}} O - (\beta_{\mathrm{d}} + \beta_{\mathrm{f}}) I, \tag{2.47}$$

$$\frac{\mathrm{d}IC}{\mathrm{d}t} = \beta_{\mathrm{d}} I + \alpha_{\mathrm{f}} C - (\alpha_{\mathrm{d}} + \beta_{\mathrm{f}}) IC, \tag{2.48}$$

where α_{d} is the transition probability from left to right (i.e. C to O or IC to I) and β_{d} is the transition probability from right to left, and α_{f} is the transition probability from bottom to top (i.e. C to IC or O to I) and β_{f} is the transition probability from top to bottom.

The current flowing through an ensemble of such channels, permeable to ion x, is given as

$$I_{\mathrm{x}} = \bar{g}O(V_{\mathrm{m}} - E_{\mathrm{x}}), \tag{2.49}$$

where O is the total open state occupancy, $\bar{g}$ is the maximal channel conductance and E_{x} is the equilibrium potential for ion x. Thus, a Markov channel formulation uses channel open probability, O in place of Hodgkin-Huxley type gating variables.

Markov chain models can be incorporated into models of the cardiac AP, so it is possible to study the effect of state occupancy during the AP; particularly useful when studying gene mutations in channelopathies, for example [329]. It is important to note, however, that Markov models are significantly more computationally intensive than Hodgkin-Huxley type formulations, and so consideration must be given as to whether their improved kinetic modelling outweighs the increased computational demand.

2.6.5 Stochastic modelling

Markov transitions are used to model the stochastic opening and closing of ion channels, made possible by the development of patch clamp technology which has allowed the recording of random single channel openings and closings. A stochastic process is one involving a number of random variables dependent on a variable parameter (time). Using Markov models, it is possible to study the stochastic dynamics of a single or collection of ion channels.

Assuming a channel is in the open state, O, at time t, and that at time $t + \Delta t$ the probability of transitioning to the closed state, C, is $\beta\Delta t$, then the probability that the channel remains open is $1 - \beta\Delta t$. It is possible to use a random number generator to select a random number, r, between 0 and 1 to decide whether the channel remains open or transitions to the closed state, based on the two probabilities. Specifically, if r falls within $[0, \beta\Delta t]$, the channel will change state to C, but if r falls in $[\beta\Delta t, 1]$, the channel will remain open. If the channel is closed, the probability of transitioning to the open state is $\alpha\Delta t$, and the probability of remaining closed is $1 - \alpha\Delta t$ [312].

Though a better representation of *in vivo* ion channel dynamics, stochastic simulation of an ensemble of channels, N, is highly computationally demanding, largely as a result of the quantity of random numbers that require generation at each step. The total ionic current of an ensemble of chanels can then be formulated as

$$I_{\mathrm{x}} = \bar{g}_{\mathrm{x}} N_{\mathrm{O}} (V - E_{\mathrm{x}}) \tag{2.50}$$

where N_{O} is the total number of open channels, which fluctuates randomly with time.

2.7 Mathematical models of the cardiac action potential

A decade after the Hodgkin and Huxley published their seminal works, Noble [280] modified their equations in order to describe the action potential observed from Purkinje fibre cells. Since then, mathematical models of cardiac electrophysiology have begun to include increasing biophysical detail, with new components and experimental observations incorporated as they were discovered or as advances in technology permitted. A review of the development of models representing the many cell types in the heart, across multiple species, is given by Denis Noble himself, and colleagues, in [282], and is summarised over the following paragraphs.

Cardiac cell models have been continuously updated over the years as the ionic basis of the cardiac AP is further determined experimentally. Following the discovery of the Ca^{2+} current [320] and further characterisation of the K^{+} current [283, 284] (then considered a single current), the McAllister-Tsien-Noble model [246] was developed in the 1970s as an improvement of Noble's Purkinje fibre model. The first ventricular muscle cell model was also developed at this time by Beeler and Reuter [32]. Changes in ionic concentrations were first captured in the DiFrancesco-Noble Purkinje fibre model [122], by incorporating descriptions of the Na^{+}-K^{+} ATPase and the Na^{+}-Ca^{2+} exchanger currents. Hilgemann and Noble [164] later sought to accurately model the Ca^{2+} transient (which had been inaccurate in previous models) in their atrial specific model, which became the basic framework for future models of ventricular calcium handling.

In the 1990s, the Luo-Rudy models were developed [234–236] which became the basis for the majority of biophysically-detailed models to this day, containing mathematical descriptions of the various membrane currents, dynamic ion concentrations, Ca^{2+} handling, β-adrenergic control [347, 348], and different metabolic pathways [104, 105, 108]. There has since been a plethora of computational models developed, capturing a range of features including (but not limited to – see [282] for a recent review) the electrophysiological alterations in diabetes [294], stretch-activated channels and force generation [275, 276], and realistic intracellular structure [101, 296]. Increases in computing power have, thankfully, permitted the inclusion of increased complexity in these models, such that large-scale spatio-temporal problems remain tractable despite increased biophysical detail.

Several models of cardiac electrophysiology and Ca^{2+} handling are discussed throughout the work presented in this thesis, summarised in Table 2.3.

Table 2.3. Summary of computational models discussed in this thesis.

Model	Citation	Summary
Pandit	[293, 294]	First rat model and subsequent adaptation for diabetes
Pasek	[296]	Includes T-tubule description
Niederer-Smith	[276]	Adds new contraction and Ca^{2+} handling models
Gattoni	[146]	Re-parameterises and adds new Ca^{2+} handling model
Devenyi-Sobie	[117]	Re-parameterises Ca^{2+} system
Colman	[97, 101]	Spatio-temporal Ca^{2+} cycling models

2.8 Numerical methods

2.8.1 Numerical integration

Cardiac electrophysiology models comprise a series of nonlinear ODEs which require numerical integration methods in order to approximate their solutions, as they are analytically intractable. Accordingly, they can be solved using finite difference methods, such as the forward (or explicit) Euler method. For a differential equation of the form

$$\frac{\mathrm{d}x}{\mathrm{d}t} = f(x), \tag{2.51}$$

then by integrating we wish to find the solution $x(t)$, assuming that $x = x_0$ at $t = t_0$. The forward Euler method assumes that over a sufficiently small time step, Δt, the function $f(x)$ remains constant, so the change in x during the time step can be approximated by $f(x_0)\Delta t$. The new value of x, x_1, at $t_0 + \Delta t$, is therefore

$$x_1 = x_0 + f(x_0)\Delta t. \tag{2.52}$$

Thus, x is now at x_1, the function is now $f(x_{1)}$, and t is $t_0 + \Delta t$. The iterations therefore follow $x_\mathrm{n} = x_{\mathrm{n}-1} + f(x_{\mathrm{n}-1})\Delta t$ where n is the total number of iterations and $n = 0$ at x_0, and $t = t_{\mathrm{n}-1} + \Delta t$. The general scheme is therefore

$$x_{\mathrm{n}+1} = x_\mathrm{n} + f(x_\mathrm{n})\Delta t, \tag{2.53}$$

which is the simplest method of numerical integration (it should be noted, however, that this method is prone to errors in the calculated solution if Δt is not sufficiently small). More accurate (hence more computationally intensive) methods of integration are available, such as the fourth order Runge-Kutta method [308], though increases in accuracy by these methods do not necessarily outweigh their drastically increased computation time.

The choice of Δt is important in order to ensure numerical stability – though a large time step will reduce computation time, it must be sufficiently small such that the numerical solution remains accurate. von Neumann linear stability analysis [308] restricts the choice of Δt (and Δx, the space step for tissue models) so that the stability criterion for any given discretisation scheme is

$$D\frac{\Delta t}{(\Delta x)^2} \leq \frac{1}{2d}, \tag{2.54}$$

where D is the diffusion coefficient and d is the number of spatial dimensions. Thus, for a one-dimensional cable, Δt and Δx must be such that

$$D\frac{\Delta t}{(\Delta x)^2} \leq 0.5. \tag{2.55}$$

Often, due to the biophysically-detailed equations used to determine I_ion, the stability of the discretisation scheme can be chcked by comparing the convergence of the solutions under variations of Δt and Δx. As work presented in this thesis is restricted to single-cell studies, only convergence of the solutions under variations Δt is necessary. The choice of Δt used in simulations presented in this thesis met the stability criterion.

2.8.2 Integrating equations for gating variables

The equations describing gating variables of the Hodgkin-Huxley type are typically integrated using the Rush-Larsen scheme [330]. Rush and Larsen showed that the general gating equation

$$\frac{\mathrm{d}f}{\mathrm{d}t} = \alpha_{\mathrm{f}}(V)(1-k) - \beta_{\mathrm{k}}(V)k, \tag{2.56}$$

has the solution

$$n = n_{\infty}(V) - (n_{\infty}(V) - n_0)\exp(-\Delta t/\tau_{\mathrm{n}}(V)), \tag{2.57}$$

where Δt replaces t from the solution as in Equation 2.24, assuming the rate coefficients α and β that define n_{∞} and τ_{∞} (Equations 2.25 and 2.26) are constant over the small time step Δt. In the following iteration, n becomes n_0. The Rush-Larsen method gives a more accurate solution than integrating Equation 2.56 by the forward Euler method, as the solution to Equation 2.57 is only dependent on membrane potential, V, not the derivative of n.

2.8.3 Adaptive time steps

Integration speed is dependent upon the time step size, Δt, so it is desirable to have a large time step, however not too large as to compromise the accuracy of solutions. If the differential equations' solutions are changing slowly, a large time step can be used without losing accuracy. As $\mathrm{d}V/\mathrm{d}t$ is the variable that changes most rapidly in most computational models, it is possible to introduce a variable time step dependent on $\mathrm{d}V\mathrm{d}t$ to be used. This means that, during the upstroke of the action potential, Δt will be small (as $\mathrm{d}V\mathrm{d}t$ is small), but in the plateau phase of the AP or at resting membrane potentials, Δt will be large. This allows for faster integration and can significantly reduce computation time.

2.8.4 Computational aspects

Models were coded in C/C++ and simulations were performed using the University of Leeds ARC3 High Performance Computing facilities.

Chapter 3

Comparing Computational Models of Rat Electrophysiology

3.1 Introduction

Despite cardiac arrhythmias such as ventricular tachycardia and fibrillation being leading causes of global morbidity and mortality today [47], major clinical trials have failed to produce sufficiently efficacious drugs capable of reducing these health burdens, and the failure of such trials (e.g. [317,450]) has even discouraged further antiarrhythmic drug development in recent years [426]. These failures can largely be attributed to dissonance between pre-clinical experimental models, which typically involve non-human data, and the resulting human outcomes [158, 337]. Given that preclinical drug screening is typically carried out across various animal species and models, it can be difficult to predict the electrophysiological bases for such failures [124], thus in order to develop novel treatments it is imperative to improve our understanding of normal and diseased electrophysiological mechanisms and their relations with arrhythmogenesis across various species [106].

Mice and rats have been used extensively in cardiac research to date to study the pathophysiology of human diseases [48, 182, 222]. The laboratory rat, in particular, is commonly used as an animal model because of its ease of manipulation, relatively low cost and modest physiological similarity to humans [6, 73, 138, 180, 260]. The transient outward, I_{to}, and inward rectifier, I_{K1}, potassium currents were first discovered in rat ventricular myocytes [16], for example, and the use of animal models remains widespread today. However, following the UK Animals (Scientific Procedures) Act 1986 and its subsequent amendment (2010/63/EU), as well as the establishment of the National Centre for the Replacement, Refinement and Reduction of Animals in Research (NC3Rs), there is an increasing awareness of the importance of – and ethical need for – developing alternative methodologies in scientific research that minimise the suffering and use of animals, despite the need to further our understanding of disease processes.

Mathematical models of rat cardiac electrophysiology are one such alternative, and there are now a range of computational models of the rat ventricular action potential [146, 276, 293, 294, 296]. Such models have been used to explore the mechanisms underlying AP heterogeneity from different regions of the heart [293], electrophysiological alterations in diabetes [294], T-tubular remodelling [296], contraction and acid-base balance [276], and the calcium-frequency response [146] in rat ventricular myocytes. As rat models can provide insight into experimental findings from experiments using rat myocytes, they are useful didactic tools, and can be used for preliminary hypothesis testing when planning future experiments. However, currently available models of rat ventricular electrophysiology are unsuitable for use in studying the processes underlying pathophysiological Ca^{2+} handling remodelling and resultant arrhythmias, as they are unable to recreate the complex, stochastic dynamics of subcellular Ca^{2+} handling, the remodelling of which as seen in heart failure, for example, is known to be pro-arrhythmic [74, 202, 365, 427]. Rat computational models remain relevant given the limited experimental data available for the development of human alternatives.

This chapter will begin with an overview of the differences in electrophysiology and calcium handling between species, to provide a solid grounding in understanding the utility and challenges in extrapolating experimental findings from one species to another. The Pandit [293, 294] and Gattoni [146] models of rat ventricular electrophysiology will be then reviewed (and later, compared), as they supply certain elements to the novel computational model detailed in the following chapter (Chapter 4). The Niederer-Smith [276] model will also be discussed as it bridges certain gaps between the Pandit and Gattoni models, which were published 13 years apart. For brevity, the Pasek [296] and Devenyi-Sobie [117] models will be reviewed but not compared, as they are predominantly modifications of the Pandit model with limited additional functionality - the Pasek model adds structural detail relating to the role of T-tubules in cardiac excitation-contraction coupling, and the Devenyi-Sobie model is a re-parameterised Pandit model with some additional components included largely to improve the balance of Ca^{2+} handling and fluxes. However, though this model addresses some of the Ca^{2+} handling limitations from the original Pandit model, some limitations remain, particularly surrounding the lack of species-specific data.

3.2 Species differences in cardiac electrophysiology

As described in Chapter 2, cardiac myocytes are cylindrical in shape and range from between 50 to 200 µm in length and 10-20 µm in radius, and these dimensions remain similar across different mammalian species such that cell volumes do not vary significantly [346]. However, different species exhibit markedly different electrophysiological profiles - larger mammals, such as human and dog, have APs with a ‘spike and dome’ morphology, whereas rats and mice have a more ‘triangular’ AP (Figure 3.1). These differences in electrophysiology mostly arise from the varying expression of the underlying membrane currents, exchangers, and transporters, with some currents absent in certain species. Hence, pro-arrhythmic mechanisms arising from electrical remodelling in one species may not manifest in the same way, or at all, in another.

3.2.1 Depolarising membrane currents: I_{Na}, I_{CaL} and I_{NaCa}

Interestingly, despite being the principal depolarising current, there are few data available to describe differences in I_{Na} across species - largely because cardiac I_{Na} is difficult to measure using microelectrode preparations [127]. Cardiac I_{Na} was first characterised in rabbit Purkinje fibres, which offered structural advantages over other cell choices for voltage clamp studies, as rabbit Purkinje fibres lack T-tubules and have wide intercellular clefts [30, 95]. Even today, modern approaches remain limited as they necessitate reductions in extracellular [Na^+], temperature, or channel availability resulting from phar-

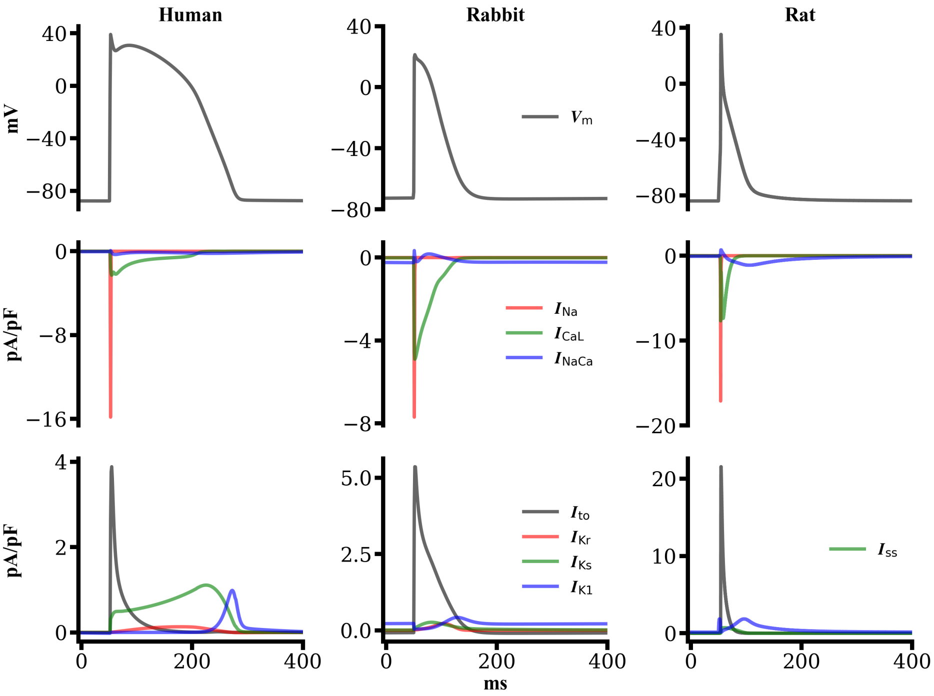

Figure 3.1. Comparison of AP morphology and underlying inward and outward membrane currents in different species. Top: Action potentials from human, rabbit and rat myocyte models. Middle: Time course of inward membrane currents I_{Na}, I_{CaL} and I_{NaCa}. Bottom: Time course of outward membrane currents I_{to}, I_{Kr}, I_{Ks} (I_{ss} for rat) and I_{K1}. Panels show steady-state APs and underlying currents at BCL = 500 ms for each model. Models shown are O'Hara *et al.* [289] (human ventricular), Aslanidi *et al.* [18] (rabbit atrial) and Gattoni *et al.* [146] (rat ventricular).

macological blockade [56, 333]. Together, these changes result in altered current kinetics and/or magnitude, so comparisons of I_{Na} between studies or groups is difficult.

Nevertheless, the molecular basis of I_{Na} has been well-studied across species. The dominant α-subunit has been identified as Nav1.5, though variable expression of other isoforms has been observed across species [53, 456]. In addition, there is a wide variety of accessory proteins, including β-subunits and signalling enzymes that may contribute towards species-dependent effects on the function of I_{Na}, by potentially altering current kinetics [1, 2, 163]. It is therefore likely that there exist systematic species differences in the functional characteristics of I_{Na} which are yet to be discovered [127].

The other principal depolarising current in ventricular myocytes, I_{CaL}, appears to be reduced in rat ventricular myocytes compared to larger mammals [377], and this reduction is largely the result of decreased channel expression [41]. It has also been shown that inactivation and recovery from inactivation of I_{CaL} are slower in rat ventricular myocytes [446], and I_{CaL} activation is negatively shifted in rat, particularly when compared to rabbit and guinea pig myocytes, which results in an increase in window current [446]. Because these observations were made under conditions in which Ca^{2+} release from the SR could not contribute to I_{CaL} inactivation, they suggest that properties independent of variations in Ca^{2+} handling promote greater I_{CaL} activity in rats when compared to mammals with longer APs [127] - thus, rat I_{CaL} will be larger and longer than in other species given the same AP waveform [446]. As the rat AP is much shorter, this I_{CaL} profile compensates to better maintain I_{CaL}-mediated Ca^{2+} influx [388,446].

The molecular bases for these effects have not been fully explained, and it is thought that high sequence homology in critical regions of the α1C and $\beta 2a$ I_{CaL} subunits leaves little room for differences in I_{CaL} gating [127,446] - thus, it remains possible that varying expression of other β subunits or accessory modulators may be important [127].

3.2.2 Fast repolarising membrane currents: I_{to} and I_{Kur}

There are a large number of K^+ currents expressed in ventricular myocytes, the varied expression of which is the primary explanation for species differences in electrophysiology. The repolarising membrane currents are typically split into 2 broad categories: transient outward (I_{to}) and inward rectifier (I_{K}) currents. For rats and mice, repolarisation proceeds so rapidly that some K^+ currents are rarely recruited (such as I_{Kr} and I_{Ks}), as these typically activate 50 ms or longer after AP initiation, which is roughly the duration of the entire murine AP [127]. Given this short duration in the murine AP, fast-activating K^+ currents contributing to initial repolarisation from the AP overshoot are much larger in magnitude than in other mammalian species, and are responsible for all but terminal AP repolarisation [127], and it is this feature that allows rats and mice to have much faster heart rates, typically above 400 bpm [331,415].

In most species, I_{to} dominates the early contribution to repolarisation, and both activates and inactivates rapidly. In rodents, the markedly high density of I_{to} dominates over other repolarisation phases, sharply abbreviating the AP and resulting in the absence of a clear plateau phase which is present in other species [279]. Murine I_{to} is the largest across all mammalian species, being approximately 4-fold larger than rabbit (which is roughly equal

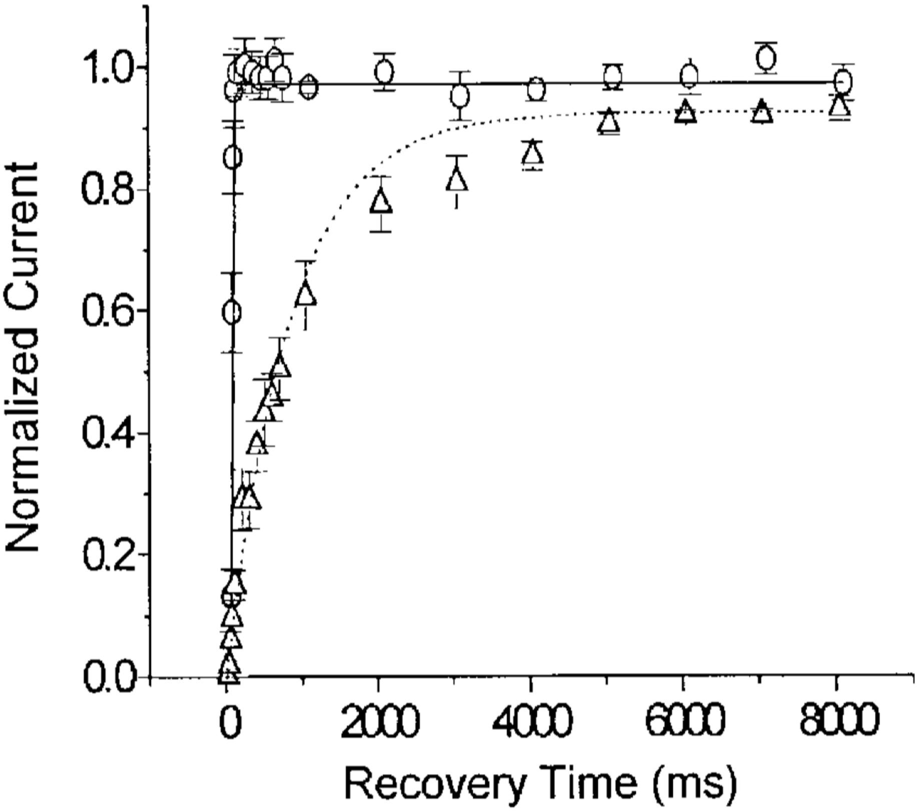

Figure 3.2. Kinetics of fast and slow I_{to} components. Mean normalised current for $I_{\text{to,f}}$ (o) and $I_{\text{to,s}}$ (Δ) as functions of inactivation time. $I_{\text{to,s}}$ inactivates much more slowly than $I_{\text{to,f}}$ which appears to inactivate almost immediately during current clamp experiments. Continuous and dotted lines represent single exponentials to fit recovery data for each current component. From [156].

to that of human), while guinea pig I_{to} is largely undetectable [137, 338, 339, 417, 454].

I_{to} can be split into 2 components which differ in their rates of inactivation and recovery from inactivation (Figure 3.2), and exhibits strong transmural variation. Typically, however, these subdivisions are summed and referred together as I_{to} [127]. The fast component, $I_{\text{to,f}}$, rapidly inactivates ($\tau \approx$ 10 ms) and recovers from inactivation ($\tau \approx 20-50$ ms) [156, 441], whereas the slow component, $I_{\text{to,s}}$, inactivates 5-8 times more slowly than $I_{\text{to,f}}$ and recovers from inactivation much slower ($\tau \approx$ 1000 ms) which can have important implications for the frequency dependence of repolarisation [127].

The final rapidly-activating K^+ current is I_{Kur}, sometimes referred to as $I_{\text{K,slow}}$ or $I_{\text{K,sus}}$ as it had been characterised using different methods and in different species and regions of the heart [269]. I_{Kur} is prominant in the atria of large mammals [215,448], and throughout the murine heart where it contributes to rapid repolarisation to shape the triangular AP waveform [57, 62, 68, 441]. I_{Kur} can be distinguished from I_{to} by its markedly slower inactivation kinetics [127], and as such contributes to repolarisation later than I_{to}.

3.2.3 Slow repolarising membrane currents: I_{Kr}, I_{Ks} and I_{K1}

The remaining delayed rectifier currents (rapidly, I_{Kr}, and slowly, I_{Ks}, activating forms) exhibit slower current development, and make only a minor contribution to repolarisation in ventricular myocytes of rats and mice [127]. In mammals with longer APs, however, the balance of I_{Kr} and I_{Ks} determines the phase 2-phase 3 plateau duration [23]. These delayed rectifier currents slowly move the membrane potential out of the I_{CaL} activation range, where the voltage-independent inward rectifier (I_{K1}) current is recruited to drive the terminal phase of repolarisation in all species and most cell types of the heart.

I_{Kr} is unique among cardiac currents as its contribution to repolarisation results from channels that are recovering from inactivation, rather than proceeding in typical activation-to-inactivation sequences - this is due to the rapid form of C-type inactivation of hERG (human ether-a-go-go-related gene) tetramers [437]. hERG channels accumulate in their inactivated conformations at the peak of the AP and during the early plateau phase – as membrane potential moves towards rest, these channels recover through the open state before deactivating, with slower kinetics [190]. In contrast, the KvLQT1 (KCNQ1) pore of I_{Ks} activates ($\tau \approx$ 1 s) and deactivates ($\tau \approx$ $100-300$ s) very slowly, exhibiting only very slight inactivation [190, 399, 411]. Though hERG-like mRNA and currents have been found in various animal species, little or none has been identified in rat ventricular myocytes [247, 438].

These differing kinetics have implications for species differences. Firstly, the kinetics of I_{Ks} cause it to accumulate in or near activation at faster heart rates or during prolonged depolarisation [124, 364], providing a reserve of outward current that can be recruited in the absence of other outward currents (such as I_{Kr}). Such accumulation was proposed by a 18-state Markov model for I_{Ks} [364] (Figure 3.3), for which two 'zones' exist for closed-state channels. Zone two represents closed channels for which all 4 voltage-sensor subunits have not yet transitioned, and zone one represents channels closed channels for which all 4 subunits have transitioned. At faster cycle lengths, the proportion of chan-

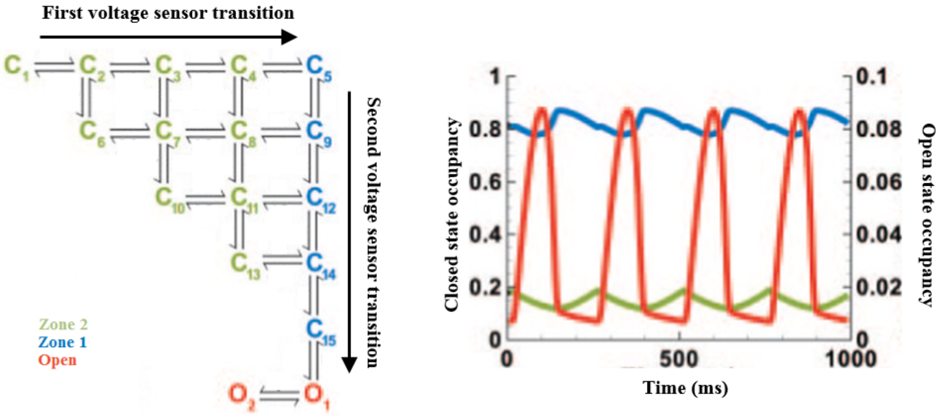

Figure 3.3. Markov model and state occupancy for I_{Ks} at different cycle lengths. A: I_{Ks} Markov model. Green zone states represent channels for which all 4 subunits have not completed the transition, blue zone states represent channels for which all 4 subunits have completed transitioning, and red states represent open channels. B: I_{Ks} zone state occupancy at BCL = 250 ms. Adapted from [364].

nelz in zone one increases, which facilitates channel opening [364]. For myocytes with short APs, the window-like activation characteristics of I_{Kr} allow it to contribute in small amounts to repolarisation when hERG is expressed [127].

The role of these currents in rats and mice remains controversial as murine KCNQ1/KCNE1 knockout results in exaggerated rate-dependent and adrenergic slowing of repolarisation [79, 125, 201]. In larger mammals, these changes indicate a reduction in repolarisation reserve, but I_{Ks} is minimally detectable in these animals and there are few changes in AP morphology. It has therefore been proposed that I_{Ks} in small rodents may only be unmasked during adrenergic modulation, which prolongs the AP secondary to enhanced Ca^{2+} cycling [126, 348]. Also, hERG currents can be detected in mice, but knockout does not result in noticeable changes to the ECG nor increases in arrhythmia susceptibility *in vivo*, thus is it believed the delayed rectifiers play minor roles in murine electrophysiology [21].

Given the high expression of I_{to}, this overwhelms other inward currents in the rat, resulting in a markedly abbreviated AP. This largely elminates the activation of other outward K^+ currents, such as I_{Kr} and I_{Ks}. As a result, in rat computational models to date, I_{Kr} and I_{Ks} are typically modelled together a single, outward current called the steady-state K^+ current, I_{ss} [293].

The final repolarising current, I_{K1}, plays a major role in final repolarisation of the AP and is the primary determinant of resting membrane potential in cardiac myocytes. In order to provide this membrane stability, I_{K1} must exhibit marked inward rectification such that its conductance is very small at positive membrane potentials and small negative potentials close to 0 mV [26]. However, it must exhibit large conductance at potentials close to resting membrane potential. Inward rectification of I_{K1} is provided by field-induced block of the channel pore (formed by Kir2.1, Kir2.2 and Kir2.3 subunits) by intracellular Mg^{2+} and polyamines [26, 230, 273]. This mechanism allows phases 1 and 2 of the AP to proceed normally with no repolarising influence of I_{K1}, which would otherwise be very large and eliminate the plateau phase in large mammalian ventricular myocytes. In addition, the properties of rectification are exaggerated in the ventricles [149, 204].

I_{K1} expression is 2-3 times lower in the atria than the ventricles of most species, and is virtually absent in the SA node, which does not exhibit a stable resting membrane potential [120]. In rat and mice, uniquely, I_{K1} distribution appears to be the opposite in that it is at least as highly expressed in the atria as in the ventricles [228]. As a result, human myocytes are potentially more susceptible to spontaneous Ca^{2+} release events during diastole, or during terminal repolarisation in the form of early afterdepolarisations.

3.2.4 Calcium handling

3.2.4.1 I_{NaCa} and I_{SERCA}

Meaningful differences have been established for the Ca^{2+} transporting proteins in ventricular myocytes, particularly I_{NaCa} (NCX). First isolated in canine myocytes [301], the NCX1 isoform was then cloned [274] and is recognised as the dominant cardiac isoform in mammals [302]. Under steady-state conditions, efflux of Ca^{2+} via I_{NaCa} is roughly equal to Ca^{2+} influx via I_{CaL} [127], which is about 7% in rats and mice [41] but nearly 30% in larger mammals [127]. The remainder, mostly, is resequestered into the SR. This large disparity in NCX contribution between murine and larger mammals results from an approximately 4-fold larger SERCA contribution in rat [41, 377], favouring SR reuptake over Ca^{2+} extrusion via NCX, as well as a reduction in I_{NaCa} activity in rat generally [355]. In addition, higher $[\mathrm{Na}^{+}]_{\mathrm{i}}$ in murine ventricular myocytes reduces the electrochemical driving force for Ca^{2+} extrusion via I_{NaCa} [214, 357]. This shift towards SR-dependent

Ca^{2+} handling has resulted in rats and mice being relatively sensitive animal models for studying SR-dependent arrhythmia mechanisms [127].

3.2.4.2 Early afterdepolarisations

Early afterdepolarisations (EADs) are abnormal changes in membrane potential occurring during the plateau phase (phase 2) or late repolarisation (phase 3) of the AP (see Figure 3.4). EADs are believed to result from disruptions to membrane currents comprising the plateau phase, resulting in AP prolongation – they are therefore the result of reduced outward and/or increased inward current [314]. However, as AP morphology varies between species, mechanisms underlying EAD generation may be different from one species to another.

In large mammals, with clear phase 2-3 plateau regions, EADs generally initiate in the late plateau and are more commonly caused by reactivation of I_{CaL} [155, 187], or from forward-mode I_{NaCa} (i.e. Ca^{2+} extrusion) resulting from abnormal SR Ca^{2+} release [375, 382]. In addition, reductions in K^+ channel conductance also contribute to EAD generation, as this results in a diminished repolarisation reserve and APD prolongation [155, 297]. However, APD prolongation can occur independently of EAD generation, but AP triangulation (increases in APD_{30}-APD_{90}) is a strong predictor of EAD generation [13, 176], and APs without plateau phases (e.g. those in rats or mice) can exhibit EADs under various circumstances. Using a model of the guinea pig AP, Tran *et al.* [398] showed that AP prolongation does not necessarily promote EAD generation if occurring at positive potentials (as I_{CaL} recovery is slow in this range of potentials), and confirmed that AP triangulation is predictive of EADs as it prolongs the duration spent in membrane potentials that I_{CaL} can recover [176, 177].

For murine myocytes, the high expression of I_{to} and I_{Kur} results in much more rapid repolarisation, which alters EAD dynamics because the I_{CaL} activation range is very quickly passed through (within 10 ms) in these species. This, however, predisposes to I_{Na} reactivation, which has the secondary impact of raising membrane potential to those in which I_{CaL} reactivates, resulting in APs similar to those of larger mammals [126]. It should be noted, though, that this interaction has not been quantitatively assessed in murine myocytes and has only been suggested by computational analyses using a human atrial model [259]. Although the morphology of the human atrial AP is similar to that of the murine ventricular

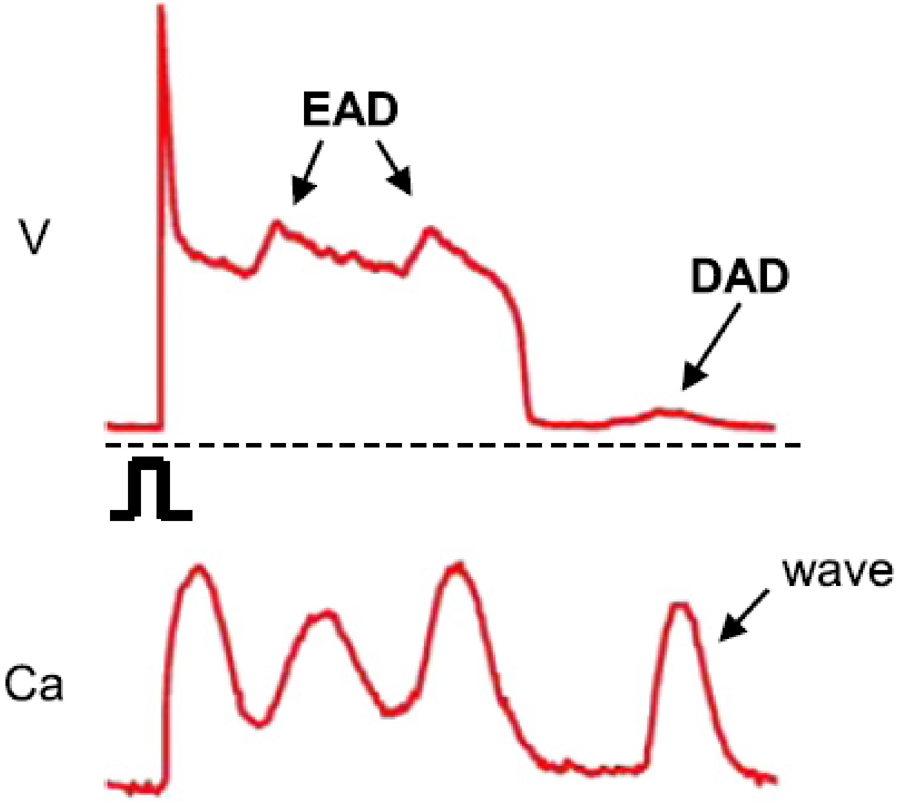

Figure 3.4. EADs and DADs in ventricular myocytes. Perturbations to membrane potential (top) resulting from Ca^{2+} waves (bottom). EADs can be seen during the normal repolarisation phase of the AP, whereas DADs manifest after terminal repolarisation. From [440].

AP, it is still longer in duration (approximately 4-fold) and so these dynamics may not necessarily be the same in rodent species.

3.2.4.3 Delayed afterdepolarisations and Ca^{2+} waves

Spontaneous release of Ca^{2+} from the SR results in phasic depolarisation of membrane potential, as the released Ca^{2+} is extruded via forward-mode I_{NaCa}. These release events manifest as propagating Ca^{2+} waves and can elicit EADs, as mentioned previously, if they occur during repolarisation of the AP. However, at resting membrane potential, spontaneous Ca^{2+} release events can still occur, resulting from abnormal RyR opening, which can trigger delayed afterdepolarisations (DADs, Figure 3.4), as intracellular Ca^{2+} ions are exchanged for extracellular Na^{+} ions (with a stoichiometry of 1:3 Ca^{2+}:Na^{+}) by reverse-mode I_{NaCa}. If the magnitude of depolarising current is sufficient, it can raise membrane potential to or above the threshold for activation of voltage-gated Na^{+} channels, eliciting a spontaneous AP (known as triggered activity) [127]. Though the general mechanisms of Ca^{2+} wave propagation and DAD genesis are similar across species, species-dependent parameters including RyR sensitivity, cellular structure, heart rate (or more specifically, diastolic interval), and the balance of Ca^{2+} fluxes.

RyR opening is dependent on $[\mathrm{Ca}^{2+}]_{\mathrm{i}}$, and many studies have reported that half-maximal RyR activation occurs between 2 to 10 μM $[\mathrm{Ca}^{2+}]_{\mathrm{i}}$ [43]. However, this appears to be species-specific, as recent studies have shown rat hearts exhibit a much lower Ca^{2+} sensitivity to those of higher mammalian species [76, 421, 442]. This is despite Ca^{2+} spark rates reportedly being higher in rat than rabbit myocytes [345]. As SERCA reuptake of Ca^{2+} into the SR dominates over other Ca^{2+} extrusion mechanisms in rat myocytes, this discrepancy may result from differences in luminal $[\mathrm{Ca}^{2+}]$, which is maintained in the rat to sustain higher RyR open probability, but diminished in rabbits due to larger Ca^{2+} extrusion via I_{NaCa} [345, 421, 455].

Differences between species in SR and sarcolemmal Ca^{2+} fluxes can determine Ca^{2+} wave susceptibility and subsequent DAD generation. In large species where I_{NaCa} contributes more to Ca^{2+} extrusion, SR load may be reduced which makes spontaneous release less likely [316, 375], but proportionally greater amounts of released Ca^{2+} are extruded as I_{NaCa} activity is higher [233]. Pro-arrhythmic DADs are therefore expected to be larger in higher mammalian species per unit of released Ca^{2+} [127]. In contrast, SERCA activity is greater in murine myocytes, so the SR is more easily overloaded but DAD amplitude may be smaller as there is reduced I_{NaCa} activity.

Rats and mice have much faster heart rates than other mammals, however SR Ca^{2+} oncentration (which is, on average, higher) is maintained relatively well across the pacing frequencies in murine myocytes [238]. Conversely, larger mammalian species have a lower SR content, but this increases with pacing frequency which potentially promotes Ca^{2+} waves. In addition, diastolic $[\mathrm{Ca}^{2+}]$ ($[\mathrm{Ca}^{2+}]_{\mathrm{ds}}$) accumulation occurs at faster frequencies, increasing the likelihood of Ca^{2+} waves by triggered RyR opening and activating CaMKII, which phosphorylates and increases the Ca^{2+} sensitivity of RyRs. However, RyRs exhibit refractoriness, and exhibit a short period of reduced availability during the period immediately following a Ca^{2+} transient. It is predicted, therefore, that rats and mice may have reduced susceptibility to Ca^{2+} waves compared to larger mammalian species [43, 127].

Lastly, structural differences between species may influence DAD generation, particularly in relation to the arrangement of dyads. In rodent species, a large proportion of RyRs are located in close proximity to dyads, thus local I_{NaCa} in the T-tubules is well positioned to extrude Ca^{2+} when spontaneous release occurs [162, 368]. Conversely, T-tubule density in larger mammalian species is lower [143, 162] and there are larger numbers of orphaned RyRs located further from NCX molecules. It is expected that Ca^{2+} will quickly be removed from RyR release sites at dyads and more slowly from orphaned RyRs, which could promote DAD generation, however this may in fact reduce recruitment of Ca^{2+} release units to limit DAD generation [154].

3.3 Existing models of rat ventricular electrophysiology

3.3.1 The Pandit model

A number of studies in the 1990s demonstrated that there are transmural differences in the action potential waveforms of mammalian epicardial and endocardial myocytes [92, 263], with endocardial myocytes having longer APDs. In addition, epicardial and endocardial cells respond differently to pathological states - in disease, these heterogeneous responses may contribute to the development of re-entrant arrhythmias [14]. To understand the underlying ionic mechanisms for such heterogeneity, Pandit *et al.* [293] developed a mathematical model of the adult left ventricular epicardial and endocardial action potentials of rat (Figure 3.5), using the Hodgkin-Huxley formalism (the endocardial cell model was based on the epicardial formulation). The authors coupled an electrical circuit to a fluid compartment model [434] to describe changes in Na^{+}, K^{+} and Ca^{2+} ions in the myoplasm, and Ca^{2+} in the SR. The fluid compartment model included a restricted subspace into which the L-type Ca^{2+} channels and RyRs empty, located between the junctional SR and T-tubules.

3.3.1.1 Pandit model components and formulations

Membrane currents included in the Pandit model and their respective peak values at a pacing frequency of 2 Hz (cycle length 500 ms) are provided in Table 3.1. Equations for

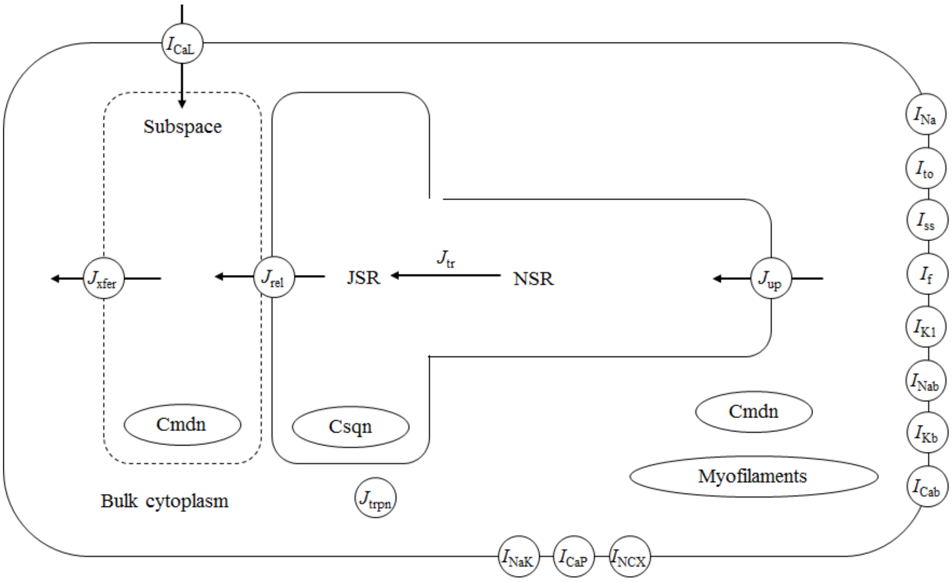

Figure 3.5. Structure of the Pandit model of rat ventricular electrophysiology. The authors coupled a fluid compartment model from [434] to an electrical circuit model. Adapted from [293].

I_{Na} in the Pandit model are of the type formulated by [32], consisting of a fast activation (m^3), fast inactivation (h) and a slow inactivation variable (j), and the steady-state activation and inactivation curves used were based on then-recent patch clamp experiments from rat ventricular myocytes [211]. The authors scaled time constants for activation and inactivation (τ_m, τ_h, τ_j) from the guinea pig model of [235], and to room temperature, then adjusted the maximum Na^+ conductance (g_{Na}) to generate an appropriate $\mathrm{d}V/\mathrm{d}t_{\mathrm{max}}$ value (g_{Na} = 1.064 μ S).

For the L-type Ca^{2+} current, the Pandit formulation followed that of Nygren *et al.* [286] (for human atria), including time- and voltage-dependent activation and inactivation along with Ca^{2+}-dependent inactivation. I_{CaL} activation and inactivation curves were based on data from isolated rat cells from [195]. Time constants for activation and inactivation ($\tau_d, \tau_{f11}, \tau_{f12}$) were based on experimental data from rat ventricular myocytes. The authors modelled Ca^{2+}-dependent inactivation as a function of Ca^{2+} concentration in the restricted subspace (see Figure 3.5). The reversal potential for I_{CaL}, E_{CaL}, was set to 65.0 mV as a constant, a value which was experimentally measured [59]. The authors then fitted a normalised I_{CaL} $I-V$ relationship based on experimental data, as I_{CaL} density had been shown to vary considerably in rat ventricular myocytes, even among cells from the same region [150, 322]. Finally, I_{CaL} maximum conductance, g_{CaL} was set as 0.031

Table 3.1. Membrane currents and fluxes in the Pandit model.

Current	Description	Steady-state peak at 2 Hz
I_{Na}	Na^+ current	-140.4 pA/pF
I_{to}	Ca^{2+}-independent transient outward K^+ current	7.12 pA/pF
I_{CaL}	L-type Ca^{2+} current	-7.24 pA/pF
I_{Iss}	Steady-state K^+ current	1.28 pA/pF
I_{f}	Hyperpolarisation-activated (funny) current	Max 0.0021 pA/pF
		Min -0.00057 pA/pF
I_{K1}	Inward rectifier current	1.06 pA/pF
I_{Nab}	Background Na^+ current	-0.017 pA/pF
I_{Kb}	Background K^+ current	0.17 pA/pF
I_{Cab}	Background Ca^{2+} current	-0.0077 pA/pF
I_{NaK}	Na^+-K^+ exchanger current	0.32 pA/pF
I_{NCX}	Na^+-Ca^{2+} exchanger current	Max 0.31 pA/pF
		Min -0.45 pA/pF
I_{CaP}	Sarcolemmal Ca^{2+} pump current	0.025 pA/pF
J_{rel}	RyR Ca^{2+} release flux	3.17 mM.s^{-1}
J_{up}	SERCA2a Ca^{2+} flux	0.013 mM.s^{-1}
J_{trpn}	SR Ca^{2+} leak flux	0.26 mM.s^{-1}
J_{tr}	SR Ca^{2+} leak flux	0.013 mM.s^{-1}
J_{xfer}	Troponin buffering	Max 0.42 mM.s^{-1}

μ S to provide close agreement between simulations and experiments.

To formulate equations for I_{to}, Pandit and colleagues used experimental steady-state activation and inactivation data, as I_{to} can be difficult to measure experimentally due to interference from I_{CaL} or from Ca^{2+} channel blockers used to halt I_{CaL} interference. The activation time constant for I_{to} was based on experimental data in the absence of divalent cations [5], which otherwise alter the properties of I_{to}. Inactivation of I_{to} has fast, s, and slow, $slow$, components, which display near-identical values positive to 0 mV ($\sim$ 35 ms) but different values at negative potentials. Values for fast and slow recovery, and their relative contributions to total I_{to} recovery, were adapted from then-recent experiments. The maximum conductance of I_{to} was set to g_{to} = 0.016 μ S.

I_{ss} (sometimes referred to as I_{K}) activates rapidly but inactivates very slowly [16], so can be measured at the end of a long depolarised voltage clamp pulse when I_{to} is assumed to have inacivated completely. The authors used experimental data from rat ventricular myocytes to formulate steady-state activation and inactivation kinetics. The inactivation time constant is approximately 10 times slower than that for activation [16], and was set to a constant of 2100 ms based on experimental measurements. The maximal conductance of I_{ss} was set to g_{ss} = 7 nS.

For their I_{K1} formulation, Pandit and colleagues adapted an earlier formulation [288] based on unpublished data, and the $I-V$ characteristics for I_{K1} closely matched experimental data for different values of $[\mathrm{K}^+]_{\mathrm{o}}$ (g_{K1} = 0.024 μ S). A small magnitude hyperpolarisation-activated current was also included in the Pandit model, adapted from earlier work and based on data recorded from rat ventricular myocytesi (g_{f} = 1.45 nS). In addition, the authors included a background current, I_{b}, which was the sum of Na^+, K^+ and Ca^{2+} components, representing the small leak of each ion across the membrane. The conductances of these currents ewre scaled to achieve intracellular ionic concentration stability (g_{bNa} = 80.15 pS, g_{bK} = 138.0 pS, g_{bCa} = 32.4 pS).

The formulation for I_{NaK} was based on earlier guinea pig formulations [235] and the maximum current parameter was adjusted to achieve a stable $[\mathrm{Na}^+]_{\mathrm{i}}$ of $\sim$ 10.74 mM ($\bar{I}_{\mathrm{NaK}}$ = 0.08 nA), which still fell within the experimentally measured range for I_{NaK}. For the sarcolemmal Ca^{2+} pump, the authors based the formulation on earlier work for rabbit sinoatrial node cells [114] ($\bar{I}_{\mathrm{CaP}}$ = 4 pA). Similarly, the authors based the I_{NaCa} formulation on earlier work for rabbit sinoatrial node cells, adjusting the scaling factor, k_{NaCa} based on a fit to experimental $I-V$ data from rat ventricular myocytes, then reduced by 20% to achieve intracellular Ca^{2+} homeostasis. Though other pumps and exchangers have been identified in rat ventricular myocytes, such as the Na^+-H^+ exchanger and Na^+-$\mathrm{HCO}_3{}^{\mathrm{i}}$ cotransporter, these were not included in the Pandit model.

The authors adapted the intracellular Ca^{2+} concentration formulation, as well as those for its associated regulatory processes, from the canine ventricular model of [434]. To simulate the Ca^{2+} transient as seen in rat ventricular myocytes, they adjusted various parameters controlling Ca^{2+} homeostasis, including the forward and reverse rates for SR Ca^{2+} uptake ($v_{\mathrm{maxf}}, v_{\mathrm{maxr}}$) and the Ca^{2+} on-rate for high-affinity troponin sites (k_{trpn^+}). The resulting Ca^{2+} transient is only somewhat similar to that observed in rats, though the resulting values for junctional and network SR Ca^{2+} concentrations were comparable to those recorded physiologically in rat ventricular myocytes [394].

Volumes for the subcellular compartments were determined from analysis of rat ventricular data, with capacitance set to 100 pF and cell volume 16 pL, giving a capacitance-to-volume ratio of 6.25 pF/pL which is comparable to experimentally reported values [59, 346]. External ionic concentrations were assumed to be constant and simulations were carried out at 22°C.

3.3.1.2 Pandit model results

The model revealed that increases in I_{Na} and I_{to} underlie increases in peak overshoot observed between epicardial and endocardial myocytes, and these currents contribute equally to this increase. It also showed that differences in expression and reactivation kinetics of I_{to} underlie regional variations in rate dependence and APD, and agreed with the consensus that I_{to} in rat consists of a fast and a slow component, with the slower component contributing more in the endocardium.

As the plateau phase of endocardial myocytes is more distinct and occurs at more depolarised potentials than the epicardium, there is a smaller driving force for I_{CaL} during the endocardial AP, so peak endocardial I_{CaL} is smaller than the epicardial peak (-0.972 vs -1.496 nA in the model). In addition, during endocardial APs I_{CaL} decays more slowly as I_{CaL} inactivation occurs around -40 mV and it takes longer for endocardial myocytes to reach this potential during an AP. These changes to I_{CaL} characteristics overall result in larger Ca^{2+} influx in endocardial myocytes.

The model also revealed that the longer APD in endocardial myocytes can contribute significantly to inotropy. As the I_{to} density in endocardial myocytes is smaller, the APD is prolonged and the profile of I_{CaL} is altered such that Ca^{2+} influx is almost doubled in the endocardial AP. Many of these Ca^{2+} ions are taken up into the SR as they cannot all be extruded via I_{NaCa}, leading to loading of the SR and subsequently higher peak systolic $[\mathrm{Ca}^{2+}]_{\mathrm{i}}$. This, in turn, increase I_{NaCa} until a steady-state is reacehed, where Ca^{2+} influx via I_{CaL} (Q_{CaL}) is balanced by Ca^{2+} extrusion via I_{NaCa} (Q_{NaCa}). In the model, APD, I_{CaL}, Q_{CaL}, I_{NaCa}, Q_{NaCa}, systolic $[\mathrm{Ca}^{2+}]_{\mathrm{i}}$, and $[\mathrm{Ca}^{2+}]_{\mathrm{jSR}}$ are all larger in endocardial myocytes than epicardial, which is in agreement with previous research [59, 91].

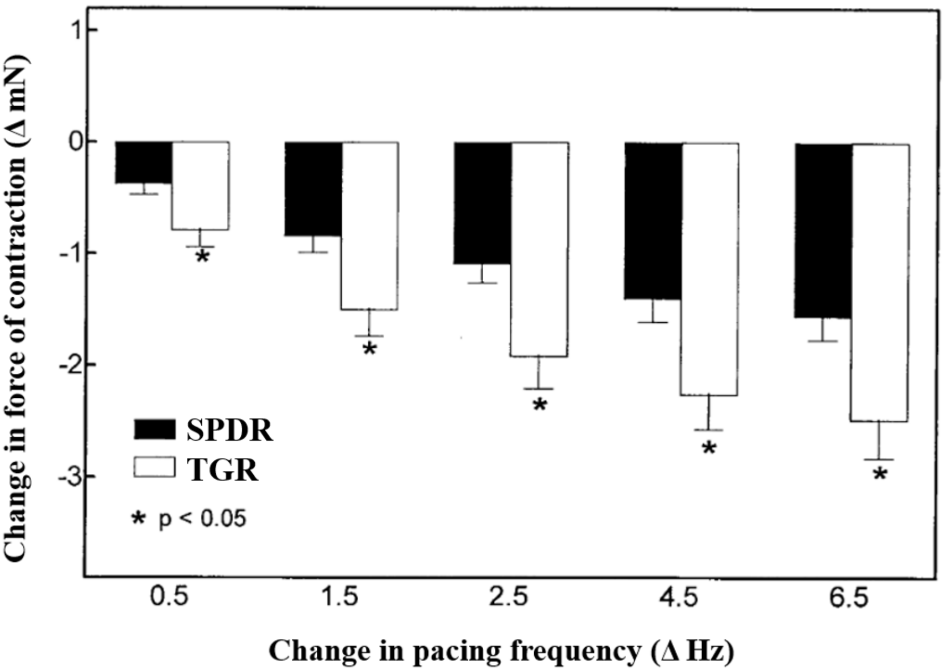

Figure 3.6. Bar graph showing change in contractile force with changes in pacing frequency in rat myocytes. The negative force-frequency response in rat myocytes results in decreases in contractile force with increased pacing frequency. SPDR, Sprague-Dawley rats; TGR, transgenic rats overexpressing the *Ren-2* gene. Adapted from [457].

3.3.1.3 Pandit model limitations

As the Pandit model was developed principally to explore how transmural differences in AP morphology and electrophysiological characteristics arise, the model used a limited description of Ca^{2+} handling based on canine midmyocardial ventricular cells [434]. One notable drawback of this is that the model relies on common pool Ca^{2+} dynamics and is unable to reproduce graded Ca^{2+} release which is an intrinsic property of cardiac myocytes [432]. Accordingly, the model does not capture the negative force-frequency relationship observed in rat myocytes [40, 457] (Figure 3.6). In addition, there may be more, or more complicated, repolarising membrane currents in rat myocytes than just I_{to} and I_{ss} as described in the model. As the model lacks a structural description of the T-tubule system, it is also not possible to investigate how changes in dyadic components affect, for example, Ca^{2+} handling.

3.3.2 The Pasek model

The T-tubular system allows rapid propagation of electrical excitation from the periphery of cardiac myocytes to the cell interior. However, accumulation or depletion of local ions in the restricted T-tubular system may result in disturbances to normal electrical activity, which can be studied quantitatively [295]. The Pasek model [296] was developed in order to quantify how changes to T-tubular morphology could affect electrical activity, specific to rat ventricular myocytes (previous work was based on data from multiple species [295]). The authors adapted the Pandit model based on ultrastructural data from rat ventricular myocytes and on data from sarcolemmal membrane currents prior to and following formamide-induced detubulation [63, 367, 443]. The model was used to investigate the extent of changes in ion concentration in the T-tubular space in response to changes in pacing frequency.

3.3.2.1 Pasek model components and formulations

In general, the Pasek model is based on the previously-described Pandit model, with descriptions of the sarcolemmal and tubular membranes included. The geometry of the T-tubular system was set to comply with data from microscopic analysis of rat ventricular myocytes [346, 367], with fractional volume of the T-tubular system equalling 3.6% – applying this fraction, alongside other ratios (e.g. T-tubular area per cellular volume), to a total modelled membrane area of 10,000 μm^2 resulted in a peripheral membrane area of 4,325 μm^2 (43.95 pF) and tubular membrane area of 5,605 μm^2 (56.05 pF), with a tubular volume of 420.38 μm^3 (total cell volume = 12,739 μm^3). The fractional volumes of the NSR, JSR and restricted subspace were kept the same as in the Pandit model.

Membrane current formulations were kept largely the same as from the Pandit model, with some minor changes to some parameters. Maximal I_{Na} conductance was adjusted to 8 mS.cm^{-2} to give a $\mathrm{d}V/\mathrm{d}t_{\mathrm{max}}$ = 160 V.s^{-1}, and the reversal potential E_{Na} was reduced to incorporate a fractional permeability for K^+ ions. The formulation of I_{CaL} was replaced by the equation from [378] which is based on constant field theory and better accounts for the dependence of I_{CaL} on extracellular Ca^{2+}. To better fit experimental data from [195], the authors omitted the constant term in the description of fast and slow I_{CaL} inactivation time constants used in the Pandit model. The authors also adapted the I_{K1} formulation to better fit experimental data from rat myocytes, and the stimulus current (of 5.2 nA for 1 ms) was incorporated into the d[K$^+$]$_i$/dt equation to comply with the charge conservation principle [181].

To maintain physiological levels of diastolic and systolic Ca^{2+} concentrations in the model (particularly at faster pacing frequencies), as well as to better recreate the proportions of transport systems in Ca^{2+} extrusion, the authors adapted some Ca^{2+}-related membrane currents from the Pandit model. These changes included increasing the I_{NaCa} scaling factor k_{NaCa} to 0.18 nA.cm^{-2}.mM^{-4}, increasing the maximal I_{CaP} parameter $\bar{I}_{\mathrm{CaP}}$ to 0.85 μA.cm^{-2}, increasing the maximum background Ca^{2+} current conductance parameter, g_{Cab} to 0.648 μS.cm^{-2}, and increasing $\bar{I}_{\mathrm{NaK}}$ to 1 μA.cm^{-2}.

For individual ion transfer mechanisms in the surface ($_\mathrm{s}$) and tubular ($_\mathrm{t}$) membranes, the maximum conductivity (g_{max}) and current density ($I_{\mathrm{X,max}}$) parameters were computed according to the relations:

$$\begin{aligned}
g_{\mathrm{Xmax,s}} &= g_{\mathrm{Xmax}}(1-f_{\mathrm{X,t}})(S_{\mathrm{m,s}}+S_{\mathrm{m,t}})/S_{\mathrm{m,s}}\\
g_{\mathrm{Xmax,t}} &= g_{\mathrm{Xmax}}f_{\mathrm{X,t}}(S_{\mathrm{m,s}}+S_{\mathrm{m,t}})/S_{\mathrm{m,t}}\\
I_{\mathrm{Xmax,s}} &= I_{\mathrm{Xmax}}(1-f_{\mathrm{X,t}})(S_{\mathrm{m,s}}+S_{\mathrm{m,t}})/S_{\mathrm{m,s}}\\
I_{\mathrm{Xmax,t}} &= I_{\mathrm{Xmax}}f_{\mathrm{X,t}}(S_{\mathrm{m,s}}+S_{\mathrm{m,t}})/S_{\mathrm{m,s}}
\end{aligned}$$

where g_{Xmax} and I_{Xmax} denote the maximum specific conductivity and current density related to total membrane, $f_{\mathrm{X,t}}$ denotes the fractions of currents flowing through the tubular membrane, and $S_{\mathrm{m,s}}$ and $S_{\mathrm{m,t}}$ stand for the areas of peripheral and tubular membrane, respectively. Values for the T-tubular fractions of I_{CaL}, I_{ss}, I_{NaCa} and I_{NaK} were set from experimental data from detubulated myocytes.

To prevent reactivation of SR Ca^{2+} release channels and to more accurately simulate dynamic changes to intracellular Ca^{2+}, the authors modified some model parameters for Ca^{2+} handling: the forward SERCA rate parameter, $SERCA_{\mathrm{Vmax,f}}$, was increased from 0.04 to 0.4 mM.s^{-1}, the time constant of NSR to JSR Ca^{2+} transfer was increased from 0.58 to 20 ms, and the time constant of subspace to cytoplasm Ca^{2+} transfer was decreased from 26.7 to 8 ms. For ionic diffusion between the T-tubular system and extracellular space, time constants were set to 500 ms for divalent and 150 ms for monovalent ions to fit experimental data [444].

3.3.2.2 Pasek model results

The model reproduced action potentials recorded experimentally, including frequency-dependent lengthening of action potential, and recreated the experimental findings of [444] in terms of the changes to tubular concentrations of K^+ and Ca^{2+} ions in response to changes to concentrations in the extracellular medium. The model responded to step-wise removal of extracellular Ca^{2+} and the resulting slow phase of exponential I_{CaL} amplitude decline correlated with that observed experimentally, although the single exponential early phase decline in model I_{CaL} departed considerably from that observed experimentally.

To explore changes to currents and concentrations at more physiological heart rates, the authors paced the model at a frequency of 5 Hz to steady-state in current-clamp mode. Simulated APs at this frequency were almost identical at the surface and tubular membranes, indicating that there is negligible delay in electrical conduction between these areas, as expected. Membrane currents varied slightly between the sarcolemmal and tubular membrane, although this was primarily due to different channel densities in these areas. Intracellular Na^+ concentration increased significantly at 5 Hz pacing frequency, from 4.52 mM at rest to over 19 mM, which has been observed experimentally [141], whereas T-tubular Na^+ concentration was neglibily different from the extracellular concentration. Intracellular K^+ concentration fluctuated negligibly in the model, whereas the T-tubular concentration of K^+ underwent transient accumulation, resulting from voltage-dependent increases in the outward K^+ currents.

At 5 Hz pacing frequency, $[Ca^{2+}]_i$ transiently increases in the model towards an end-diastolic value of 0.024 μM (higher than that at rest), whereas $[Ca^{2+}]_{\mathrm{JSR,NSR}}$ increase as the SR loads to values above that at rest. Though $[Ca^{2+}]_t$ depletes initially at the beginning of the AP (owing to I_{CaL} and outward I_{NaCa}), the latter reverses direction to replenish tubular Ca^{2+} concentrations.

Frequency-dependent changes in tubular ion concentrations are illustrated in Figure 3.7), which shows the maximal (light grey) and end-diastolic (dark grey) tubular K^+ (a) and mimimal (light grey) and end-diastolic (dark grey) Ca^{2+} (b) concentrations. Tubular Ca^{2+} depletion progressively increased from 7% at 1 Hz to 13.1% at 5 Hz, whereas maximal Ca^{2+} accumulation decreased to near zero at 4 Hz - tus, tubular Ca^{2+} depletes and accumulates at pacing frequencues between 1 and 4 Hz, but is depleted throughout pacing at 5

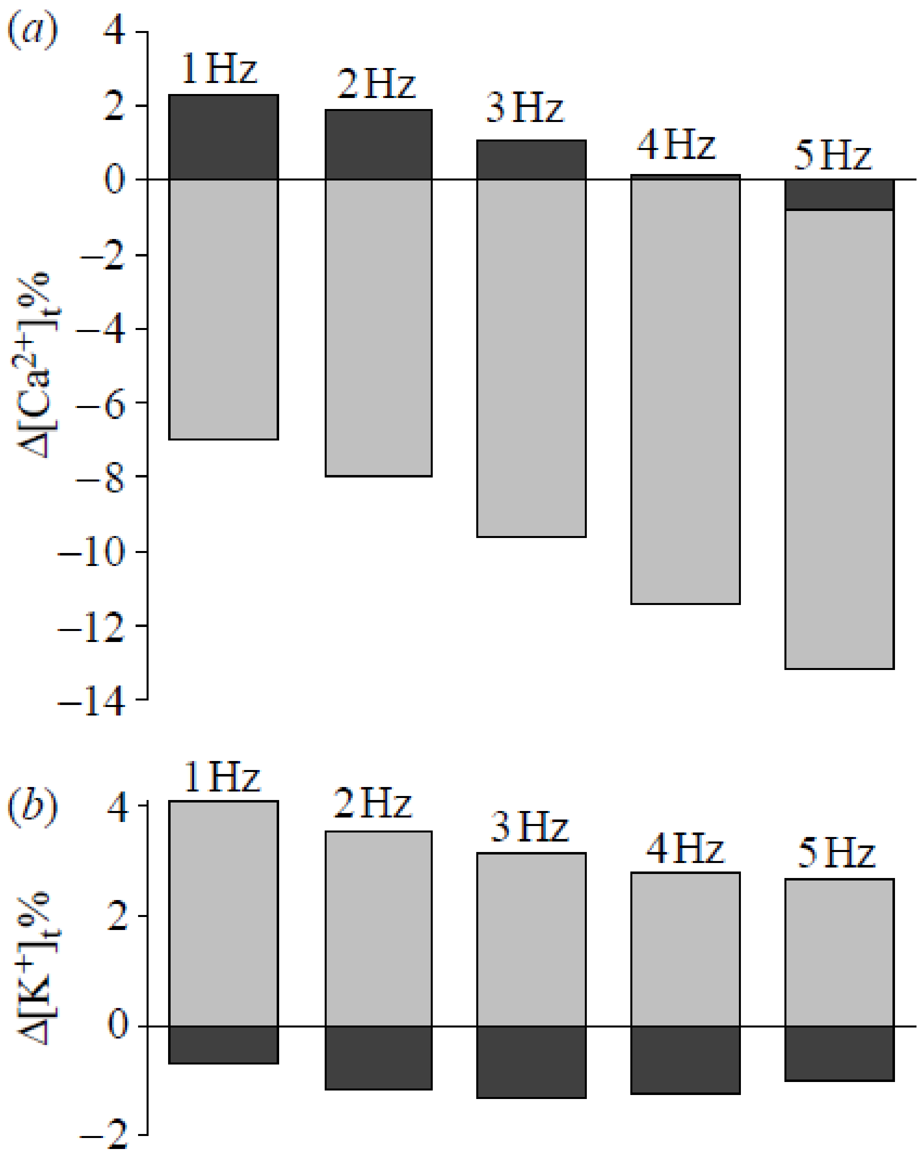

Figure 3.7. K^+ accumulation and Ca^{2+} depletion in the T-tubular system in the Pasek model under current-clamp in the Pasek model. Concentrations of Ca^{2+} (a) and K^+ (b) in the T-tubular system at steady-state at frequencies from 1 to 5 Hz are expressed as difference in percentage from the bulk extracellular concentrations, respectively. Difference for the peak value is plotted in light grey and the difference for end-diastolic value is plotted in dark grey. From [296].

Hz. Tubular K^+ accumulation peaks at 4.1% at 1 Hz and reduces with increases in pacing frequency to 2.7% at 5 Hz. Tubular K^+ depletion, meanwhile, increased up to 1.3% at 3 Hz but then decreases at higher pacing frequencies.

3.3.2.3 Pasek model limitations

The model's single-compartment tubular system neglects the varying depth of T-tubules as seen experimentally [367], as well as the heterogeneity in ion channel distribution along the T-tubular system [353]. Accordingly, the model does not capture the wave-like propagation of Ca^{2+} in the T-tubular system when local regions of higher channel density are included [52]. In addition, similar to the Pandit model, the simple description of Ca^{2+} in terms of the common-pool dynamics of Ca^{2+} handling means that the model fails to recreate experimental observations such as graded Ca^{2+} release and high-gain of excitation-contraction coupling. The SERCA formulation utilised also does not lead to shortening of Ca^{2+} transients with increased pacing frequency as observed experimentally [141,210]. Finally, the SR progressively loads with Ca^{2+} when pacing frequency is increased, resulting in larger Ca^{2+} transients at faster rates. Though this has been observed experimentally by some groups [210, 384], the opposite has also been reported [39, 40, 239], and this positive or negative freqency-dependent behaviour remains controversial.

3.3.3 The Niederer-Smith model

Strain is an important regulator of cardiac output, as increased filling results in increased cardiac output, and there is a biphasic increase in developed tension if this increased diastolic volume is maintained. The slow-force response to stretch (SFR) follows the initial increase in developed tension in the myocardium attributed to the Frank-Starling mechanism, and occurs over a period of 15-20 minutes to result in a further 20-50% increase in generated tension [9]. However, the underlying mechanisms for the SFR had not been determined, with three potential mechanisms implicated: 1) stretch-activation of the Na^+-H^+ exchanger (NHE), 2) increased cation conductance through stretch-activated channels (SACs), and 3) nitric oxide (NO) signalling [11, 70, 300, 413]. To investigate the contribution of these proposed mechanisms, Niederer and Smith [276] developed a computational model, which combined 3 existing models; the Niederer *et al.* contraction-relaxation model [275], the Pandit *et al.* electrophysiology model, and the Hinch *et al.* Ca^{2+} dynamics model. The Hinch framework was selected as it was able to reproduce graded Ca^{2+} release, which was not possible in the Pandit model as described previously.

The SFR is often observed in the presence of elevated intracellular Na^+ concentrations, and may increase NHE activity by increasing the rate of NHE cycling through a stretch-activated pathway, ultimately resulting in increased Ca^{2+} influx via I_{NaCa} and so increases in tension. SACs are reported to modulate the AP and Ca^{2+} transient in ventricular myocytes in response to stretch, as they alow entry of both K^+ and Na^+ ions which may result in elevated $[Na^+]_i$ levels and have subsequent effects on I_{NaCa} and Ca^{2+} loading as described for NHE. Finally, NO is known to regulate cardiac contraction [33, 78] and this may be through increased open probability of RyR due to stretch-induced increases in NO [300]. The Niederer-Smith model sought to explore and quantify the effects of each of these proposed mechanisms in regulating the SFR in rat ventricular myocytes, using species-specific data and models as much as possible.

3.3.3.1 Niederer-Smith model components and formulations

The basic model utilised by the authors was the Pandit model [293], which was coupled with the Hinch Ca^{2+} framework [166] and the Niederer *et al.* contraction model, all of which had been developed for rat cardiac myocytes at room temperature. As changes in $[Ca^{2+}]_i$ in the model are considerably greater than for Na^+ or K^+, these were more sensitive to cell volume and so the Hinch model values for SR and myocyte volumes were utilised over the Pandit values. $[Ca^{2+}]_i$ binding kinetics to troponin C were set to the more recent Niederer *et al.* values, and the number of regulatory units for the Hinch Ca^{2+} framework was increased from 50,000 to 75,000 so as to ensure Ca^{2+} influx in the model was comparable to the original Pandit model. SR leak maximum conductance was reduced to $5x10^{-6}$ ms^{-1} to give an equilibrium SR Ca^{2+} concentration of 700 μM.

Intracelluar pH in cardiac myocytes is regulated through various cotransporters and exchangers, with the NHE and Na^+-HCO_3^- cotransporter (NBC) acting as acid extruders and the Cl^--HCO_3^- exchanger (AE) and Cl^--H^+ exchanger (CHE) acting as base extruders [212]. In the Niederer-Smith model, the authors used the six-state CHE, AE and NBC transporter models from [108], and a NHE model was developed to greater account for Na^+ dependencies resulting from the range of $[Na^+]_i$ values encoutered during the SFR. The NHE model comprises a transporter and a regulatory component, fitted using pH and $[Na^+]_i$-dependent data. A simple background H^+ flux was added, with maximal conductance $4x10^{-6}$ mS, to ensure a resting pH of 7.26 as reported in experiments. As the inclusion of CHE and AE results in an inward flux of Cl^- ions, a small leak current for Cl^-

was included with maximal conductance 2x10^{-5} mS to ensure resting membrane potential was maintained.

Experiments have shown that stretch can induce minor alkolisis, with a corresponding increase in [Na$^+$]$_i$ and peak active tension, which has been posited to result from increased NHE activity and resulting Ca^{2+} influx via I_{NaCa}. This stretch-dependence of NHE has been shown to be the result of protein kinase C (PKC) activity [90], which was modelled by assuming this phosphorylation via PKC alters the dissociation constant of protons and occurs instantaneously, as data describing time-dependence of phosphorylation is not available. Changes in pH were modelled assuming that acid efflux through NHE increases in response to stretch, but acts against a persistent acid influx via CHE and the background H$^+$ flux. The change in AE flux with stretch was constrained by experimental data showing no change to pH in the presence of a 30% decrease in the proton dissociation constant to the NHE regulatory site.

It has been reported that stretch-dependent currents in rat myocytes may result from a specific K$^+$ current, I_{Ko}, and a non-specific current, I_{ns}. The authors therefore adapted the I_{Kp} current formulation from [309] and fitted it to rat data using $I-V$ curves obtained during strain [220]. I_{ns} was split into Na$^+$ and K$^+$ components. These two new formulations meant that there is no description of background Na$^+$ and K$^+$ currents in the Niederer-Smith model, as with the Pandit model. As increased NO production has been reported following stretch [300], it has been proposed that NO may selectively increase RyR open probability, acting as a second messenger for stretch. The authors therefore assumed that increased frequency of Ca^{2+} frequency is the result of increased shift of RyRs from closed to open state, and incorporated a strain-dependent scaler to account for increases in the proportion of open RyRs which closely matches the experimental observations.

Finally, the authors identified that the I_{NaK} description of the Pandit model is derived from a guinea pig model [235] and scaled to achieve a resting [Na$^+$]$_i$ of 10.7 mM. However, experimental data suggested that I_{NaK} is highly dependent on [Na$^+$]$_i$ in rat myocytes [115], so the maximal flux was increased to 9.5 μA.mm^{-2} to give a better fit to the experimental Na$^+$ concentration-frequency response.

3.3.3.2 Niederer-Smith model results

The model was stable over long periods, essential for the SFR which can occur over $\sim$ 15 minutes, with o changes occurred to Na$^+$, K$^+$ or Ca^{2+} concentrations in the quiescent state, nor changes $>0.1\%$ over a 20 minute period of pacing at a frequency of 1 Hz. APD and peak tension increased with pacing frequency, as observed experimentally.

Examining the SFR, the model was paced to steady-state at a pacing frequency of 1 Hz, then paced for 5 minutes at resting sarcomere length before the application of 10% stretch for 15 minutes. The Frank-Starling response was defined as the percentage change in tension in the period prior to stretch and 10 s after application of stretch. The authors ran multiple simulations including combinations of SACs, NO and pH regulation of the SFR, and found that only SACs were capable of reproducing a SFR consistent with experimental observations – stretch-dependent pH had 37% of the SAC-response, and NO-induced RyR open probability increases resulted in a negative effect. To further explore these mechanisms, simulated Ca^{2+} transients before, 10 s after, and 15 minutes after 10% stretch were compared with experimental results from [198]. Only SAC alone, SAC + pH, and SAC + pH + NO combinations were capable of producing a SFR greater than 20%. In the presence of SACs and stretch-dependent NHE and AE, Ca^{2+} transients increased by 5% (compared to 11% observed experimentally). SACs alone resulted in Ca^{2+} transients qualitatively similar to experimental results, but in the presence of NO there were notable differences in Ca^{2+} transient magnitude, time to peak, and time to 50% relaxation. NHE and AE stretch-dependence had negligible effects on the Ca^{2+} transient, despite NHE being consistently believed to cause the SFR, though this was primarily due to abbreviation of the SFR when NHE is blocked. Simulations showed a 32% and 56% decrease in SFR after NHE inhibition in models containing SACs and SACs + NHE/AE stretch-dependence, respectively.

3.3.3.3 Niederer-Smith model limitations

Comparing the broad range of stretch-dependent mechanisms is difficult as the standard definition of stretch varies across groups and protocols, which may present a limitation given the simplified assumption that strain was a percentage of reference length used in the model. In addition, simple background fluxes to maintain pH, [H$^+$]$_i$ and [Cl$^-$]$_i$ concentrations incorporated in the model did not necessarily have a physiological basis. Such processes may not necessarily exist, or could be more complex than the simple formulations presented – experimental characterisation would be necessary, as there is little experimental data to date. As a deterministic model, the model is unable to account for stochastic Ca^{2+} dynamics which could play a significant role in the SFR, as it is possible Ca^{2+} sparks play a role in modulating tension generation and relaxation as well as the normal, coordinated Ca^{2+} transient.

3.3.4 The Gattoni model

The Gattoni model [146] (Figure 3.8) is a species and temperature-specific data-driven model of the rat ventricular myocyte. The model combined the Pandit electrophysiology model, the Hinch Ca^{2+} framework and the Na^+-K^+ model of Lewalle *et al.* [214]. These choices were made as the authors identified that the Ca^{2+} handling and Na^+-K^+ descriptions used in the Pandit model were derived from non-rodent data, whereas the Hinch and Lewalle models were fitted using rat data. New and existing rat data, collected at 37°C, were then used to parameterise the model, giving temperature and species-specificity.

Four variants of the Gattoni model were developed: the base model (stable at either 1.0 or 6.0 Hz, depending on the parameter set used), the CaMK model (which included a description of CaMKII-mediated I_{CaL} and I_{to} facilitation), the NO CaMK model (which inhibited CaMKII activation of SERCA), and the RNaK model (in which the affinity of I_{NaK} to Na^+ was reduced). The latter three variants were used to investigate how CaMKII-mediated modulation and inhibition of I_{CaL}, I_{to} and SERCA, and altered Na^+-K^+ ATPase activity affect the force-frequency response in rat ventricular myocytes.

3.3.4.1 Gattoni model components and formulations

Membrane currents included in the Gattoni model and their respective peak values at a pacing frequency of 6 Hz (cycle length 167 ms) are provided in Table 3.2. The authors analysed different components of the Pandit electrophysiology model and their dependence on experimental data, to highlight where derivations from non-rat data existed – they identified the Ca^{2+} handling system, and the Na^+-K^+ ATPase model as being derived from canine and guinea pig data. As a result, they replaced the Ca^{2+} handling system with

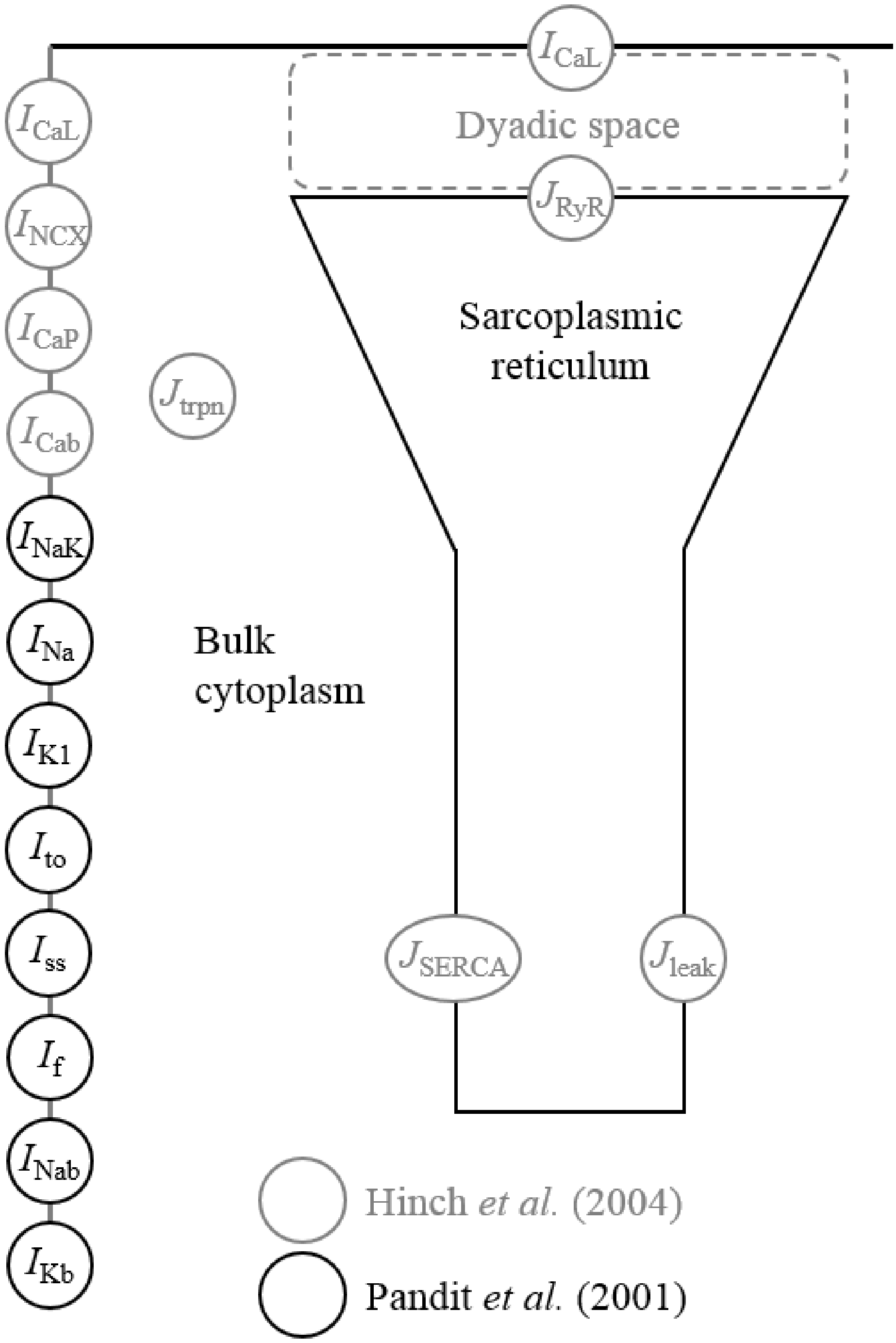

Figure 3.8. Structure of the Gattoni model of rat ventricular electrophysiology. The Gattoni model was a combination of the Pandit, Hinch and Lewalle models. Grey circles indicate components inherited from the Hinch model and black circles represent those from the Pandit model. Adapted from [146].

that of Hinch *et al.* [166], and replaced the Na^+/K^+ model with the Lewalle *et al.* model, which was fitted to rat data at 37°C. They also introduced equations for the CaMKII-mediated increase in SERCA activity from Li *et al.* [219].

Table 3.2. Membrane currents and fluxes in the base Gattoni model.

Current	Description	Steady-state peak at 6 Hz
I_{Na}	Na^+ current	-130.9 pA/pF
I_{to}	Ca^{2+}-independent transient outward K^+ current	17.83 pA/pF
I_{CaL}	L-type Ca^{2+} current	-7.07 pA/pF
I_{Iss}	Steady-state K^+ current	0.48 pA/pF
I_{f}	Hyperpolarisation-activated (funny) current	0
I_{K1}	Inward rectifier current	1.85 pA/pF
I_{Nab}	Background Na^+ current	-0.03 pA/pF
I_{Kb}	Background K^+ current	0.16 pA/pF
I_{Cab}	Background Ca^{2+} current	-0.22 pA/pF
I_{NaK}	Na^+-K^+ exchanger current	1.36 pA/pF
I_{NCX}	Na^+-Ca^{2+} exchanger current	Max 0.7 pA/pF Min -0.9 pA/pF
I_{CaP}	Sarcolemmal Ca^{2+} pump current	0.2 pA/pF
J_{RyR}	RyR Ca^{2+} release flux	2.837 $mM.s^{-1}$
J_{SERCA}	SERCA2a Ca^{2+} flux	0.619 $mM.s^{-1}$
J_{leak}	SR Ca^{2+} leak flux	0.012 $mM.s^{-1}$
J_{trpn}	Troponin buffering	Max 0.24 $mM.s^{-1}$ Min -0.00129 $mM.ms^{-1}$

The authors evaluated fluxes through NCX and I_{CaP} using caffeine-evoked Ca^{2+} transients at 1 and 6 Hz, then fitted the NCX parameters so that it extruded 90% of the measured Ca^{2+} from a transient, with the remaining 10% used to fit the parameters for I_{CaP}. Ca^{2+} influx through I_{CaL} was fitted using the peak current for I_{CaL} from the $I-V$ curve, and RyR flux was modulated to match the time to peak of stimulated Ca^{2+} transients. SR Ca^{2+} leak was fitted to constrain SR Ca^{2+} concentration to fall within maximum and minimum values, defined by the integral of NCX during a caffeine-evoked transient (maximum) and the integral of SERCA during a stimulated Ca^{2+} transient. I_{Cab} was modified to match the peak of the Ca^{2+} transients at frequencies of 1 and 6 Hz, and the remaining Na^+ and K^+ membrane currents were modified using rat data taken at physiological temperatures. A summary of the fitted Ca^{2+} parameters is given in Table 3.3.

Table 3.3. Fitted Ca^{2+} parameters in the Gattoni model.

Parameter	Description	Value
g_{NCX}	NCX pump rate	$0.0515\text{x}10^{-3}$ $\mu M^{-3}.ms^{-1}$
g_{CaP}	Max rate of sarcolemmal Ca^{2+} pump	$0.005\text{x}10^{-3}$ $\mu M^{-3}.ms^{-1}$
K_{CaP}	Half-saturation of sarcolemmal Ca^{2+} pump	$0.35\text{x}10^{-3}$ mM
$g_{\mathrm{SERCA,1}}$	Max pump rate of SERCA (1 Hz)	$0.47\text{x}10^{-3}$ $\mu M^{-3}.ms^{-1}$
$g_{\mathrm{SERCA,6}}$	Max pump rate of SERCA (6 Hz)	$0.68\text{x}10^{-3}$ $\mu M^{-3}.ms^{-1}$
K_{SERCA}	Half-saturation of SERCA	$0.45\text{x}10^{-3}$ mM
J_{L}	Permeability of a single LTCC	$7\text{x}10^{-4}$ $\mu M^{-3}.ms^{-1}$
K_{L}	Concentration at LTCC inactivation	0.6 nM
V_{L}	Potential when half LTCCs open	-9 mV
δ_{VL}	Width of LTCC opening potentials	7 mV
ϕ_{L}	Proportion of time LTCC closed in open mode	11.5
τ_{L}	Inactivation time constant for LTCC	1450 ms
K_{RyR}	Half-concentration of activation	0.065 mM
g_{D}	Permeability of leak current to dyadic space	0.099 $\mu M^{-3}.ms^{-1}$
g_{SRL}	Rate of leak from SR to cytosol	$7.11\text{x}10^{-6}$ ms^{-1}
g_{Cab}	Background Ca^{2+} current rate	$5.10875\text{x}10^{-8}$ $mM.mV^{-1}.ms^{-1}$

As mentioned previously, three further variants of the Gattoni model were developed from this baseline model, which itself had 2 parameter sets stable at pacing frequencies of either 1 or 6 Hz. As previous studies have reported facilitation of I_{to} and I_{CaL} by CaMKII [96, 439], the CaMK variant was developed which included such modulation and was fitted using murine data from the literature. For the NO CaMK variant, CaMKII SERCA activation was inhibited by fixing the SERCA conductivity parameter to the 6 Hz value (g_{SERCA} = 0.00068 $mM.ms^{-1}$) for all pacing frequencies (fixing to the 1 Hz parameter value g_{SERCA} = 0.00047 $mM.ms^{-1}$, resulted in alternans at pacing frequencies above 4 Hz). Finally, the RNaK variant was developed in which the affinity of the Na^{+}-K^{+} ATPase to Na^{+} was reduced and the maximum I_{NaK} parameter was reduced to 0.2 nA to sustain $[Na^{+}]_{i}$ of around 10 mM.

3.3.4.2 Gattoni model results

The baseline model closely reproduced experimental data for APs and Ca^{2+} transients at 37°C, with similar values for peak $[Ca^{2+}]_i$, diastolic $[Ca^{2+}]_i$, time to 50% relaxation and time to peak Ca^{2+} at frequencies of 1 and 6 Hz. Ca^{2+} extrusion via SERCA, I_{NaCa} and I_{CaP} also fell within experimental ranges.

In the baseline and RNaK models, the peak Ca^{2+} frequency response (PCFR) showed biphasic behaviour with pacing frequency, decreasing in the range of 1 to 2 or 3 Hz but increasing in the range 2 or 3 Hz to 6 Hz (depending on $[Ca^{2+}]_o$). In the CaMK model, the PCFR is positive at $[Ca^{2+}]_o = 1.8$ mM but the same response as for the baseline model is observed at lower extracellular Ca^{2+} concentrations, while in the NO CaMK model there is a shift in the biphasic PCFR response depending on $[Ca^{2+}]_o$.

The magnitude of the peak Ca^{2+} frequency response (MCFR) was biphasic in the baseline model, negative from 1 to 4 Hz and positive from 4 to 6 Hz at $[Ca^{2+}]_o = 1.8$ mM, shifting to lower frequencies as $[Ca^{2+}]_o$ was reduced. The CaMK and RNaK models also showed a biphasic MCFR at most tested levels of $[Ca^{2+}]_o$, but shifted towards lower frequencies than the baseline model. For the NO CaMK model, the MCFR was negative at all tested extracellular Ca^{2+} concentrations. The diastolic Ca^{2+} frequency response (DCFR) was positive in all model variants.

The $[Ca^{2+}]_{SR}$ frequency response in the baseline model is biphasic and decreases with frequency at higher extracellular Ca^{2+} concentrations. The RNaK model also shows a biphasic $[Ca^{2+}]_{SR}$ frequency response. For the CaMK and NO CaMK models, $[Ca^{2+}]_{SR}$ decreases with frequency. In general, the model produces increases in peak $[Ca^{2+}]_i$ and Ca^{2+} transient magnitude for all variants.

3.3.4.3 Gattoni model limitations

One of the primary limitations of the Gattoni model is that there are 4 variants of the model: a baseline variant, a variant incorporating CaMKII regulation of I_{CaL} and I_{to}, a variant in which CaMKII-regulation of SERCA is inhibited, and a variant in which the affinity of the Na^+-K^+ exchanger to Na^+ is altered. The baseline model has 2 subvariants, one stable at 1.0 Hz (but unable to simulate APs at cycle lengths shorter than 640 ms) and one at 6.0 Hz (but unable to simulate APs at cycle lengths longer than 980 ms). *In vivo*, cardiac myocytes are capable of adapting to rate, and this trait is a fundamental for their function. The inclusion of 2 subvariants, therefore, limits the utility of the model for the consistent studying of rate-dependent changes.

Though the model addresses many limitations by being validated against rat-specific experimental data, often recorded at body temperature (37°C), there are some inherent experimental limitations associated with collecting data at this temperature. Given that physiological processes typically increase in speed at higher temperatures, the step from room to body temperature results in faster reactions, meaning it is more difficult to control the clamped voltage during experiments, which may result in artefacts. In addition, many of the parameters controlling Ca^{2+} handling remain to be derivatives of measurements taken from ferret or canine myocytes, notably parameters relating to Ca^{2+} buffering and the geometry of the SR (although the rat-specificty of these parameters is yet to be determined, so this is understandable). Though the Hinch Ca^{2+} framework offers greater rat-specificity and produces more physiological Ca^{2+} homeostasis, the model lacks explicit descriptions of the junctional and network SR.

To reduce the model complexity, the authors elected not to include descriptions of the interplay between Ca^{2+}, troponin C and tension generation. Though inclusion of these would significantly increase computation time for the model, they are potentially important aspects that can regulate Ca^{2+} handling and their omission must always be balanced against the need for computational efficiency.

Finally, the deterministic nature of the model represents a notable limitation. Ca^{2+} handling is largely stochastic in nature, particularly in disease where summation of Ca^{2+} sparks and spontaneous Ca^{2+} release events (which are increased in frequency) can result in triggered activity and potentially be pro-arrhythmic [189].

3.3.5 The Devenyi-Sobie model

Emergent behaviours from cardiomyocytes result from the complex interplay between many ion channels, exchangers, pumps and transporters, resulting in a dynamic system that can be difficult to study experimentally. However, mathematical models, as described, provide an important tool to gain quantitative insight into the various underlying mechanisms. However, as models increase in complexity, there is an increasing need to understand how model behaviours arise from inputs [116]. Parameter sensitivity analysis is one such strategy, which can be used to quantify how changes in model parameters influence key model behaviours. Accordingly, Devenyi and Sobie [117] performed a sensitivity analysis of the Pandit model, generating a population of model variants by randomly scaling various ion channels, pumps and transporters, and quantitatively related these adjusted parameters to measureable outputs such as Ca^{2+} transient amplitude. The result was a targeted, adjusted Pandit model variant that better matched experimental findings.

3.3.5.1 Devenyi-Sobie model adjustments and results

As the Devenyi-Sobie model is a re-parameterised version of the Pandit model, the model components and formulations are largely the same as the original model. However, following sensitivity analysis, the authors identified that the balance of Ca^{2+} fluxes in the Pandit model is inconsistent with experimental data, with SERCA accounting for only a small proportion of Ca^{2+} extrused from the cytosol, compared to the 92% extrusion via SERCA observed in experiments [27]. In addition, the SR Ca^{2+} concentration in the model is much lower than has been recorded experimentally [29, 72, 393, 406], and so the Pandit model greatly underestimates the contribution of SR Ca^{2+} release to the Ca^{2+} transient magnitude. Accordingly, the model was adjusted to better reproduce the balance of Ca^{2+} fluxes as observed experimentally (see Figure 3.9).

To begin, the authors increased the contribution of SERCA to Ca^{2+} efflux by increasing SERCA levels and decreasing those for NCX and I_{CaP}. Following this, the SERCA formulation was unable to maintain diastolic Ca^{2+} concentrations lower than 300 nM, so it was replaced with the formulation developed by Tran *et al.* [398], which better reproduces the physiological dependence of SERCA on SR load. Further adjustments were then made to produce the appropriate balance of Ca^{2+} fluxes. However, this then led to unphysiologically large Ca^{2+} transients, and so Ca^{2+} influx into the cell via I_{CaL} and the background Ca^{2+} current was reduced and the buffering capacity was increased. To better maintain APD, which was abbreviated by the reduced I_{CaL}, repolarising K^{+} currents were therefore decreased as well. Finally, to better reproduce the experimentally-observed Ca^{2+} transient duration, the gating parameters for RyR were adjusted to lead to more rapid closure. A summary of the adjusted parameters is given in Table 3.4.

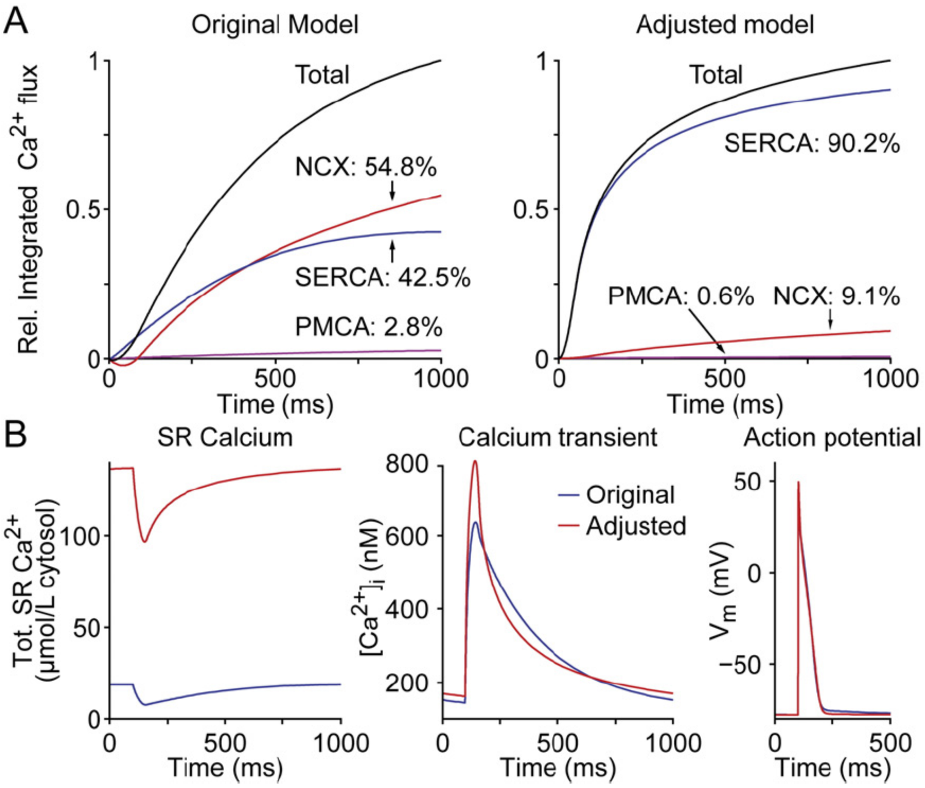

Figure 3.9. Adjustments made to the Pandit model to improve Ca^{2+} flux balance. A: Adjustments to different transport mechanisms to improve Ca^{2+} flux balance over the course of a steady-state Ca^{2+} transient. B: SR load and Ca^{2+} transients are larger in the adjusted model, but Ca^{2+} transient decay is faster and the AP remains similar. From [117].

3.3.5.2 Devenyi-Sobie model limitations

The adjustments made for the Devenyi-Sobie model are somewhat limited in scope, made largely to tune the model for new experimental data. This leaves some features of the model in need of updating. Though phenomenological models can provide useful insight into, in this example, the balance of Ca^{2+} fluxes across the SR and membrane, more realistically stochastic triggering of Ca^{2+} release events is an essential requirement for modelling Ca^{2+}-induced Ca^{2+} release [75, 88]. The model could further be improved by addition of subsarcolemmal space where there are known to be higher concentrations of membrane proteins such as NCX [395, 429].

The parameter sensitivity analysis procedure used to adjust the model has its own limitations. Firstly, for the simulation of disease states or changes to expression, a parameter's importance could change, which is not accounted for by its adjustment in the control

Table 3.4. Parameter adjustments in the Devenyi-Sobie model.

Parameter	Description	Pandit Value	Adjusted Value
K_{NaCa}	NCX scaling factor	9.984x10^{-6}	2.29632x10^{-6} nA.mM^{-4}
$\bar{I}_{\mathrm{CaP}}$	Max I_{CaP}	0.004	0.002 nA
g_{CaL}	I_{CaL} conductance	0.031	0.0124 μS
g_{Cab}	I_{Cab} conductance	3.24x10^{-5}	8.1x10^{-6} μS
$\mathrm{HTRPN_{tot}}$	[High affinity troponin sites]	0.14	0.21 mM
$\mathrm{LTRPN_{tot}}$	[Low affinit troponin sites]	0.07	0.105 mM
$\mathrm{CMDN_{tot}}$	Calmodulin concentration	0.05	0.075 mM
g_{to}	I_{to} conductance	0.0162265	0.0081325 μS
g_{ss}	I_{ss} conductance	0.007	0.0049 μS
v_1	RyR release velocity	1800	1530 s^{-1}
k_{b}^{-}	RyR transition rate O2 to O1	1930	5790 s^{-1}
k_{c}^{+}	RyR transition rate O1 to C2	100	300 s^{-1}
k_{c}^{-}	RyR transition rate C2 to O1	0.8	0.8/3 s^{-1}

model. Additionally, there may be cross-interaction of multiple parameter-sensitivities, for example the reduction of one parameter may enhance the contribution of another. Varying parameters independently and to the same degree is also an assumption that may not necessarily be valid – neuronal studies, for example, have shown that expression levels of different ion channels are often correlated [352, 386, 390]. Finally, as with the original Pandit model, the Devenyi-Sobie model is unsuitable for pacing at rapid rates, so its use for the study of arrhythmia mechanisms, and as a tool for explaining experimental results, is still limited.

3.4 Comparison of Pandit and Gattoni models

As shown in the previous section, there are a number of available computational models of rat ventricular electrophysiology, each of which has been validated against experimental data and provided useful insight into various mechanisms. The Pandit model was the first such model, and new models since then have built on the foundations of the Pandit model by adapting certain components in some way or by adding components from other models, so as to provide better or further functionality lacking in the original model. For the

Pasek model, structural changes were incorporated to account for the T-tubular system; for the Niederer-Smith model, the Ca^{2+} handling system was replaced and combined with a model of contraction and acid-base balance; for the Gattoni model, the Ca^{2+} handling system was replaced, the Na^{+}-K^{+} exchanger formulation was replaced, and the whole model was re-parameterised against recent rat-specific data at physiological temperature; and finally in the Devenyi-Sobie model, the parameter sensitivity of the Pandit model was analysed and certain parameters were refitted, and the SERCA formulation was replaced to give a better balance of Ca^{2+} fluxes. However, it is difficult to say whether one model is more valid than another, as they are often constrained for specific investigations, are not always validated against experimental data from a variety of sources, and may not have much utility for investigating other processes beyond those they were designed for.

It is therefore of benefit to compare these models, incorporating them into a framework to allow direct comparison in model outputs (with consistency in units, methods of integration, etc) after identical simulation protocols. However, comparison of all existing rat models of electrophysiology to date would be laborious, and likely reveal only minor differences between each model iteration except where new model components are incoporated. Of the models published since the original Pandit model, only the Niederer-Smith and Gattoni models add further functionality related to Ca^{2+} handling, the remodelling of which is known to be pro-arrhythmic – though the Devenyi-Sobie model updates the Ca^{2+} handling system from the original Pandit model, the same functional limitations persist in terms of the lack of graded Ca^{2+} release. Accordingly, in the following section, the original Pandit model will be compared to the Gattoni model. This choice was made as the Gattoni model replaces the Ca^{2+} handling system of the Pandit model with the same framework as the Niederer-Smith model, but further adds an updated Na^{+}-K^{+} ATPase formulation and re-parameterises to more recent experimental data recorded at physiological temperatures. The Pandit and Gattoni models form the basis of the novel computational model of rat ventricular electrophysiology and Ca^{2+} handling presented in Chapter 4.

To do so, each model was incorporated in the framework introduced later in Chapter 4 [97] – this provides a consistent framework where simulation data are outputted in a consistent format and simulation protocols can be applied equally and consistently between models. The following subsections detail differences in action potential characteristics, membrane currents, Ca^{2+} handling, concentration changes, and restitution properties of the Pandit and Gattoni models. In addition, the utility of each model for exploring changes in electrophysiology is compared, a property that is important if a model is to be used outside of its original scope.

3.4.1 Action potential characteristics

Steady-state action potentials at various cycle lengths for each model are shown in Figure 3.10. Both models are capable of simulating action potentials at cycle lengths between 1000 and 350 ms, however the Pandit model is unable to simulate beyond that at shorter cycle lengths. The Gattoni model can still simulate action potentials up to cycle lengths of 167 ms (Figure 3.11). However, it should be noted that the Gattoni model has 2 variants, stable at pacing frequencies of either 1.0 or 6.0 Hz. The 1.0 Hz variant is unable to simulate action potentials at cycle lengths faster than 640 ms, whereas the 6.0 Hz variant is capable of simulating action potentials across a much broader range of cycle lengths, from 167 to 980 ms. Unless otherwise mentioned, 'Gattoni model' hereby refers to the 6.0 Hz variant for this reason.

At BCL = 1000 ms, APDs (as APD_{90}) in each model were 70.2 (Pandit) and 42.9 ms (Gattoni). In the Pandit model, APD prolonged with increases in pacing frequency to 89.4 ms at BCL = 500 ms, and 119.0 ms at BCL = 350 ms – the latter being unphysiological in rat ventricular myocytes as APD has not been shown to exceed 100 ms experimentally [121, 159, 290, 299, 407, 431]. In the Gattoni model, APD initially shortens with increases in pacing frequency to 33.4 ms at BCL = 500 ms, and 32.5 ms at BCL = 350 ms. At faster pacing frequencies, however, APD then increased to 38.8 ms at BCL = 167 ms. Other measures of APD at different stages of repolarisation increased in line with APD_{90} for the Pandit model. However, in the Gattoni model, APD_{30} increased with pacing frequency, but APD_{50} and APD_{70} followed the same pattern as APD_{90}. These changes are shown in Table 3.5. APD restitution characteristics for each model are given in greater detail in Section 3.4.4.

In general, APD in the Pandit model is longer than in the Gattoni model. At cycle lengths of 1000 ms, there is little difference in APD between models ($\sim$ 2 ms), however at BCL = 500 ms, APD in the Pandit model is longer by 36 ms, and by 69 ms at BCL = 350 ms (though whether the Pandit model APD at BCL = 350 ms is physiological is debateable, as described previously). The Pandit model shows considerable APD_{30} prolongation from cycle lengths of 1000 to 350 ms, with APD_{30} nearly doubling with pacing frequency from

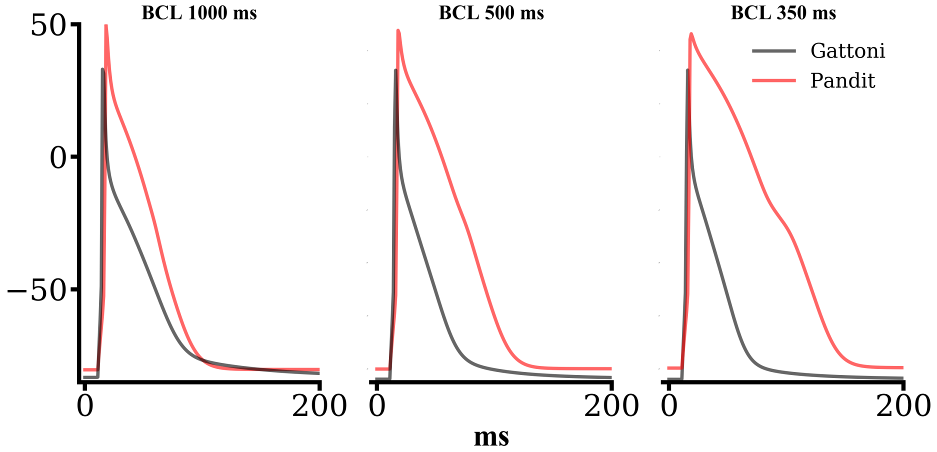

Figure 3.10. Comparison of action potentials in the Pandit and Gattoni models at various cycle lengths. Each model can simulate action potentials at cycle lengths between 1000 and 350 ms, but the 6.0 Hz variant of the Gattoni model can additionally reproduce action potentials up to cycle lengths of 167 ms.

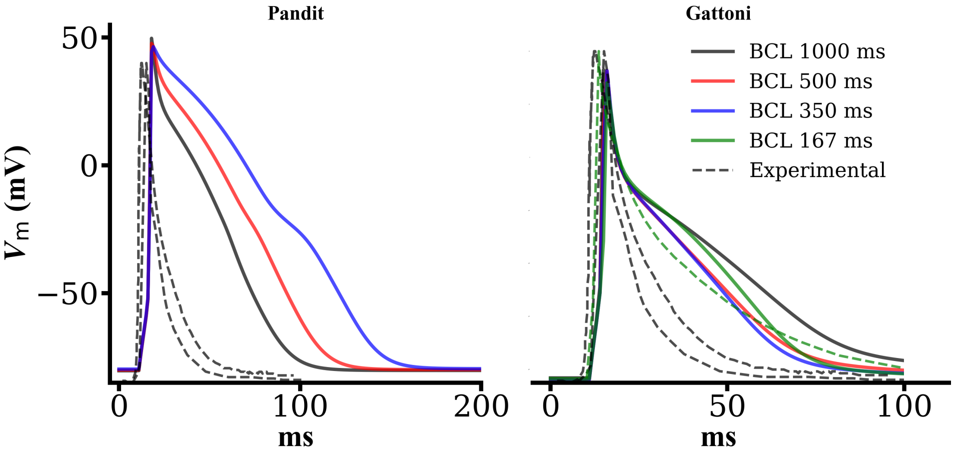

Figure 3.11. Comparison of adaptation to pacing frequency of action potentials in the Pandit and Gattoni models. APD in the Pandit model prolongates with increases in pacing frequency, whereas in the Gattoni model APD initially shortens before lengthening. Dashed lines show experimental AP traces from [121, 290, 299].

1.0 Hz to 2.0 Hz. The Gattoni model, conversely, does not exhibit much change in APD_{30} across the pacing frequencies, being only 1.6 ms longer at BCL = 167 ms compared to BCL = 1000 ms. A similar pattern is observed for APD_{50} and APD_{70} in the Pandit model, each value increasing with pacing frequency. However, in the Gattoni model, APD_{50} and APD_{70} initially decrease with increased pacing frequency, before prolonging at BCL =

Table 3.5. Changes to APD with pacing frequency in the Pandit and Gattoni models.

Parameter	BCL 1000	BCL 500	BCL 350	BCL 167	Experimental ranges
APD_{30}	P 17.1 G 4.1	P 30.2 G 4.3	P 45.6 G 4.37	G 5.8	No data
APD_{50}	P 36.5 G 19.8	P 50.5 G 16.4	P 68.3 G 16.7	G 23.5	13.0 to 29.0 [31, 299, 408]
APD_{70}	P 51.4 G 42.9	P 70.0 G 33.4	P 98.2 G 32.5	G 38.8	No data
APD_{90}	P 70.2 G 68.2	P 89.4 G 53.3	P 119.0 G 49.6	G 54.4	26 to 72 [35, 121, 159, 277, 290, 299, 408]

167 ms.

In both models, the maximum AP upstroke rate ($\mathrm{d}V/\mathrm{d}t_{\mathrm{max}}$) decreases as pacing frequency increases from BCL = 1000 ms to BCL = 350 ms, from 190.3 to 158.3 V.s^{-1} in the Pandit model and from 180.6 to 173.0 V.s^{-1} in the Gattoni model (with a further decrease to 136.7 V.s^{-1} at BCL = 167 ms). This is paralleled by a reduction in AP amplitude (V_{amp}) in both models from 130.1 to 126.2 mV in the Pandit model and from 121.1 to 118.9 mV in the Gattoni model across the same cycle length range (V_{amp} decreases further to 111.7 mV at BCL = 167 ms in the Gattoni model). This reduction in V_{amp} arises from both a decrease in AP overshoot (V_{max}) in both models, and is contributed to further in the Pandit model by a concomitant increase in resting membrane potential (RMBP, or V_{min}) from -80.4 to -79.7 mV. Resting membrane potential in the Gattoni model actually becomes more negative with increases in cycle length from 1000 to 350 ms, before increasing slightly at BCL = 167 ms, but this value is still lower than for BCL = 1000 ms. These changes are summarised in Table 3.6.

3.4.1.1 Pandit APD prolongation at faster cycle lengths

As described earlier, the Pandit model is capable of simulating APs at BCL = 350 ms, however the APD at this pacing frequency is 119.0 ms, which is unphysiologically large for rat ventricular myocytes. Experimental APD values from the literature typically range from $\sim$ 31 to 72 ms in healthy cells [121, 159, 290, 299, 407]. Even in failing ventricular myocytes, in which APD is known to be prolonged, APD typically does not exceed 110

Table 3.6. Changes to V_{min}, V_{max} and V_{amp} in the Pandit and Gattoni models in response to alterations in pacing frequency.

Parameter	BCL 1000	BCL 500	BCL 350	BCL 167	Experimental ranges
V_{min} (mV)	P -80.4	P -80.1	P -79.7	G -83.6	-87.5 to -74 [3, 22, 50, 299, 397, 431]
	G -83.2	G -83.9	G -84.0		
V_{max} (mV)	P 49.7	P 48.2	P 46.5	G 28.1	No data
	G 37.9	G 35.6	G 35.0		
V_{amp} (mV)	P 130.1	P 128.3	P 126.2	G 111.7	90.5 to 114 [8, 31, 121, 299, 458]
	G 121.1	G 119.5	G 118.9		
dV/dt_{max} (V.s^{-1})	P 190.3	P 177.9	P 158.3	G 136.7	140.6 to 194.1 [8, 31]
	G 180.6	G 175.9	G 173.0		

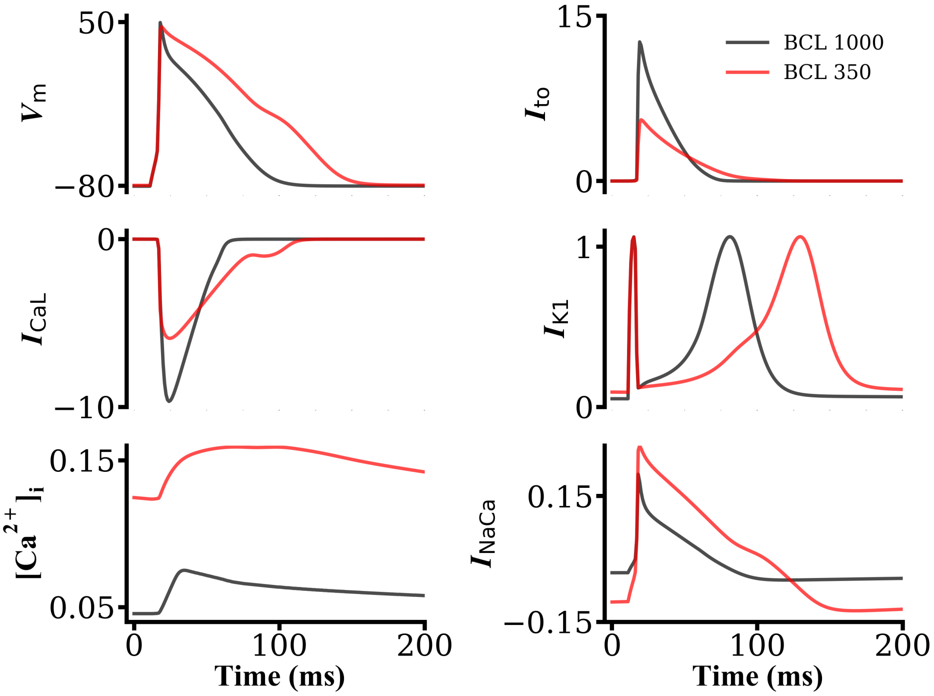

Figure 3.12. Comparison of APs and membrane currents in the Pandit model at cycle lengths of 1000 and 350 ms. At BCL = 350 ms, the Pandit model produces an abnormally prolonged APD (A), resulting from a reduced I_{to} current (B), a longer-lasting I_{CaL} waveform (C), and a slower-activating I_{K1} current. In addition, elevation of $[\mathrm{Ca}^{2+}]_{\mathrm{i}}$ (E) favours further depolarisation via I_{NaCa} (F).

ms [159].

Analysis of the underlying membrane currents in the Pandit model at BCL = 350 ms appears to reveal the cause of this abnormal prolongation (Figure 3.12). I_{Na} remains relatively unchanged compared to at BCL = 1000 ms, however I_{to} (responsible for initial repolarisation) is greatly reduced at BCL = 350 ms, from 12.6 pA/pF to 5.5 pA/pF (Figure 3.12B). In addition, although I_{CaL} is reduced by $\sim$ 4 pA/pF (Figure 3.12C), I_{CaL} remains activated for a longer duration, and appears to partially reactive at approximately 80 ms. These factors combine to extend the duration of phase 2 and 3 repolarisation, which results in a longer lasting but slowly-activating I_{K1} waveform (Figure 3.12D) that prolongs terminal repolarisation further. In addition, the elevation of intracellular Ca^{2+} concentration at BCL = 350 ms favours inward, depolarising I_{NaCa} (Figure 3.12E, F).

As the Pandit model AP at BCL = 350 ms is unphysiological (i.e. abnormally prolonged over experimental ranges [121,159,290,299,407]), from here on comparison will only be made between each model at cycle lengths of 1000 and 500 ms. In addition, the Gattoni model results at BCL = 167 ms will be shown.

3.4.2 Membrane currents

3.4.2.1 Depolarising currents: I_{Na} and I_{CaL}

Changes in the main depolarising (I_{Na}, I_{CaL}) and repolarising (I_{to}, I_{K1}) membrane currents with pacing frequency are shown in Figure 3.13. I_{Na} in the Pandit model changes little when pacing frequency is doubled from BCL = 1000 to 500 ms, with peak values of -182.2 and -175.1 pA/pF, respectively. In the Gattoni model, however, I_{Na} is much more rate-sensitive. At BCL = 1000 ms, peak I_{Na} is -57.5 pA/pF, considerably lower than in the Pandit model, and this peak increases nearly 2.5-fold to -141.5 pA/pF at BCL = 500 ms. Peak I_{Na} is then reduced at BCL = 167 ms to -81.9 pA/pF in the Gattoni model.

Peak I_{CaL} is similar in both models, though appears relatively rate-insensitive in the Gattoni model, with peak values of -7.5, -7.4 and -7.0 pA/pF at cycle lengths of 1000, 500 and 167 ms, respectively. Conversely, there is a 2.3 pA/pF reduction in peak I_{CaL} in the Pandit model when halving the cycle length to 500 ms (-7.6 vs -9.7 pA/pF).

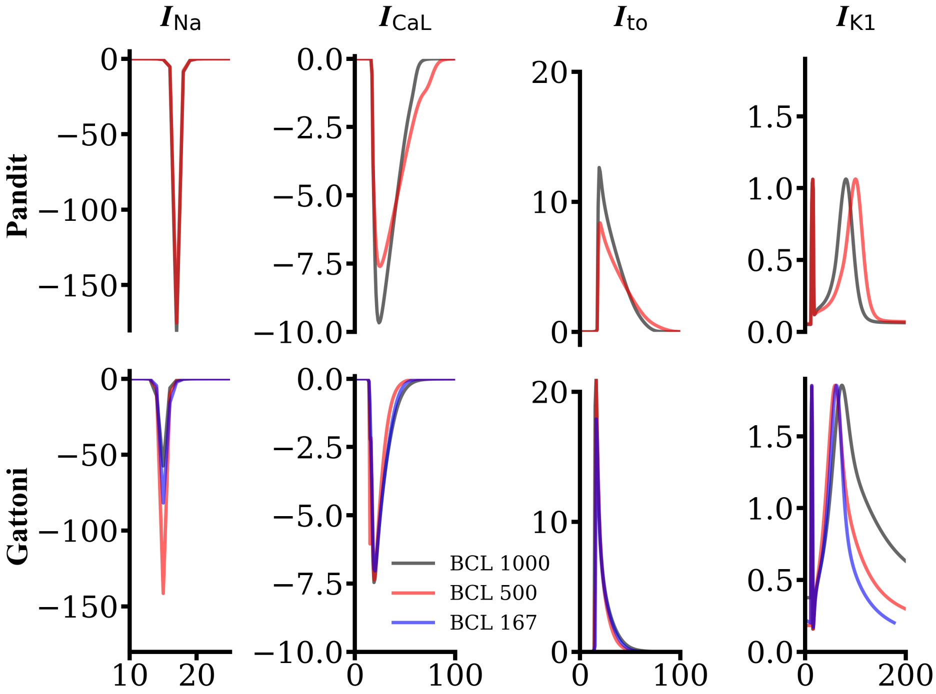

Figure 3.13. Membrane current changes with pacing frequency in the Pandit and Gattoni models. Changes to I_{Na}, I_{CaL}, I_{to} and I_{K1} in the Pandit (top) and Gattoni (bottom) models. Currents are shown for cycle lengths of 1000 and 500 ms (both models), and 167 ms (Gattoni model). Currents are in pA/pF.

3.4.2.2 Repolarising currents: I_{to}, I_{ss} and I_{K1}

I_{to} is higher in the Gattoni model than the Pandit model, and, similar to I_{Na}, is more sensitive to rate in the Pandit model than the Gattoni model. Peak I_{to} was 12.6 pA/pF at BCL = 1000 ms in the Pandit model, compared to 8.4 pA/pF at BCL = 500 ms. In the Gattoni model, I_{to} gradually decreases with increased pacing frequency, from 21.0 to 20.9 to 17.9 pA/pF for BCLs of 1000, 500 and 167 ms. I_{ss} (not shown in Figure 3.13) is relatively insensitive to rate in both models. For the Pandit model, peak I_{ss} is 1.2 pA/pF at BCL 1000 ms compared to 1.3 pA/pF at BCL 500 ms. Peak I_{ss} is lower in the Gattoni model in general, with peak values of 0.8, 0.7 and 0.5 pA/pF at cycle lengths of 1000, 500 and 167 ms. I_{K1} is larger in the Gattoni model, with peak values of 1.9 pA/pF at all pacing frequencies, compared to 1.1 pA/pF in the Pandit model.

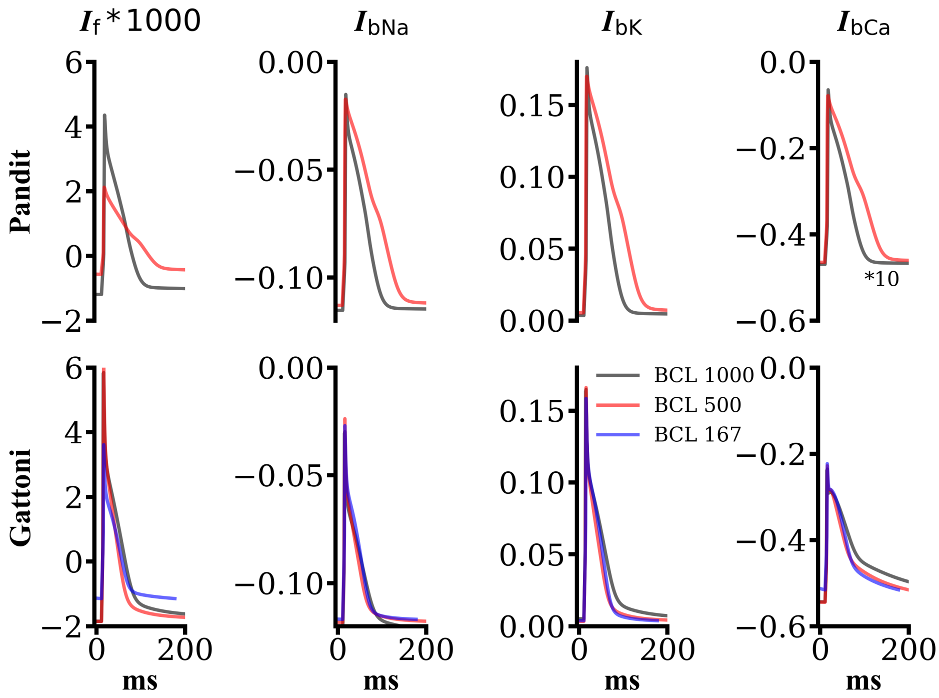

Figure 3.14. Background currents and the hyperpolarisation-activated current in the Pandit and Gattoni models. I_f, I_{bNa}, I_{bK} and I_{bCa} in the Pandit (top) and Gattoni (bottom) models. Currents are in pA/pF. Note that I_f in both models is scaled 1000x for clarity, and I_{bCa} in the Pandit model is scaled 10x for comparison to the Gattoni model.

3.4.2.3 Other membrane currents: I_f and I_b

Though small in magnitude, other membrane currents such as I_f and the background currents $I_{bNa,K,Ca}$, can play an important role in dictating the membrane potential of ventricular myocytes. It has been posited that the background Na^+ current, for example, may explain the deviation of resting membrane potential from the K^+ reversal potential, E_K [199]. The hyperpolarisation-activated current, I_f, though more highly expressed in pacemaking cells of the heart, can also be an important modulator of the rat ventricular AP [344]. In particular, I_f is thought to be upregulated in heart failure and could play an arrhythmogenic role in both rats and human [81, 82, 374]. Changes to these currents in response to changes in cycle length are shown in Figure 3.14.

For both models, I_f is 1000-times smaller in magnitude than the background currents. In the Pandit model, I_f decreases in magnitude by 2.6 fA/pF when cycle length drops from 1000 ms to 500 ms, however its duration is prolonged by approximately 40 ms. For the

Gattoni model, I_f changes little over the same change in cycle length (in fact, it increases very slightly), but there is then a modest decrease in peak current from 7.9 to 4.8 fA/pF.

The background and funny currents show greater rate-dependence in the Pandit model than in the Gattoni model. All 3 background currents in the Pandit model reduce in peak magnitude as cycle length decreases to BCL = 500 ms, though only by small amounts, however the duration is prolonged by approximately 20-30 ms for each current. Conversely, for the Gattoni model, the background currents change very little in both magnitude and duration as cycle length decreases to BCL = 500 ms from 1000 ms, however their peak magnitudes then reduce slightly at BCL = 167 ms. The resting and peak current magnitudes for I_f and $I_\mathrm{bNa,K,Ca}$ are given in Table 3.7.

Table 3.7. Changes to I_f and $I_\mathrm{bNa,K,Ca}$ in response to changes in pacing frequency.

Parameter	BCL 1000	BCL 500	BCL 167
I_f (fA/pF)	P 5.5 G 7.7	P 7.7 G 7.9	G 4.8
I_bNa (pA/pF)	P 0.10 G 0.093	P 0.096 G 0.094	G 0.090
I_bK (pA/pF)	P 0.17 G 0.16	P 0.16 G 0.16	G 0.15
I_bCa (pA/pF)	P 0.040 G 0.31	P 0.040 G 0.32	G 0.29

3.4.3 Calcium handling and concentration changes

The intracellular Ca^{2+} concentration in the Gattoni model is higher overall than that in the Pandit model. After steady-state pacing at BCL = 1000 ms, the diastolic Ca^{2+} concentration in the Pandit model is 0.045 μM, compared to 0.11 μM in the Gattoni model. Peak systolic Ca^{2+} reaches 0.075 μM in the Pandit model, so the magnitude of the Ca^{2+} transient is just 0.03 μM (representing a 66% increase from diastolic levels). Such a small magnitude of the Ca^{2+} transient is inconsistent with experimental data, in which $[Ca^{2+}]_i$ is repeatedly reported to rise by at least 0.5 μM [89, 121, 240, 340, 394, 397, 418, 418] In contrast, peak systolic Ca^{2+} in the Gattoni model rises to 1.38 μM, with a Ca^{2+} transient magnitude of 1.27 μM. This represents a 1154% increase from diastolic levels in the Gattoni model, a considerably larger magnitude transient than the Pandit model. At BCL = 500 ms, the Pandit model Ca^{2+} transient represents just a 42% increase in $[Ca^{2+}]_i$, whereas the magnitude of the Ca^{2+} transient increases for the same cycle length in the Gattoni model, representing a 1300% increase from diastolic levels. At BCL = 167 ms, the increase from diastolic Ca^{2+} levels in the Gattoni model then decreases to 472%, though this is still significantly higher than at any pacing frequency for the Pandit model. $[Ca^{2+}]_{SR}$ levels are similarly higher in the Gattoni model than the Pandit model, with peak SR Ca^{2+} concentrations of 1.9 and 0.03 mM, respectively. A summary of changes to intracellular and SR Ca^{2+} concentrations is given in Table 3.8.

Table 3.8. Changes to Ca^{2+} handling parameters in response to alterations in cycle length.

Parameter	BCL 1000	BCL 500	BCL 167
$[Ca^{2+}]_{i,min}$ (μM)	P 0.045 G 0.11	P 0.12 G 0.11	G 0.25
$[Ca^{2+}]_{i,max}$ (μM)	P 0.075 G 1.38	P 0.16 G 1.54	G 1.43
Transient magnitude (μM)	P 0.03 G 1.4	P 0.03 G 1.3	G 1.2
$[Ca^{2+}]_{SR,min}$ (mM)	P 0.032 G 1.33	P 0.11 G 1.83	G 1.33
$[Ca^{2+}]_{SR,max}$ (mM)	P 0.035 G 1.90	P 0.065 G 2.40	G 1.75

For both models, increasing pacing frequency from BCL = 1000 to 500 ms results in increases in peak systolic Ca^{2+}, as well as diastolic and peak SR Ca^{2+} concentrations. For the Gattoni model, diastolic Ca^{2+} remains the same at BCL = 500 ms as for BCL = 1000 ms, whereas this is increased in the Pandit model. Further increasing pacing frequency to a cycle length of 167 ms results in an increased diastolic Ca^{2+} concentration in the Gattoni model, whereas the other Ca^{2+} handling parameters all decrease. This means that, for the Pandit model, the Ca^{2+} transient magnitude remains constant (a 1 nM increase at BCL = 500 ms is negligible), whereas this increases at BCL = 500 ms in the Gattoni model but then falls again at BCL = 167 ms.

Peak normal-mode (inward, exporting Ca^{2+}) I_{NaCa} is higher (i.e. more negative) at all

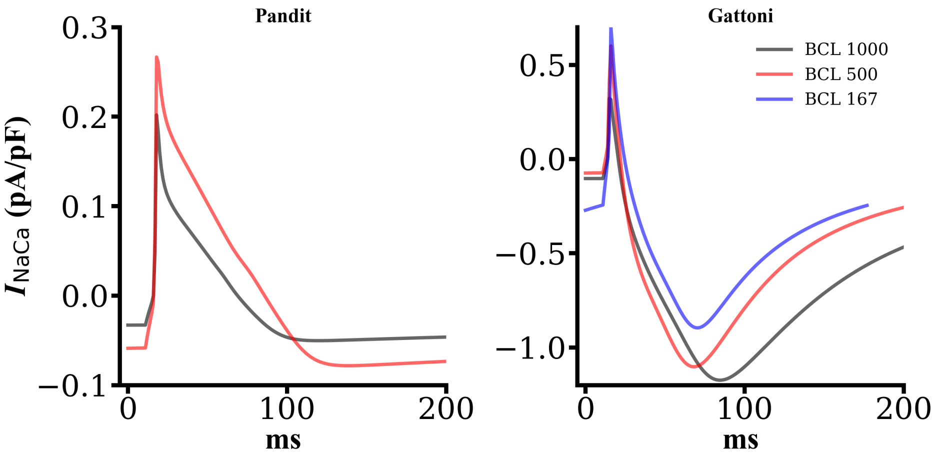

Figure 3.15. Rate-dependent changes to I_{NaCa} in the Pandit and Gattoni models. Peak inward and outward I_{NaCa} is higher in the Gattoni model than the Pandit model. Note the change in y-axis scale for the Gattoni model and the larger current peaks.

pacing frequencies in the Gattoni model. At BCL = 1000 ms, peak inward I_{NaCa} is -0.05 vs -1.2 pA.pF in the Pandit vs Gattoni models. In the Pandit model, the current magnitude increases (becomes further negative) at BCL = 500 ms to -0.08 pA/pF, whereas the value becomes more positive in the Gattoni model at this cycle length (to -1.1 pA/pF). Inward I_{NaCa} magnitude becomes even smaller at BCL = 167 ms in the Gattoni model, reaching -0.9 pA.pF. Peak reverse-mode (outward, exporting Na^+) I_{NaCa} is also higher at all pacing frequencies in the Gattoni model, and increases with pacing frequency from 0.32 pA/pF at BCL = 1000 ms to 0.60 pA/pF at BCL = 500 ms and to 0.70 pA/pF at BCL = 167 ms. For the Pandit model, peak outward I_{NaCa} rises from 0.20 pA/pF at BCL = 1000 ms to 0.27 pA/pF at BCL = 500 ms. These changes to I_{NaCa} are illustrated in Figure 3.15. It can be seen that I_{NaCa} takes longer to reach the peak outward magnitude at different cycle lengths and the pattern of this change in time courses mirrors that of changes to APD in each model at the different cycle lengths (i.e. APD is longer in the Pandit model at BCL 500 ms so the peak is reached later, whereas APD is longest at BCL = 1000 ms in the Gattoni model and so the peak is reached slowest at this cycle length).

In the Pandit model, the intracellular concentrations of Na^+ and K^+ drift over long pacing periods, decreasing gradually over the course of the simulation. This can be an issue when simulating for long durations, for example during a dynamic restitution protocol, in which it may take several hundred beats to reach a steady-state before pacing continues for several hundred more beats at a new pacing frequency, and so on. Over time, $[Na^+]_i$

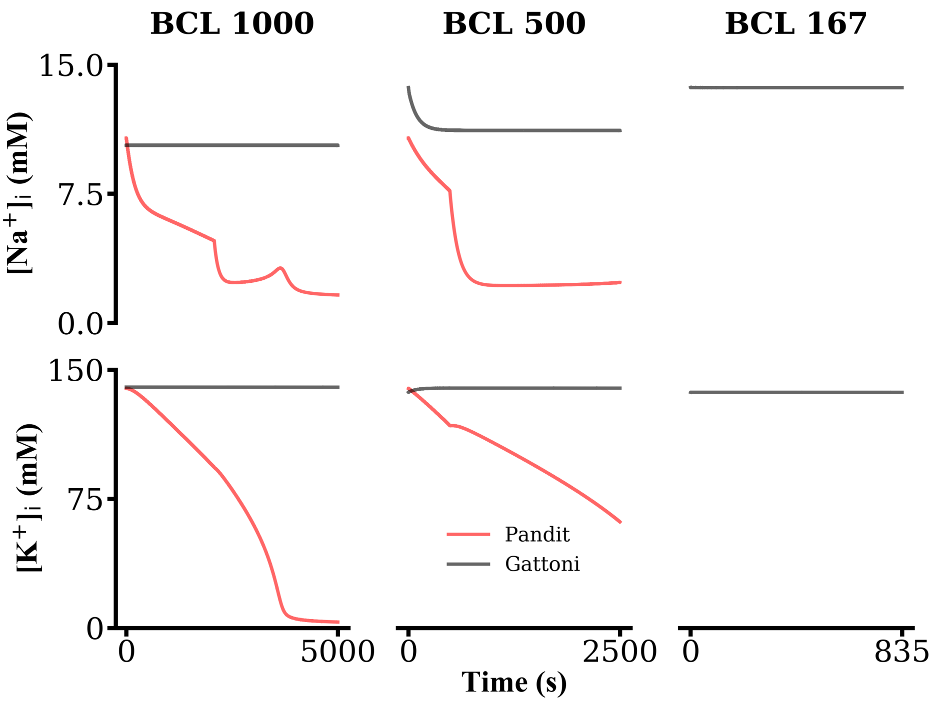

Figure 3.16. Changes to Na^+ and K^+ concentrations over extended pacing periods for the Pandit and Gattoni models. In the Pandit model, $[Na^+]_i$ and $[K^+]_i$ levels deplete over time, resulting in model failure. Conversely, in the Gattoni model, steady-states are achieved at each cycle length and the model continues to reproduce APs even after 5000 simulated beats.

and $[K^+]_i$ drop well below physiological levels, resulting in model failure as APs fail to initiate, ion currents fail to active and membrane potential fails to repolarise. Figure 3.16 illustrates the gradual decline in these intracellular ions over time in each model. When pacing for a long duration at BCL = 1000 ms in the Pandit model, the model begins to fail after 2079 beats, or after 979 beats at BCL = 500 ms. At these points, $[Na^+]_i$ falls to 4.8 mM (BCL = 1000 ms) and 7.7 mM (BCL = 500 ms) from the initial condition of 10.7 mM, and $[K^+]_i$ falls to 95.0 mM (BCL = 1000 ms) and 117.5 mM (BCL = 500 ms) from the initial condition of 139.3 mM.

Conversely, in the Gattoni model, Na^+ and K^+ concentrations drift only very slightly, and the model is able to reach a steady-state which persists for at least 5000 beats at cycle lengths of 1000, 500 and 167 ms. This stability can be clearly observed in contrast to the Pandit model in Figure 3.16.

3.4.4 APD restitution

As described in Chapter 2, APD restitution describes the relationship between action potential duration and cycle length (as either the diastolic interval, DI, or the cycle length/pacing frequency). Steep APD restitution is thought to be a pro-arrhythmic phenomenon that occurs in several conditions, such as heart failure [197, 354]. Multiple mechanisms are thought to influence APD restitution properties, including region or species-specific variations in K^+ channels [328, 362], the L-type Ca^{2+} channel [133, 217], the Na^+-Ca^{2+} exchanger [188, 265] and the late Na^+ current [257]. Experimental dynamic and S1-S2 restitution protocols can be used to characterise various aspects of the adaptation of APD to pacing frequency, however it can be difficult to gain mechanistic insight into the underlying multi-scale mechanisms from these types of experiments. Computational models, though, can be used to generate APD restitution curves and provide insight into the processes that may regulate APD rate-adaptation [336]. In this section, the Pandit and Gattoni (1 and 6 Hz variants) were used to generate restitution curves for direct comparison to those from the literature by replicating the experimental protocol as close as possible.

In Figure 3.17, a comparison of the experimental restitution curve from [34] to that generated from the Gattoni model (6 Hz variant) is shown. For this paper, the authors implemented an S1-S2 restitution protocol in which Langendorff-perfused hearts were paced to steady-state at a pacing frequency of 5 Hz, after which a single S2 stimulus was applied at decreasing intervals of 200 to 40 ms, and the resulting APD_{90} was plotted against the corresponding S2 interval. For comparison, the Gattoni model was paced to steady-state at the same pacing frequency before perturbation at matching S2 intervals to those used experimentally. Again, the 1 Hz variant and the Pandit model were not used as they are unable to reproduce APs at pacing frequencies of 5 Hz.

Experimentally, APD decreased across the range of S2 intervals used, from 42.0 ms at S2 = 200 ms to 30.3 ms at S2 = 40 ms. For the simulated restitution curve, APD increased from 50.1 ms at S2 = 200 ms to 59.27 ms at S2 = 160 ms. The model was unable to simulate APs beyond this S2 interval, after which APD prolonged drastically to over 1000 ms resulting from extended I_{CaL} reactivation and a Ca^{2+} transient magnitude over 30 times larger than normal. These results further suggest that Gattoni model is unable to reproduce experimentally-determined APD restitution characteristics. However, it should be noted that this comparison is made between a single cell model and a whole-heart preparation.

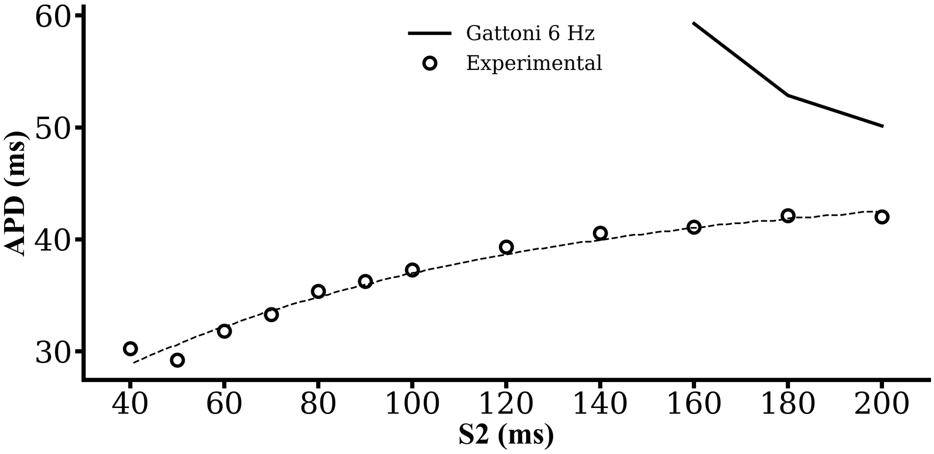

Figure 3.17. Comparison of Gattoni model restitution to data from [34]. Experimentally (unfilled circles, dashed trendline), APD decreases as the S2 interval shortens. In the model (solid line), however, APD increases as the S2 interval decreases from 200 to 160 ms. However, the model is unable to simulate shorter S2 intervals than 160 ms.

In tissue preparations, APD is recorded as a monophasic APD (MAPD) which is recorded extracellularly and so may be inaccurate due to electrode placement or motion artefacts. In addition, the effects of neighbouring cells in tissue, and the implications of cell-cell coupling, constitute an electrical sink which means direct comparison between single cell and tissue APDs may not be viable in isolation. Nevertheless, in combination with further comparisons it can provide a supplemental aspect of model validation.

In [159], a simple restitution protocol was implemented where APD_{90} was determined after steady-state pacing at frequencies from 1 to 9 Hz. Figure 3.18 shows a comparison between the resulting experimental restitution curve and that simulated by the Gattoni (6 Hz) model, which was paced to steady state at cycle lengths from 980 to 100 ms in 10 ms steps, as described earlier. The 1 Hz variant and Pandit models are unable to simulate pacing frequencies greater than 3 Hz and so were unsuitable for comparison. Experimentally, APD did not change from frequencies of 1 to 5 Hz, for which mean APD_{90} was 43.0 ms. Between frequencies of 5 to 9 Hz, APD then appears to decrease, to 38.5 ms at 9 Hz. For the Gattoni model, APD decreased from 69.7 ms at a cycle length of 980 ms, to 48.6 ms at BCL = 260 ms. APD was then seen to increase with pacing frequency, to 54.4 ms at BCL = 167 ms (6 Hz). The Gattoni model was unable to simulate cycle lengths above 980 and below 167 ms, as described previously. These results suggest that the Gattoni model is unsuitable for reproducing experimental restitution curves, as

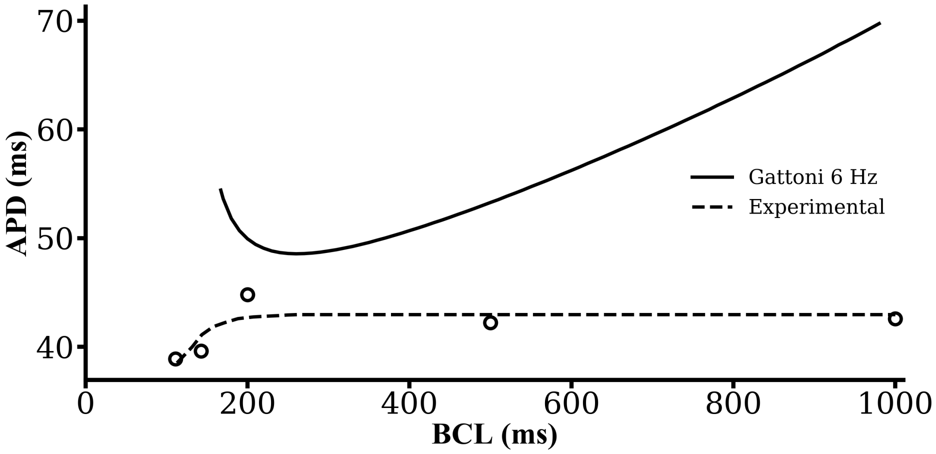

Figure 3.18. Comparison of Gattoni model restitution to data from [159]. Experimentally, (unfilled circles, dashed trendline), APD remains constant until BCL = 200 ms at which point APD appears to decrease at shorter cycle lengths. In the Gattoni (6 Hz variant) model (solid line), APD decreased from BCL = 980 to BCL = 260 ms, then increased until the limit of the model at BCL = 167 ms.

it appeared to produce the opposite response to that observed experimentally, as APD prolonged in the model at faster pacing frequencies.

In [24], an S1-S2 restitution protocol was employed where myocytes were paced to steady-state at a cycle length of 1000 ms, before perturbation by a single extra stimulus at intervals between 50 and 5000 ms, and APD_{50} was plotted against the S2 interval. For comparison, the Pandit and Gattoni (1 Hz variant) models were paced at 1 Hz before the application of an extra S2 stimulus at the same intervals as those experimentally (Figure 3.19).

Experimentally, APD_{50} increased gradually as the S2 interval decreased from 9.8 to 13.8 ms. For both models, the same trend in APD prolongation was observed as the S2 interval decreased, albeit at higher overall durations. In the Pandit model, S2 intervals of 5000 to 125 ms were simulated, as below this minimum S2 interval APs did not initiate as they fell during the ERP. At S2 = 5000 ms, APD_{50} in the Pandit model was 28.4 ms, compared to 60.91 ms at S2 = 125 ms. In the Gattoni model, S2 intervals of 4425 to 550 ms. Above S2 = 4425 ms and below S2 = 550 ms, unphysiological APD prolongation beyond 100 ms was observed as described earlier. Nevertheless, at S2 = 4425 ms, APD_{50} in the Gattoni model was 17.2 ms, compared to 22.3 ms at S2 = 550 ms. Though both models captured the shape of the restitution curve determined experimentally in [24], the Gattoni

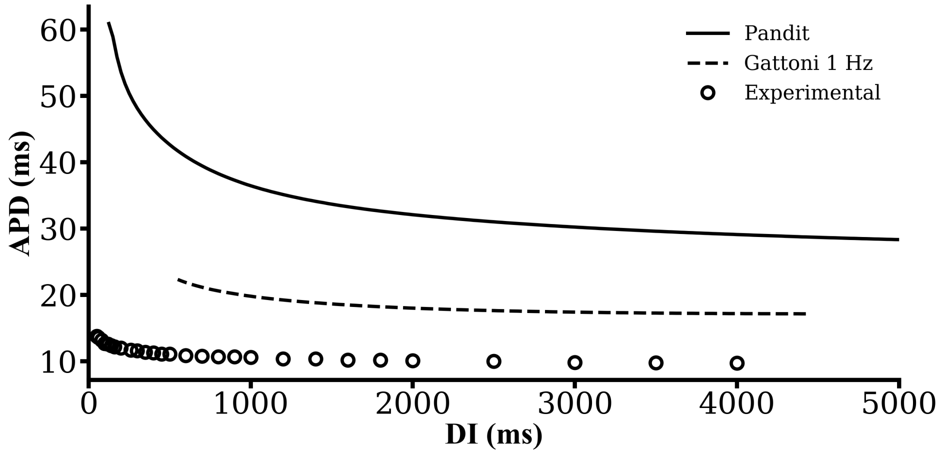

Figure 3.19. Comparison of Pandit and Gattoni model restitution curves to data from [24]. APD_{50} increased as S2 interval decreased experimentally (unfilled circles), and this was replicated in both the Pandit (solid line) and Gattoni (1 Hz variant, dashed line) models, though APD was higher in both models.

(1 Hz variant) model produced quantitatively more similar APDs, though these simulated values were nearly double those observed experimentally.

Finally, a comparison between the restitution curve from [265] is compared to that generated by the Pandit and Gattoni (1 Hz variant) models in Figure 3.20. Similar to that just described, here the restitution protocol was to pace to steady-state at a cycle length of 1000 ms prior to perturbation with S2 stimuli at intervals ranging from 4000 to 0 ms. Experimentally, APD_{50} increased from S2 = 4000 to 50 ms (from 5.0 to 6.7 ms), before decreasing until S2 = 0 ms (to 5.9 ms). Both models reproduced the increase in APD_{50} from S2 = 4000 ms, but were unable to simulate APs at shorter S2 intervals where decreases in APD_{50} were observed. For the Pandit model, the limit was S2 = 125 ms, shorter than which APs failed to initiate as they fell in the ERP. For the Gattoni (1 Hz variant) model, the limit was S2 = 550 ms, shorter than which unphysiological APD prolongation beyond 100 ms was observed as described previously. Both models were, therefore, able to capture the shape of the restitution curve seen experimentally in [265], albeit at longer APDs in general. However, the models were unable to reproduce APDs at shorter S2 intervals, at which APD was seen to decrease experimentally.

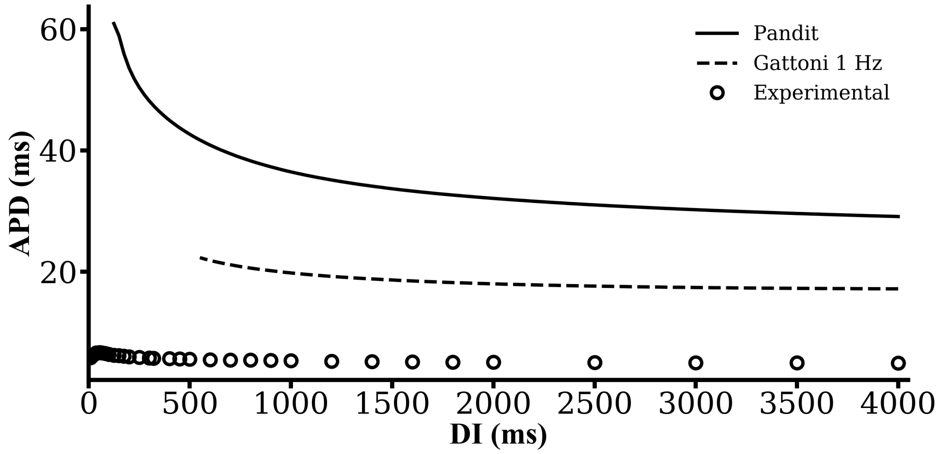

Figure 3.20. Comparison of Pandit and Gattoni model restitution curves to data from [265]. APD_{50} increased as S2 interval decreased experimentally (unfilled circles) until S2 = 50 ms, at which point APD prolonged. For both models, the same trend in APD increase was observed however neither model was able to simulate APs at S2 intervals shorter than 125 (Pandit) and 550 (Gattoni 1 Hz variant) ms.

3.4.5 Response to electrophysiological alterations

Computational models can be useful explorative tools for studying the effects of electrical remodelling in ventricular myocytes, without the need to develop knockout/knockdown animal models or use pharmacological agents, which can be expensive. Electrical remodelling, for example in the form of increased electrical heterogeneity, can increase susceptibility to arrhythmias [15, 197, 354], by increasing the dispersion of refractoriness and altering restitution curve steepness [35], which decreases stability of APD. This remodelling is often complex, multi-faceted and multi-scale, and so is difficult to explore experimentally, but computational models provide an avenue for exploration. Experimental data from our laboratory, for example, has previously shown that I_{CaL}, I_{CaT}, I_{Ks}, I_{Kr}, I_{Kur}, I_{K1}, I_{to} and I_{KACh} expression is altered in failing ventricular myocytes [34] – it would be experimentally intractable to dissect how each of these altered currents contributes to the heart failure phenotype.

Accordingly, an important aspect of a model's utility is its ability to explore how electrophysiological alterations such as those described can impact on AP characteristics and Ca^{2+} handling. For this section, various membrane currents in the Pandit and Gattoni models were scaled between 0 and 200% of their normal values at cycle lengths of 500 ms, to assess the utility of each model for exploring electrophysiological alterations. Currents scaled in this way were I_{Na}, I_{CaL}, I_{to}, I_{ss}, I_{K1}, I_{NaK} and I_{NaCa}, and the time course of the current, AP and Ca^{2+} transient is shown at control, and the minimum and maximum scales before the model is unable to produce a normal AP.

3.4.5.1 Scaling I_{Na}

Both models can still simulate APs when I_{Na} is scaled between 40 and 200% of its normal value (Figure 3.21), and these scales do not drastically affect either the AP or the Ca^{2+} transient in the Gattoni model despite their effects on peak I_{Na}. Below 40% I_{Na}, APs fail to initiate in both models as the threshold for generation is not reached. However, both models can handle a doubling in I_{Na} from its control value.

For the Pandit model, 40% I_{Na} results in a much slower increase in inward current, thus the AP upstroke phase is slowed. dV/dt_{max} decreases from 177.9 to 81 V.s^{-1}, and APD increases slightly from 89.4 to 89.56 ms. In addition, V_{max} falls from 48.2 to 32.0 mV. In comparison, 200% I_{Na} results in a smaller peak I_{Na} magnitude, but this peak is reached approximately 1 ms earlier than control. dV/dt_{max} rises to 297 V.s^{-1}, and V_{max} increases to 59.32 mV. APD is mostly unchanged at 87.22 ms. 40% I_{Na} results in a slight lowering of diastolic Ca^{2+} concentration compared to control (0.074 vs 0.079 µM), whereas it is slightly raised at 200% I_{Na} (0.079 µM). Both 40% and 200% I_{Na} result in higher peak systolic Ca^{2+} concentrations compared to control (0.118 and 0.129 µM, respectively, vs 0.109 µM for control). The Ca^{2+} transient duration is slightly shortened at 40% I_{Na}, and prolonged at 200%.

In the Gattoni model, peak I_{Na} follows the same pattern as for the Pandit model, being smaller but slightly faster at 200% I_{Na} and slower and smaller at 40%. dV/dt_{max} falls to 79 V.s^{-1} at 40% but increases to 288 V.s^{-1} at 200%, compared to 175.9 V.s/super-1 for control. Similarly, V_{max} at 40% falls to 14.24 mV but increases to 49.9 mV at 200% I_{Na}, compared to the control value of 35.6 mV. Despite the smaller V_{max}, APD increases at 40% I_{Na} to 59.72 ms, compared to 53.3 ms and 200% I_{Na} at 45.51 ms. Neither change to I_{Na} impacts on the Ca^{2+} transient in the Gattoni model, in which it takes only slightly longer to reach peak systolic Ca^{2+}, but this value and the Ca^{2+} transient duration is otherwise unchanged. Both models produce considerably larger peak I_{Na} than is observed experimentally (e.g. -7.5 to -41 pA/pF in [4, 50, 84, 213, 332]).

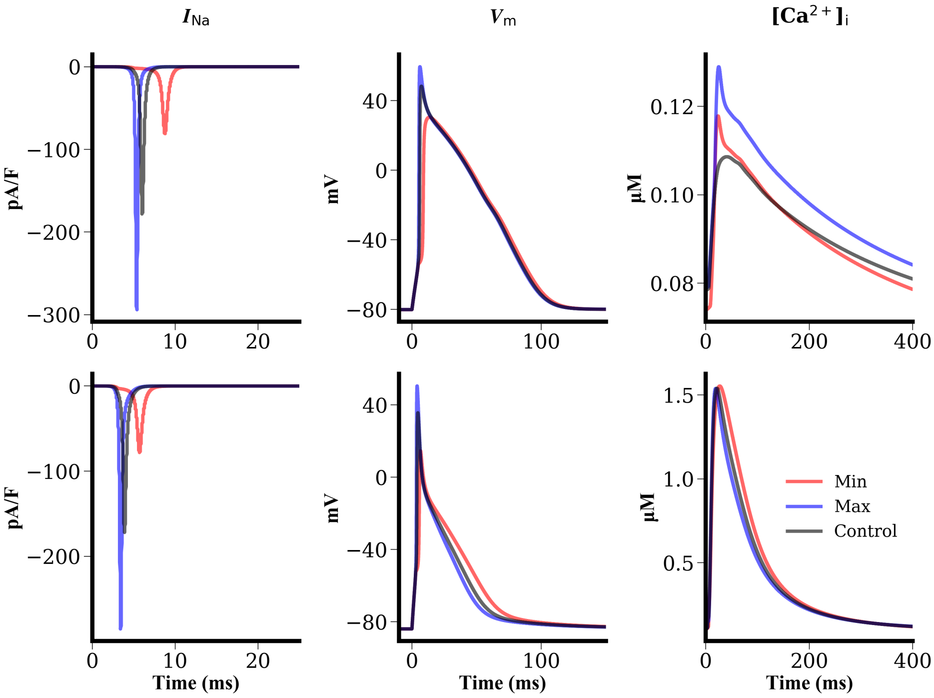

Figure 3.21. Effect of scaling I_{Na} in the Pandit and Gattoni models. Top: Pandit model, Bottom: Gattoni model. Both models handle scaling of I_{Na} from 40 to 200% of its control value, with only slight changes to APD and Ca^{2+} handling occurring as a result.

3.4.5.2 Scaling I_{CaL}

In the Pandit model, I_{CaL} can be scaled between 0 and 130% of its control value and physiological APs are still reproduced (Figure 3.22). Above 130% of control, APs in the Pandit model fail to repolarise and the membrane potential 'hangs' at around -10 mV. For the Gattoni model, I_{CaL} can only be reduced (to 0%, while still maintaining a physiological AP) as scaling it above 100% results in significant re-activation of I_{CaL} and an unphysiologically-prolonged APD (beyond the cycle length).

Eliminating I_{CaL} in the Pandit and Gattoni models results in drastically shortened APDs vs control, of 30.4 v 89.4 ms and 28.3 v 53.3 ms, respectively. Increasing I_{CaL} to 1.3x control in the Pandit model prolongs APD considerably to 118.9 ms, as there is an increased peak and duration of I_{CaL}. This also results in increased diastolic and systolic Ca^{2+} concentrations, though the magnitude of the Ca^{2+} transient remains the same – this illustrates the lack of graded release in the Pandit model as the Ca^{2+} transient magnitude remains unchanged despite changes in Ca^{2+} influx via I_{CaL}. Abolishing I_{CaL} in the Pandit

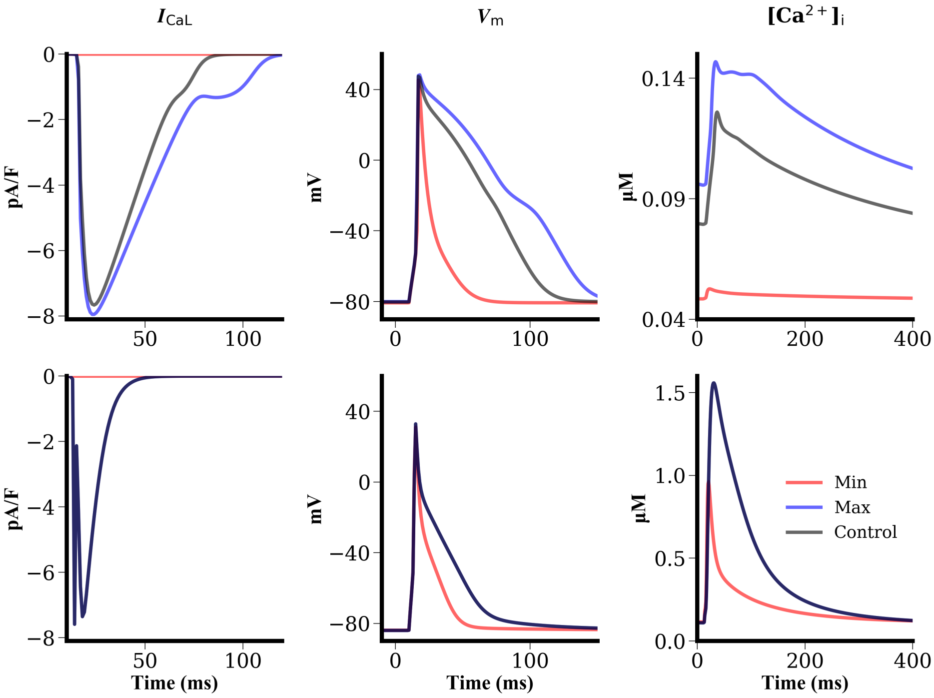

Figure 3.22. Effect of scaling I_{CaL} in the Pandit and Gattoni models. Top: Pandit model, Bottom: Gattoni model. Abolishing I_{CaL} in both models still allows for simulation of APs. Additonally, in the Pandit model, I_{CaL} can be increased to 130% of its control value.

model results in vastly reduced diastolic Ca^{2+} concentration, which changes little during the course of the AP. $V_{\max}$, $V_{\min}$ and $\mathrm{d}V/\mathrm{d}t_{\max}$ are unchanged in both models.

3.4.5.3 Scaling I_{to}

In the Pandit model, I_{to} can be scaled between 50% and 200% of its control value and still produce physiological APDs (Figure 3.23). Below 50% I_{to}, APD prolongs to unphysiological levels (over 120 ms in duration). At 50% I_{to}, however, APD prolongs to 119.9 ms (at the likely limit for a physiological AP in rat ventricular myocytes [121, 159, 290, 299, 407]), compared to 89.4 ms at control. Doubling I_{to} results in a much shorter APD of 49.2 ms. Peak current is altered in line with the percentage increase, unlike with I_{Na} and I_{CaL} are described earlier, but the current duration is largely unaltered (inactivating more quickly at 200% I_{to}). Increasing I_{to} to 200% results in lower diastolic and systolic Ca^{2+} concentrations, whereas decreasing to 50% does not alter peak systolic Ca^{2+} concentration but does raise the diastolic concentration and slightly increases the time to peak Ca^{2+}.

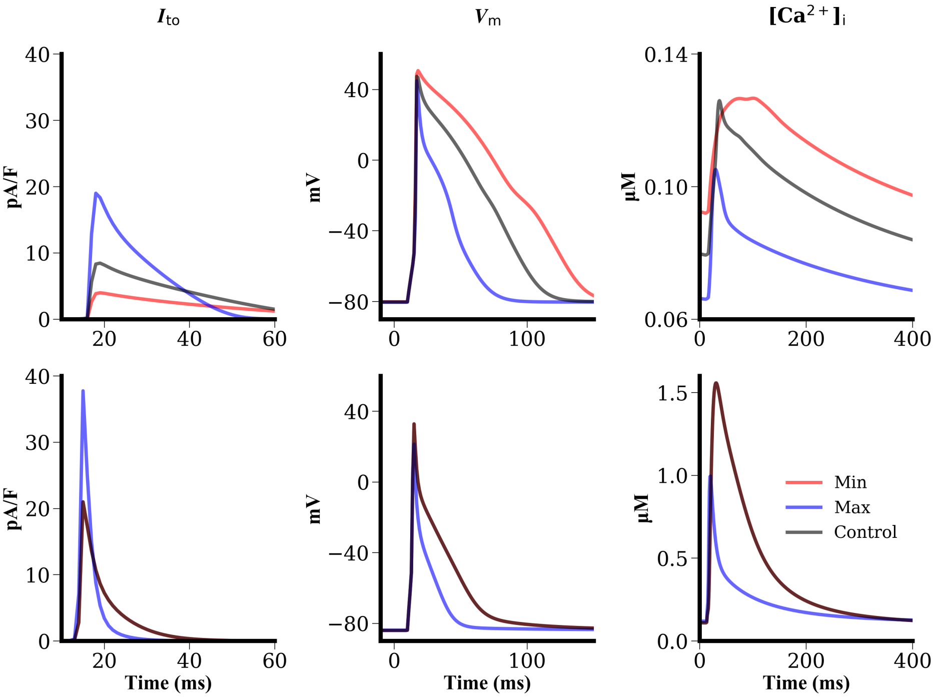

Figure 3.23. Effect of scaling I_{to} in the Pandit and Gattoni models. Top: Pandit model, Bottom: Gattoni model. The Pandit model still produces physiological APs with 50% to 200% I_{to}, however the Gattoni model is unable to simulate APs below 100% of the control value for I_{to}.

Ca^{2+} transient duration, however, remains relatively unaltered in the Pandit model. V_{max} is increased to 50.7 mV at 50% and decreased to 44.9 mV at 200% I_{to}, compared to the control value of 48.2 mV.

For the Gattoni model, reducing I_{to} below its control value results in significant APD prolongation resulting from reactivation of I_{CaL}, with APD exceeding the cycle length. However, the model can handle scaling I_{to} to at least 200% of its value. Doubling I_{to} results in shortening of APD, from 53.3 to 26.9 ms, and a near doubling of peak current. This increase does not affect diastolic Ca^{2+} concentration in the Gattoni model, but systolic Ca^{2+} is reduced by approximately 0.5 µM and the Ca^{2+} transient duration is significantly shortened. Increasing I_{to} to 200% results in a decrease in V_{max} from 35.6 to 29.8 mV compared to control in the Gattoni model.

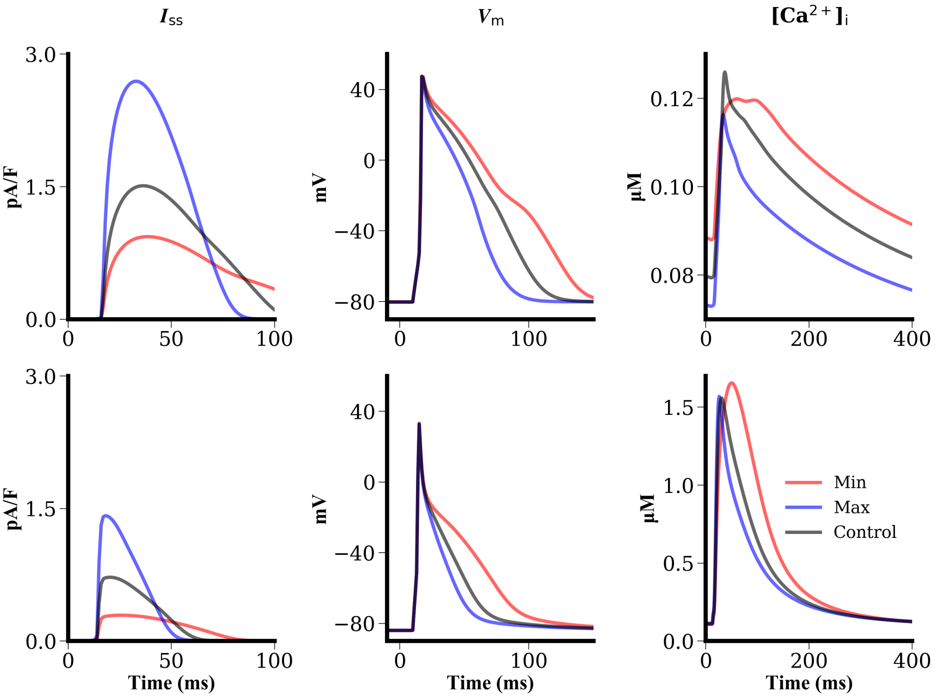

Figure 3.24. Effect of scaling I_{ss} in the Pandit and Gattoni models. Top: Pandit model, Bottom: Gattoni model. Similar effects are observed for I_{ss}, AP and Ca^{2+} transient characteristics in each model. Both models allow doubling of I_{ss}, and reduction of I_{ss} to 60% (Pandit) and 40% (Gattoni).

3.4.5.4 Scaling I_{ss}

Both models still produce physiological APs when I_{ss} is increased to 200% of control (Figure 3.24). For the Pandit model, a reduction to 60% also still produces APs, however APD is prolonged to 116.5 ms compared to 89.4 ms for control. At 60% I_{ss}, peak I_{ss} is reduced but the current duration is increased. This reduction results in increased diastolic Ca^{2+} levels but a reduced peak systolic Ca^{2+} concentration compared to control, thus an overall decreased magnitude of the Ca^{2+} transient. Doubling I_{ss}, meanwhile, increases peak current and decreases the current duration slightly, resulting in a shorter APD of 64.5 ms. Both diastolic and systolic Ca^{2+} concentrations are reduced. Reducing I_{ss} lower than 60% in the Pandit model results in failure to repolarise and a ‘hanging’ membrane potential of approximately -10 mV.

For the Gattoni model, I_{ss} can be reduced to 40% of its normal value, resulting in an increase in APD to 75.9 ms compared to 53.3 ms at control. Doubling I_{ss}, though, results in APD shortening to 39.5 ms. I_{ss} itself follows a similar pattern as for the Pandit model at these scales, reducing in peak but increasing in duration at 40% and increasing in peak but shortening in duration at 200% I_{ss}. Increasing I_{ss} in the Gattoni model does not drastically affect the Ca^{2+} transient, slightly shortening its duration but not changing diastolic or peak systolic Ca^{2+} concentrations. Reducing I_{ss} to 40%, however, increases peak systolic Ca^{2+} concentration by approximately 50 nM, and increases Ca^{2+} transient duration. Decreasing I_{ss} in the Gattoni model to below 40% prolongs APD to beyond the cycle length, resulting in model failure.

3.4.5.5 Scaling I_{K1}

For both models, physiological APs are still produced when I_{K1} is reduced and increased by 50% (Figure 3.25). Reducing I_{K1} to 50% significantly increases the duration of I_{K1} to beyond 200 ms, compared to 100 ms at control values. Increasing I_{K1} also increases the duration of the current, but to a lesser extent. Reducing I_{K1} by 50% results in APD prolongation in both models, to 121.2 ms (v control 89.4 ms) in the Pandit model and to 122.78 ms (v control 53.3 ms) in the Gattoni model. Increasing I_{K1} by 50%, meanwhile, shortens APD to 76.4 ms in the Pandit model and 36.7 ms in the Gattoni model.

In the Pandit model, reducing I_{K1} results in increased diastolic and peak systolic Ca^{2+} concentrations, and a longer Ca^{2+} transient duration. Increasing I_{K1} has the opposite effect, although the extent is lesser, with small decreases to diastolic and peak systolic Ca^{2+} concentrations, and a marginally shorter Ca^{2+} transient duration. In the Gattoni model, peak systolic Ca^{2+} concentration is unchanged for decreases or increases in I_{K1} by 50%. In addition, increasing I_{K1} by 50% does not noticeably alter the Ca^{2+} transient, resulting in only a small reduction in Ca^{2+} transient duration. However, decreasing I_{K1} by 50% results in an increased time to peak Ca^{2+} and an increased Ca^{2+} transient duration.

As with I_{ss}, reduction in I_{K1} beyond 50% results in membrane potential ‘hanging’ in the Pandit model at around -10 mV, and significant APD prolongation beyond cycle length in the Gattoni model. At 150% I_{K1}, there is insufficient inward current via I_{Na} to initiate APs. For both models, V_{max} remains unchanged (within 0.1 mV) despite changes in I_{K1}. Similarly, V_{min} remains within 0.5 mV of the control value in both models (Pandit -80.1 mV, Gattoni -83.9 mV), and V_{max} remains within 1 mV of control values (Pandit 48.2 mV, Gattoni 35.6 mV).

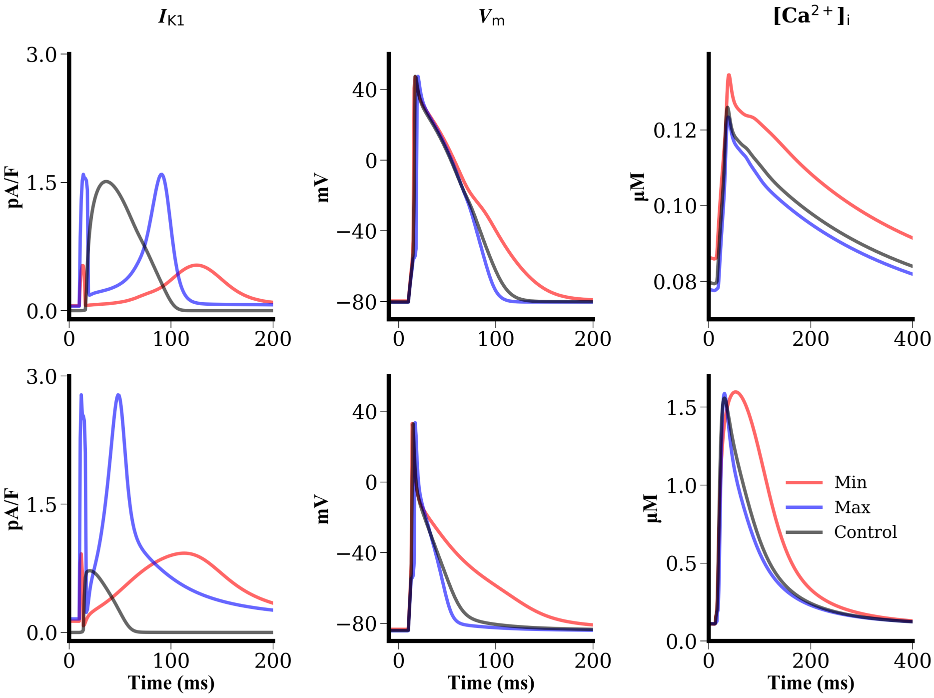

Figure 3.25. Effect of scaling I_{K1} in the Pandit and Gattoni models. Top: Pandit model, Bottom: Gattoni model. Both models still produce physiological APs when I_{K1} is increased or decreased by 50%.

3.4.5.6 Scaling I_{NaK}

In the Pandit model, I_{NaK} can be reduced to 10% and doubled from control and still produce physiological APs (Figure 3.26). Decreasing I_{NaK} to 10% its control value results in a smaller current peak and a reduced basal current of 0.019 pA/pF compared to 0.16 pA/pF at control. This results in a longer APD of 114.9 compared to 89.4 ms at control. In addition, both diastolic and systolic Ca^{2+} concentrations rise compared to control, and the magnitude of the Ca^{2+} transient is increased, as is its duration. Increasing I_{NaK} generally has opposite effects, with peak and resting I_{NaK} increased, a shorter APD of 76.9 ms and smaller diastolic and systolic Ca^{2+} concentrations. However, the magnitude and duration of the Ca^{2+} transient remains relatively unchanged. Below 10% I_{NaK}, the APD is prolonged to over 150 ms in the Pandit model, which is unphysiological.

These observations are largely similar in the Gattoni model, although the extent to which I_{NaK} can be scaled is less – only reductions to 70% and increases to 160% still result in AP production. At 70% I_{NaK}, peak and resting current is reduced and the APD is prolonged

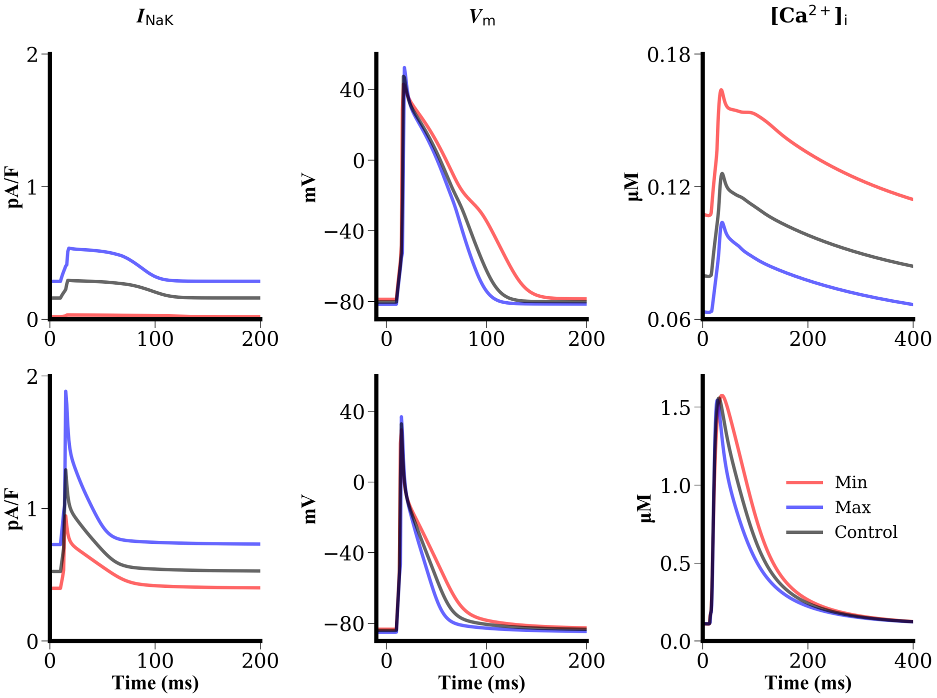

Figure 3.26. Effect of scaling I_{NaK} in the Pandit and Gattoni models. Top: Pandit model, Bottom: Gattoni model. I_{NaK} can be scaled to 10 and 200% of control in the Pandit model, but to only 70 and 160% in the Gattoni model. The effects of such scaling are similar in both models.

to 63.1 ms compared to 53.3 ms for control. The time to peak Ca^{2+} and Ca^{2+} transient durations are also slightly increased compared to control. Increasing I_{NaK} to 160% of control results in increased peak and resting current, and a shorter APD of 40.9 ms. Time to peak Ca^{2+} remains the same as for control, however the duration of the Ca^{2+} transient is slightly decreased.

3.4.5.7 Scaling I_{NaCa}

The responses of each model to changes in I_{NaCa} are shown in Figure 3.27. For the Pandit model, I_{NaCa} can be reduced to 10% and doubled to 200% and still produce physiological APs. Reducing to 10% results in a significantly smaller peak I_{NaCa} but a higher basal current of -0.03 pA/pF compared to -0.05 pA/pF at control. APD remains unchanged despite this reduction, but diastolic and peak systolic Ca^{2+} concentrations increase, though the magnitude of the Ca^{2+} transient stays the same as control. Increasing I_{NaCa} two-fold

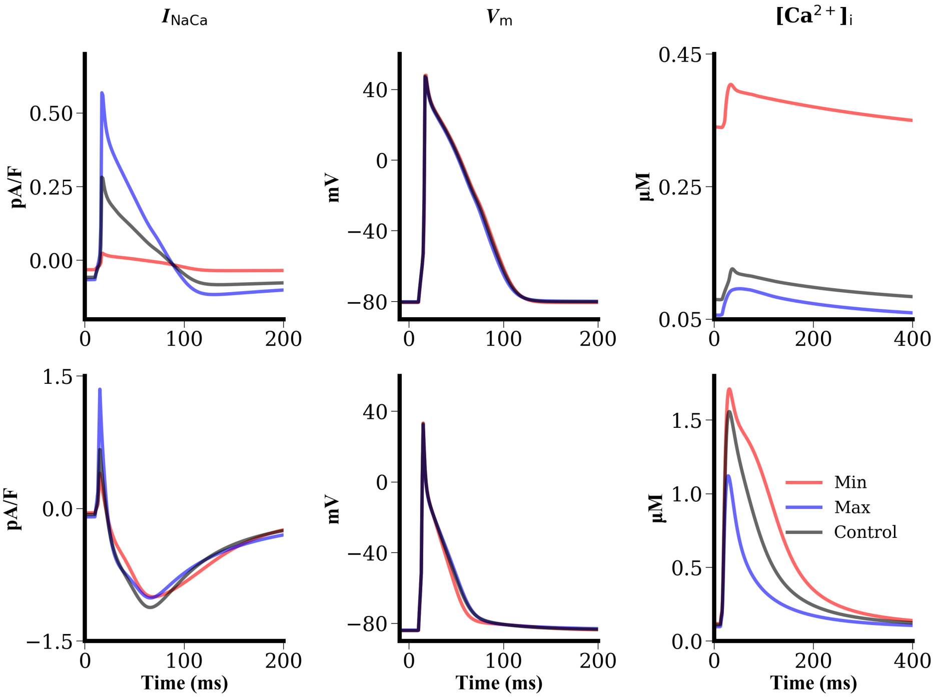

Figure 3.27. Effect of scaling I_{NaCa} in the Pandit and Gattoni models. Top: Pandit model, Bottom: Gattoni model. Both models still produce physiological APs when I_{NaCa} is increased to 200% of control. The Pandit model can further simulate APs at 10% of control I_{NaCa}, but the Gattoni model cannot simulate APs below 60% I_{NaCa}.

results in an increased peak current but a similar basal current of -0.05 pA/pF. Diastolic and peak systolic Ca^{2+} concentrations are smaller, but the magnitude of the Ca^{2+} transient remains the same, albeit with a slightly longer time to peak Ca^{2+}. APD remains unchanged. Reductions in I_{NaCa} below 10% result in progressive Ca^{2+} loading of the cell before significant unphysiological APD prolongation.

For the Gattoni model, decreases in I_{NaCa} to 60% and increases to 200% still result in physiological APs. For 60% I_{NaCa}, peak current is decreased and basal current is reduced (i.e. is less negative) compared to control, whereas peak current is increased for 200% I_{NaCa} despite a reduced basal current. Reducing I_{NaCa} to 60% slightly reduces APD in the Gattoni model to 44.8 ms vs 53.3 ms at control, but APD remains unchanged at 200% I_{NaCa}. 60% I_{NaCa} results in an increase in systolic Ca^{2+} concentration and Ca^{2+} transient magnitude and duration, though diastolic Ca^{2+} remains the same, whereas 200% I_{NaCa} leads to decreases in systolic Ca^{2+}, Ca^{2+} transient magnitude and duration but diastolic Ca^{2+} remains constant. Reducing I_{NaCa} below 60% leads to unphysiological APD prolongation beyond the cycle length.

3.5 Discussion and conclusions

As has been described, there are notable differences in electrophysiology between different species, particularly in the expression and contribution of K^+ currents to AP morphology and the relative contributions of various Ca^{2+} handling proteins to the shape, magnitude and duration of the Ca^{2+} transient, which can vary considerably between species and within species under different conditions (such as changes to pacing frequency). The rat AP is much shorter than many other mammals and has a more triangular shape, owing to a reduction in I_{CaL} expression (reducing the amount of phase 2 depolarisation) but an increase in I_{to} (approximately 4-fold that in human) and I_{K1} expression (resulting in stronger repolarising currents). In addition, the contribution of SERCA to Ca^{2+} extrusion in rat myocytes is approximately 4-fold higher than other species, and as a result the SR of rat cardiomyocytes is more prone to Ca^{2+} loading, which may favour the generation of DADs via spontaneous Ca^{2+} release events. However, existing computational models of rat ventricular electrophysiology do not incorporate the necessary stochastic Ca^{2+} dynamics in order to explore how these pro-arrhythmic mechanisms may arise.

Nevertheless, the computational models developed to date have provided quantitative electrophysiological insight into the mechanisms for which they were developed to investigate. The original Pandit model was developed to gain insight into the ionic mechanisms responsible for transmural heterogeneity in APD which had been observed experimentally, and revealed that the smaller density and slower kinetics of I_{to} in endocardial myocytes account for longer endocardial APDs and more prominent rate-dependence. Later, the Pasek model was developed to explore how modulation of electrical activity could be influenced by the T-tubular system, so the Pandit model was adapted to account for geometrical and electrophysiological characteristics of the T-system. Simulation results supported the concepts that transient K^+ accumulation and Ca^{2+} depletion occur in the T-tubules, and are frequency-dependent. The Niederer-Smith model was then developed which sought to explore how the slow-force response to stretch arises in rat ventricular myocytes, so the Pandit model was modified to include a previously-developed contraction and acid-base model and a new Ca^{2+} handling framework. The model results suggested that stretch-activated currents predominantly modulate the SFR in rats, and that the effects of nitrous oxide on the SFR must act through a different mechanism of RyR open probability potentiation. Lastly, the Devenyi-Sobie and Gattoni models were developed. The former sought to address the imbalance of Ca^{2+} fluxes in the Pandit model, and included a new SERCA formulation to better represent experimental data, whereas the latter replaced the Ca^{2+} framework with that of Hinch *et al.* and the Na^+-K^+ ATPase formulation with that of Lewalle *et al.*. The Gattoni model revealed that the peak Ca^{2+}-frequency response is biphasic in rat ventricular myocytes, and that CaMKII-mediated L-type Ca^{2+} channel and I_{to} activity enhances the positive Ca^{2+} transient magnitude response, which is otherwise negative when CaMKII is inhibited.

As the Pandit model is the foundation of the other models developed to date, and only the Gattoni model includes significant changes and re-parameterisation, these two models were chosen for direct comparison, which revealed advantages and disadvantages to both. The Pandit model is unsuitable for pacing at cycle lengths of 350 ms or faster, which makes it largely incompatible for simulating rat cardiac APs as the resting heart rate of rat comfortably exceeds 3 Hz [34, 35, 331, 415, 451, 453]. However, the Pandit model does capture the prolongation of APD with increases in pacing frequency, which is observed experimentally, although only between cycle lengths of 350 and 1000 ms. Conversely, the Gattoni model is capable of simulating cycle lengths from 167 to 1000 ms, though this is partly dependent on the parameter set used as there are two model variants stable at either 1 or 6 Hz. APD in the Gattoni model appears to shorten with increases in pacing frequency up to 4 Hz, where it then prolongs up to frequencies of 6 Hz. However, experimentally-reported restitution mechanisms and characteristics do vary between research groups, and the exact nature of the restitution curve shape remains debated. Neither model is able to recreate simple experimental restitution curves from some groups [34, 35, 159], yet produces similarly-shaped S1-S1 restitution curves to those in [24, 265], albeit at higher overall values for APD. As evidenced in Figures 3.17 to 3.20, there is a wide range of experimentally-reported restitution curves, largely a result of differences in the protocols used to generate them. Such wide variation makes experimental validation of restitution difficult, and thus is further complicated by the variation in measurement of key AP or Ca^{2+} handling characteristics, which are not always explicitly reported. APD_{90}, for example, can be measured as the time to 90% of repolarisation from the peak AP overshoot, or as the time taken to 90% repolarisation back to V_{min}, which may result in small yet significant differences in reported APD values. Typically, APs are stimulated experimentally by application of a supra-threshold stimulus [159] (in order to sufficiently cause I_{Na}

channels to open), however the magnitude of such a stimulus can vary and may result in abnormally large values for peak AP overshoot or greater $[Na^+]_i$.

For exploring electrophysiological alterations, each model responds differently at cycle lengths of 500 ms. APs failed to initiate in both models when I_{Na} was reduced to 40%, but still produced physiological APs at 200% I_{Na}. The range for altered I_{K1} was also the same for both models, but for between 50 and 150% of normal I_{K1} – below 50%, APD unphysiologically prolonged in the Gattoni model and did not repolarise in the Pandit model, and over 150% the repolarising current was so strong that APs did not initiate at all. For I_{CaL}, the scale range was between 0 and 130% in the Pandit model and 0 and 100% in the Gattoni model. Other membrane currents allowed varying degrees of scaling, but in general outside of these ranges the Gattoni model produced unphysiologically-prolonged APDs (sometimes, over 1000 ms), and the Pandit model failed to repolarise at all (resulting in membrane potential 'hanging', whereby it stays around -10 mV except for perturbations by the stimulus current). However, in experiments and *in vivo* physiology, it is not uncommon for complete block, or considerable downregulation (as low as 15% has been reported for some K^+ channels experimentally [34, 139]), of individual channel proteins (e.g. data from our laboratory in [34]), and so gaining quantitative insight at these levels of remodelling would be beneficial, but appear not to be possible with currently available models. In addition, any impacts of electrophysiological remodelling on Ca^{2+} handling are not able to be dissected given the deterministic nature of the models to date, as they do not account for stochastic release of Ca^{2+} from individual CRUs. One notable limitation of this sort of computational investigation is that a 50% reduction in a channel's expression observed experimentally, for example, does not necessarily mean a 50% reduction in observed current, particularly given the wide variation in channels and their subunits (e.g. I_{to} may be encoded for by the KCNA4, KCND2 and KCND3 genes), and so reducing current by the same proportion as observed channel expression may be an oversimplification.

In the Pandit model, the adapted canine and guinea pig Ca^{2+} handling system shows several limitations. As mentioned previously, it is not capable of simulating graded Ca^{2+} release which is a known phenomenon in ventricular myocytes from all species. In addition, the contribution of Ca^{2+} efflux pathways in the Pandit model is inconsistent with experimental data, as are various measures of the Ca^{2+} transient – this explains why these components were replaced in the more recent Niederer-Smith and Gattoni models, and updated in the Devenyi-Sobie model. The Gattoni model reproduces more closely experimental data relating to Ca^{2+} handling, and so is more suited for simulation of excitation-contraction coupling in rat. However, it is clear that to investigate pro-arrhythmic mechanisms resulting from aberrant Ca^{2+} handling, it is necessary to further replace the Ca^{2+} handling system in these models with one that can simulate the stochastic dynamics regulating Ca^{2+} release at the sub-cellular level, so that the interacting effects of remodelled electrophysiology and Ca^{2+} handling can be dissected in detail. Despite the described differences in electrophysiology between rat myocytes and those of larger mammals, rodent myocytes exhibit a greater dependence on intracellular Ca^{2+} cycling and so rat-specific computational models are ideally suited for the investigation of spontaneous Ca^{2+} release mechanisms at the cellular level [127].

Chapter 4

A Novel Model of Rat Ventricular Electrophysiology and Calcium Handling

4.1 Introduction

Failure in any of the underlying processes governing excitation-contraction coupling in the heart can result in a myriad of pathologies, including heart failure, hypertrophy, arrhythmias and sudden cardiac death. As described previously, these processes can be difficult to explore and quantify using traditional experimental methodologies as they occur across multiple spatial and temporal scales, however computational models provide powerful research tools that can provide quantitative and mechanistic insight into the underlying multi-scale mechanisms as they can be dissected in time, space, and by parameter.

EC coupling is inherently a two-part process. In response to an electrical stimulus, changes to membrane currents and ion concentrations result in the action potential, resulting in a concomitant release of intracellular Ca^{2+} from the SR and subsequent contraction of the cell. However, as described in Chapter 3, existing computational models of rat ventricular electrophysiology are limited in their capacity to explore changes in the contraction aspect of EC coupling, as they utilise deterministic implementations for Ca^{2+} cycling dynamics which are typically inherited from previously-developed, non-rodent computational models (the Pandit model Ca^{2+} handling system, for example, is derived from canine, guinea pig and ferret data), and so are unable to recreate the complex, stochastic dynamics of subcellular Ca^{2+} handling, the remodelling of which is pro-arrhythmic [74, 202, 365, 427]. Thus, despite the common use of rats as animal models in cardiovascular research, computational models of rat ventricular electrophysiology poorly recapitulate experimental Ca^{2+} handling characteristics, which is necessary as the rate-dependent electrophysiological properties of rat rely more on subcellular Ca^{2+} handling than other species [146]. Accordingly, the extrapolation of results to human disease is further complicated, which represents a significant limitation to their use. Rodents, however, do remain an important reseach tool, and as rodent myocytes exhibit a greater dependence on intracellular Ca^{2+} cycling, rat-specific computational models are ideally suited for investigating pro-arrhythmic spontaneous Ca^{2+} release mechanisms [127].

There remains a need, therefore, for the development of a comprehensive computational model of rat ventricular myocytes, to provide mechanistic and quantitative insight into the link between electrophysiological and calcium handling remodelling, which existing models are unable to provide. In this chapter, the development of a novel computational model of rat ventricular electrophysiology and calcium handling will be described. The new model takes membrane currents from the Gattoni model, parameterised against recent experimental data from rat ventricular myocytes at 37°C, and couples them with the Colman [97] stochastic spatio-temporal Ca^{2+} cycling model which is suitable for the incorporation of an array of electrophysiology models and can provide important insight into the microscopic, spontaneous Ca^{2+} dynamics that may underlie pro-arrhythmic behaviour. The parameterisation and validation of the newly-developed model against experimental data will then be described.

4.2 Model development

As shown in Chapter 3, the Gattoni model of rat ventricular electrophysiology is the most recent rat-specific computational model of the ventricular myocyte, and has been thoroughly parameterised against recent experimental data recorded at physiological temperatures. The Gattoni model more closely reproduces experimental data, particularly relating to Ca^{2+} handling, but its deterministic implementation limits its ability to explore remodelled Ca^{2+} handling and for investigating Ca^{2+}-mediated pro-arrhythmic behaviour. The Colman model [97] is a recent spatio-temporal Ca^{2+} cycling framework comprising a hierarchy of models. The microsopic, 3D spatio-temporal cell model is the baseline model which incorporates spatially distributed dyads, Ca^{2+} diffusion throughout the cell, and stochastic state transitions for the L-type Ca^{2+} channels and ryanodine receptors. The framework and model have been shown as useful to explore structure-function relationships at the whole cell level, for normal and pathophysiological states, and so can provide mechanistic insight into pro-arrhythmic behaviour arising from Ca^{2+}-handling remodelling [97, 101]. Over the following sections, the Ca^{2+} cycling model will be described alongside the incorporated membrane current components from the Gattoni model. The developed model will hereby be referred to as the SC model.

4.2.1 Spatio-temporal Ca^{2+} cycling model

The microscopic, 3D spatio-temporal Ca^{2+} handling model, a simplified version of a previous model [101], consists of an idealised 3D intracellular Ca^{2+} system coupled to an ion current and point-source V_m model (Figure 4.1). The model incorporates a 3D CRU grid, each containing five compartments: the bulk cytoplasm, subspace (ss) and restricted dyadic cleft space (ds) comprise the intracellular components, and the network (NSR) and junctional (JSR) SR compartments comprise the SR spaces. The NSR, subspace and bulk cytosolic compartments are coupled to neighbouring CRUs, and each dyad contains $\approx$ 10 LTCCs and $\approx$ 100 RyRs (though this can vary and be heterogeneous within a cell), described by stochastic differential equations [101].

Fundamentally, Ca^{2+} concentrations are described by the following equations:

$$\frac{d[Ca^{2+}]_{\mathrm{i}}}{d\mathrm{t}} = \beta_{\mathrm{i}}(\mathbf{D}\nabla^2[Ca^{2+}]_{\mathrm{i}} + \phi_{\mathrm{i}} + (v_{\mathrm{ss}}/v_{\mathrm{i}})J_{\mathrm{ss}}) \tag{4.1}$$

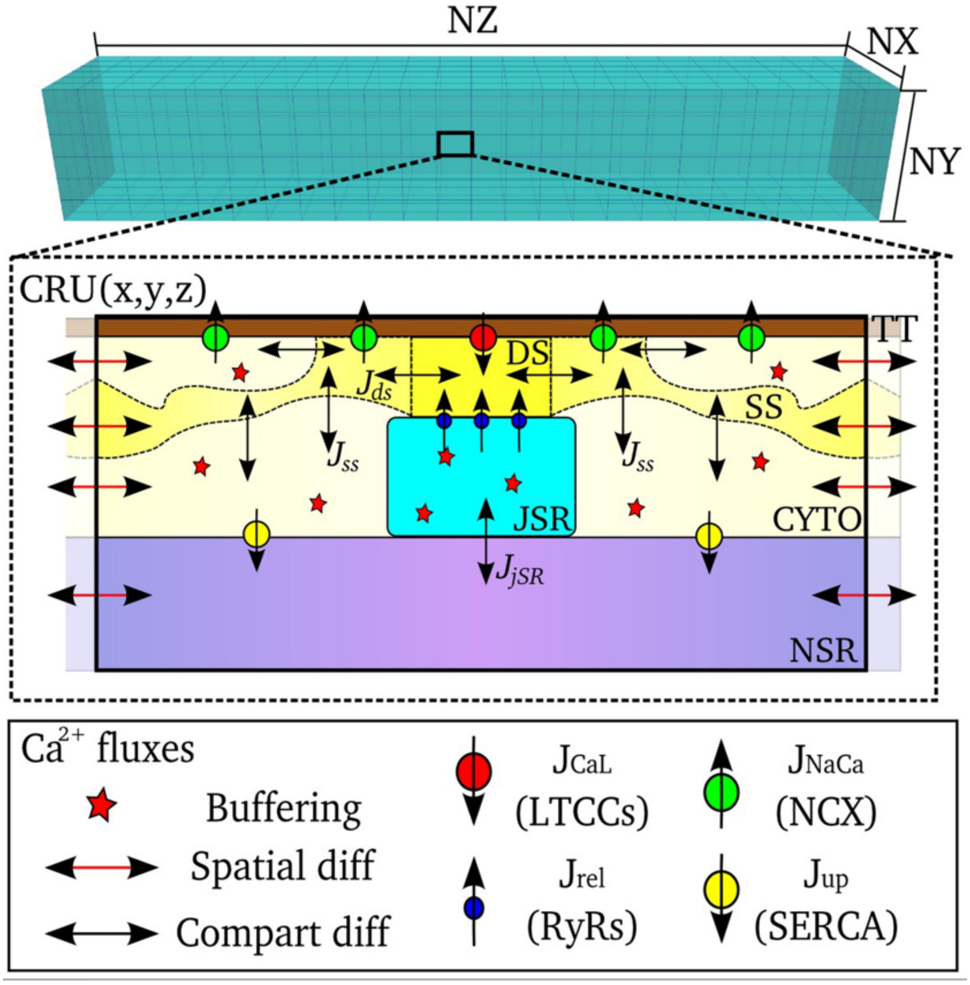

Figure 4.1. Schematic of the single cell Ca^{2+} handling model. 3D microscopic Ca^{2+} handling model showing the 3D grid of CRUs (top) and the compartments and associated Ca^{2+} fluxes within a single CRU (bottom). Dyadic space (DS), subspace (SS), bulk cytoplasm (CYTO), network (NSR) and junctional SR (JSR) spaces are shown, alongside a T-tubule (TT). Fluxes through LTCCs, RyRs, NCX and SERCA are illustrated by the key. Double-headed black arrows show transfer between compartments; red arrows show diffusion between neighbouring CRUs. Adapted from [97].

$$\frac{d[Ca^{2+}]_{\mathrm{ss}}}{dt} = \beta_{\mathrm{ss}}(\mathbf{D}\nabla 2[Ca^{2+}]_{\mathrm{ss}} + \phi_{\mathrm{ss}} - J_{\mathrm{ss}} + (v_{\mathrm{ds}}/v_{\mathrm{ss}})J_{\mathrm{ds}}) \tag{4.2}$$

$$\frac{d[Ca^{2+}]_{\mathrm{NSR}}}{dt} = \mathbf{D}\nabla^2[Ca^{2+}]_{\mathrm{NSR}} + \phi_{\mathrm{NSR}} - (v_{\mathrm{JSR}}/v_{\mathrm{NSR}})J_{\mathrm{JSR}} \tag{4.3}$$

$$i\frac{d[Ca^{2+}]_{\mathrm{ds}}}{dt} = \phi_{\mathrm{ds}} - J_{\mathrm{ds}} \tag{4.4}$$

$$\frac{d[Ca^{2+}]_{\mathrm{JSR}}}{dt} = \beta_{\mathrm{JSR}}(\phi_{\mathrm{JSR}} + J_{\mathrm{JSR}}) \tag{4.5}$$

where $\mathbf{D}$ is the diffusion coefficient, ∇^2 is the spatial Laplacian operator in 3D, ϕ is a general reaction term (defined below), v is the volume of a single voxel of each of the 5 compartments, J represents transfer between compartments, and β_{i} is the instantaneous buffering term [414], described later.

Transfer between compartments is given by:

$$J_{\mathrm{ss}} = \left([Ca^{2+}]_{\mathrm{ss}} - [Ca^{2+}]_{\mathrm{i}}\right) \tau_{\mathrm{ss}}^{-1} \tag{4.6}$$

$$J_{\mathrm{ds}} = \left([Ca^{2+}]_{\mathrm{ds}} - [Ca^{2+}]_{\mathrm{ss}}\right) \tau_{\mathrm{ds}}^{-1} \tag{4.7}$$

$$J_{\mathrm{JSR}} = \left([Ca^{2+}]_{\mathrm{NSR}} - [Ca^{2+}]_{\mathrm{JSR}}\right) \tau_{\mathrm{ds}}^{-1}, \tag{4.8}$$

with the reaction terms given by:

$$\phi_{\mathrm{i}} = J_{\mathrm{NaCa}} + J_{\mathrm{CaP}} + J_{\mathrm{Cab}} - (J_{\mathrm{up}} - J_{\mathrm{leak}}) - J_{\mathrm{trpn}} \tag{4.9}$$

$$\phi_{\mathrm{NSR}} = (J_{\mathrm{up}} - J_{\mathrm{leak}})(v_{\mathrm{i}}/v_{\mathrm{NSR}}) \tag{4.10}$$

$$\phi_{\mathrm{ss}} = J_{\mathrm{NaCa\_ss}} \tag{4.11}$$

$$\phi_{\mathrm{ds}} = J_{\mathrm{rel}} + J_{\mathrm{CaL}} \tag{4.12}$$

$$\phi_{\mathrm{JSR}} = -J_{\mathrm{rel}}(v_{\mathrm{ds}}/v_{\mathrm{JSR}}). \tag{4.13}$$

At each voxel ($n = 1, 2..N_{\mathrm{cyto}}$), the Laplacian (spatial diffusion) is described by a 6-node nearest neighbours finite difference approximation:

$$\mathbf{D}\nabla^2[Ca^{2+}]_{\mathrm{x}} \approx J_{\mathrm{Ca\_diff\_x}} = \sum_{i=1}^{i=3} \left(\frac{{}^{e_{\mathrm{i}}+1}[Ca^{2+}]_{\mathrm{x}} + {}^{e_{\mathrm{i}}-1}[Ca^{2+}]_{\mathrm{x}} - 2^{e_{\mathrm{i}}}[Ca^{2+}]_{\mathrm{x}}}{\tau_{\mathrm{x},e_{\mathrm{i}}}} \right) \tag{4.14}$$

where e_{i} refers to the three dimensions (x, y, z) and $\tau_{\mathrm{x},e_{\mathrm{i}}}$ is the spatial discretisation step. Note that Equation 4.14 describes inter-compartment diffusion, so $\tau_{\mathrm{x},e_{\mathrm{i}}}$ is approximately equal to $\mathbf{D}/\Delta x^2$ for a discretised full diffusion model.

As the dyadic cleft volume is small, the dyadic cleft Ca^{2+} concentration is described using an analytical description under the approximation that the volume reaches its steady-state concentration within the time step, δt. Thus, an approximation for Equation 4.4 can be obtained as:

$$[Ca^{2+}]_{\mathrm{ds}} = [Ca^{2+}]_{\mathrm{ss}} + \frac{\tau_{\mathrm{ds}} \cdot \left(k_{\mathrm{rel}} \cdot [Ca^{2+}]_{\mathrm{JSR}} + J_{\mathrm{CaL}}\right)}{(1 + \tau_{\mathrm{ds}} \cdot k_{\mathrm{rel}})} \tag{4.15}$$

where k_{rel} is the RyR dissociation constant [165]. A full list of model parameters relating to cell structure and diffusion is given in Table 4.1.

Table 4.1. Colman model cell structure and diffusion parameters.

Parameter	Description	Value
v_{i}	Cytoplasm volume per CRU	1.0 μm^3
v_{NSR}	Network SR volume per CRU	0.05 μm^3
v_{ss}	Subspace volume per CRU	0.0175 μm^3
$< v_{\mathrm{ds}} >$	Average individual dyad volume	1.712x10^{-3} μm^3
v_{JSR}	Individual JSR volume	0.015 μm^3
τ_{ds}	Time constant of dyad→ ss diffusion	0.022 ms
τ_{ss}	Time constant of ss→ cyto diffusion	0.1 ms
τ_{JSR}	Time constant of NSR→ JSR diffusion	5 ms
$\tau_{\mathrm{i,transverse}}$	Time constant of transverse cyto diffusion	2.3 ms
$\tau_{\mathrm{i,longitudinal}}$	Time constant of longitudinal cyto diffusion	2.9 ms
$\tau_{\mathrm{ss,transverse}}$	Time constant of transverse ss diffusion	1.35 ms*
$\tau_{\mathrm{ss,longitudinal}}$	Time constant of longitudinal ss diffusion	2.20 ms*
$\tau_{\mathrm{NSR,transverse}}$	Time constant of transverse NSR diffusion	7 ms
$\tau_{\mathrm{NSR,longitudinal}}$	Time constant of longitudinal NSR diffusion	14 ms

* control values

4.2.1.1 Intracellular Ca^{2+} release; J_{rel}

Intracellular Ca^{2+} release, J_{rel} is described by:

$$^{m}J_{\mathrm{rel}} = ^{m}k_{\mathrm{rel}}(^{m}[Ca^{2+}]_{\mathrm{JSR}} - ^{m}[Ca^{2+}]_{\mathrm{ds}}), \tag{4.16}$$

$$^{m}k_{\mathrm{rel}} = ^{m}n_{\mathrm{o\_RyR}} . g_{\mathrm{RyR}} . ^{m}v_{\mathrm{ds}}^{-1}, \tag{4.17}$$

where $^{m}n_{\mathrm{o\_RyR}}$ is the number of open RyR channels in dyad m, and g_{RyR} is the maximal flux rate through the RyRs. Dynamics of RyRs are described by a 4-state Markov chain model (Figure 4.2), similar to previously implementations [319, 371], with a functional monomer-induced inactivation based on the calsequestrin dynamics of [147]. The governing equations for J_{rel} are given by:

$$\frac{d^{m}CA}{dt} = ^{m}OA.\beta_{\mathrm{C-O}} + ^{m}CI.\beta_{\mathrm{A-I}} - ^{m}CA.(\alpha_{\mathrm{C-O}} + \alpha_{\mathrm{A-I}}) \tag{4.18}$$

$$\frac{d^{m}OA}{dt} = ^{m}CA.\alpha_{\mathrm{C-O}} + ^{m}OI.\beta_{\mathrm{A-I}} - ^{m}OA.(\beta_{\mathrm{C-O}} + \alpha_{\mathrm{A-I}}) \tag{4.19}$$

$$\frac{d^{m}CI}{dt} = ^{m}OI.\beta_{\mathrm{C-O}} + ^{m}C.\alpha_{\mathrm{A-I}} - ^{m}CI.(\alpha_{\mathrm{C-O}} + \beta_{\mathrm{A-I}}) \tag{4.20}$$

$$\frac{d^mOI}{dt} = {}^mCI.\alpha_{\mathrm{C-O}} + {}^mOA.\alpha_{\mathrm{A-I}} - {}^mOI.(\beta_{\mathrm{C-O}} + \beta_{\mathrm{A-I}}) \tag{4.21}$$

where

$$\alpha_{\mathrm{C-O}} = k_{\mathrm{a}}({}^m[Ca^{2+}]_{\mathrm{ds}})^H \tag{4.22}$$

$$\beta_{\mathrm{C-O}} = k_{\mathrm{b}} \tag{4.23}$$

$$\alpha_{\mathrm{A-I}} = (1 - {}^mMi_{\mathrm{ss}})/\tau_{\mathrm{Mi,1}} \tag{4.24}$$

$$\beta_{\mathrm{A-I}} = {}^mMi_{\mathrm{ss}}/\tau_{\mathrm{Mi,2}} \tag{4.25}$$

$${}^mMi_{\mathrm{ss}} = 1/(1 + e^{({}^mM - 0.5)/0.04167}) \tag{4.26}$$

$$\frac{dM}{dt} = \alpha_{\mathrm{M}}(1 - M) + \beta_{\mathrm{M}}M \tag{4.27}$$

$$\alpha_{\mathrm{M}} = M_{\mathrm{ss}}/\tau_{\mathrm{M,1}} \tag{4.28}$$

$$\beta_{\mathrm{M}} = (1 - M_{\mathrm{ss}})/\tau_{\mathrm{M,2}} \tag{4.29}$$

$$M_{\mathrm{ss}} = 1/(1 + e^{(-6.5(csqn - 6.37))}) \tag{4.30}$$

$$csqn = \beta_{\mathrm{csqn}}.K_{\mathrm{mcsqn}}/({}^m[Ca^{2+}]_{\mathrm{JSR}} + K_{\mathrm{mcsqn}}) \tag{4.31}$$

where H is the RyR open rate Ca^{2+} power, k_{a} is the RyR activation rate constant, k_{b} is the RyR deactivation rate constant, $\tau_{\mathrm{M,1}}$ is the time constant of monomer binding, $\tau_{\mathrm{Mi,1}}$ is the time constant of monomer inactivation, $\tau_{\mathrm{Mi,2}}$ is the time constant of monomer unbinding and $\tau_{\mathrm{Mi,2}}$ is the time constant of de-inactivation. *OA* is the only state in which flux occurs, thus ${}^mn_{\mathrm{o_{RyR}}}$ is equal to the number of channels in state *OA* for dyad *m*.

4.2.1.2 L-type Ca^{2+} channel flux; J_{LTCC}

Flux through the L-type Ca^{2+} channel, J_{CaL}, is described by:

$${}^mJ_{\mathrm{CaL}} = -{}^mn_{\mathrm{o\_LTCC}}\,{}^m\bar{J}_{\mathrm{CaL}} \tag{4.32}$$

where ${}^mn_{\mathrm{o\_LTCC}}$ is the number of open L-type Ca^{2+} channels for dyad *m*, and $\bar{J}_{\mathrm{CaL}}$ is the maximal flux rate per channel [235]:

$${}^m\bar{J}_{\mathrm{CaL}} = 4P_{\mathrm{Ca}}zF\frac{\frac{1}{2}\gamma_{\mathrm{Ca}}\,{}^m[Ca^{2+}]_{\mathrm{ds}}e^{2z} - \gamma_{\mathrm{Ca}}[Ca^{2+}]_{\mathrm{o}}}{e^{2z} - 1} \tag{4.33}$$

$$z = \frac{V_{\mathrm{m}}F}{RT} \tag{4.34}$$

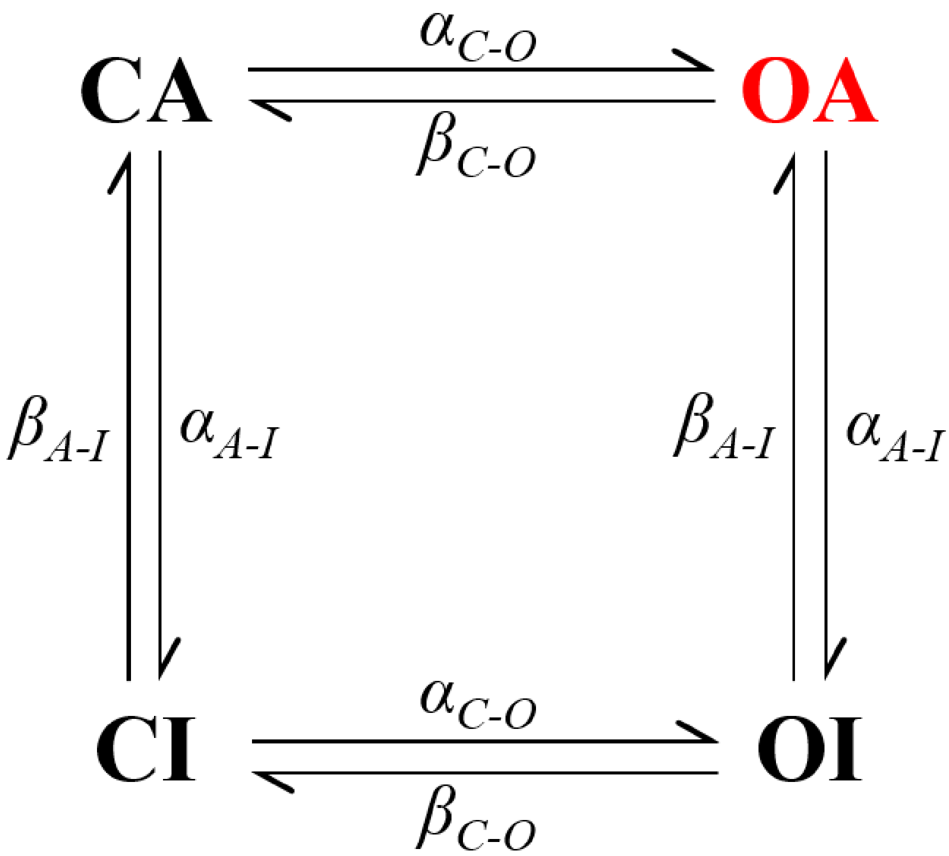

Figure 4.2. Four-state Markov model for the RyR. Ca^{2+} flux only occurs in state *OA*.

where P_{Ca} is the maximum permeability for an individual LTCC, $[Ca^{2+}]_{\text{o}}$ is the extracellular Ca^{2+} concentration, γ_{Ca} is the LTCC activity coefficient and F is the Faraday constant. LTCCs are described by a Markov chain implementation of a Hodgkin-Huxley model as in [235, 369], shown in Figure 4.3 and is equivalent to the three gate Hodgkin-Huxley model:

$$\text{d1} \xrightleftharpoons[\alpha d_1 -]{\alpha d_1 -} \text{d2} \xrightleftharpoons[\alpha d_2 - \alpha]{\alpha d_1 - \alpha} \text{d3}$$

$$\text{f1} \xrightleftharpoons[\alpha_{f1-f2}]{\alpha_{f1-f2}} \text{f2}$$

$$\text{fca}_1 \xrightleftharpoons[\beta_{fca_1-fca_2}]{\alpha\alpha_{f1-f2}} \text{fca}_2$$

and thus described by:

$$\frac{d(d_1)}{dt} = d_2\beta_{d_1-d_2} - d_1\alpha_{d_1-d_2} \tag{4.35}$$

$$\frac{d(d_2)}{dt} = d_1\alpha_{d_1-d_2} + d_3\beta_{d_2-d_3} - d_2(\beta_{d_1-d_2} + \alpha_{d_2-d_3}) \tag{4.36}$$

$$\frac{d(d_3)}{dt} = d_2\alpha d_2 - d_3 - d_3\beta_{d_2-d_3} \tag{4.37}$$

$$\frac{d(f_1)}{dt} = f_2\beta_{f_1-f_2} - f_1\alpha_{f_1-f_2} \tag{4.38}$$

$$\frac{d(fca_1)}{dt} = fca_2\beta_{fca_1-fca_2} - fca_1\alpha_{fca_1-fca_2} \tag{4.39}$$

where the transition rates for each couplet of variables ($x = d_1 - d_2, f_1 - f_2, fca_1 - fca_2$) are defined from the steady-state and time constant:

$$\alpha_x = x_{ss}/\tau_x \tag{4.40}$$

$$\beta_x = (1 - x_{ss})/\tau_x \tag{4.41}$$

and:

$$\alpha_{d_2-d_3} = k_{d2d3} \tag{4.42}$$

$$\beta_{d_2-d_3} = k_{d3d2} \tag{4.43}$$

$$d_{ss} = 1/(1 + e^{(-(V_m-5)/6.24)}) \tag{4.44}$$

$$f_{ss} = 1 - 1/(1 + e^{((V_m+32.06)/8.6)}) \tag{4.45}$$

$$\tau_d = d_{ss}.(1 - e^{(-(V_m-5)/6.24)})/(0.035(V_m - 5)) \tag{4.46}$$

$$\tau_f = 2/(0.0197e^{-([0.0337(V_m+7)]^2+0.02)}) \tag{4.47}$$

$$fca_{ss} = 1 - 1/(1 + ({}^m[Ca^{2+}]_{ds}/\bar{\mathrm{Ca}})^2) \tag{4.48}$$

where k_{d2d3} is the rate constant for transition $d_2 - d_3$, k_{d3d2} is the rate constant for transition $d_3 - d_2$ and $\bar{\mathrm{Ca}}$ is the Ca^{2+} constant for Ca^{2+}-induced inactivation. Note that the inactivation gate steady states ($f_{\mathrm{ss}}, fca_{\mathrm{ss}}$) are inverse to those in the standard Hodgkin-Huxley model as f_2 is the inactivated state in this Markov description, equivalent to $(1-f)$ in the original description (and f_1 is equivalent to f). RyR and LTCC parameters are summarised in Table 4.2.

4.2.1.3 SR uptake and leak; J_{up} and J_{leak}

The equations for SR uptake, J_{up}, and SR leak, J_{leak}, based on previous studies [319, 356, 360], are:

$${}^mJ_{\mathrm{up}} = g_{\mathrm{up}}\frac{({}^m[Ca^{2+}]_{\mathrm{i}}/K_{\mathrm{cyto}})^2 - ({}^m[Ca^{2+}]_{\mathrm{NSR}}/K_{\mathrm{NSR}})^2}{1 + ({}^m[Ca^{2+}]_{\mathrm{i}}/K_{\mathrm{cyto}})^2 + ({}^m[Ca^{2+}]_{\mathrm{NSR}}/K_{\mathrm{NSR}})^2} \tag{4.49}$$

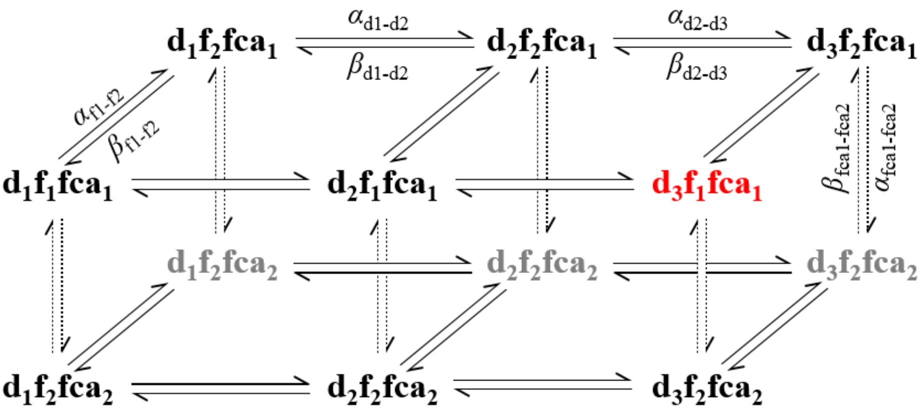

Figure 4.3. Markov scheme of the Hodgkin-Huxley I_{CaL} model.

$$^{m}J_{\mathrm{leak}} = g_{\mathrm{leak}} \frac{^{m}[Ca^{2+}]_{\mathrm{NSR}}^{2}}{^{m}[Ca^{2+}]_{\mathrm{NSR}}^{2} + K_{\mathrm{leak}}{}^{2}} (^{m}[Ca^{2+}]_{\mathrm{NSR}} - ^{m}[Ca^{2+}]_{\mathrm{i}}) \tag{4.50}$$

where g_{up} is the maximal flux rate of J_{up}, K_{cyto} is the cytoplasm constant for J_{up}, K_{NSR} is the network SR constant for J_{up}, g_{leak} is the maximal flux rate of J_{leak} and K_{leak} is the J_{leak} constant. Values for these parameters are given in Table 4.3.

4.2.1.4 Membrane fluxes; J_{NaCa}, J_{CaP} and J_{Cab}

The equations for the membrane fluxes J_{NaCa}, J_{CaP} and J_{Cab}, based on previous studies [319,356,360], are:

$$^{m}J_{\mathrm{NaCa}} = \frac{K_{\mathrm{a}} g_{\mathrm{NaCa}} v_{\mathrm{vox}}^{-1} (e^{\eta z}[Na^{+}]_{\mathrm{i}}[Ca^{2+}]_{\mathrm{o}} - e^{(\eta-1)z}[Na^{+}]_{\mathrm{o}}\, ^{m}[Ca^{2+}]_{\mathrm{cyto}})}{(t_1, t_2, t_3)(1 + K_{\mathrm{sat}} e^{(\eta-1)z})} \tag{4.51}$$

$$^{m}J_{\mathrm{CaP}} = (v_{i}^{-1} g_{\mathrm{CaP}}\, ^{m}[Ca^{2+}]_{\mathrm{i}})/(K_{\mathrm{mCaP}} + ^{m}[Ca^{2+}]_{\mathrm{i}}) \tag{4.52}$$

$$^{m}J_{\mathrm{Cab}} = v_{\mathrm{vox}}^{-1} g_{\mathrm{Cab}} (V_{\mathrm{m}} - E_{\mathrm{Ca}}) \tag{4.53}$$

where g_{NaCa} is the maximal flux rate of the Na^{+}-Ca^{2+} exchanger, η is the NCX voltage sensitivity coefficient, K_{sat} is the NCX saturation constant, g_{CaP} is the maximal flux rate of the sarcolemmal Ca^{2+} pump, K_{mCaP} is the Ca^{2+} saturation constant for the sarcolemmal Ca^{2+} pump, g_{Cab} is the maximal flux rate of the background Ca^{2+} current, and where

$$t_1 = K_{\mathrm{mCai}}[Na^{+}]_{\mathrm{o}}^{3}(1 + ([Na^{+}]_{\mathrm{i}}/K_{\mathrm{mNai}})^{3}) \tag{4.54}$$

$$t_2 = K_{\mathrm{mNao}}^{3}\, ^{m}[Ca^{2+}]_{\mathrm{i}}(1 + (^{m}[Ca^{2+}]_{\mathrm{i}}/K_{\mathrm{mCai}})) \tag{4.55}$$

$$t_3 = K_{\mathrm{mCao}}[Na^{+}]_{\mathrm{i}}^{3} + [Na^{+}]_{\mathrm{i}}^{3}[Ca^{2+}]_{\mathrm{o}} + [Na^{+}]_{\mathrm{o}}^{3}\, ^{m}[Ca^{2+}]_{\mathrm{i}} \tag{4.56}$$

Table 4.2. Colman model RyR and LTCC flux parameters.

Parameter	Description	Value
g_{ryr}	Max RyR flux rate	2.05x10^{-4} µm^{3}ms^{-1}
P_{Ca}	Max LTCC permeability	11.9 µmolC^{-1}ms^{-1}
γ_{Ca}	LTCC activity coefficient	0.341
N_{RyR}	Number of RyRs per dyad	100
H	RyR open rate Ca^{2+} power	2.5
k_{a}	RyR activation rate constant	1.58x10^{-4} µM$^{-2.5}$ms^{-1}
k_{b}	RyR deactivation rate constant	1.0 ms^{-1}
$\tau_{\mathrm{M,1}}$	Time constant of monomer binding	25 ms
$\tau_{\mathrm{Mi,1}}$	Time constant of monomer inactivation	30 ms
$\tau_{\mathrm{M,2}}$	Time constant of monomer unbinding	156 ms
$\tau_{\mathrm{Mi,2}}$	Time constant of monomer de-inactivation	75 ms
N_{LTCC}	Number of L-type Ca^{2+} channels per dyad	15
k_{d2d3}	Rate constant for $d_2 - d_3$ transition	0.3 ms^{-1}
k_{d3d3}	Rate constant for $d_3 - d_2$ transition	6.0 ms^{-1}
τ_{fca}	Time constant for Ca^{2+}-induced inactivation	15 ms
$\bar{Ca}$	Ca^{2+} constant for Ca^{2+}-induced inactivation	6.0 µM
$[Ca^{2+}]_o$	Extracellular Ca^{2+} concentration	1.8 mM

$$K_{\mathrm{a}} = [1 + (K_{\mathrm{da}}/{}^{m}[Ca^{2+}]_{\mathrm{i}})] \tag{4.57}$$

$$z = \frac{V_{\mathrm{m}}F}{RT} \tag{4.58}$$

in which $K_{\mathrm{mCai,mNai}}$ are the intracellular and $K_{\mathrm{mCao,mNao}}$ the extracellular constants for Ca^{2+} and Na^{+}, respectively, and K_{da} is a Ca^{2+} scaling constant for NCX. Membrane flux parameter values are provided in Table 4.4.

4.2.1.5 Instantaneous buffering

Cytoplasmic instantaneous buffering follows that of previous models [278, 319, 414]. At each voxel, m, the buffering term is given by:

$$^{m}\beta_{\mathrm{cyto,SS}} = \left[1 + C_{\mathrm{cyto,SS}} \sum_{\mathrm{x}} \frac{B_{\mathrm{x}}K_{\mathrm{x}}}{^{m}[Ca^{2+}]_{\mathrm{cyto,SS}} + K_{\mathrm{x}})^{2}}\right] \tag{4.59}$$

Table 4.3. Colman model SR Ca^{2+} uptake and leak parameters.

Parameter	Description	Value
g_{up}	Max J_{up} flux rate	0.339 μM.ms^{-1}
K_{cyto}	Cytoplasm constant for J_{up}	0.15 μM
K_{NSR}	NSR constant for J_{up}	1700 μM
g_{leak}	Max flux rate of J_{leak}	1.412x10^{-5} ms^{-1}
K_{leak}	J_{leak} constant	450 μM

Table 4.4. Colman model membrane flux parameters.

Parameter	Description	Value
g_{NaCa}	Max NCX flux rate	0.3726 μm^3.μM.ms^{-1}
K_{da}	NCX Ca^{2+} scaling constant	0.11 μM
η	NCX voltage-sensitivity coefficient	0.35
K_{sat}	NCX saturation constant	0.27
K_{mCai}	NCX intracellular Ca^{2+} constant	3.59 μM
K_{mCao}	NCX extracellular Ca^{2+} constant	1.3 mM
K_{mNai}	NCX intracellular Na^{+} constant	12.3 mM
K_{mNao}	NCX extracellular Na^{+} constant	87.5 mM
g_{CaP}	Max flux rate of sarcolemmal Ca^{2+} pump	1.37x10^{-3}μm^3.μM.ms^{-1}
g_{Cab}	Max flux rate of background Ca^{2+} current	1.82x10^{-5}μm^3.μM.ms^{-1}.mV^{-1}
$[Na^+]_i$	Intracellular Na^{+} concentration	7.95 mM
$[Na^+]_o$	Extracellular Na^{+} concentration	136 mM

where x refers to four buffering processes (calmodulin, SR sites, myosin Ca, and myosin Mg), K_{x} is the dissociation constant at these buffering sites, B_{x} is the total concentration of these buffering sites, and $C_{\mathrm{cyto,ss}}$ is the buffering strength coefficient for the cytoplasm (1) and subspace (0.1).

Buffering in the JSR takes the form of [147]:

$$ {}^{m}\beta_{\mathrm{JSR}} = \left[1 + \frac{B_{\mathrm{csqn}}K_{\mathrm{csqn}}}{\left({}^{m}[Ca^{2+}]_{\mathrm{JSR}} + K_{\mathrm{mcsqn}}\right)^2}\right]^{-1} \tag{4.60} $$

where B_{csqn} is the total concentration of csqn buffering sites and K_{mcsqn} is the respective dissociation constant.

Table 4.5. Colman model Ca^{2+} buffering parameters.

Parameter	Description	Value
K_{CAM}	Calmodulin dissociation constant	7.0 μM
B_{CAM}	Total concentration calmodulin buffering sites	24.0 μM
K_{SR}	SR buffering sites dissociation constant	0.6/0.9 μM (cyto/SS)
B_{SR}	Total concentration SR buffering sites	47.0 μM
$K_{\mathrm{M,Ca}}$	Myosin (Ca) dissociation constant	0.033/0.0615 μM (cyto/SS)
$B_{\mathrm{M,Ca}}$	Total concentration myosin (Ca) buffering sites	140.0μM
$K_{\mathrm{M,Mg}}$	Myosin (Mg) dissociation constant	3.64/5.46 μM (cyto/SS)
$B_{\mathrm{M,Mg}}$	Total concentration myosin (Mg) buffering sites	140.0 μM
$C_{\mathrm{cyto,SS}}$	Buffering strength coefficient	1/0.1 (cyto/SS)
K_{mcsqn}	Csqn dissociation constant	0.8 mM
B_{csqn}	Total concentration csqn buffering sites	10 mM
$k^{+}_{\mathrm{H,trpn}}$	On rate for high affinity troponin sites	100 $\mathrm{mM^{-1}\ ms^{-1}}$
$k^{-}_{\mathrm{H,trpn}}$	Off rate for high affinity troponin sites	$1.0\mathrm{x}10^{-3}\ \mathrm{ms^{-1}}$
$k^{+}_{\mathrm{L,trpn}}$	On rate for low affinity troponin sites	100 $\mathrm{mM^{-1}\ ms^{-1}}$
$k^{-}_{\mathrm{L,trpn}}$	Off rate for low affinity troponin sites	$4.0\mathrm{x}10^{-2}\ \mathrm{ms^{-1}}$
$B_{\mathrm{H,trpn}}$	Total troponin high affinity sites	0.14 mM
$B_{\mathrm{L,trpn}}$	Total troponin low affinity sites	0.7 mM
f_{XB}	Weak→ strong crossbridge transition rate	0.05 $\mathrm{ms^{-1}}$
$g_{\mathrm{XB,min}}$	Max strong→ weak transition rate	0.1 $\mathrm{ms^{-1}}$
SL	Sarcomere length	2.15 μm
$K_{\mathrm{pn,TRPN}}$	Permissive→ non-permissive transition rate	0.04 $\mathrm{ms^{-1}}$

Force generation and buffering by troponin takes the form from [148, 321]:

$$
{}^{m}J_{\mathrm{trpn}} = \frac{dH_{\mathrm{trpn,Ca}}}{dt} + \frac{dL_{\mathrm{trpn,Ca}}}{dt} \tag{4.61}
$$

$$
\frac{d^{m}H_{\mathrm{trpn,Ca}}}{dt} = k^{+}_{\mathrm{H,trpn}}\ {}^{m}[Ca^{2+}]_{\mathrm{cyto}}(B_{\mathrm{H,trpn}} - H_{\mathrm{trpn,Ca}}) - k^{-}_{\mathrm{H,trpn}} H_{\mathrm{trpn,Ca}} \tag{4.62}
$$

$$
\frac{d^{m}L_{\mathrm{trpn,Ca}}}{dt} = k^{+}_{\mathrm{L,trpn}}\ {}^{m}[Ca^{2+}]_{\mathrm{cyto}}(B_{\mathrm{L,trpn}} - L_{\mathrm{trpn,Ca}}) - k^{-}_{\mathrm{L,trpn}} \left(1 - \frac{2}{3}F_{\mathrm{norm}}\right) L_{\mathrm{trpn,Ca}} \tag{4.63}
$$

where $k^{+,-}_{\mathrm{Htrpn,Ltrpn}}$ is the troponin high (H) or low (L) affinity site on (+) or off (−) rates, $B_{\mathrm{H,Ltrpn}}$ is the total high or low affinity sites on troponin, and F_{norm} is the normalised force:

$$F_{\text{norm}} = \left(\frac{P_1 + N_1 + 2P_2 + 3P_3}{P_1^{max} + 2P_2^{max} + 3P_3^{max}} \right) \tag{4.64}$$

and:

$$\phi = 1 + \frac{2.3 - SL}{(2.3 - 1.7)^{1.6}} \tag{4.65}$$

$$f_{01} = 3f_{\text{XB}} \tag{4.66}$$

$$f_{12} = 10f_{\text{XB}} \tag{4.67}$$

$$f_{23} = 7f_{\text{XB}} \tag{4.68}$$

$$g_{01} = g_{\text{XB}} \tag{4.69}$$

$$g_{12} = 2g_{\text{XB}} \tag{4.70}$$

$$g_{23} = 3g_{\text{XB}} \tag{4.71}$$

$$g_{01,SL} = 1\phi g_{\text{XB,min}} \tag{4.72}$$

$$g_{12,SL} = 2\phi g_{\text{XB,min}} \tag{4.73}$$

$$g_{23,SL} = 3\phi g_{\text{XB,min}} \tag{4.74}$$

$$K^{Ca}_{\text{TRPN}} = \frac{k^-_{\text{L,TRPN}}}{k^+_{\text{L,TRPN}}} \tag{4.75}$$

$$N_{\text{TRPN}} = 3.5SL - 2.0 \tag{4.76}$$

$$K^{\text{TRPN}}_{1/2} = \left[1 + \frac{K^{Ca}_{\text{TRPN}}}{1.4 \times 10^{-3} - 8 \times 10^{-4}((SL - 1.7)/0.6)} \right]^{-1} \tag{4.77}$$

$$k_{\text{np,TRPN}} = k_{\text{pn,TRPN}} \left(\frac{[TRPN^{\text{L}}_{\text{Ca}}]}{K_{1/2}TRPN^{\text{L}}_{\text{tot}}} \right)^{N_{\text{TRPN}}} \tag{4.78}$$

$$\sum Paths = g_{01}g_{12}g_{23} + f_{01}g_{12}g_{23} + f_{01}f_{12}g_{23} + f_{01}f_{12}f_{23} \tag{4.79}$$

$$P_1^{\text{max}} = \frac{f_{01}g_{12}g_{23}}{\sum Paths} \tag{4.80}$$

$$P_2^{\text{max}} = \frac{f_{01}f_{12}g_{23}}{\sum Paths} \tag{4.81}$$

$$P_3^{\text{max}} = \frac{f_{01}f_{12}f_{23}}{\sum Paths} \tag{4.82}$$

$$\frac{dP_0}{dt} = -(k_{\text{pn,TRPN}} + f_{01})P_0 + k_{\text{np,TRPN}}N_0 + g_{01,SL}P_1 \tag{4.83}$$

$$\frac{dP_1}{dt} = -(k_{\text{pn,TRPN}} + f_{12} + g_{01,SL})P_1 + k_{\text{np,TRPN}}N_1 + f_{01}P_0 + g_{12,SL}P_1 \tag{4.84}$$

$$\frac{dP_2}{dt} = -(f_{23} + g_{12,SL})P_2 + f_{12}P_1 + g_{23,SL}P_3 \tag{4.85}$$

$$\frac{dP_3}{dt} = -g_{23,SL}P_3 + f_{23,SL}P_2 \tag{4.86}$$

$$\frac{dN_1}{dt} = k_{\text{pn,TRPN}}P_1 - (k_{\text{np,TRPN}} + g_{01,SL})N_1 \tag{4.87}$$

$$\frac{dN_0}{dt} = \frac{dP_0}{dt} - \frac{dP_1}{dt} - \frac{dP_2}{dt} - \frac{dP_3}{dt} - \frac{dN_1}{dt} \tag{4.88}$$

where f_{XB} is the weak-to-strong cross bridge transition rate, g_{XB} is the maximum strong-to-weak rate, SL is the sarcomere length, and $k_{\text{pn,TRPN}}$ is the permissive to non-permissive transition rate. Buffering parameters are summarised in Table 4.5.

4.2.2 Electrophysiology model

Membrane currents from the Gattoni model of rat ventricular electrophysiology were coupled to the Colman Ca^{2+} cycling model, in order to reproduce the rat ventricular AP. These membrane currents and their maximal conductances are shown in Table 4.6.

Table 4.6. Gattoni model membrane currents and their maximal conductances.

Current	Description	Maximal conductance
I_{Na}	Sodium current	g_{Na} = 7 s/mF
I_{to}	Ca^{2+}-independent transient outward K^+ current	g_{to} = 0.196 s/mF
I_{ss}	Steady-state outward K^+ current	g_{ss} = 0.12 s/mF
I_{K1}	Inward rectifier K^+ current	g_{K1} = 0.4 s/mF
I_{f}	Hyperpolarisation-activated current	g_{f} = 0.0145 s/mF
I_{NaK}	Na^+-K^+ ATPase	$\bar{I}_{\text{NaK}}$ = 0.08 s/mF
I_{Nab}	Background Na^+ current	g_{Nab} = 8.015x10^{-4} s/mF
I_{Kb}	Background K^+ current	g_{Kb} = 1.38x10^{-3} s/mF

4.2.2.1 Sodium current; I_{Na}

The sodium current, I_{Na}, takes the form:

$$I_{\text{Na}} = g_{\text{Na}}.m^3.h.j(V_{\text{m}} - E_{\text{Na}}) \tag{4.89}$$

where

$$\begin{aligned}
\bar{m} &= 1.0/(1.0 + e^{((V_\mathrm{m}+45.0)/-6.5)}) \\
\bar{h} = \bar{j} &= 1.0/(1.0 + e^{((V_\mathrm{m}+76.1)/6.07)}) \\
\frac{dm}{dt} &= \frac{\bar{m}-m}{\tau_m} \\
\frac{dh}{dt} &= \frac{\bar{h}-h}{\tau_h} \\
\frac{dj}{dt} &= \frac{\bar{j}-j}{\tau_j} \\
\tau_m &= \frac{1.36}{\frac{0.32(V_\mathrm{m}+47.13)}{1.0-e^{-0.1(V_\mathrm{m}+47.13)}} + 0.08e^{V_\mathrm{m}/11}}
\end{aligned}$$

If $V_m \geq$ -40 mV

$$\begin{aligned}
\tau_h &= 0.4537(1.0 + e^{(V_\mathrm{m}+10.66)/11.1}) \\
\tau_j &= \frac{11.63(1.0 + e^{-0.1(V_\mathrm{m}+32.0)})}{e^{-2.535\times10^{-7}V_\mathrm{m}}}
\end{aligned}$$

Else if $V_m <$ -40 mV

$$\begin{aligned}
\tau_h &= \frac{3.49}{0.135e^{(V_\mathrm{m}+80.0)/6.8} + 3.56e^{0.079V_\mathrm{m}} + 3.1\times10^5 e^{0.35V_\mathrm{m}}} \\
\tau_j &= \frac{3.49}{\left[\frac{V_\mathrm{m}+37.78}{1.0+e^{0.311(V_\mathrm{m}+79.23)}}(-127140e^{0.2444V_\mathrm{m}} - 3.474\times10^{-5}e^{-0.04391V_\mathrm{m}}) + \frac{0.1212e^{-0.01052V_\mathrm{m}}}{1.0+e^{-0.1378(V_\mathrm{m}+40.14)}}\right]}
\end{aligned}$$

with m being the activation and h and j the I_Na inactivation gates.

4.2.2.2 $\mathbf{Ca^{2+}}$-independent transient outward $\mathbf{K^+}$ current; $\boldsymbol{I_\mathrm{to}}$

The Ca^{2+}-independent transient outward K^+ current, I_to, takes the form:

$$I_\mathrm{to} = g_\mathrm{to}.r(as + bs_\mathrm{slow})(V_\mathrm{m} - E_\mathrm{K}) \tag{4.90}$$

where

$$
\begin{aligned}
\bar{r} &= \frac{1}{1+e^{(V_\mathrm{m}+10.6)/-11.42}} \\
\bar{s} = \bar{s}_\mathrm{slow} &= \frac{1}{1+e^{(V_\mathrm{m}+45.3)/6.8841}} \\
\frac{dr}{dt} &= \frac{\bar{r}-r}{\tau_r} \\
\frac{ds}{dt} &= \frac{\bar{s}-s}{\tau_s} \\
\frac{ds_\mathrm{slow}}{dt} &= \frac{\bar{s}_\mathrm{slow}-s_\mathrm{slow}}{\tau_{s_\mathrm{slow}}} \\
\tau_r &= \frac{100.0}{45.16e^{0.03577(V_\mathrm{m}+50.0)}+98.9e^{-0.1(V_\mathrm{m}+38.0)}} \\
\tau_s &= 20e^{\left(-(V_\mathrm{m}+75.0)/25.0\right)^2}+35.0 \\
\tau_{s_\mathrm{slow}} &= 1300e^{\left(-(V_\mathrm{m}+70.0)/30.0\right)^2}+35.0 \\
a &= 0.883 \\
b &= 0.117
\end{aligned}
$$

with r being the activation and s and s_slow the I_to inactivation gates, and a and b being fractional contributions of the normal and slow gates to inactivation, respectively.

4.2.2.3 Steady-state outward K$^+$ current; I_ss

The steady-state outward K$^+$ current, I_ss, takes the form:

$$I_\mathrm{ss} = g_\mathrm{ss}.r_\mathrm{ss}.s_\mathrm{ss}(V_\mathrm{m}-E_\mathrm{K}) \tag{4.91}$$

where

$$
\begin{aligned}
\bar{r}_{\mathrm{ss}} &= \frac{1}{1+e^{(V_{\mathrm{m}}+11.5)/-11.82}} \\
\bar{s}_{\mathrm{ss}} &= \frac{1}{1+e^{(V_{\mathrm{m}}+87.5)/10.3}} \\
\frac{dr_{\mathrm{ss}}}{dt} &= \frac{\bar{r}_{\mathrm{ss}}-r_{\mathrm{ss}}}{\tau_{r\mathrm{ss}}} \\
\frac{ds_{\mathrm{ss}}}{dt} &= \frac{\bar{s}_{\mathrm{ss}}-s_{\mathrm{ss}}}{\tau_{s\mathrm{ss}}} \\
\tau_{r\mathrm{ss}} &= \frac{10000.0}{45.16e^{0.03577(V_{\mathrm{m}}+50.0)}+98.9e^{-0.1(V_{\mathrm{m}}+38.0)}} \\
\tau_{s\mathrm{ss}} &= 2100
\end{aligned}
$$

with r_{ss} being the activation and s_{ss} being the inactivation gate for I_{ss}.

4.2.2.4 Inward rectifier K$^+$ current; I_{K1}

The inward rectifier K$^+$ current, I_{K1}, takes the form:

$$
\begin{aligned}
I_{\mathrm{K1}} = & \left[\frac{0.048}{\left(e^{(V_{\mathrm{m}}+37.0)/25.0}+e^{(V_{\mathrm{m}}+37.0)/25.0}\right)}+0.01\right] \\
& \cdot\left[\frac{0.001}{1+e^{(V_{\mathrm{m}}-E_{\mathrm{K}}-76.77)/-17.0}}\right] \\
& +\frac{g_{\mathrm{K1}}(V_{\mathrm{m}}-E_{\mathrm{K}}-1.73)}{\left(1+e^{1.613F((V_{\mathrm{m}}-E_{\mathrm{K}}-1.73)/RT)}\right).\left(1+e^{[K^+]_o-0.9988/-0.124}\right)}
\end{aligned}
$$

4.2.2.5 Hyperpolarisation-activated current; I_{f}

The hyperpolarisation-activated current, I_{f}, carries K$^+$ and Na$^+$ ions, and takes the form:

$$
I_{\mathrm{f}} = g_{\mathrm{f}}y[f_{\mathrm{Na}}(V_{\mathrm{m}}-E_{\mathrm{Na}})+f_{\mathrm{K}}(V_{\mathrm{m}}-E_{\mathrm{K}})] \tag{4.92}
$$

where

$$\begin{aligned}
y_\infty &= \frac{1}{1+e^{(V_\mathrm{m}+138.6)/10.48}} \\
\frac{dy}{dt} &= \frac{f_\infty - y}{\tau_y} \\
\tau_y &= \frac{1000}{(0.11885e^{(V_\mathrm{m}+80.0)/28.37}+0.5623e^{(V_\mathrm{m}+80.0)/-14.19})} \\
f_\mathrm{Na} &= 0.2 \\
f_\mathrm{K} &= 1 - f_\mathrm{Na}
\end{aligned}$$

with y being the I_f activation gate and $f_\mathrm{Na,K}$ being the fractional contributions of the Na$^+$ and K$^+$ components of I_f, respectively.

4.2.2.6 Na$^+$-K$^+$ pump current, I_NaK

The Na$^+$-K$^+$ pump current, I_NaK, takes the form of Lewalle *et al.* [214], directly parameterised from rat data at 37$^\mathrm{o}$C:

$$I_\mathrm{NaK} = I_{\mathrm{NaK}_\mathrm{max}} \cdot \frac{\gamma+1}{v_1} \tag{4.93}$$

where $\gamma = 3.6$ is a constant, and

$$v_1 = \left(1+\frac{K_\mathrm{dNaio}}{[\mathrm{Na}^+]_\mathrm{i}}\right)^2 \left(1+\frac{K_\mathrm{dNais}}{[\mathrm{Na}^+]_\mathrm{i}} e^{(\frac{-\delta FVT}{1000R})} + \left(1+\frac{\alpha}{[\mathrm{K}^+]_\mathrm{o}}\right)^2 \left(1+\frac{[\mathrm{Na}^+]_\mathrm{o}}{K_\mathrm{dNaes}} e^{(-\frac{(1-\delta)FVT}{1000R})}\right)\right)$$

in which $\alpha = 1.8$ mM is a constant, $K_\mathrm{dNaio} = 19$ mM and $K_\mathrm{dNais} = 22$ mM are intracellular and $K_\mathrm{dNaes} = 880$ mM extracellular dissociation constants, and $\delta = 0.3$ is a constant specifying the strength of I_NaK voltage-dependence.

4.2.2.7 Background currents; I_Nab and I_Kb

The background currents for Na$^+$ and K$^+$, I_Na and I_K, take the form:

$$I_\mathrm{Nab} = g_\mathrm{Nab}(V_\mathrm{m} - E_\mathrm{Na}) \tag{4.94}$$

$$I_\mathrm{Kb} = g_\mathrm{Kb}(V_\mathrm{m} - E_\mathrm{K}). \tag{4.95}$$

4.2.3 Parameterisation

The SC model is a combination of components from two existing models, which have already undergone parameterisation and validation against experimental data. However, to ensure close reproduction of action potential and Ca^{2+} handling characteristics of those observed experimentally, small adjustments were made to certain parameters. These adjustments are summarised in Table 4.7.

Table 4.7. Updated parameters in the SC model.

Parameter	Description	New value
v_{NSR}	NSR volume per CRU	0.1 μm^3
$\tau_{M,1}$	Time constant of monomer binding	5 ms
$\tau_{Mi,1}$	Time constant of monomer inactivation	5 ms
$\tau_{M,2}$	Time constant of monomer unbinding	1 ms
$\tau_{Mi,2}$	Time constant of monomer de-inactivation	1 ms
g_{up}	Max flux rate of J_{up}	0.29481 $\mu M.ms^{-1}$
g_{leak}	Max flux rate of J_{leak}	$1.284228 x 10^{-5}$ ms^{-1}
k_{d2d3}	Rate constant for $d_2 - d_3$ transition	0.15 ms^{-1}

Time constants for RyR monomer binding, unbinding, inactivation and de-inactivation were all reduced to allow quicker recovery of the RyR at faster pacing frequencies associated with rat ventricular myocytes, up to 10 Hz. The rate constant for $d_2 - d_3$ transition was similarly decreased to 0.15 ms^{-1}. The conductance of the SR Ca^{2+} leak current was reduced, so as prevent excessive leak of SR Ca^{2+} and maintain a steady SR concentration. The maximal flux rate of J_{up} was reduced to 0.29481 $\mu M.ms^{-1}$ to account for the smaller Ca^{2+} transient magnitudes observed in rat ventricular myocytes compared to larger mammalian myocytes. The NSR volume per CRU was increased to 0.1 μm^3 to better reproduce spatial Ca^{2+} dynamics. Full initial conditions are given in Table 4.8.

4.3 Results

For the following sections, the SC model was paced to steady-state at stated cycle lengths or pacing frequencies, and comparisons are made to the Pandit and Gattoni (6 Hz variant) models where appropriate, as well as to experimental data where possible.

Table 4.8. Initial conditions in the SC model.

Variable	Description	Initial value
V_{m}	Membrane potential	-83.61 mV
m	I_{Na} activation gate	0.0026
h	I_{Na} inactivation gate	0.77
j	I_{Na} inactivation gate	0.6
r	I_{to} activation gate	0.017
s	I_{to} inactivation gate	0.94
s_{slow}	I_{to} inactivation gate	0.29
d	I_{CaL} activation gate	2.17×10^{-6}
f_{11}	I_{CaL} inactivation gate (voltage-dependent)	0.99
f_{12}	I_{CaL} inactivation gate (voltage-dependent)	0.99
f_{Ca}	I_{CaL} inactivation gate (Ca^{2+}-dependent)	0.99
rss	I_{ss} activation gate	0.0022
sss	I_{ss} inactivation gate	0.26
y	I_{f} inactivation gate	0.0029
$[Ca^{2+}]_{\mathrm{ds}}$	Dyadic Ca^{2+} concentration	0.08 μM
$[Ca^{2+}]_{\mathrm{SS}}$	Subspace Ca^{2+} concentration	0.08 μM
$[Ca^{2+}]_{\mathrm{cyto}}$	Cytosolic Ca^{2+} concentration	0.08 μM
$[Ca^{2+}]_{\mathrm{NSR}}$	Network Ca^{2+} concentration	0.8 mM
$[Ca^{2+}]_{\mathrm{JSR}}$	Junctional Ca^{2+} concentration	0.8 mM
$csqn$	Free calmodulin concentration	0.74 mM
CA	Proportion of RyRs in closed activated state	1
$[TRPN^{\mathrm{L}}_{\mathrm{Ca}}]$	Ca^{2+} bound to low affinity troponin sites	0.018 mM
$[TRPN^{\mathrm{H}}_{\mathrm{Ca}}]$	Ca^{2+} bound to high affinity troponin sites	0.054 mM

4.3.1 Action potential characteristics

Steady-state action potentials in the SC model are compared to those from previous models at pacing frequencies of 1, 2 (Pandit and Gattoni models) and 6 Hz (Gattoni 6 Hz variant only) in Figure 4.4. For these 3 pacing frequencies, APD in the SC model is shorter than in previous models. At 1 Hz, APD in the SC model is 37.5 ms (compared to 70.2 and 68.2 ms in the Pandit and Gattoni models, respectively) and remains at 37.5 ms at 2 Hz (vs 89.4 and 53.3 ms), then increasing an to 40.89 ms at 6 Hz (vs 54.4 ms in the

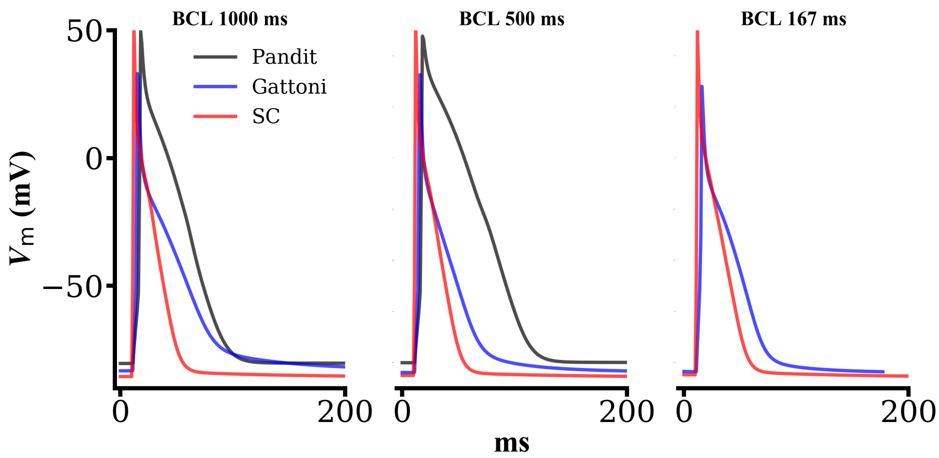

Figure 4.4. Comparison of action potentials in the Pandit, Gattoni and SC models at 1, 2 and 6 Hz. The SC model produces shorter APDs than the Pandit and Gattoni models at all tested pacing frequencies.

Gattoni 6 Hz variant model).

The SC model is able to simulate physiological APs after steady-state pacing at frequencies of up to 10 Hz. APD in the SC model does not change much between pacing frequencies of 1 Hz (37.5 ms) and 4 Hz (38.7 ms, Figure 4.5A), but then begins to prolong at faster pacing frequencies, to 43.9 ms at 8 Hz and 48.5 ms at 10 Hz (Figure 4.5B), observed similarly in experimental data from [35,159]. Such prolongation in APD with increases in pacing frequency is well-reported in the literature [24,133,265,361–363,428] for rat ventricular myocytes. These values and changes to other measures of APD are summarised in Table 4.9. Other measures of APD at different stages of repolarisation increase in similar fashion, staying relatively constant between frequencies of 1 and 4 Hz before increasing more substantially at frequencies above 6 Hz (Table 4.9). The SC model is also able to simulate APs at pacing frequencies from 10 to 12 Hz, although at these frequencies alternans is observed (discussed in Section 4.3.4).

Simulated APD_{90} values at different pacing frequencies fall within expected values based on experimental data from the literature: 37.5 ms at 1 Hz (vs 31±5 ms [290] and 46.3±8 ms [299]), 38.7 ms at 4 Hz (vs 44.7±7 ms [159]), 40.9 ms at 6 Hz (vs 39.1±8 ms [121] and 41.9±3 ms [159]), and 43.9 ms at 8 Hz (vs 40±3 [159], 46.3±14 [299]). There are negligible experimental data at faster pacing frequencies due to the difficulties pacing single myocytes at these faster rates, though generally APD is seen to prolong further [24, 133,361].

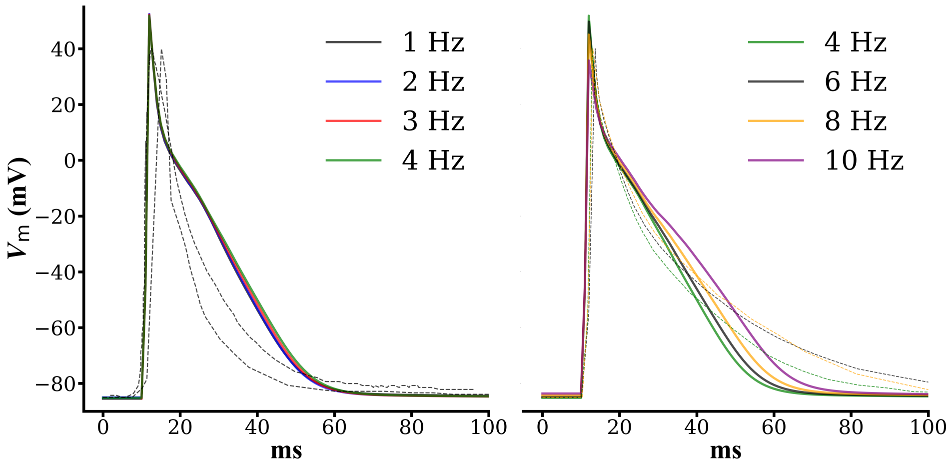

Figure 4.5. Action potentials in the SC model. A: APs at 1-4 Hz, for which APD stays relatively constant. B: APs at 4-10 Hz, for which APD prolongs as pacing frequency increases. The SC model continues to simulate physiological APs at frequencies up to 10 Hz, compared to the previously possible maximum of 6 Hz. Dashed lines show normalised experimental AP traces from [121, 290, 299].

Table 4.9. Changes to APD with pacing frequency in the SC model.

	Frequency (Hz)						
APD (ms)	1	2	3	4	6	8	10
APD_{30}	3.9	4.0	4.1	4.2	4.6	5.9	9.2
APD_{50}	14.9	15.1	15.2	15.4	16.2	17.9	22.4
APD_{70}	25.1	25.4	25.9	26.3	28.3	31.0	35.8
APD_{90}	37.5	37.5	38.1	38.7	40.9	43.9	46.5

The maximum AP upstroke rate (dV/dt_{max}) decreases as pacing frequency increases for the SC model, from 213.1 V.s^{-1} at 1 Hz to 128.8 V.s^{-1} at 10 Hz. This is matched by reductions in AP amplitude (V_{amp}) in the same manner, from 138.2 mV at 1 Hz to 119.9 mV at 10 Hz. This reduction in amplitude arises from an increasingly depolarised resting membrane potential (V_{min}) from -85.9 to -84.0 mV and a concomitant reduction in AP overshoot (V_{max}) from 52.3 to 35.9 mV as pacing frequencies increases from 1 to 10 Hz. Changes to these AP characteristics are summarised for all tested pacing frequencies in Table 4.10 and fall within expected experimental ranges [50, 92, 121, 146, 310].

Table 4.10. Changes to other AP characteristics with pacing frequency in the SC model.

	Frequency (Hz)						
Parameter	1	2	3	4	6	8	10
V_{min} (mV)	-85.9	-85.8	-85.7	-85.6	-85.2	-84.7	-84.0
V_{max} (mV)	52.3	52.4	52.4	52.0	49.8	45.2	35.9
V_{amp} (mV)	138.2	138.2	138.1	137.6	135.0	129.8	119.9
$\mathrm{d}V/\mathrm{d}t_{max}$ (V.s^{-1})	213.1	212.6	211.2	207.5	192.1	166.2	128.8

4.3.2 Membrane currents

In the following sections, membrane current changes in the SC model at pacing frequencies of 1, 2 and 6 Hz will be described, for direct comparison between the new and previous models (Pandit and Gattoni). Further membrane current changes at frequencies greater than 6 Hz are described in Chapter 6 as these underlie the prolongation of APD at faster pacing frequencies for rat ventricular myocytes.

4.3.2.1 Depolarising currents: I_{Na} and I_{CaL}

Changes to the main depolarising currents, I_{Na} and I_{CaL}, at different pacing frequencies are illustrated in Figure 4.6. In the Pandit and Gattoni models, peak I_{Na} remains similar at 1 and 2 Hz. However, there is a subsequent decrease in peak I_{Na} in the Gattoni model at 6 Hz, to -133.7 pA/pF. In the SC model, peak I_{Na} rises from -16.2 to -17.7 pA/pF from 1 to 2 Hz, then falls to -15.1 pA/pF at 6 Hz. These values are in line with those observed experimentally (-7.5 to -41.0 pA/pF in [4,50,84,213,306,332,334]), whereas the Pandit and Gattoni models are larger by an order of magnitude. In the Pandit model, I_{CaL} decreases from 1 to 2 Hz, however it remains relatively constant in the Gattoni models between frequencies of 1 to 6 Hz. In the SC model, I_{CaL} remains relatively constant at all tested frequencies (-11.0, -11.5 and -10.4 pA/pF at 1, 2 and 6 Hz, respectively), and these values fall within experimental ranges (-2.36 to -16.1 pA/pF in [12,121,223,416,451]).

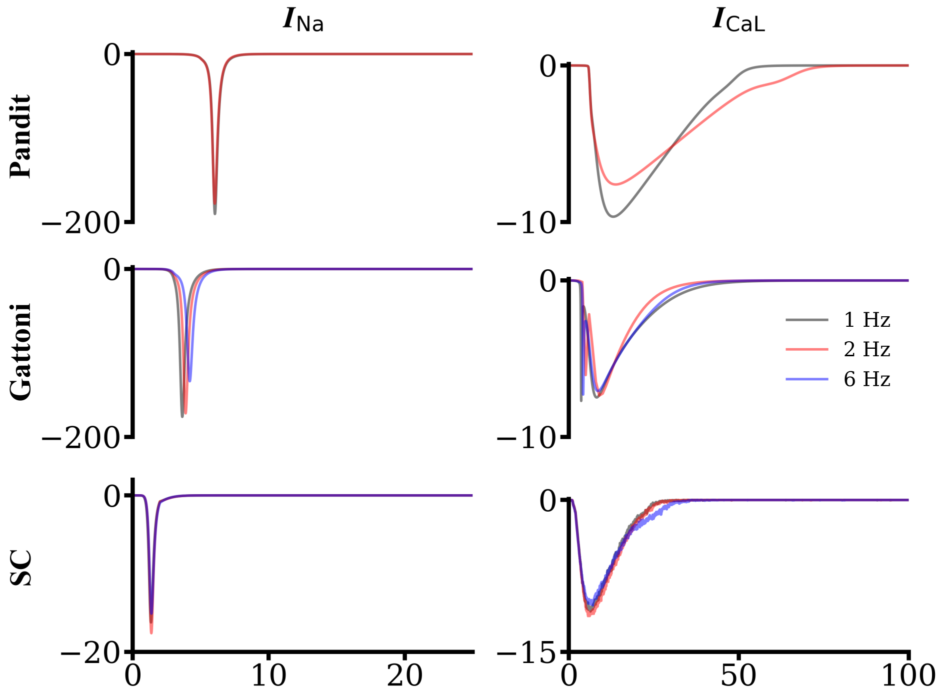

Figure 4.6. Depolarising membrane current changes with pacing frequency in the Pandit, Gattoni and SC models. Changes to I_{Na} and I_{CaL} are shown at pacing frequencies of 1, 2 and 6 Hz. Currents are in pA/pF.

4.3.2.2 Repolarising currents: I_{to}, I_{ss} and I_{K1}

In the Pandit and Gattoni models, peak I_{to} decreases as pacing frequency increases, and this pattern is followed in the SC model. Peak I_{to} decreases slightly from 25.72 to 25.21 pA/pF from 1 to 2 Hz, then further to 22.77 pA/pF at 6 Hz. I_{to} is larger in general in the SC model than previous models. Peak I_{ss} exhibits the same behaviour, decreasing slightly from 1.47 to 1.43 pA/pF from 1 to 2 Hz, then further to 1.1 pA/pF at 6 Hz, whereas I_{ss} is relatively rate-insensitive in the Pandit and Gattoni models. Peak I_{K1} in the SC model, unlike previous models, is also rate-insensitive, remaining at 1.85 pA/pF for all tested pacing frequencies and with little change to duration or activation/inactivation kinetics.

4.3.2.3 Other membrane currents: I_{f} and I_{b}

There is some debate surrounding the presence of the hyperpolarisation-activated current, I_{f}, in ventricular myocytes. I_{f} is abundantly expressed in foetal and neonatal ventricular

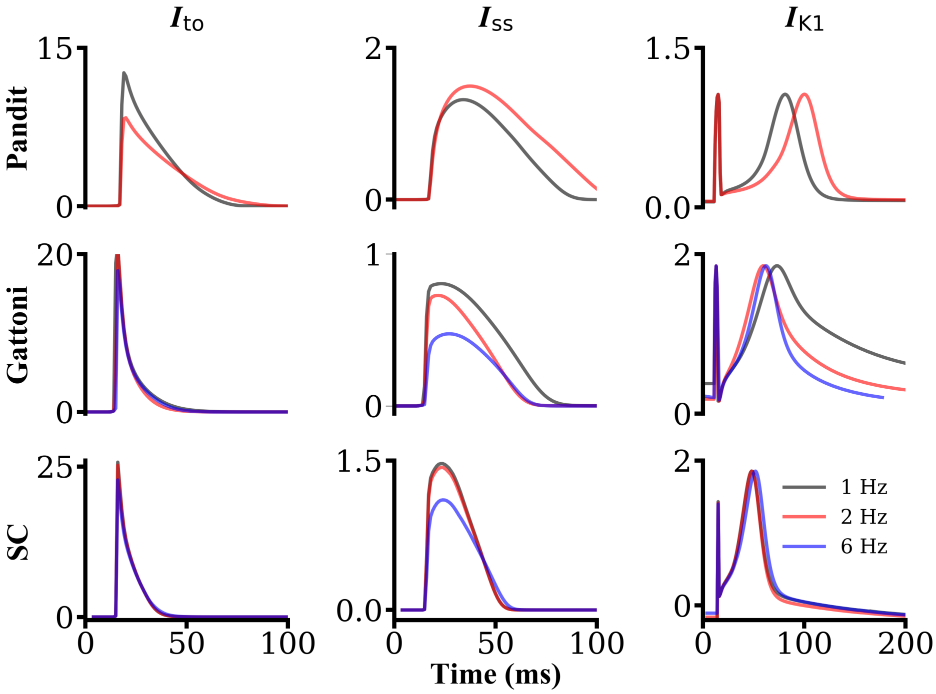

Figure 4.7. Repolarising membrane current changes with pacing frequency in the Pandit, Gattoni and SC models. Changes to I_{to}, I_{ss} and I_{K1} are shown at pacing frequencies of 1, 2 and 6 Hz. Currents are in pA/pF.

myocytes, but during electrophysiological maturation towards adulthood there is a progressive decrease in I_{f} expression [83, 327, 445]. Though primarily found in pacemaking cells of the heart, I_{f} has been identified in ventricular myocytes from animal models and humans [326, 374]. Nevertheless, in pathophysiological conditions such as cardiac hypertrophy and heart failure, I_{f} is commonly found to be upregulated in ventricular myocytes and may contribute towards arrhythmia development [80, 81, 373]. Accordingly, a formulation for I_{f} was included in the SC model, so as to allow for future investigation of its role in arrhythmogenesis.

Peak I_{f} in the Pandit and Gattoni models increases slightly as pacing frequency is increased from 1 to 2 Hz, though decreases slightly in the Gattoni model at 6 Hz. In the SC model, I_{f} decreases as pacing frequency is increased, from 9.7 to 8.9 to 6.0 fA/pF from 1 to 2 to 6 Hz. In the Pandit and Gattoni models, the background currents decrease in magnitude slightly as pacing frequency increase. However, peak I_{Nab} remains constant at -0.01 pA/pF for all tested pacing frequencies in the SC model, as does I_{Kb} at 0.19 pA/pF. Peak I_{Cab} remains constant at -0.06 pA/pF at 1 and 2 Hz, but decreases slightly to -0.05

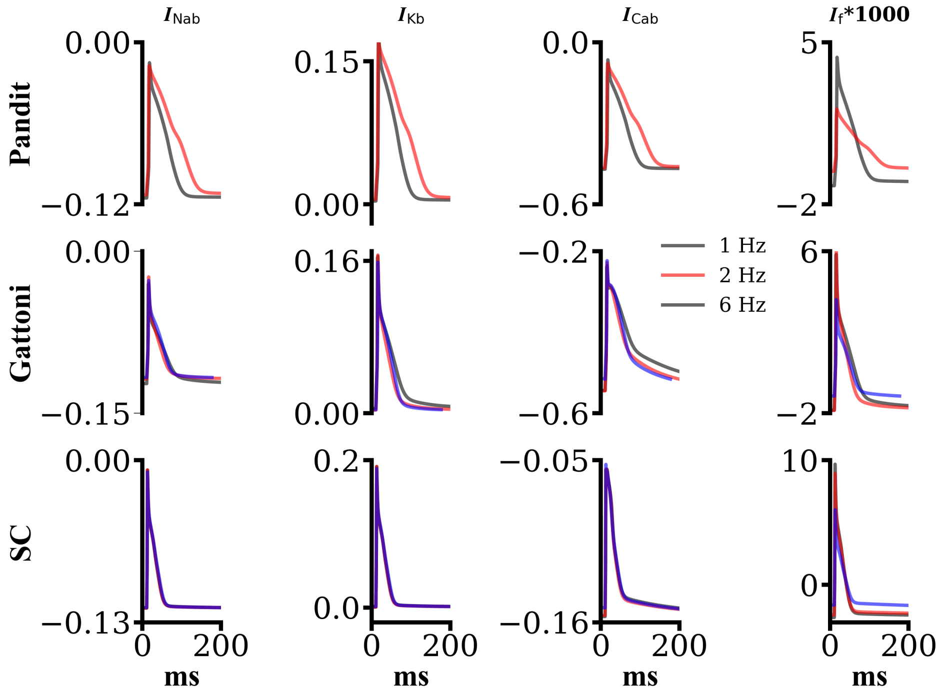

Figure 4.8. Changes to background currents and I_f with pacing frequency in the Pandit, Gattoni and SC models. Changes to the Na^+, I_{Nab}, K^+, I_{Kb}, and Ca^{2+}, I_{Cab}, and hyperpolarisation-activated, I_f, currents are shown for pacing frequencies of 1, 2 and 6 Hz. Currents are in pA/pF apart from I_f which is in fA/pF.

pA/pF at 6 Hz. These changes are shown in Figure 4.8.

4.3.3 Calcium handling and concentration changes

The diastolic Ca^{2+} concentration increases with pacing frequency in the SC model (Figure 4.9), a phenomenon observed experimentally (e.g. in [121, 340]). At 1 Hz, diastolic $[Ca^{2+}]_i$ is 69.7 nM (*vs* 68-120 nM [66, 121, 205, 340]), rising to 72.8 nM at 2 Hz (*vs* 76-157 nM [340, 397]), 86.9 nM at 3 Hz (*vs* 183-353 nM [144, 193, 240, 340]), 105.9 nM at 4 Hz (*vs* 133-190 nM [121]), 158.4 nM at 6 Hz (*vs* 156-245 nM [121]), 239.2 nM at 8 Hz (*vs* 179-295 nM [121]) and 357.7 nM at 10 Hz (no experimental data available). Systolic Ca^{2+} concentration, meanwhile, shows a biphasic response to increases in pacing frequency. From 1 to 2 Hz, systolic $[Ca^{2+}]_i$ falls from 683.3 (*vs* 268 nM to 3 μM [121, 146, 205]) to 644.5 nM (*vs* 257-774 nM [340, 397]), then further to 619.4 nM at 3 Hz (*vs* 389-467 nM [144, 193]). At faster pacing frequencies, however, systolic

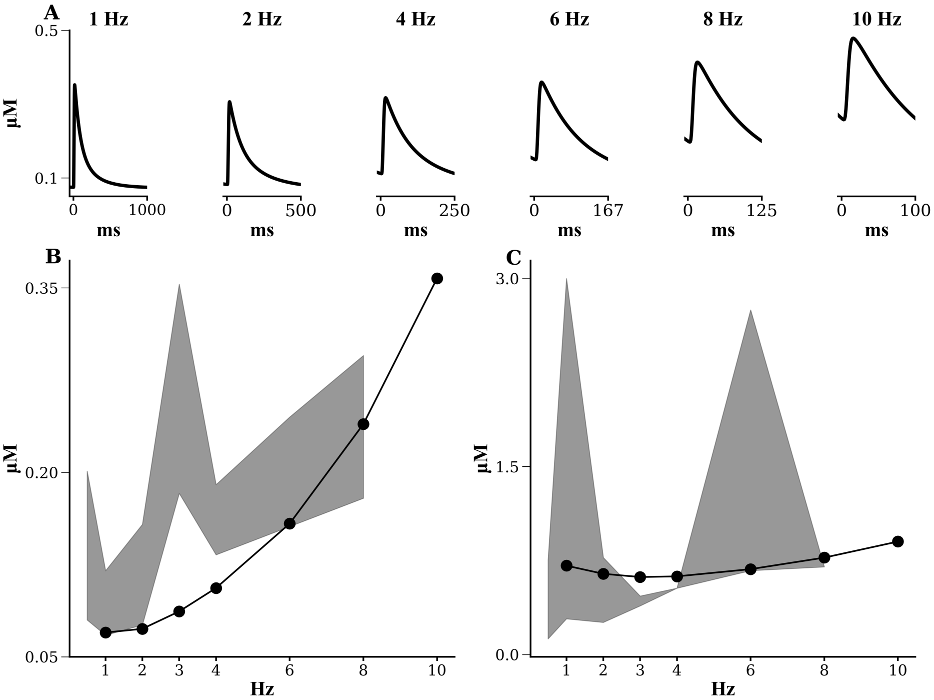

Figure 4.9. Ca^{2+} handling in the SC model. **A:** Representative simulated steady-state Ca^{2+} transients from 1 to 10 Hz. Elevation of diastolic Ca^{2+} concentration can clearly be seen at faster frequencies (shared y-axis). Frequency-dependence of diastolic (**B**) and systolic (**C**) Ca^{2+} concentrations also shown in the model (black) compared to experimental data ranges (shaded grey areas).

Ca^{2+} concentration then rises, to 626.3 nM at 4 Hz (*vs* 530 nM [121]), 684.2 nM at 6 Hz (*vs* 670 nM to 2.75 µM [121, 146]), 778.3 nM at 8 Hz (*vs* 700 nM [121]), and 908.8 nM at 10 Hz (no experimental data available). Thus, the model shows close agreement with experimental data across a range of pacing frequencies, though there are limited data available at the fastest frequencies (8-10 Hz). The Ca^{2+} transient magnitude-frequency response is biphasic, decreasing from 614 to 520 nM from 1 to 4 Hz, but then increasing to 551 nM at 10 Hz, which is in agreement with previously published data [146]. SR Ca^{2+} concentrations at tested pacing frequencies also fall within experimental ranges (0.147 to 170 µM [54, 89, 121, 144, 153, 251, 392, 396, 397, 418]). A comparison of simulated Ca^{2+} transients to those seen experimentally in [121] at frequencies of 4, 6 and 8 Hz is shown in Figure 4.10, and there is close agreement between simulated and experimental Ca^{2+} transients at physiological pacing frequencies (i.e. over 6 Hz).

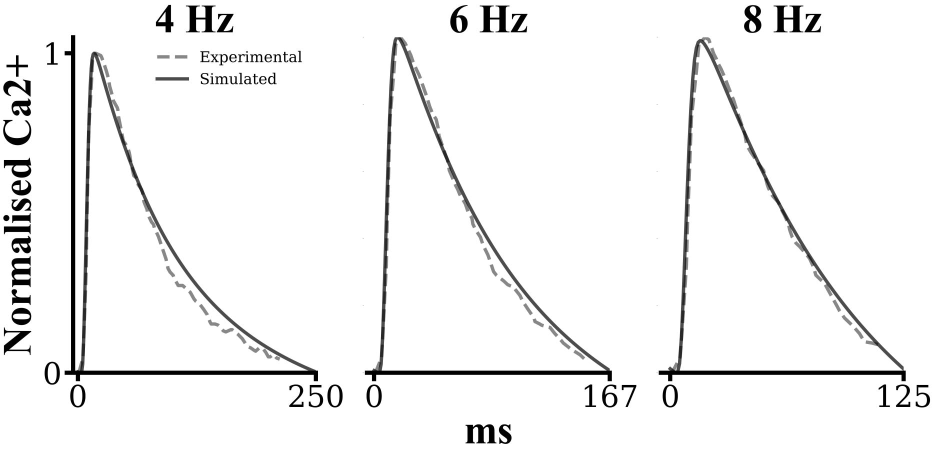

Figure 4.10. Comparison of simulated and experimental Ca^{2+} transients. Normalised Ca^{2+} transients are shown at frequencies of 4, 6 and 8 Hz for the SC model and from [121].

4.3.4 Alternans

Alternans refers to the condition in which cardiac electrical activity and/or contractile strength undergo beat-to-beat oscillations [314]. It is now well established that cardiac alternans is associated with increased risk for arrhythmias and sudden cardiac death, across many pathophysiological conditions [17, 51, 123, 128, 366]. Ca^{2+} alternans can occur when SR reuptake is impaired, meaning the SR has insufficient time to completely refill following an AP. The subsequent release of SR Ca^{2+} will therefore be smaller, resulting in a smaller Ca^{2+} transient and a shorter APD. This, however, results in a longer time for recovery (i.e. a longer DI) and the next release will again be larger. Calcium alternans are therefore more likely to occur at shorter cycle lengths where SR filling time is compromised.

In the SC model, AP and Ca^{2+} alternans manifest spontaneously at fast pacing frequencies above 10 Hz, resulting in oscillating long-short APDs and Ca^{2+} transient magnitudes. Figure 4.11 shows V_m, $[Ca^{2+}]_i$ and 6 principal membrane currents for the SC model after steady-state pacing at a frequency of 12 Hz. I_{Na}, I_{CaL}, I_{to} and I_{ss} exhibit more pronounced alternation between the long and short beats, although I_{NaCa} is also affected as a result of the alternating Ca^{2+} transient magnitude. I_{K1} is largely unaffected during alternans. Changes to APD, Ca^{2+} transient magnitude and the aforementioned membrane currents are summarised in Table 4.11.

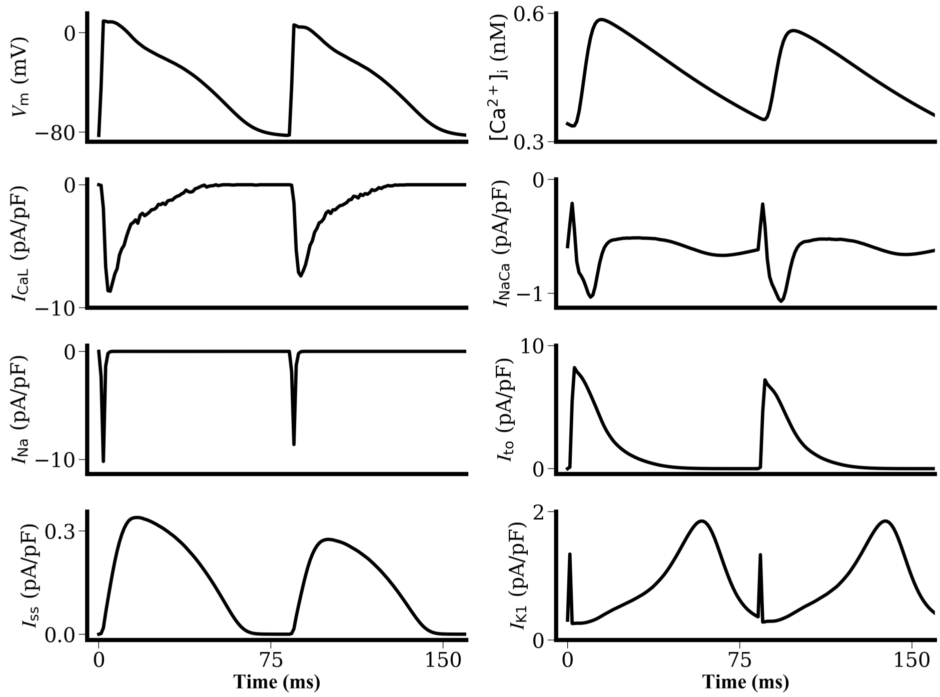

Figure 4.11. Currents during alternans in the SC model. Data are shown for the penultimate and final beat after steady-state pacing at a frequency of 12 Hz.

Table 4.11. AP, Ca^{2+} transient and membrane current changes during alternans in the SC model.

Parameter	Penultimate beat	Final beat
APD_{90} (ms)	63.3	61.4
Peak systolic Ca^{2+} (nM)	0.585	0.560
Peak I_{CaL} (pA/pF)	-8.65	-7.41
Peak I_{NaCa} (pA/pF)	-1.03 (min), -0.21 (max)	-1.07 (min), -0.22 (max)
Peak I_{Na} (pA/pF)	-10.2	-8.6
Peak I_{to} (pA/pF)	8.21	7.21
Peak I_{ss} (pA/pF)	0.34	0.28
Peak I_{K1} (pA/pF)	1.85	1.85

4.3.5 APD restitution

For this section, the deterministic 0D variant of the Colman model was used, to drastically reduce computation time over the long pacing periods required to generate an APD restitution curve. The 0D model is identical to a single CRU of the spatial 3D model, and of the same form as the majority of cell electrophysiology models that use the Hodgkin-Huxley formalism. The 0D model comprises the same components as for the spatial 3D model for one CRU, with the LTCC dynamics solved by the forward-Euler method. However, deterministic solutions for the RyR model do not properly capture dynamics of CICR. Accordingly, the dyadic Ca^{2+} concentration (seen by RyRs) was solved to be dependent only on I_{CaL}, to provide more continuous RyR opening behaviour, and k_{a} (the RyR activation rate constant) was increased to $2.37\mathrm{x}10^{-3}$ $\mu M^{-2.5}ms^{-1}$. Accordingly, the open transition rate in the 0D model is:

$$\alpha_{C-O} = k_{\mathrm{a}} \left({}^{m}[\mathrm{Ca}^{2+}]_{\mathrm{ss}} + \tau_{\mathrm{ds}} . {}^{m}J_{\mathrm{CaL}} \right)^{H} . \tag{4.96}$$

Simulated restitution curves from the Gattoni (6 Hz) variant and SC models are compared to that determined experimentally from [34] in Figure 4.12. For this S1-S2 restitution protocol, APD was determined following perturbation of steady-state pacing with S2 intervals from 200 to 40 ms. Experimentally, APD decreased as the S2 interval shortened from 42.0 (S2 = 200 ms) to 30.3 ms (S2 = 400 ms). In the Gattoni model, which was unable to simulate APs at S2 intervals shorter than 160 ms, APD instead increased from 50.1 to 59.3 ms, in contrast to the experimental data. In the SC model, APD remains slowly increases as the S2 interval is decreased from 200 (37.2 ms) to 80 ms (37.9 ms), however APD then increases more steeply towards S2 = 50 ms (41.2 ms) before decreasing slightly at S2 = 40 ms (40.2 ms). Unlike the Gattoni model, in which APD is much longer than the experimental data, the SC model more closely reproduces experimentally-observed APD values.

In Figure 4.13, restitution curves from the Gattoni and SC models are compared to that determined experimentally in [159], in which APD was determined after steady-state pacing at frequencies from 1 to 9 Hz. Experimentally, APD remained constant between frequncies of 1 and 5 Hz (43.0 ms), then decreased from 5 to 9 Hz (at which APD = 38.5 ms). For the Gattoni model, APD decreases from 69.7 to 48.6 ms from 1 to 4 Hz, then prolongs to 54.4 ms at 6 Hz. In the SC model, similarly to the experimental data, APD remains relatively constant between pacing frequencies of 1 and 5 Hz (though is shorter than in the experiments at 37.6 ms), however it then prolongs to 9 Hz at which APD = 41.4 ms.

Figure 4.14 shows a comparison of restitution curves produced by the SC, Gattoni (1 Hz variant) and Pandit models alongside experimental data from [24]. For this protocol, models were paced to steady-state at 1 Hz, following which a solitary S2 stimulus was applied

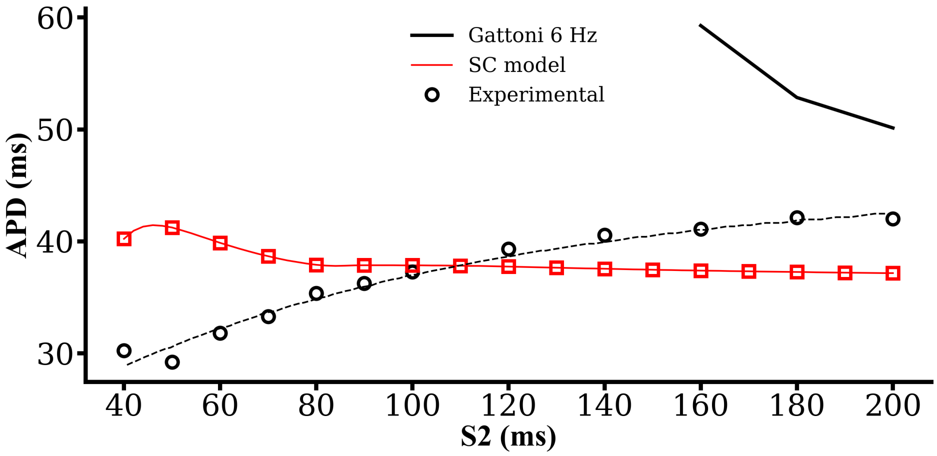

Figure 4.12. Comparison of Gattoni and SC model restitution curves to data from [34]. APD decreases with S2 interval experimentally (unfilled circles, dashed trendline). In the Gattoni model (solid line), APD increases between S2 intervals of 200 and 160 ms, but the model is unable to simulate APs at shorter intervals. In the SC model (unfilled red squares, dashed line shows shorter S2 decrements), the restitution curve appears triphasic as APD increases slowly with shorter S2 intervals, then more steeply until S2 = 50 ms, when APD then decreases.

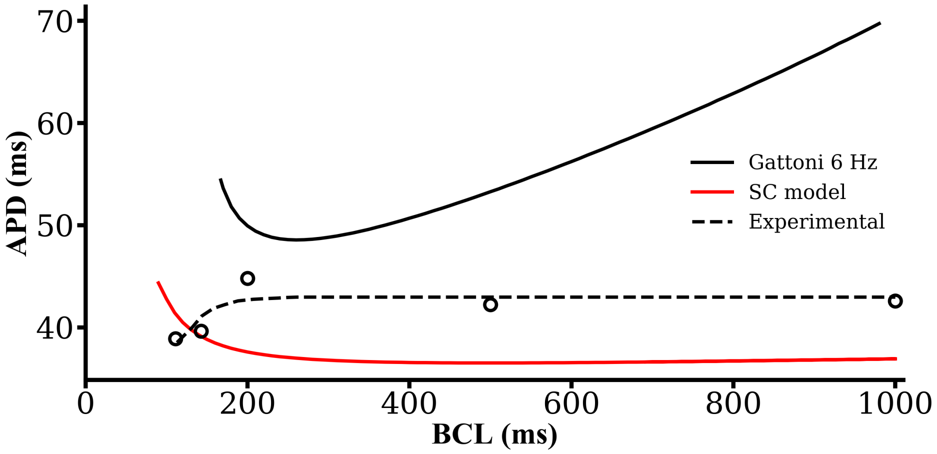

Figure 4.13. Comparison of model restitution curves to data from [159]. APD remains relatively constant experimentally (unfilled circles, dashed trendline) between pacing frequencies of 1 and 5 Hz, but then shortens as pacing frequency increases to 9 Hz. APD decreases towards 4 Hz then increases to 6 Hz in the Gattoni model (solid black line). In the SC model (red line), APD stays relatively constant between pacing frequencies of 1 and 5 Hz, then prolongs as pacing frequency increases to 9 Hz.

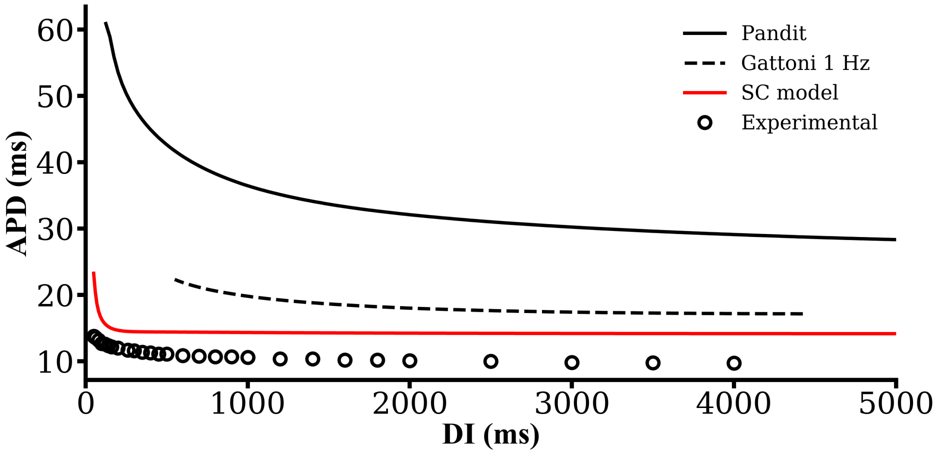

Figure 4.14. Comparison of SC, Gattoni (1 Hz) and Pandit model restitution curves to experimental data from [24]. APD_{50} gradually increases as the S2 interval shortens experimentally (unfilled cirlces), and in all models, but is more closely reproduced by the SC model (red line).

decreasing intervals from 5000 to 50 ms. As described in Chapter 3, the Pandit and Gattoni (1 Hz variant) models produced similarly-shaped restitution curves to that observed experimentally, but for longer APDs (as APD_{50}) in general (particularly the Pandit model, where APD was at least 3-fold longer). However, the SC model reproduces the shape of the experimental restitution curve in this protocol for APDs closer to experimental data than in other models. The SC model, in addition, is capable of simulating APs for all S2 intervals used, which was not possible in previous models.

In Figure 4.15, restitution curves from the Pandit, Gattoni (1 Hz) and SC models are compared to that determined experimentally in [265]. As per the experimental protocol, models were paced to steady-state at a frequency of 1 Hz prior to perturbation with an extra S2 stimulus at progressively decreasing intervals from 4000 to 0 ms. Experimentally, APD_{50} slowly increased between S2 intervals of 4000 and 500 ms, however shorter intervals resulted in a steeper increase in APD_{50} until S2 = 50 ms, at which point APD decreased (the shortest and longest APD_{50} values experimentally, however, only differed by 1.7 ms). As shown previously, the Pandit and Gattoni (1 Hz) models produce a similar-shape restitution curve, albeit at longer APDs overall, and the steeper increase at shorter S2 intervals is also reproduced. However, these models were unable to simulate APs at shorter APs, during which there appears to be a subsequent shortening of APD_{50} experimentally. The SC model reproduces this abbreviation of APD_{50} at the shorter S2

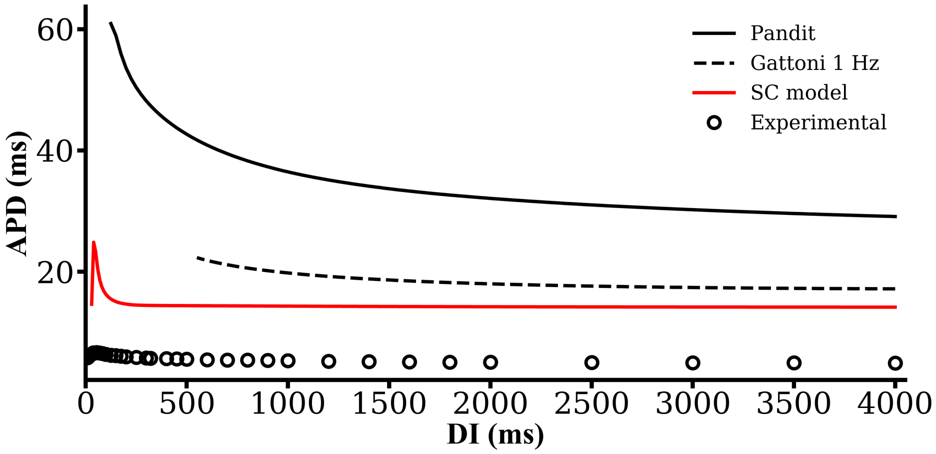

Figure 4.15. Comparison of SC, Gattoni (1 Hz) and Pandit model restitution curves to experimental data from [265]. APD_{50} shows a biphasic response with changes in S2 interval, prolonging between S2 intervals of 4000 and 50 ms before shortening from 50 to 0 ms. Previous models reproduce the shape of the restitution curve at longer S2 intervals but with longer APDs overall, and are unable to simulate APs at S2 intervals below 50 ms. The SC model reproduces the experimental restitution curve shape more closely, and captures the reduction in APD_{50} at the shortest S2 intervals.

intervals, and more closely reproduces the experimental restitution curve shape and APD values than previous models.

4.4 Conclusions

A novel model of rat ventricular electrophysiology and Ca^{2+} handling has been developed, which reproduces an array of action potential and Ca^{2+} handling characteristics based on isolated myocyte experimental data obtained from numerous sources in the literature. The model couples a biophysically-detailed electrophysiology model with a stochastic, spatio-temporal Ca^{2+} cycling model and reproduces action potential morphology, APD restitution curves and Ca^{2+} transients observed experimentally, at pacing frequencies up to 10 Hz. In addition, the model is capable of simulating Ca^{2+} transient and APD alternans at faster frequencies up to 12 Hz, which are pro-arrhythmic phenomena.

Previous computational models of the rat ventricular myocyte have implemented simplified, deterministic descriptions of the L-type Ca^{2+} channel and RyR, which do not capture many of the inherently spontaneous characteristics of Ca^{2+} handling observed experimentally. The poor recapitulation of experimental restitution curves by previous models (Chapter 3) is particularly noticeable at pacing frequencies corresponding to physiological heart rates for rat (greater than 400 bpm, i.e. above 6.5 Hz [34, 35, 331, 415]), at which these models are unable to simulate APs. Through inclusion of stochastic descriptions of the L-type Ca^{2+} channel and RyR, the SC model is capable of simulating APs and Ca^{2+} transients at these faster rates, which implies a role for the processes regulating Ca^{2+} homeostasis in the inverse rate-dependence of APD. By reproducing APs at up to 10 Hz (or 12 Hz, with the onset of alternans, as in Figure 4.11), the SC model is also suitable for studying processes that may underlie ventricular tachycardia, which has been reported at rates from 10 to 14 Hz for rats in the literature [207, 423, 430]. As such, the SC model more closely reproduces experimental restitution curves (Figures 4.12 to 4.15), and is suitable for investigating the mechanisms underlying the inverse rate-dependence of APD. Furthermore, the underlying stochastic dynamics for Ca^{2+} cycling in the model provide a platform for the investigation of arrhythmogenic mechanisms, as many pro-arrhythmic phenomena arise from abnormal spontaneous Ca^{2+} release events, such as EADs and DADs.

The development of a new computational model incorporating rat-specific electrophysiology and stochastic Ca^{2+} handling dynamics permits the investigation of pro-arrhythmic phenomena (Chapter 5), and the exploration of mechanisms underlying the inverse rate-dependence of the rat ventricular APD, which prolongs at short cycle lengths in contrast to other mammalian species (Chapter 6).

Chapter 5

I_{K1} Remodelling and Spontaneous Ca^{2+} Release Events

5.1 Introduction

Over 500,000 people in the UK are currently living with heart failure, and of these patients up to 50% are likely to die from sudden cardiac death, likely as a result of lethal ventricular arrhythimias such as ventricular fibrillation [349, 391]. These arrhythmias are largely driven by rapid, chaotic electrical activation of the ventricles, leading to fatally-compromised filling and pumping of blood [424]. Such abnormal excitation patterns arise from electrophysiological remodelling, where changes to the characteristics, kinetics and expression of the many ion channels involved in the cardiac action potential occur which result in deviations from the normal, coordinated process of excitation-contraction coupling. Multiple studies have identified remodelling, in the form of changes to peak current density or expression (which may be increased, or decreased) in I_{Na} [179, 183, 241, 404], I_{to} [45, 192], $I_{\mathrm{Kur,Kr,Ks}}$ [44, 401, 402], I_{K1} [186, 216, 226], I_{CaL} [194,200,292,303], I_{NaCa} [118,318,376], and many others (including ATP-sensitive K^{+} channels [403] and stretch-activated channels [325, 425]).

Of these ion channels known to be remodelled in heart failure, the inward rectifier current, I_{K1}, has a significant role in stabilising the resting membrane potential in ventricular myocytes, close to the equilibrium potential for K^+ [230]. During the late phase of the cardiac action potential, I_{K1} also transiently carries outward current, and plays a major role in membrane potential repolarisation [230, 249]. During hyperpolarisation I_{K1} conductance increases, and decreases during depolarisation. I_{K1} passes less outward current than inward, a property referred to as 'inward rectification'. Inward rectification is attributed to depolarisation-induced blockade of the channels by polyamines and intracellular cations, such as Mg^{2+} and Ca^{2+} [119]. Decreases in I_{K1} and alterations to resting membrane potential have been reported in a number of animal models and in human cells from heart failure patients [34, 44, 139, 192, 216, 227, 267]. However, heart failure is also characterised by significant remodelling of the intracellular Ca^{2+} handling system, and abnormal Ca^{2+} cycling contributes to both mechanical and electrical dysfunction, the latter of which promotes arrhythmogenesis [305]. Further complicating matters, there are bi-directional interactions between I_{K1} and Ca^{2+} handling remodelling in heart failure, as Ca^{2+}-dependent reductions in I_{K1} have been reported [134], and various features of heart failure can potentially be attributed to I_{K1} downregulation (e.g. prolonged APD and increased propensity for DADs) [225, 379].

Computational models provide a powerful tool for investigating such observations, as they negate the need for expensive knockdown/knockout models and experimental reagents. The aim of this chapter was to investigate the role of I_{K1} remodelling in pro-arrhythmic behaviour in single rat myocytes. As shown in Chapter 3, previous computational models of rat ventricular electrophysiology are unable to simulate reductions in various membrane currents in the ranges observed in the literature, as expression as low as 15% has been observed for some K^+ channels experimentally [34, 139]. Nevertheless, the deterministic implementations of Ca^{2+} handling components in these models does not permit the study of spontaneous Ca^{2+} release events, which underlie pro-arrhythmic activity [129, 130, 268, 412]. In this chapter, the SC model described in Chapter 4 is used to elucidate the link between I_{K1} channel remodelling and increased propensity for the emergence of spontaneous Ca^{2+} release events.

5.2 Methods

For this chapter, the SC model is used to explore the effects of I_{K1} downregulation. To do so, the parameter controlling maximum I_{K1} conductance, g_{K1}, was decreased by 50% in simulations. Such a reduction was chosen to; (a) reflect that observed experimentally in our laboratory for *KCNJ2* (Kir2.1, I_{K1}) mRNA expression (56-63% in [34, 139]), whilst (b) still allowing sufficient generation of repolarising I_{K1} to ensure resting membrane potential is still achieved, particularly at faster pacing frequencies where simulated I_{K1} shifts towards sustained outward current (as shown in Chapter 6).

Then, to illustrate the impacts of I_{K1} remodelling on the genesis of DADs and triggered activity (TA), rapid pacing protocols were applied to load the sarcoplasmic reticulum Ca^{2+} content, promoting spontaneous Ca^{2+} release events. In some simulations, a representative (but non-specific) model for isoprelaine-induced sympathetic modulation (ISO) was included, to enhance Ca^{2+}-induced Ca^{2+} release (CICR), the adjusted parameters for which are given in Table 5.1. Though the isoprenaline model is not biophysically-detailed nor representative of a specific regulated process, the parameter modifications outlined in Table 5.1 are informed from the experimentally-observed effects of isoprenaline in cardiac myocytes. These effects, principally, are increases in systolic and diastolic $[\mathrm{Ca}^{2+}]_i/[\mathrm{Ca}^{2+}]_{\mathrm{SR}}$ (hence increased Ca^{2+} influx through I_{CaL} and SR Ca^{2+} uptake via J_{up}), as well as shorter action potential durations (hence increased repolarising K$^+$ currents I_{to} and I_{ss}). Thus, the isoprenaline model facilitiates the induction of pro-arrhythmic behaviour not observed under control conditions.

Table 5.1. Scaling factors for the isoprenaline model.

Parameter	Description	Scaling factor	Reference
g_{CaL}	Maximum I_{CaL} conductance	1.5	[12, 121, 340, 341, 409, 451, 452]
g_{to}	Maximum I_{to} conductance	1.5	[121, 311]
g_{ss}	Maximum I_{ss} conductance	2	[121, 311, 351]
g_{up}	Maximum J_{up} flux rate	2	[121, 298]

5.2.1 Simulation protocols

Rapid pacing protocol. To study the genesis of triggered activity in single cell simulations, a rapid pacing protocol was applied to promote Ca^{2+} loading of the SR and the emergence of spontaneous Ca^{2+} release events (SCRE). The 3D model was paced to steady-state at various basic cycle lengths (BCL = 150-200 ms, chosen to encompass the range of rat heart rates reported in the literature, i.e. 300-450 bpm [34, 35, 331, 415, 451]); state variables were then saved at these steady-state values and used as initial conditions for the efficient running of multiple simulations of a short pacing period followed by a quiescent period (i.e. pacing was ceased). In this way, stochastic Ca^{2+} release events could be analysed for a range of simulations. Simulations were performed either for wild-type (WT, to distinguish from control pacing, i.e. without ISO) or heart failure (HF, including a 50% reduction in I_{K1} conductance, g_{K1}) conditions, with or without isoprenaline-induced (ISO) remodelling. The influence of Ca^{2+} diffusion rate from the subspace was also investigated.

Spontaneous release functions. The spontaneous release functions (SRF) describe whole-cell RyR dynamics associated with stochastic Ca^{2+} release events observed in the 3D cell model [97, 98, 100]. These functions are waveforms that approximate the range of morphologies for the time series of the whole-cell ratio of open to total RyRs ($N_{\mathrm{RyR\_O}}/N_{\mathrm{RyR}}$) as observed during stochastic Ca^{2+} release events, so that 0D model behaviour is in line with the 3D cell model.

The analytical formulations of the SRF, describing the variability in spontaneous release $N_{\mathrm{RyR\_O}}$ waveforms, were derived from a Ca^{2+} clamp ladder protocol across a range of SR Ca^{2+} values. For this protocol, at each step (2 s total duration), the intracellular and SR Ca^{2+} concentrations were initially clamped to specified values, with SR Ca^{2+} concentration gradually increasing over successive steps. Following the emergence of spontaneous Ca^{2+} release, the clamp constraint was removed to allow the Ca^{2+} concentrations to evolve dynamically; and the conductances of I_{Na} and I_{CaL} were set to zero to prevent excitation and CICR. This protocol illustrates the range of SCRE observed and their underlying spatio-temporal dynamics (Figure 5.1).

There are two $N_{\mathrm{RyR\_O}}$ waveform types observable in Figure 5.1; plateau-like, for long, small-amplitude release, and spike-like, for short, large-amplitude release. The spike-like

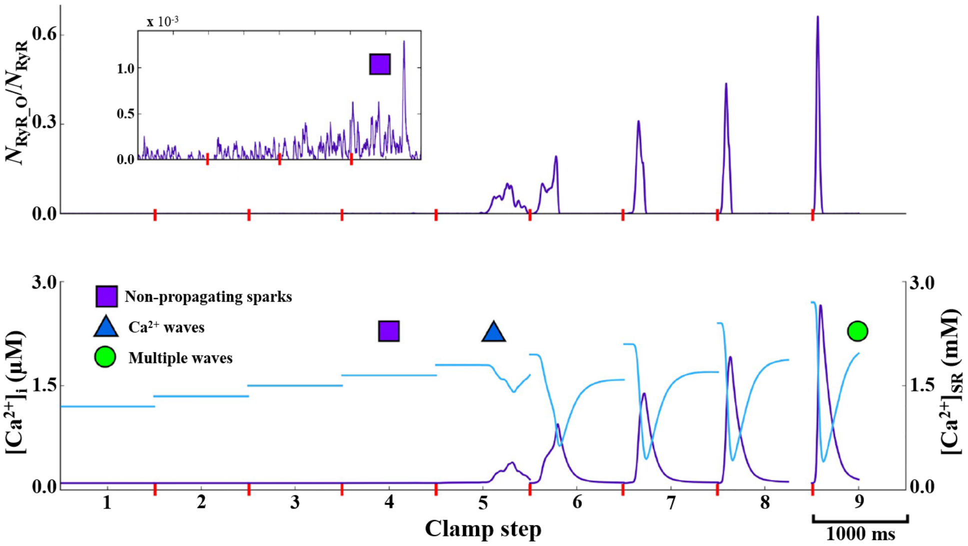

Figure 5.1. Ca^{2+} clamp protocol used to derive and validate SRF for the 0D model. Top: Proportion of open RyR in the 3D cell model. Bottom: Intracellular (purple) and SR (blue) Ca^{2+} concentrations. Results are shown for 9 steps of SR Ca^{2+} concentration (bottom, blue lines). Each clamp step duration was 1000 ms. Adapted from [97].

waveform can be well-approximated (Figure 5.2) with the function:

$$N_{\mathrm{RyR\_O}} = N^{\mathrm{peak}}_{\mathrm{RyR\_O}}\left[\left(1+e^{-(t-t_1)/k_1}\right)\left(1+e^{-(t-t_2)/k_2}\right)\right]^{-1} \tag{5.1}$$

$$t_1 = t_i + 0.5(t_p - t_i) \tag{5.2}$$

$$t_2 = t_p + 0.5(t_f - t_p) \tag{5.3}$$

$$k_1 = 0.1689(t_p - t_i) + 0.00255 \tag{5.4}$$

$$k_2 = 0.1689(t_f - t_p) + 0.00255 \tag{5.5}$$

where t_i is the SCRE initiation time, t_f is the end time (duration, $\lambda = t_f - t_i$), t_p is the time of the waveform peak, and $N^{\mathrm{peak}}_{\mathrm{RyR\_O}}$ is the open proportion RyR peak (Figure 5.2). Constants for Equations 5.4 and 5.5 were obtained from best fits to the observed waveforms.

For plateau-like waveforms (durations over 300 ms), the function is derived from the same parameters:

$$\begin{gathered} N_{\mathrm{RyR\_O}} = \\ N^{\mathrm{plateau}}_{\mathrm{RyR\_O}}\left[\left(1+e^{-(t-(t_i+17.5))/5.946}\right)\left(1+e^{t-(t_f-17.5))/5.946}\right)\right]^{-1} + \\ \left(N^{\mathrm{peak}}_{\mathrm{RyR\_O}} - N^{\mathrm{plateau}}_{\mathrm{RyR\_O}}\right)\left[\left(1+e^{-(t-(t_p-25))/5.946}\right)\left(1+e^{(t-(t_p+17.5))/5.946}\right)\right]^{-1} \end{gathered} \tag{5.6}$$

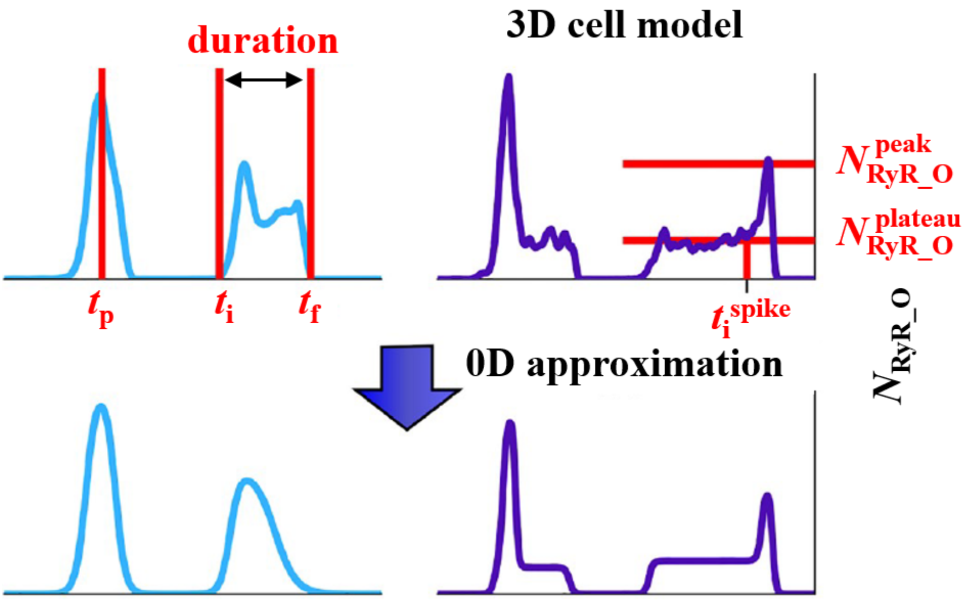

Figure 5.2. 0D approximation of the 3D $N_{\text{RyR\_O}}$ waveform. Examples of two $N_{\text{RyR\_O}}$ waveforms (top), and the SRF that approximate them (bottom). Parameters describing the waveforms are labelled: t_i (initiation time), t_p (peak time), t_f (final time), t_i^{spike} (spike initiation time during plateau), $N_{\text{RyR\_O}}^{\text{peak}}$ (peak open RyR), and $N_{\text{RyR}}^{\text{plateau}}$ (plateau open RyR).

where $N_{\text{RyR\_O}}^{\text{plateau}}$ is the plateau amplitude. Equation 5.6 assumes the same form for the spike occurring within the plateau, with an upstroke time of 50 ms and decay time of 35 ms. t_i^{spike} therefore corresponds to $t_p - 50$ (and its half maximal activation time, $t_p - 25$). Constants were similarly obtained from best fits to the observed waveforms.

The $N_{\text{RyR\_O}}$ waveform can therefore be completely described by four (for spike-like) or five (for plateau-like) parameters; (1) initiation time, t_i; (2) duration ($\lambda = t_f - t_i$); (3) peak time, t_p; and (4-5) amplitude ($N_{\text{RyR\_O}}^{\text{peak}}$; $N_{\text{RyR\_O}}^{\text{plateau}}$). The nature of stochastic variation of relevant parameters used for this section (t_i, λ) is described below (full SRF parameter descriptions and derivations can be found in the original paper and its supplement [97]).

(1) t_i: The probability density functions for inititation time associated with each SR Ca^{2+} value exhibit skewed distributions, however the cumulative frequency was well approximated by the use of two simple sigmoidal functions:

$$F(t_i) =$$

$$\left.\begin{aligned} F_1(t_i) &= (2CF_{t_{i,Sep}})(1+e^{-(t_i-t_{i,Sep})/k_{F_1}})^{-1} \\ F_2(t_i) &= (2(1-CF_{t_{i,Sep}}))(1+e^{-(t_i-t_{i,Sep})/k_{F_2}})^{-1}-1+2CF_{t_{i,Sep}} \end{aligned}\right\} \begin{aligned} t &< t_{i,Sep} \\ t &\geq t_{i,Sep} \end{aligned} \tag{5.7}$$

The t_i distribution is therefore determined by four parameters: $t_{i,Sep}$, the initiation time corresponding to the point at which the functions are separated; $CF_{ti,Sep}$, the cumulative frequency at this point ($CF_{ti,Sep} = F(t_i)|_{ti=ti,Sep})$), and k_{F1}, k_{F2}, the gradient parameters for each function (corresponding to the width of the distribution either side of $t_{i,Sep}$).

(2) λ: The duration distributions are also non-normal, but well-approximated by two sigmoidal functions describing CF for half of the data either side of the median duration, MD:

$$F(MD) = \left.\begin{aligned} F_{D1}(MD) &= (1+e^{-(\lambda-MD)/0.261DW_1})^{-1} \\ F_{D2}(MD) &= (1+e^{-(\lambda-MD)/0.261DW_2})^{-1} \end{aligned}\right\} \begin{aligned} \lambda &< MD \\ \lambda &\geq MD \end{aligned} \tag{5.8}$$

where the widths (DW_1, DW_2, in ms) are functions of MD:

$$DW_1 = A_{DW1}(1+e^{-(MD-a_{DW1})/k_{DW1}})^{-1} + DW_1^{\text{min}} \tag{5.9}$$

$$DW_2 = A_{DW2}(1+e^{-(MD-a_{DW2})/k_{DW2}})^{-1} + DW_2^{\text{min}} \tag{5.10}$$

The duration distribution is therefore completely desribed by MD, the median duration, and the above parameters.

5.3 Results

5.3.1 Effects of isoprenaline on APD and Ca^{2+} handling

Figure 5.3 shows the effects of isoprenaline on action potential and Ca^{2+} handling characteristics in the SC model. At BCL = 150 ms, APD decreases from 40.95 to 37.76 ms (WT vs WT+ISO), and from 38.72 to 36.07 ms at BCL = 200 ms. APD is seen to similarly shorten experimentally [121]. Diastolic Ca^{2+} concentrations are seen to increase experimentally under ISO conditions (e.g. by 21±3% in [340]), and this is reproduced in the model as diastolic [Ca^{2+}]$_\text{i}$ increases by 19% at BCL = 150 ms (56 vs 47 nM) and 21% at BCL = 200 ms (57 vs 47 nM).

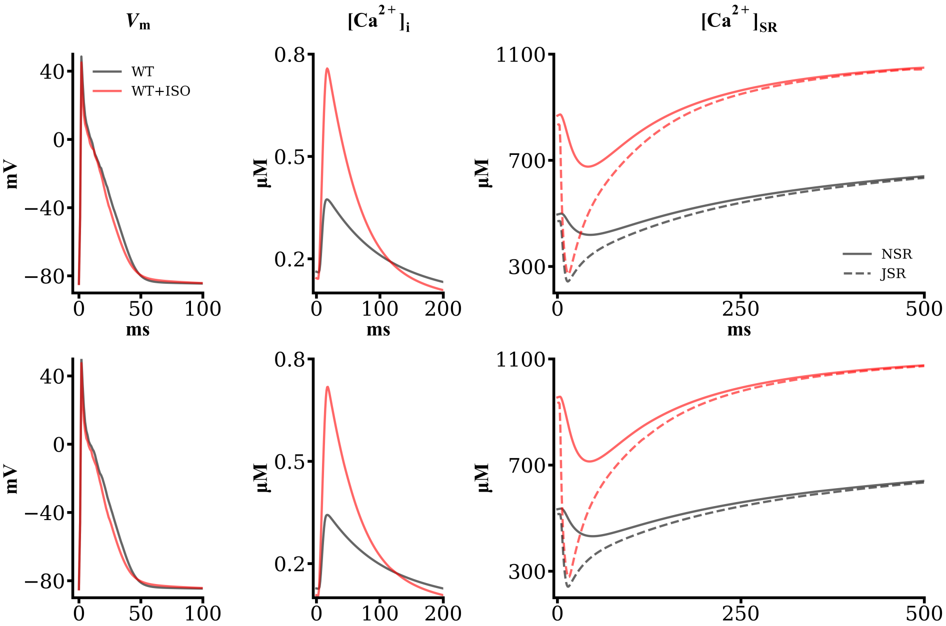

Figure 5.3. Simulated effects of ISO on AP and Ca^{2+} handling characteristics. Top: BCL 150 ms, Bottom: BCL 200 ms. ISO decreases APD at both cycle lengths (left), whilst increasing Ca^{2+} transient magnitude (middle) and SR Ca^{2+} concentrations (right) as observed experimentally. WT, wild-type (no remodelling); ISO, isoprenaline remodelling; NSR, network SR. One representative simulation per condition (WT, WT+ISO) shown.

Systolic Ca^{2+} concentrations also increase under ISO conditions in the model, from 379 to 657 nM at BCL = 150 ms, and from 342 to 719 nM at BCL = 200 ms, representing a 113% and 124% increase in Ca^{2+} transient magnitude, respectively. Increases in systolic Ca^{2+} concentration and the Ca^{2+} transient magnitude are also reported experimentally [121, 341]. At both cycle lengths, diastolic $[Ca^{2+}]_{SR}$ increases to around 1100 µM, close to the threshold for spontaneous Ca^{2+} release.

5.3.2 I_{K1} downregulation prolongs APD and promotes SR Ca^{2+} loading

Implementing a 50% reduction in I_{K1} conductance (HF) results in APD prolongation at both cycle lengths. For BCL = 150 ms, APD prolongs by 39% from 40.95 to 56.84 ms (WT vs HF), and by 31% at BCL = 200 ms from 38.72 to 50.75 ms. Thus, APD prolongation at faster pacing frequencies is still observed despite HF remodelling. Diastolic and systolic intracellular and SR Ca^{2+} concentrations are also slightly increased in HF

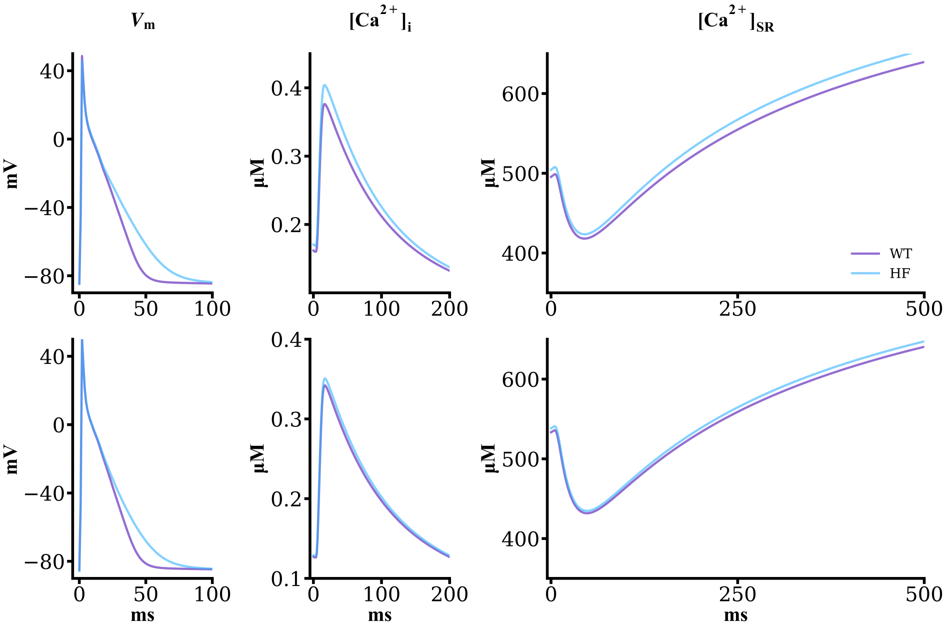

Figure 5.4. Simulated effects of I_{K1} downregulation on AP and Ca^{2+} handling characteristics under normal conditions. Top: BCL 150 ms. Bottom: BCL 200 ms. HF remodelling increases APD at both cycle lengths (left). Diastolic and systolic Ca^{2+} concentrations are also slightly increased (middle), as are SR Ca^{2+} concentrations (right). WT, wild-type (no remodelling); HF; heart failure remodelling ($0.5 \times g_{\mathrm{K1}}$); NSR, network SR. One representative simulation per condition (WT, HF) shown.

simulations at both cycle lengths. These effects are shown in Figure 5.4.

Under pro-loading conditions (ISO) the effects of I_{K1} remodelling (as observed in HF) are sufficient to promote greater SR Ca^{2+} loading (Figure 5.5). Under these conditions, APD decreases from 56.84 to 53.76 ms (HF vs HF+ISO) for BCL = 150 ms, and from 50.75 to 49.35 ms for BCL = 200 ms. Thus, under dual-remodelled conditions (HF+ISO), APD is 31% longer than WT at BCL = 150 ms and 27% longer at BCL = 200 ms. Therefore, the effect on the AP of I_{K1} remodelling (in terms of APD prolongation) are still observed, even under ISO conditions (which result in shorter APDs). At BCL = 150 ms, systolic Ca^{2+} concentration increases by a further 29 nM (vs WT+ISO), and diastolic SR Ca^{2+} concentration rises by 23 μM to 1121 μM. These effects are similar for BCL = 200 ms.

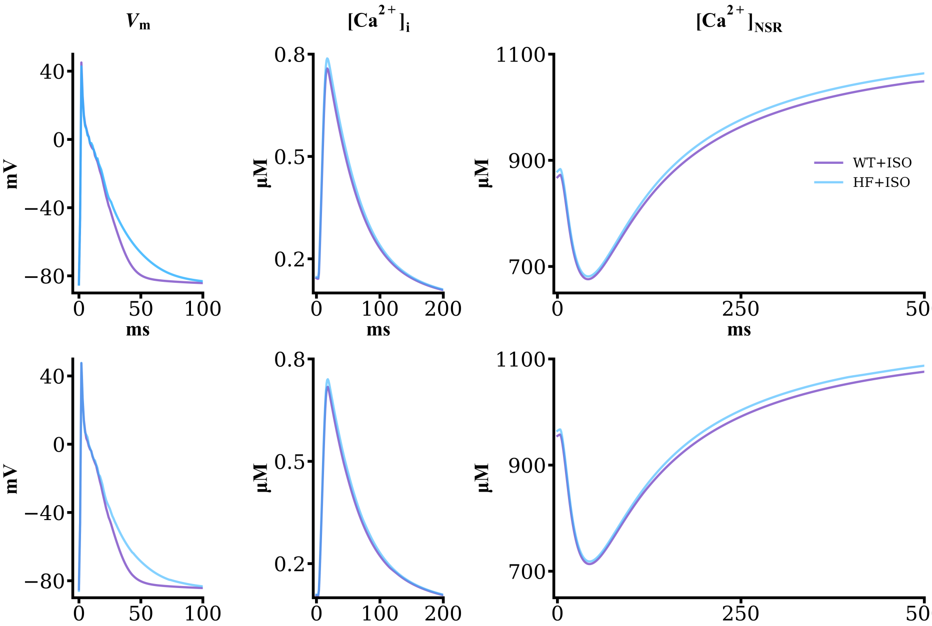

Figure 5.5. Simulated effects of I_{K1} downregulation on AP and Ca^{2+} handling characteristics under pro-loading conditions. Top: BCL 150 ms. Bottom: BCL 200 ms. HF remodelling increases APD for both cycle lengths under ISO-remodelling (left). Diastolic and systolic Ca^{2+} concentrations are also slightly increased (middle), as are SR Ca^{2+} concentrations which approach the threshold for spontaneous Ca^{2+} release ($\sim$ 1100 μM, right). WT+ISO, wild-type plus ISO remodelling; HF+ISO, heart failure plus ISO remodelling. NSR, network SR. One representative simulation per condition (WT+ISO, HF+ISO), shown.

5.3.3 I_{K1} remodelling influences DAD timing and morphology

For the following sections, only simulations involving ISO remodelling are discussed, as under control simulations (no ISO), spontaneous Ca^{2+} release events were not observed. SCREs were determined if a threshold for N_{RyR_O}/N_{RyR} of 0.035 was reached or surpassed, and the resulting t_i, duration and N_{RyR}^{peak} were calculated.

In WT and HF simulations (+ISO), SR Ca^{2+} concentration was increased close to or beyond the threshold for spontaneous Ca^{2+} release events ($\sim$ 1100 μM). Thus, SCRE were observed in both simulations. However, HF remodelling (50% g_{K1}) altered the timings and morphology of Ca^{2+} release events and DADs at both tested cycle lengths. Figure 5.6 shows emergent SCRE dynamics at BCL = 150 ms for WT and HF conditions (100 simulations each). The average N_{RyR}^{peak} was higher at both cycle lengths in HF simulations (WT

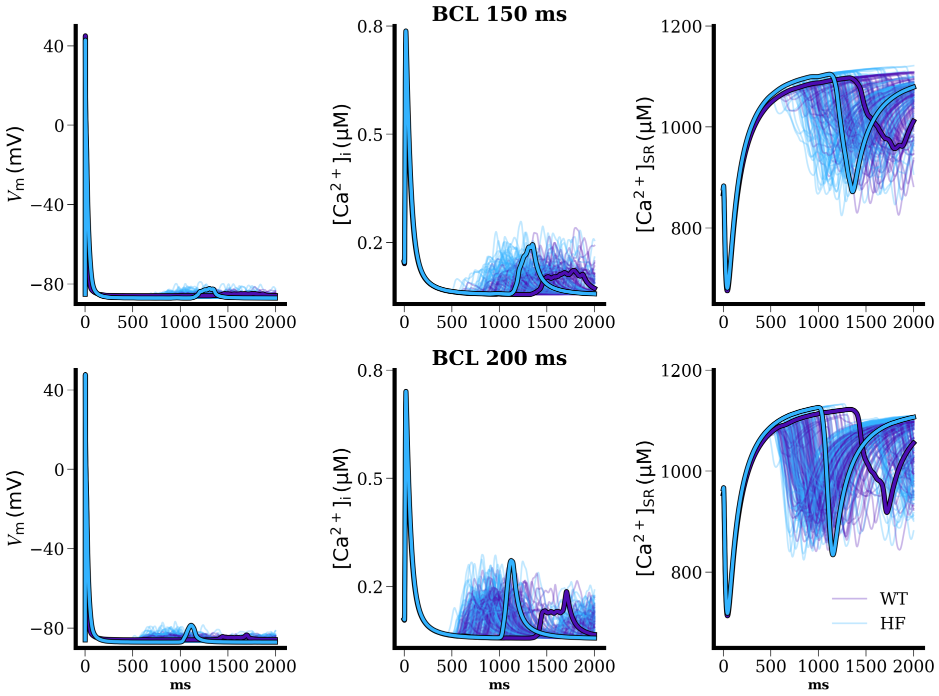

Figure 5.6. Spontaneous Ca^{2+} release events under isoprenaline-induced remodelling. Membrane potential (left), $[Ca^{2+}]_i$ (middle) and $[Ca^{2+}]_{SR}$ (right) following steady-state pacing at BCL = 150 and 200 ms under WT and HF conditions. Traces show 100 simulations, with one trace highlighted for each condition and cycle length. WT+ISO, wild-type plus ISO remodelling; HF+ISO, heart failure plus ISO remodelling.

vs HF 0.06 vs 0.08 at BCL = 150 ms, 0.07 vs 0.09 at BCL = 200 ms). At BCL = 150 ms, APD was prolonged from 37.7 (WT) to 53.7 ms (HF), and this was matched by an increase in SCRE magnitude in HF simulations. APD prolongation in HF simulations consistently resulted in greater magnitude SCRE (Figure 5.8).

At BCL = 150 ms, 90 out of 100 WT simulations resulted in SCRE, compared to 98 out of 100 for HF simulations, suggesting an increased probability for DAD generation in HF. At BCL = 200 ms, however, the probability of SCRE generation was about equal (100/100 WT, 99/100 for HF). For both cycle lengths, the average initiation time for SCRE was reduced in HF simulations, from 1287 to 1085 ms at BCL = 150 ms, and from 839 to 760 ms at BCL = 200 ms. Average SCRE duration was higher in HF than WT at BCL = 150 ms (200 vs 116 ms), but lower at BCL = 200 ms (252 vs 261 ms). These effects are shown in Figure 5.7.

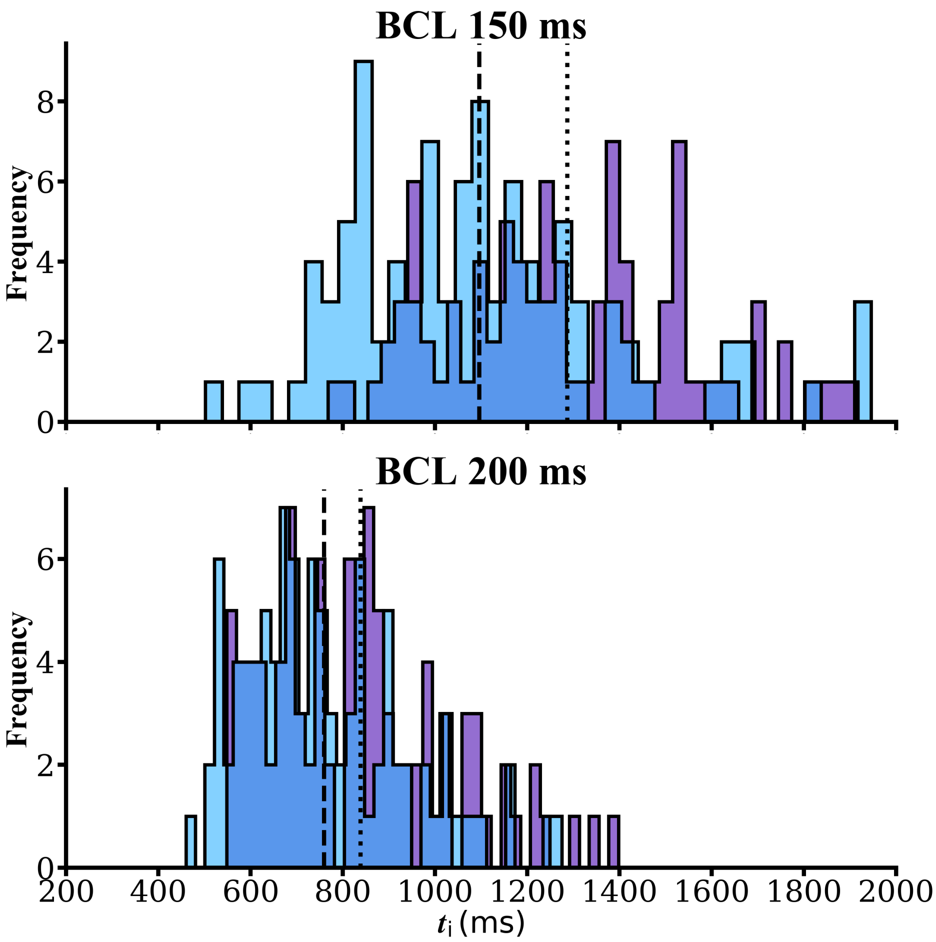

Figure 5.7. Histogram describing initiation time for SCRE. HF remodelling (blue) reduced the initiation time for SCRE compared to WT (purple) at both tested cycle lengths (darker blue areas indicate overlap). Histograms show the t_i distribution for simulations where SCRE occurred; in 90/100 and 98/100 simulations at BCL = 150 ms, and 100/100 and 99/100 simulations at BCL = 200 ms for WT and HF conditions, respectively. Average t_i indicated by dashed (HF) and dotted (WT) lines.

5.3.4 Rate of subspace Ca^{2+} diffusion influences SCRE frequency and amplitude in heart failure

For the previous sections, the time constant for Ca^{2+} diffusion from the subspace (τ_{ss}) was set to the default parameter set *slow* (corresponding to a transverse time constant of 1.35 ms and longitudinal time constant of 2.2 ms), giving a Ca^{2+} wave velocity of $\sim$ 90 μm.ms^{-1}, similar to that observed experimentally for ventricular myocytes [132, 184, 381]. However, the velocity of Ca^{2+} waves may be altered in heart failure [229].

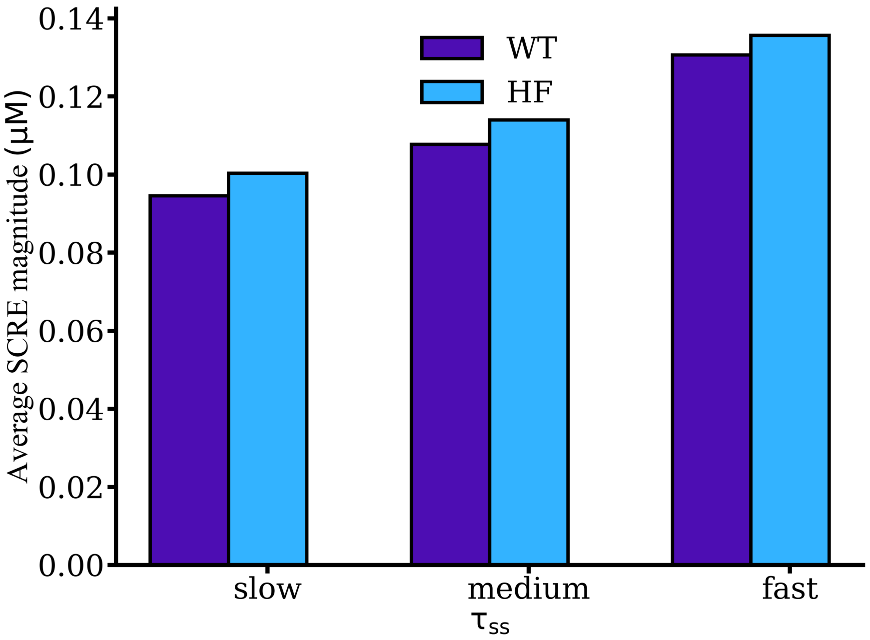

Figure 5.8. Average SCRE magnitude for different τ_{ss} speeds. SCRE magnitude increased as τ_{ss} became faster, and was consistently greater in heart failure (HF) simulations, in which APD was prolonged, than for wild-type (WT).

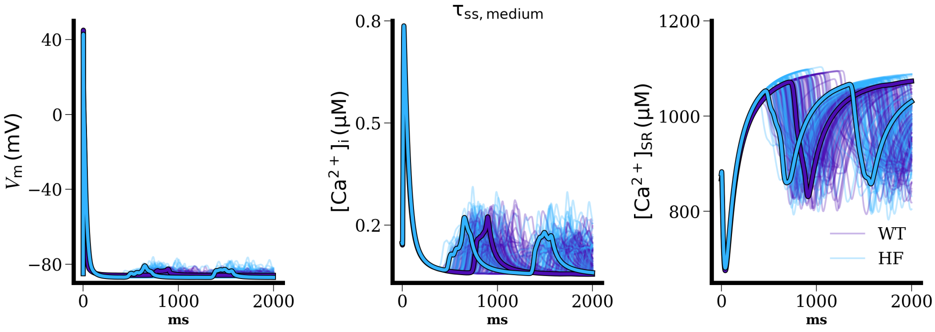

Figure 5.9. Spontaneous Ca^{2+} release events for $\tau_{\mathrm{ss,medium}}$. Membrane potential (left), $[Ca^{2+}]_{\mathrm{i}}$ (middle) and $[Ca^{2+}]_{\mathrm{SR}}$ (right) following steady-state pacing at BCL = 150 ms, with the *medium* τ_{ss} parameter set. Traces show 100 simulations, with one highighted for each condition. WT, wild-type plus ISO remodelling; HF, heart failure plus ISO remodelling.

In addition, detubulation and RyR orphaning in ventricular myocytes (hallmarks of heart failure) have been shown to result in increased Ca^{2+} wave velocity, possibly through the positive influence of $[Ca^{2+}]_{\mathrm{ds}}$ accumulation on RyR open probability [86, 368], which may be further attenuated by increased RyR Ca^{2+} leak in HF [244]. In the SC model,

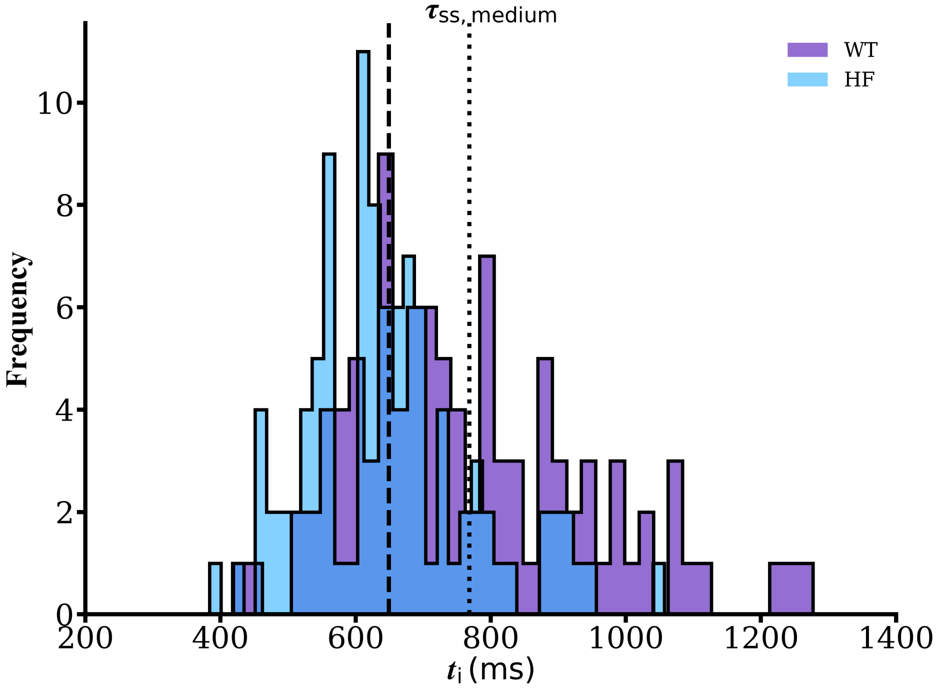

Figure 5.10. Histogram showing initiation time for SCRE for the *medium* τ_{ss} parameter set. Setting τ_{ss} to *medium* induces SCRE at shorter t_i values for both conditions, though HF simulations are shorter on average. SCRE occurred in 100/100 simulations for each condition. Average t_i indicated by dashed (HF) and dotted (WT) lines. Darker blue areas indicate overlap.

Ca^{2+} concentrations were generally increased in HF compared to WT. Thus, the influence of shorter τ_{ss} values (i.e. faster diffusion) was investigated at a cycle length of 150 ms, for *medium* (transverse = 1.25 ms, longitudinal = 1.95 ms) and *fast* (transverse = 1.0 ms, longitudinal = 1.5 ms) τ_{ss} parameter sets.

Results from 100 simulations with τ_{ss} set to *medium* are shown in Figure 5.9. Increasing τ_{ss} to *medium* speed resulted in a further leftward-shift in initiation time for both WT and HF simulations, with t_i of SCRE in HF simulations being shorter (649 vs 768 ms, Figure 5.10). In addition, the duration of Ca^{2+} waves was shorter in HF simulations by 10 ms (226 vs 236 ms). There was no difference between the probability of SCRE (100/100 simulations for both conditions), although the $N_{\text{RyR}}^{\text{peak}}$ was higher in HF simulations (0.11 vs 0.1). SCRE magnitude was larger in HF than WT simulations (107 vs 113 nM, Figure 5.8), and larger for $\tau_{\text{ss,medium}}$ than $\tau_{\text{ss,slow}}$.

The same trends were observed when increasing τ_{ss} to *fast*. SCRE occurred in 100/100

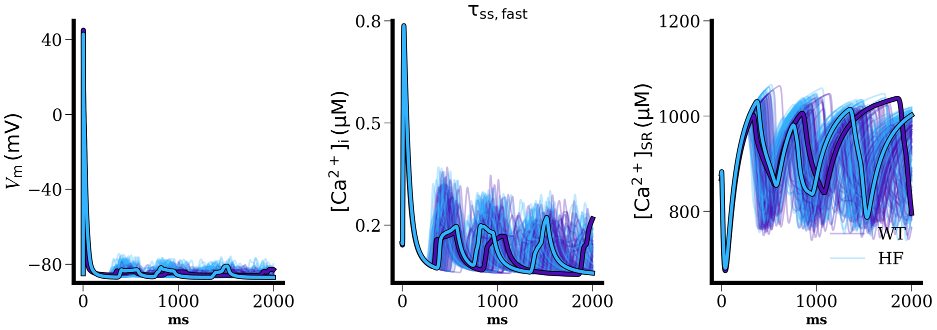

Figure 5.11. Spontaneous Ca^{2+} release events for $\tau_{ss,fast}$. Membrane potential (left), $[Ca^{2+}]_i$ (middle) and $[Ca^{2+}]_{SR}$ (right) following steady-state pacing at BCL = 150 ms, with the *fast* τ_{ss} parameter set. SCRE frequency and magnitude are increased at faster τ_{ss} values. Traces show 100 simulations, with one highlighted for each condition. WT, wild-type plus ISO remodelling; HF, heart failure plus ISO remodelling.

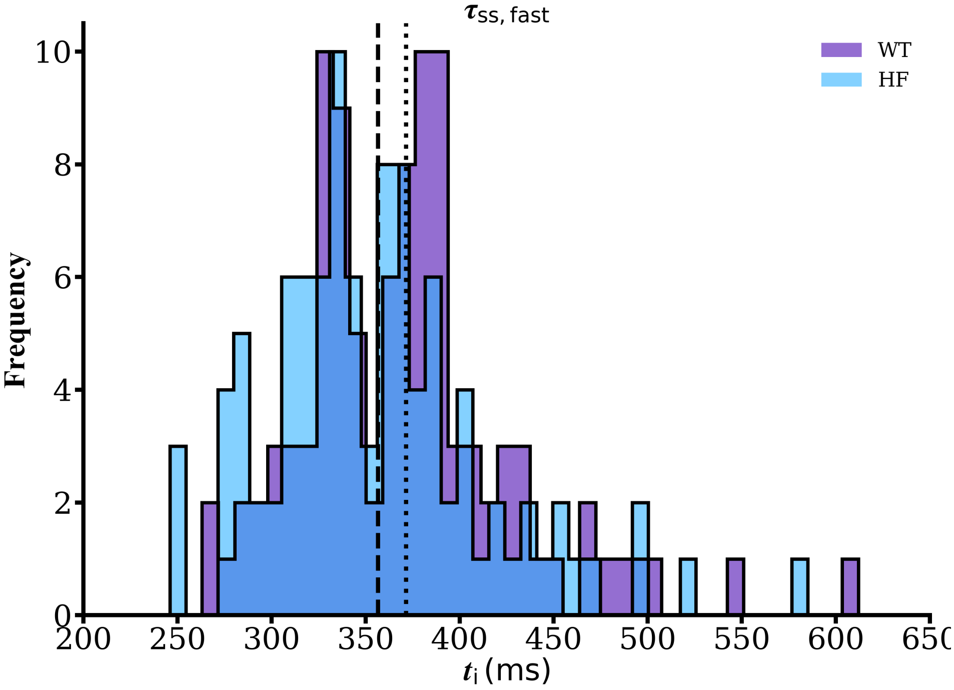

Figure 5.12. Histogram showing initiation time for SCRE for the *fast* τ_{ss} parameter set. For the *fast* τ_{ss} parameter set, SCRE were induced at shorter t_i values for both conditions, though HF simulations had a lower t_i on average. SCRE occurred in 100/100 simulations for each condition. Average t_i indicated by dashed (HF) and dotted (WT) lines.

simulations for WT and HF conditions, but the average t_i was shorter in HF than WT simulations (356 vs 371 ms). The average duration was slightly shorter in HF simulations

(140 vs 142 ms), and the average peak $N_{\mathrm{RyR\_O}}^{\mathrm{peak}}$ was higher (0.156 vs 0.154). SCRE magnitude was higher in HF than WT simulations (136 vs 131 nM, Figure 5.8) and higher than for both $\tau_{\mathrm{ss,medium}}$ and $\tau_{\mathrm{ss,slow}}$.

5.3.5 APD prolongation alone alters spontaneous Ca^{2+} release event frequency and magnitude in HF

Results thus far have shown that, under pro-loading conditions, I_{K1} downregulation as observed in HF results in greater SR Ca^{2+} concentrations, close to or above the threshold for spontaneous Ca^{2+} release. The increased loading of the SR in HF simulations results in greater magnitude of spontaneous Ca^{2+} release events, and a shortening of the t_i for these events. Thus, SCRE occur sooner after the AP and are of larger magnitude than for WT conditions. Diastolic and systolic Ca^{2+} concentrations are similarly increased. In addition, there is a concomitant increase in the APD in HF simulations, resulting from reduced repolarising current via I_{K1}.

Here, the role of this prolonged APD in SCRE dynamics is investigated, using the 0D model SRF functions. After steady-state pacing at BCL 150 ms under control or pro-loading (ISO) conditions, [Ca^{2+}]$_{\mathrm{SR}}$ was set to one of two values, 750 or 1100 μM. These values were chosen as they correspond to the time of peak [Ca^{2+}]$_{\mathrm{SR}}$ following the cessation of pacing for WT or ISO conditions in the SC model (Figure 5.4 and Figure 5.5), and were set at 975 ms after the AP initiated (t_i = 975 ms, corresponding roughly to the time of peak [Ca^{2+}]$_{\mathrm{SR}}$ following pacing cessation). For direct comparison of the effects of APD on SCRE characteristics between conditions, the probability of SCRE was set to 1, the cumulative frequency (CF) was set to 0.5, the duration widths DW_1 and DW_2 were set to 0 ms, and the median duration (MD, effectively the absolute duration, λ, as DW_1 DW_2 = 0) was varied between 30 to 185 ms to reflect the range of SCRE durations observed.

The effects of the prolonged APD in HF are shown in Figure 5.14. At a lower [Ca^{2+}]$_{\mathrm{SR}}$ concentration (750 μM), triggered activity can be seen in HF simulations, which is absent under WT conditions. This activity manifests despite larger magnitude SCRE in WT simulations, which have have a lesser effect on membrane potential despite their larger size. At a higher [Ca^{2+}]$_{\mathrm{SR}}$ concentration (1100 μM), triggered activity is still not observed under WT conditions, but manifests with higher frequency in HF simulations (Figure 5.13),

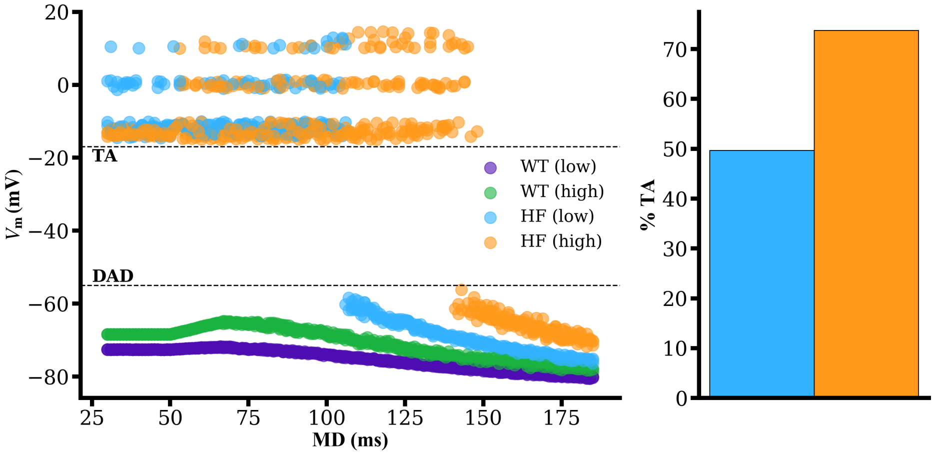

Figure 5.13. Relationship between median duration (MD) of SCRE and frequency of DADs and TA. Left: Maximum membrane potential achieved by DADs at low and high SR Ca^{2+} concentrations under control (WT) or fail (HF) conditions, as a function of MD. Under WT conditions, DADs do not result in triggered activity, but under HF conditions TA is observed, and is more common at higher SR Ca^{2+} concentrations. Right: Percentage of simulations resulting in triggered activity for under HF conditions at low (blue) or high (orange) SR Ca^{2+} loads. Dashed lines separate sub-threshold DADs from supra-threshold triggered APs. WT, wild-type; HF, heart failure conditions.

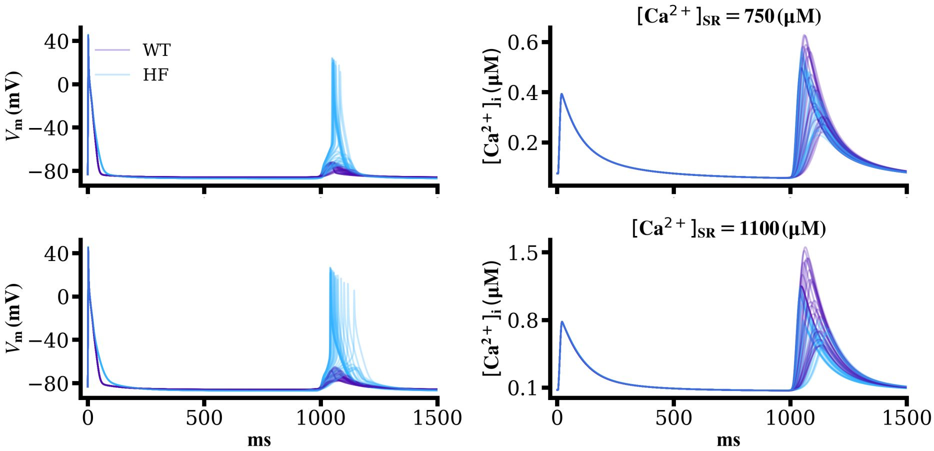

Figure 5.14. Effects of APD on DADs and triggered activity using the SRF functions. Following initiation of SCRE at 975 ms of varying durations (30 to 185 ms), higher magnitude DADs (left) were observed in HF at low and high SR Ca^{2+} concentrations, with some resulting in triggered activity, despite SCRE magnitude being higher in WT simulations (right). WT, wild-type; HF, heart failure conditions.

still in spite of the larger magnitude SCRE in WT simulations. Furthermore, resting membrane is more hyperpolarised in HF simulations than WT (despite reduced repolarising I_{K1}). Triggered activity was observed in 49.7% of HF simulations at low [Ca^{2+}]$_{\text{SR}}$ and 73.8% at high [Ca^{2+}]$_{\text{SR}}$ concentrations.

5.4 Discussion and conclusions

A myriad of pathophysiological changes are associated with heart failure, principally electrical remodelling at the sub-cellular level. Multiple ion channels have been shown to be remodelled, however the complex and dynamic nature of excitation-contraction coupling makes it experimentally difficult to determine the contribution of each of these remodelled currents or processes to the heart failure phenotype, and arrhythmogenesis. In this chapter, the SC model was used to explore how one salient remodelling process in heart failure, I_{K1} downregulation, can contribute towards arrhythmia development. A 50% reduction in I_{K1} conductance, g_{K1}, was implemented for steady-state pacing at fast cycle lengths to determine its effect on the emergence of spontaneous Ca^{2+} release events (SCRE) under conditions that favour spontaneous release for two cycle lengths (BCL = 150 and 200 ms). For this, a simple model of isoprenaline (ISO) was implemented, in which the conductances for I_{to}, I_{ss} and I_{CaL} were increased, as was the SERCA uptake rate, J_{up}. The ISO model resulted in raised levels of [Ca^{2+}]$_{\text{i}}$ and [Ca^{2+}]$_{\text{SR}}$ at shorter APDs, in line with experimental observations [121, 340, 341]. The HF model ($0.5 \times g_{\text{K1}}$) resulted in APD prolongation, and increases to intracellular and SR Ca^{2+} concentrations.

ISO simulations resulted in emergent SCRE for WT (no remodelling) and HF ($0.5 \times g_{\text{K1}}$) conditions, however the time of SCRE initiation (t_i) was shorter in HF simulations, as was the duration of SCRE. In addition, SCRE in HF simulations resulted in a larger proportion of open RyRs ($N_{\text{RyR}}^{\text{peak}}$) for both tested cycle lengths. HF remodelling also resulted in an increased incidence of DAD generation (in 98/100 vs 90/100 simulations for WT conditions at BCL = 150 ms).

The effect of changes to subspace Ca^{2+} diffusion rate (τ_{ss}) were also investigated, as this is also known to be altered in HF. Step-wise increases to τ_{ss} resulted in progressive shortening of t_i, increases in $N_{\text{RyR}}^{\text{peak}}$ and overall increased magnitude of SCRE and DADs. However, HF simulations consistently had shorter SCRE initiation times and larger $N_{\text{RyR}}^{\text{peak}}$

proportions. There were no changes to SCRE probability (100% in both conditions for $\tau_{\text{ss,medium}}$ and $\tau_{\text{ss,fast}}$) and neither condition evoked triggered activity in the 3D model. These results suggest that, alongside APD prolongation, I_{K1} remodelling observed in HF results in greater Ca^{2+} loading of the SR, promoting SCRE of greater magnitude occurring sooner after the cessation of pacing.

However, the effects of I_{K1} remodelling in HF are not just related to greater SR Ca^{2+} loading. Using the spontaneous release functions (SRF) for the 0D model, which well approximate 3D cell behaviour [97], the influence of APD changes resulting from I_{K1} downregulation on SCRE was investigated for two SR Ca^{2+} concentrations corresponding to low (750 μM) and high (1100 μM) loads. For the same t_i, probability of SCRE and cumulative frequency, the prolonged APD in HF resulted in larger magnitude DADs (despite smaller SCRE magnitudes) at both SR Ca^{2+} concentrations. In addition, triggered activity was observed for both SR Ca^{2+} loads under HF conditions, but not at all under WT conditions. In addition, these effects are observed despite a paradoxically more hyperpolarised membrane potential in HF simulations (Figure 5.14), when it would be expected a reduced repolarising I_{K1} current results in slight membrane depolarisation. These results suggest that changes to APD resulting from I_{K1} remodelling alone can promote the emergence of SCRE, DADs and triggered activity in single cells, and that destabilisation of the resting membrane potential favours larger magnitude DADs for given releases of SR Ca^{2+}.

In combination, these results have significant implications for arrhythmogenesis. The shift towards shorter initiation times for SCRE in HF remodelling potentially means there is a greater likelihood of a DAD or triggered activity occurring in the vulnerable window (VW). The VW represents the spatio-temporal location at which a supra-threshold excitation can produce a unidirectional propagating wave [49, 370]. The VW typically has a very narrow width ($\sim$ 1% of the ventricular APD), but can be increased by heterogeneity or electrical remodelling, and occurs between the plateau phase of the AP and diastole [358]. Thus, SCRE manifesting closer to the end of the action potential have a greater likelihood of falling within the VW and inducing undirectional propagation block. Extrapolating to 3D, this shift may increase the probability of the development of re-entrant arrhythmias [36]. Furthermore, as the 0D simulations showed, even under the same SR Ca^{2+} load and given the same dynamics of SCRE, the increased APD under HF-associated I_{K1} remodelling promotes DADs and triggered activity, in combination with a destabilised resting membrane potential which is more easily perturbed by smaller magnitude spontaneous Ca^{2+} releases. Though HF simulations showed a more hyperpolarised membrane under HF conditions, I_{K1} downregulation is commonly seen to result in depolarised membrane potentials [175, 315]. Nevertheless, DADs were of greater magnitude in HF simulations and triggered activity was increased, thus these effects are likely to be further attenuated at depolarised membrane potentials. The results therefore suggest that I_{K1} remodelling in HF can promote arrhythmogenesis via two mechanisms in tandem: (i) greater SR Ca^{2+} loading and shorter initation times for SCRE, and (ii) electrophysiological alterations that prolong the APD and sensitise the membrane potential to DADs (and, by extension, triggered activity).

Chapter 6

Mechanisms of Action Potential Prolongation in Rat Ventricular Myocytes

---

6.1 Introduction

Heart rate is an essential determinant of cardiac performance, and in many species an increase in heart rates leads to positive inotropic effects. This phenomenon is known as the force-frequency relationship (FFR), also referred to as the Bowditch staircase [60]. At the cell-level, the increase in contractile force results from modifications to Ca^{2+} and Na^{+} homeostasis (see [131] for a review). Alongside changes to contraction, APD is also modified by pacing rate and in most species, increases in pacing frequency yield shorter APDs. However, in rat myocytes, the opposite is observed and APD is often seen to prolong [133, 361–363, 428], yet both positive and negative FFRs have been reported in rat [38, 58, 77, 112, 141, 248, 350, 383]. APD prolongation is also seen when regular pacing is perturbed by an extra stimulus, as in an S1-S2 restitution protocol [24, 265]. As the rat is the most commonly used animal model of cardiac physiology [6, 138, 336], it is important to understand the mechanisms underlying APD prolongation and the positive and negative FFRs, which remain controversial, particularly as a switch from positive to negative FFRs is seen in, for example, detubulated myocytes [140] which implies a role of the FFR in cardiac diseases such as heart failure [231, 237]. Furthermore, increased steepness of the restitution curve is a known indicator of arrhythmia development [142].

It was first proposed that frequency-dependent decreases in K^+ currents may underlie APD prolongation in rat ventricular myocytes [362, 363], and that this response was independent of the L-type Ca^{2+} current. Later, however, it was proposed that frequency-dependent increases in I_{CaL} may contribute to APD prolongation, with a limited role for K^+ currents. Frequency-dependent increases in I_{CaL}, known as I_{CaL} facilitation, has been characterised experimentally for a variety of mammalian species [65, 323], but typically using unphysiological test pulses (+ 100 mV) which does not predict a physiological role for facilitation. However, a role for I_{CaL} in APD prolongation during physiological action potentials has been identified using the Pandit model [293] of rat ventricular electrophysiology [336], suggesting that greater influx of Ca^{2+} at faster pacing frequencies contributes to the positive FFR. However, the study utilised only a simplified implementation of I_{CaL} facilitation, in which its inactivation rate at 1 Hz was reduced by 25%. The results also confirmed a role for reduced K^+ currents in APD prolongation, though only through I_{to}. In addition, it has been shown by Fauconnier *et al.* [133] that application of ryanodine (which binds to open state RyRs, resulting in SR Ca^{2+} depletion) and thapsigargin (an irreversible inhibitor of SERCA, thus preventing SR Ca^{2+} loading) prolong the AP in rat ventricular myocytes but also prevent its adaptation to high pacing rates, which implies a role for SR Ca^{2+} release in APD modulation, possibly by the effect of Ca^{2+}-dependent inactivation of I_{CaL}. This effect is likely to be more prominent in rat ventricular myocytes where high SERCA activity favours high SR Ca^{2+} loads [42].

As shown in Chapter 3, existing models of rat ventricular electrophysiology are unable to recreate a range of experimental restitution curves. In particular, previous models have been unable to simulate APs at shorter cycle lengths, corresponding to the faster pacing rates at which APD is seen to prolong for rat ventricular myocytes in contrast to other mammalian species. However, the SC model described in Chapter 4 is capable of simulating APs and Ca^{2+} handling at faster pacing frequencies up to 12 Hz. Accordingly, the model provides a useful tool to investigate the mechanisms underlying APD prolongation with increases in pacing frequency. In this chapter, the SC model is used to explore changes to membrane currents and their influences on APD prolongation at fast pacing frequencies.

6.2 Methods

In Chapter 4, the 0D implementation of the SC model was used to generate a range of restitution curves for direct comparison to those observed experimentally. The 0D model has been validated to reproduce 3D cell model behaviour, at significantly reduced computational cost [97], and so is suitable for the long pacing durations required to generate steady-state restitution curves. Here, the 3D implementation (described in detail in Chapter 4) of the SC model is used to investigate the influence of altered current densities and gating kinetics for the currents postulated to play a role in the inverse rate-dependence of APD observed in rat ventricular myocytes. For generation of restitution curves in the latter part of this chapter, the 0D model was again used for computational efficiency.

The 3D SC model was paced to steady-state under control conditions, then for the final beat various parameters were altered to investigate the subsequent effects on APD for a range of cycle lengths. These parameters were: current magnitude scales for I_{to}, I_{ss}, I_{K1}, I_{CaL} and I_{NaCa} ($g_{\mathrm{to}}, g_{\mathrm{ss}}, g_{\mathrm{K1}}, g_{\mathrm{CaL}}, g_{\mathrm{NaCa}}$); time constant scales for I_{to} and I_{ss} inactivation gates ($\tau_{s/s_{\mathrm{slow}}}, \tau_{rss}$); and scaling factors controlling SERCA uptake rate (J_{up}) and RyR open probability ($\mathrm{RyR}_{\mathrm{P\_O}}$). Parameters were scaled to between ±50% of their control values, to reflect ranges observed experimentally in diseased or remodelled states (e.g. [34, 121, 409]).

6.3 Results

6.3.1 Insufficient inactivation recovery time contributes to reduced K^+ currents and prolonged APD

A decrease in repolarising currents has been proposed to contribute to APD prolongation at faster pacing frequencies in rat ventricular myocytes. As shown in Chapter 4, between pacing frequencies of 1 and 6 Hz, the amplitude of the repolarising currents I_{to} and I_{ss}

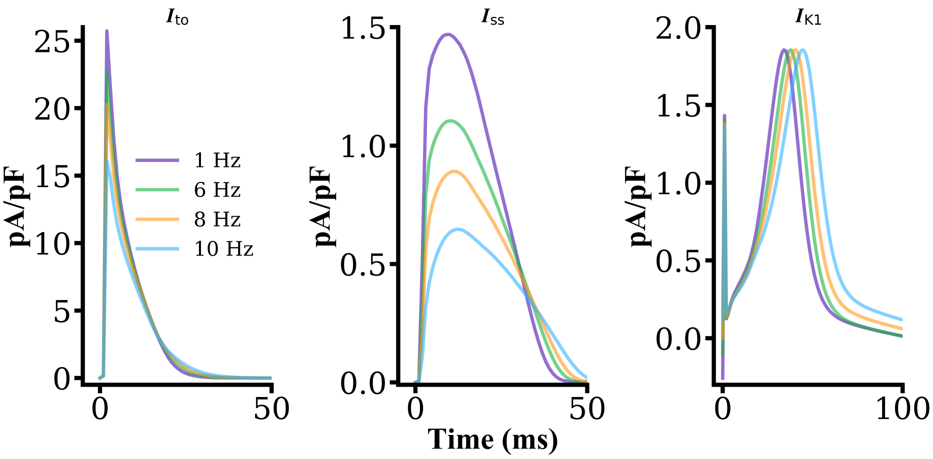

Figure 6.1. Repolarising currents at faster pacing frequencies in the SC model. The densities of I_{to} and I_{ss} both decrease as pacing frequency increases to 10 Hz in the SC model. For I_{K1}, the peak current magnitude stays relatively constant, however there is a shift towards sustained outward current in place of transient outward current at 10 Hz.

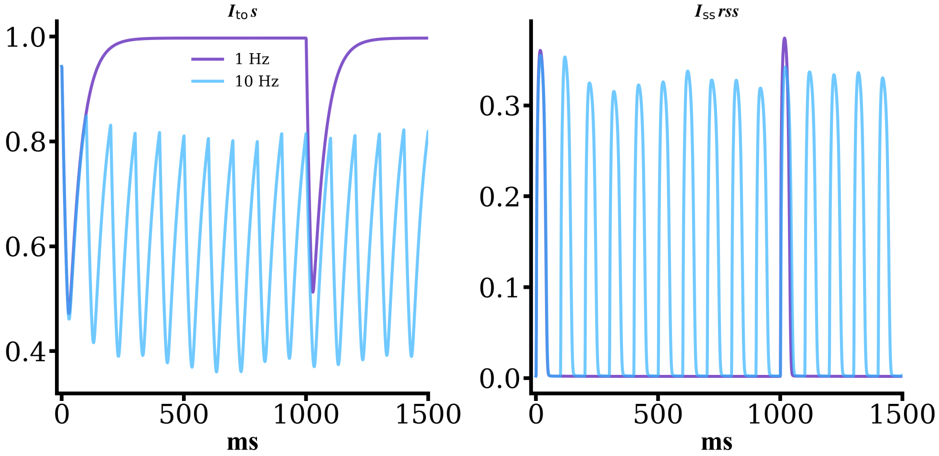

Figure 6.2. Time course of I_{to} and I_{ss} gates during steady-state pacing. The time course of I_{to} inactivation gate s (left) and I_{ss} activation gate rss (right) recovery after steady-state pacing from initial conditions is shown for BCL = 1000 and 100 ms. At faster cycle lengths, the gates have insufficient time to recover, resulting in reduced overall current.

decrease in the SC model, from 25.72 to 22.77 pA/pF for I_{to} and from 1.47 to 1.1 pA/pF for I_{ss}. In Figure 6.1, it is shown that these repolarising currents further decrease at faster pacing frequencies. I_{to} falls to 20.28 and 16.08 pA/pF and I_{ss} to 0.89 and 0.75 pA/pF at 8 and 10 Hz, respectively. At 10 Hz, these magnitudes are just 62.5 and 44.0% of the peak densities at 1 Hz (for I_{to} and I_{ss}, respectively). Such a decrease likely contributes signif-

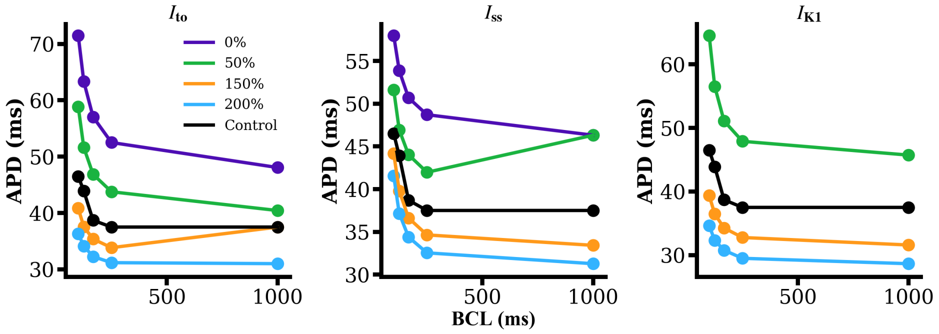

Figure 6.3. Effect of changing repolarising K$^+$ current magnitude on APD. Increasing the conductances of I_{to} (left), I_{ss} (middle) and I_{K1} (right) results in shorter APDs but does not abolish the inverse rate-dependency of APD. Effects of partial or full blockade of each current also shown, which results in enhanced APD prolongation. Note full block of I_{K1} does not permit sufficient repolarisation for APs to generate.

icantly to APD prolongation at 10 Hz compared to 1 Hz (46.5 vs 37.5 ms). Figure 6.2 shows that these reductions arise as the recovery time from inactivation is compromised at short cycle lengths, meaning a greater proportion of channel gates are inactivated during steady-state pacing. These reductions in repolarising membrane currents seen in the model simulations are consistent with experimental observations of reduced K$^+$ currents at faster pacing frequencies [61, 362, 363].

However, increasing the magnitude of repolarising currents (by increasing I_{to}, I_{ss} and I_{K1} conductance), or shortening the time constants of inactivation (I_{to} τ_s) and activation (I_{ss} τ_{rss}) does not abolish the inverse rate-dependency of the rat ventricular APD in simulations. Figure 6.3 shows the effects on APD of changing the conductances of I_{to}, I_{ss} and I_{K1}. Though increasing the conductances of these currents results in shorter APDs for each cycle length, APD is still seen to prolong at shorter cycle lengths. Similarly, enhancing the rate of recovery from inactivation for I_{to} and towards activation for I_{ss} results in shorter APDs but does not prevent APD prolongation at faster pacing frequencies. These results suggest other mechanisms may contribute towards APD prolongation in rat ventricular myocytes.

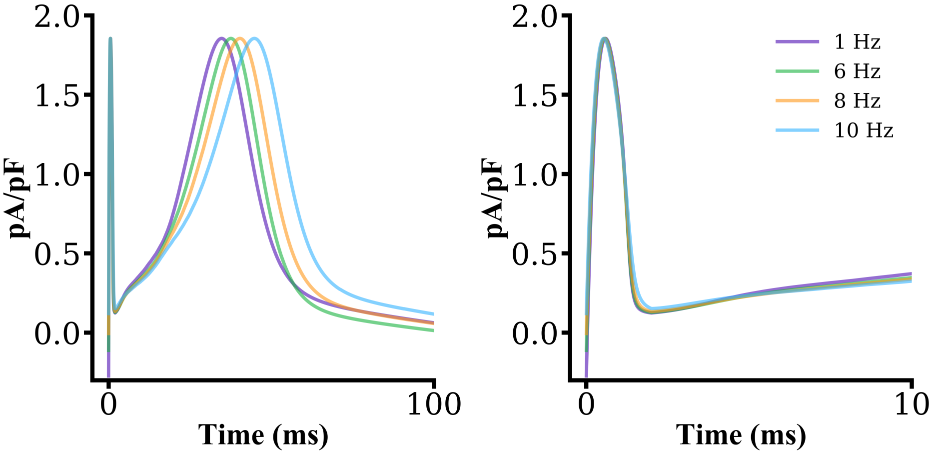

Figure 6.4. Adaptation of I_{K1} to pacing frequency in the SC model. The peak magnitude of I_{K1} remains constant at all tested frequencies, however the time to peak increases (left). At faster pacing frequencies, the magnitude of diastolic inward current via I_{K1} gradually reduces until 10 Hz, at which the diastolic current remains outward (right).

6.3.2 I_{K1} current magnitude maintained but shifted towards outward current at fast pacing rates

For I_{K1}, peak current magnitude remains constant at all tested frequencies at 1.85 pA/pF. However, there are changes to the time to peak (T_{peak}) diastolic current as pacing frequency increases. At 1 Hz, the $T_{peak,IK1}$ is 34 ms, and the diastolic current is slightly inward at -0.27 pA/pF. At 6 Hz, $T_{peak,IK1}$ rises to 38 ms, and the diastolic current remains inward but at a reduced magnitude of -0.11 pA/pF. These trends continue at 8 Hz, where $T_{peak,IK1}$ is 40 ms and diastolic current is negligibly inward at -0.005 pA/pF. At 10 Hz, $T_{peak,IK1}$ is 44 ms, however interestingly the current remains outward during diastole, at 0.12 pA/pF. These changes are illustrated in Figure 6.4. These results are in agreement with previous studies [336,361,362] showing that decreases in repolarising currents contribute towards APD prolongation at faster pacing frequencies.

Together, these results suggest a role for all repolarising K^+ currents in the prolongation of APD with increased pacing frequency for rat ventricular myocytes, in contrast to the previous study by Salle *et al.* [336] in which only I_{to} was implicated. Though peak I_{K1} remains constant in the SC model at all tested frequencies, there is a shift towards favouring outward current via I_{K1} as pacing frequency increases, particularly at 10 Hz stimulation during which inward I_{K1} is abolished.

6.3.3 I_{CaL} magnitude decreases less than for K^+ currents, favouring maintained depolarising currents and APD prolongation

Though repolarising currents are decreased at faster pacing frequencies, favouring APD prolongation, various Ca^{2+} handling processes have also been implicated in the rate-dependence of APD in rat ventricular myocytes, and there is inherent interaction between electrophysiology and Ca^{2+} handling. Changes to I_{CaL} at different pacing frequencies are shown in Figure 6.5 alongside the time course of the slow recovery gate, f_{12}. Peak I_{CaL} magnitude decreases at shorter cycle lengths, from -11.63 pA/pF at 1 Hz to -8.77 pA/pF at 10 Hz (-10.27 and -9.84 pA/pF at 6 and 8 Hz, respectively). Despite the reduced peak, the duration of the I_{CaL} waveform increases with pacing frequency, thus Ca^{2+} influx occurs over longer periods but at reduced magnitudes. Peak systolic Ca^{2+} concentration is increased at 10 Hz (478 nM) compared to 10 Hz (351 nM), but the elevated diastolic Ca^{2+} concentration at 10 Hz (257 nM vs 75 nM) means this represents a reduction in the magnitude of the Ca^{2+} transient.

As shown previously in Chapter 4, diastolic Ca^{2+} concentration increases with pacing frequency, from 75 nM at 1 Hz to 257 nM at 10 Hz, and systolic Ca^{2+} concentration rises similarly. Overall, however, the amplitude of the Ca^{2+} transient decreases. Given these changes, and those to I_{CaL}, it would be expected that the Na^+-Ca^{2+} exchanger current, I_{NaCa}, will be affected at different pacing frequencies given its dependence on $[Ca^{2+}]_i$. Indeed, there are changes to the peak current magnitude of I_{NaCa} (Figure 6.6). Peak inward current magnitude decreases with increases in pacing frequency, from -1.39 to -1.14 pA/pF at 1 and 10 Hz, respectively. Inward current via I_{NaCa} is generated through Ca^{2+} ion extrusion in exchange for 3 Na^+ ions, thus this reduction in inward current is likely to contribute towards the elevated levels of $[Ca^{2+}]_i$ despite reduced I_{CaL} magnitudes.

6.3.4 Role of SR Ca^{2+} regulation and I_{NaCa} in APD prolongation

Beyond the K^+ currents and I_{CaL} changes already investigated, RyR open probability, SERCA and I_{NaCa} have also been posited to contribute towards APD prolongation at shorter cycle lengths. In Fauconnier *et al.* [133] the SERCA inhibitor thapsigargin and the RyR sensitiser ryanodine were shown to result in longer APDs (compared to control), but to prevent the further prolongation of APD at shorter cycle lengths. In addition, Janvier *et*

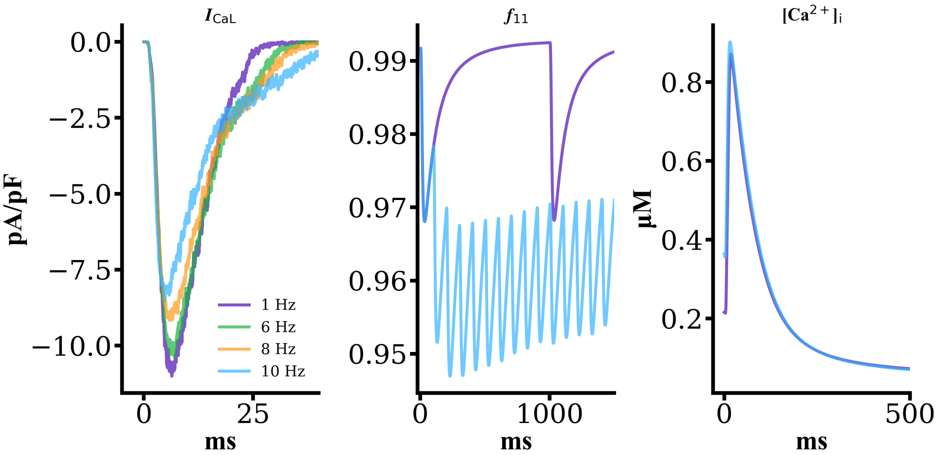

Figure 6.5. Changes to I_{CaL}, its slow inactivation gate f_{12}, and intracellular Ca^{2+} at faster pacing frequencies. I_{CaL} magnitude (left) decreases as pacing frequency increases (steady-state current shown), resulting from impaired inactivation recovery for the slow inactivation gate (middle) at faster frequencies (response to pacing from initial conditions shown). At 10 Hz, there is an elevated diastolic Ca^{2+} concentration and reduced Ca^{2+} transient magnitude compared to 1 Hz (right).

al. [188] showed that I_{NaCa} block by BAPTA resulted in longer APDs, although the effects were lessened at shorter test intervals where control and BAPTA APDs were similar. To examine these effects, here the 0D SC model was used to simulate electrical restitution curves under conditions similar to those observed in these experiments: (i) increased (150%) RyR_{P_O}, (ii) decreased (50%) J_{up}, and (iii) decreased (50%) I_{NaCa}.

Restitution curves implementing these effects are shown in Figure 6.7. Decreasing RyR_{P_O} made little difference to APD across the range of cycle lengths tested, and did not abolish prolongation at shorter cycle lengths. Decreasing I_{NaCa} resulted in consistently shorted APDs across the range of cycle lengths tested, but also did not abolish the prolongation at shorter BCLs. Reducing J_{up} shortened APD even further still, although led to the development of Ca^{2+} and APD alternans at cycle lengths below 210 ms (Figure 6.7B) and an accelerated rate of APD prolongation at these faster cycle lengths. At BCL = 1000 ms, where APDs were different (CON vs J_{up}), simulations suggested this resulted from reductions to $[Ca^{2+}]_{SR}$ (as SERCA uptake was reduced), leading to decreased Ca^{2+} transient magnitudes and a concomitant reduction in I_{NaCa}. At BCL = 250 ms, however, corresponding to a cycle length at which APDs were more similar (and before the development of alternans), $[Ca^{2+}]_{SR}$ content in control and reduced J_{up} simulations was more

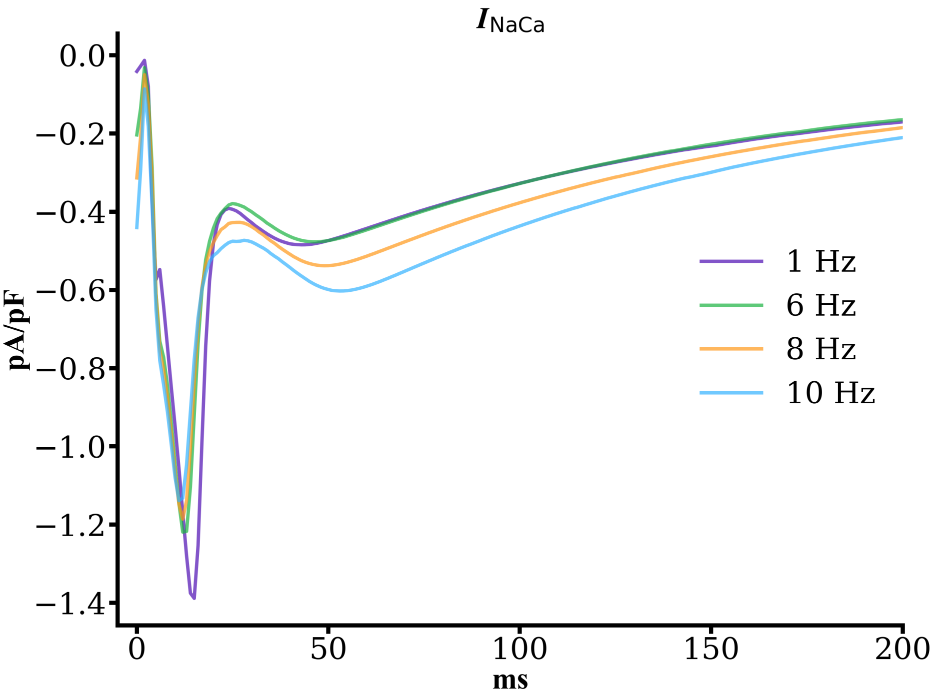

Figure 6.6. Changes to I_{NaCa} with pacing frequency. At shorter cycle lengths, there is a reduced inward I_{NaCa} amplitude, which likely contributes towards the elevated $[\mathrm{Ca}^{2+}]_i$ concentrations at faster pacing frequencies.

similar, leading to similar Ca^{2+} transient and I_{NaCa} magnitudes. These results suggest the effects of SERCA inhibition are more pronounced at longer cycle lengths.

Reducing I_{NaCa} magnitude resulted in shorter APDs compared to control at all cycle lengths in the 0D model. As Janvier *et al.* observed a lesser effect of I_{NaCa} at shorter cycle lengths (although APD increased experimentally, but simulations showed a decrease), the 3D model was used to investigate the role of I_{NaCa} at shorter cycle lengths (Figure 6.8). Here, the final beat after steady-state pacing under control conditions was perturbed by a 50% decrease in I_{NaCa} current amplitude. Reducing I_{NaCa} by 50% resulted in shorter APDs at BCL = 100 ms, from 46.5 to 38.2 ms, and BCL = 500 ms, from 37.5 to 32.2 ms. Such a reduction in I_{NaCa} was sufficient to restore APD at BCL = 100 ms to close to the control APD at BCL = 500 ms. These results suggest that I_{NaCa} inhibition shortens APD, and the degree of abbreviation to APD is itself rate-dependent, being larger at shorter cycle lengths.

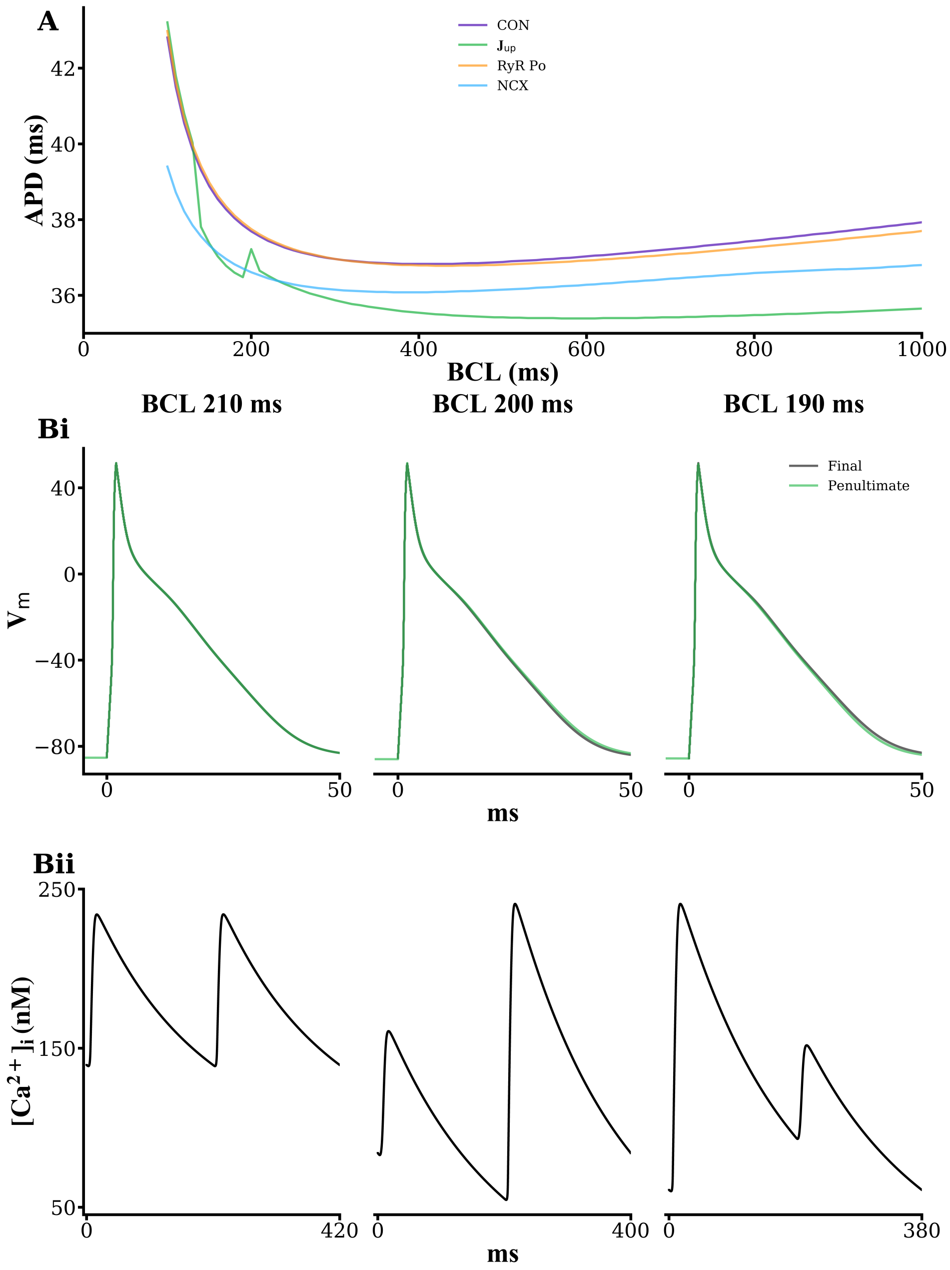

Figure 6.7. Restitution curves and alternans under altered conditions. **A:** Restitution curves in the 0D model under control, 50% RyR$_{\mathrm{P\_O}}$, 50% J_{up}, and 50% I_{NaCa} conditions. **B:** Snapshots of alternans when SERCA uptake is halved, showing **(i)** final and penultimate action potentials (overlaid) and **(ii)** final and penultimate Ca^{2+} transients at BCL 210, 200 and 190 ms.

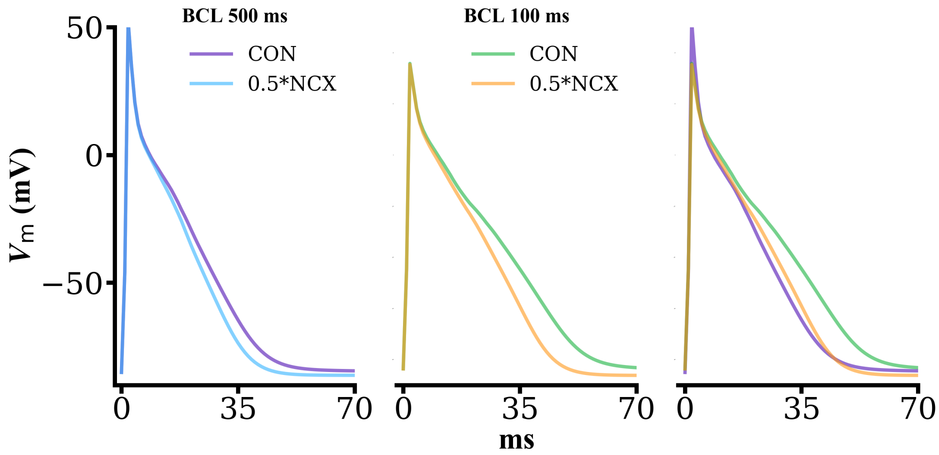

Figure 6.8. Effects of I_{NaCa} downregulation on APD in the 3D cell model. I_{NaCa} downregulation results in shorter APDs at all tested pacing frequencies, though its effects on APD were more pronounced at shorter cycle lengths. A 50% reduction in I_{NaCa} was sufficient to reduce the APD at 10 Hz close to that of the control APD at 2 Hz. CON, control; NCX; reduced I_{NaCa}.

6.4 Discussion and conclusions

APD prolongation with increased pacing frequency is an inherent characteristic of rat ventricular myocytes commonly observed experimentally [133, 361], in contrast to other mammalian species in which APD shortens. However, the mechanisms underlying this inverse rate-dependence are poorly understood, partly due to conflicting observations depending on the restitution protocol utilised. In control myocytes, action potential duration remains relatively constant at different pacing frequencies. However, the slope of the restitution curve is generally seen to be steeper in heart failure, and failing myocytes appear to be more sensitive to changes in pacing frequency [145, 159]. Thus, dissecting the mechanisms dictating the rate prolongation in rat ventricular myocytes can potentially highlight therapeutic targets for flatting cardiac restitution and preventing the development of arrhythmias. In this chapter, the roles of implicated membrane currents and Ca^{2+} handling processes in determining restitution characteristics were investigated, informed from previous observations in the literature.

Previous studies have suggested that APD prolongation at faster pacing frequencies in rat ventricular myocytes is the result of reduced repolarising K^+ currents, with a role for increased I_{CaL} also proposed [336, 362, 363]. Simulations using the SC model support the hypothesis that reducing repolarising K^+ currents promote APD prolongation. Simulations showed that these reduced K^+ currents at faster pacing frequencies result from insufficient time to recover from inactivation, thus during steady-state pacing a greater proportion of channels remain in the inactivated state. In addition, simulations suggest a role for both I_{to} and I_{ss}, in contrast to previous studies. Furthermore, a shift towards outward I_{K1} was observed at faster pacing frequencies, potentially a compensatory mechanism to ensure sufficient repolarising current is maintained so as to restore resting membrane potential in the absence of other repolarising membrane currents.

However, in contrast to previous research, the model results suggest that I_{CaL} does not contribute to APD prolongation, as it was seen to decrease at faster pacing frequencies. These reductions are caused by insufficient time for recovery from inactivation, though to a lesser extent than for K^+ currents and so the reduction in magnitude is smaller. In the previous study [336], I_{CaL} was reported to be larger at a pacing frequency of 1 Hz, compared to 0.1 Hz. However, the authors implemented a simplified mathematical description of I_{CaL} facilitation at 1 Hz to match their experimental data, but not at 0.1 Hz. Thus, the increased I_{CaL} is artificially-induced in the model, not solely as a result of changes to pacing frequency. In addition, the frequencies tested in the previous study (0.1 to 1 Hz) do not correspond to rates seen physiologically in rat (i.e./ over 6 Hz [34, 35, 331, 415]). In fact, over a more physiological range (from 1 to 8 Hz), I_{CaL} has been reported to decrease [121], which is in agreement with the presented modelling results. Other Ca^{2+} handling processes, however, may be implicated. As diastolic Ca^{2+} concentrations are observed to increase at faster pacing frequencies, there are concomitant changes to I_{NaCa} amplitude and morphology. Peak inward I_{NaCa} magnitude was seen to decrease in simulations, which is likely to contribute towards the elevated levels of diastolic $[Ca^{2+}]_i$. These increased diastolic Ca^{2+} concentrations may underlie the frequency-dependent shift in I_{K1} towards outward currents, as it has been shown that reductions in I_{K1} up to 50% can be attributed to elevated diastolic intracellular Ca^{2+}levels [134]. Though peak I_{K1} amplitude in the model is unaffected, the increased diastolic $[Ca^{2+}]_i$ may therefore underlie this shift towards sustained early outward I_{K1} current at 10 Hz.

These results suggests a greater role for reduced K^+ currents in APD prolongation than other mechanisms, however these alone are not sufficient to fully explain the observed restitution characteristics. Thus, the model was used to explore the roles of $\mathrm{RyR}_{\mathrm{P\_O}}$, J_{up} and I_{NaCa} which have been reported to alter the restitution profile of rat ventricular myocytes experimentally. In Fauconnier *et al.* [133], RyR blockade and SERCA inhibition were shown to result in prolonged action potential durations and to prevent the prolongation of APD at faster pacing frequencies. However, in our simulations, this was not the case. Decreasing the RyR open probability resulted in minor shortening of APD, and decreasing J_{up} resulted in more significant shortening of APD, and the development of alternans at shorter cycle lengths (below BCL = 210 ms). Furthermore, the rate of APD prolongation appeared to be accelerated at faster cycle lengths. The discrepancies between our simulation results and previous experimental data could have multiple causes. Firstly, the reductions to $\mathrm{RyR}_{\mathrm{P\_O}}$ and J_{up} used in our simulations were simplified changes to individual parameters that may not necessarily reflect the (a) magnitude and (b) complexity of the changes observed experimentally. Primarily, ryanodine and thapsigargin are posited to have additional effects on cardiac myocytes beyond reducing Ca^{2+} release from the SR, including slowing I_{CaL} inactivation [113,252,380]. Such mechanisms are not captured by our simplistic implementation of reduced $\mathrm{RyR}_{\mathrm{P\_O}}$. However, these wide-ranging effects could be incorporated in a similar manner to those from isoprenaline modulation discussed in Chapter 5 for future studies.

The model has, however, identified a role for I_{NaCa} in the inverse rate-dependency of APD for rat ventricular myocytes. Decreases in I_{NaCa} resulted in reductions in APD at faster pacing frequencies, and the degree of reduction appeared to be larger at shorter cycle lengths. This is in contrast to experimental findings in Janvier *et al.* [188], however, in which reduced I_{NaCa} with BAPTA prolonged action potential duration, with a lesser effect at shorter intervals. Implementing a 50% reduction in I_{NaCa} for the final beat after steady-state pacing in the 3D model similarly reduced APD at cycle lengths of 100 and 500 ms. Interestingly, at BCL = 100 ms, this reduction in I_{NaCa} was sufficient to restore APD to close to that for control pacing at BCL = 500 ms.

In summary, there is a fine balance between repolarising and depolarising membrane currents at different pacing frequencies, however the simulation results suggests a greater contribution of reduced repolarising currents in the prolongation of APD at faster pacing frequencies. The larger reduction in repolarising K^{+} currents than depolarising I_{CaL} together promotes AP prolongation. Elevated diastolic Ca^{2+} concentrations also promote reductions in I_{NaCa}, which the model reveals can be sufficient to prevent AP prolongation, and may explain a shift towards sustained outward I_{K1} at faster pacing frequencies. Thus, modulation of I_{NaCa} activity when electrical restitution is steeper (as in heart failure) may prevent the development of pro-arrhythmic behaviours [145].

Chapter 7

Conclusions and Future Works

7.1 Aims

To date, a plethora of animal-specific computational models of cardiac electrophysiology have been developed. Such models (a useful summary of which is given in Noble *et al.* [282]), have provided mechanistic and quantitative insight into experimental observations and phenomena, allowing detailed investigation into the multi-scale mechansims underlying the complex, dynamic behaviour seen in normal, and abnormal, cardiac physiology. Models of human cardiac physiology are most desirable, so as to directly translate and compare between experimental, theoretical and clinical observations. However, there are scarce data available for human myocytes (especially control data), as well as significant ethical challenges, and so the development of models for higher mammalian species (such as canine) has been a particular focus in computational biology. As higher mammalian species share similar action potential and Ca^{2+} handling characteristics, they can provide insight that can be more directly translated to human cardiac physiology.

Nevertheless, resulting from ethical, financial and technical implications, rats are the most commonly used animal model in cardiovascular research, yet existing computational models of rat ventricular electrophysiology have lagged behind those of other mammalian species in terms of their complexity, species-specificity and ability to capture inherently stochastic dynamics. As a result, many experimental phenomena observed in rat ventricular myocytes, particularly relating to spontaneous Ca^{2+} release events and pro-arrhythmic behaviour, are not able to be simulated by existing computational models. Thus, important quantitative or mechanistic insight that is not possible to extract due to experimental or technical limitations has also not been available for exploration using computational models. Those models that have been developed to date, in addition, have largely been adapted from non-rodent data sources, cannot be paced at frequencies corresponding to the physiological heart rates observed in rats, and use deterministic implementations of sub-cellular Ca^{2+} handling processes.

For these reasons, the first aim of the work presented in this thesis was the development of a novel computational model of rat ventricular electrophysiology and Ca^{2+} handling, validated against experimental data from rat ventricular myocytes from a range of sources and capable of pacing at frequencies encompassing the physiological heart rate range of rats. The second aim was to utilise the model to explore the effects of experimentally-observed alterations to electrophysiology in the context of arrhythmias in heart failure on spontaneous Ca^{2+} release events. The third aim was to explore the processes underlying the inverse rate-dependence of the rat ventricular action potential, which prolongs at faster frequencies in contrast to other mammalian species.

7.2 Summary of results

In Chapter 3, existing computational models of rat ventricular electrophysiology were introduced and reviewed. Many of the later-developed rat models add certain functionality or extensions to the original Pandit model, with the most recent Gattoni model incorporating several previous amendments (including the addition of a contraction model and updated Ca^{2+} and Na^{+}-K^{+} ATPase models) as well as re-parameterising and validating against more recent experimental data. Accordingly, only the Pandit and Gattoni models were selected for comparison through their incorporation into the multi-scale cardiac simulation framework developed by Colman [97], which allows for comphrensive, direct comparison within a consistent framework and under identical simulation protocols. The results showed that the Pandit model, as well as being incapable of simulating APs at frequencies above 3 Hz, does not simulate graded release of Ca^{2+} and exhibits various Ca^{2+} handling characteristics which are inconsistent with those observed experimentally in rat ventricular myocytes. The Gattoni model, meanwhile, replaces the Ca^{2+} handling system from the Pandit model, so more closely reproduces experimental data, however the deterministic RyR and I_{CaL} implementation does not permit the investigation into spontaneous Ca^{2+} release mechanisms, as is one of the aims of this work. Finally, both models largely do not recapitulate experimental restitution curves, not least by being unable to simulate fast pacing frequencies above 6 Hz, and so are unsuitable for investigating the mechanisms underlying the restitution characteristics of rat.

A new model was developed in Chapter 4 that couples the biophysically-detailed rat-specific electrophysiology model of Gattoni *et al.* [146] to the Colman stochastic spatio-temporal Ca^{2+} cycling model [97], re-parameterised to capture Ca^{2+} handling characteristics observed experimentally in rat ventricular myocytes from a variety of sources in the literature. This model, the SC model, reproduces AP morphology, APD restitution curves and Ca^{2+} handling observed experimentally across a range of pacing frequencies, from 1 to 10 Hz. In addition, at frequencies from 10 to 12 Hz, the model spontaneously produces Ca^{2+} transient and APD alternans, pro-arrhythmic phenomena not captured by previous computational models.

The effects of electrophysiological alterations to membrane currents were investigated in Chapter 3 for the Pandit and Gattoni models, although their deterministic implementations do not permit investigation of pro-arrhythmic behaviour that may arise resulting from, for example, spontaneous Ca^{2+} release events. As the SC model is capable of simulating such phenomena, the effects of alterations to I_{K1} as observed experimentally from our laboratory [34, 139] were investigated in the context of pro-arrhythmic behaviour in Chapter 5. Under pro-loading conditions, I_{K1} downregulation, associated with heart failure, was shown to promote greater loading of the SR with Ca^{2+} and prolonged action potential durations. These conditions influenced the characteristics of spontaneous Ca^{2+} release events, which had shorter initiation times and durations as well as increased ratio of open RyRs. Independent of SR Ca^{2+} load, the longer APD in HF-associated I_{K1} remodelling promotes greater frequency and magnitude of DADs, resulting in triggered activity, observations which are amplified at higher SR loads.

The SC model was then used to explore the mechanisms underlying action potential prolongation with increases in pacing frequency observed experimentally in rat ventricular myocytes. In agreement with previous studies, the model showed a frequency-dependent decrease in I_{to}, but also showed a role for I_{ss}. The effects of remodelled K^+ currents outweigh reductions to depolarising I_{CaL} to result in APD prolongation. In addition, an important role for I_{NaCa} in the inverse rate-dependence of the rat ventricular APD was identified, as reductions in I_{NaCa} shortened the APD across all tested frequencies, and could restore the APD at 10 Hz to the value observed under control conditions at 2 Hz.

7.3 Limitations

Throughout this thesis, frequent references are made to experimental data from the literature which were used to validate the model and inform some of the computational investigations. However, there is wide variation in experimental conditions, protocols employed and reagents used, thus experimental data ranges are sometimes large. Such variations may be a reflection of normal physiology, but may also represent a technical limitation. Thus, ideally, model validation would be performed against experimental data from a single, congruent, species-specific data source. This, however, is not always possible, and is particularly evident when validating against published restitution curves, the experimental protocols for which vary considerably between groups. Reasonable compromises must often be made, but it remains essential to check model outputs are reflective of normal cardiac physiology, and there is a growing need for the publication of experimental data so as to maxmise opportunities for model validation against a range of datasets.

In Chapters 5 and 6, experimental observations of ion channel or calcium handling remodeling were used to inform changes to model parameters in order to reflect either pharmacological blockade or pathophysiological remodelling. Changing model parameters in line with experimentally-observed mRNA or gene expression may not necessarily be valid, as reductions in expression and resultant decreases to current density may not occur to the same degree. Thus, for example, the 50% reduction to I_{K1} conductance used to simulate one aspect of heart failure observed experimentally in Chapter 5 may not be an accurate reflection of real changes to I_{K1} current density. However, correlations between mRNA expression and current density have been reported [191, 410]. Systemic correlative analysis is required in order to validate these changes.

Further, the reduction in I_{K1} implemented in Chapter 5, though informed from experimental data from heart failure myocytes, does not fully represent the heart failure phenotype. Pathophysiological ion channel remodelling is vast and multi-faceted, not involving changes to a solitary channel. Additionally, it is important to note that these HF-associated remodelling processes reflect only the electrophysiological alterations observed in diseases such as HF, which equally result in structural changes as well. Thus, the development of a full heart failure model is required, encorporating the full range of (validated) electrophysiological changes seen in the diseased state (and structural changes at the tissue-level), and would provide a powerful research tool for further mechanistic and *in silico* safety pharmacology investigations, as the emergence of spontaneous Ca^{2+} release events in heart failure is likely determined by a fine balance of the myriad of electrophysiological changes. Similarly, the simplified isoprenaline model used in this thesis represents a limitation, as it does not include validated dose-dependent effects of isoprenaline on cardiac electrophysiology. In tandem, a fully validated heart failure and isoprenaline model would provide a comprehensive framework for future investigations.

Works presented in this thesis are focused on single cell behaviours, however the heart comprises billions of single cells, and the behaviour of individual single cells has little impact on tissue or organ function. Thus, there is a requirement for the development of validated tissue models of rat ventricular electrophysiology, so that the link between sub-cellular pathophysiological remodelling and arrhythmogenesis at the tissue level can be dissected. It follows that the development of regional-specific single cell and tissue models would also be advantageous. Transmural heterogeneity throughout the ventricular wall influences the dynamics of excitation wave propagation, and further changes to heterogeneity such as in electrical remodelling can increase the propensity for arrhythmogenesis, for example by increasing the vulnerable window. This could have significant implications for the genesis of pathological excitation at the tissue level resulting from single cell spontaneous Ca^{2+} release events.

In addition, the works presented in this thesis are specific to rat ventricular myocytes, necessitated by the frequent of use of rats as animal models in cardiac electrophysiology. However, as detailed in Chapter 3, there are notable differences in the electrophysiological phenotypes of rats and human cardiomyocytes, which may be further exacerbated by other heterogeneities (e.g. transmural differences in channel expression). In particular, the triangular morphology of the rat action potential is markedly different from the spike and dome waveform seen in human ventricular myocytes, and these differences are underlain by differential expression of various K^+ currents, along with differing I_{CaL} kinetics. Thus, results such as those from the I_{K1} downregulation investigation in Chapter 5 may not have direct relevance to human cardiac physiology, given the longer APD and greater involvement of later K^+ currents in the human AP, which may compensate for reductions to I_{K1} by providing a larger repolarisation reserve. Also, the greater SR-dependence of Ca^{2+} handling in rat ventricular myocytes (compared to the larger contribution of I_{CaL} in human myocytes) mean that pro-arrhythmic mechanisms arising from Ca^{2+} mishandling may differ between the two species. However, there are still many similarities between human and rat electrophysiology, thus findings can still be important. In particular, the shift towards SR-dependent Ca^{2+} handling in the rat make it a sensitive model for the study of SR-dependent arrhythmia mechanisms, which are still prevalant in human [127]. It is still pertinent, however, to conduct similar investigations using a human computational model, in order to validate such findings. Nevertheless, the framework utilised throughout this thesis is suitable for the incorporation of models of other species, and this would allow direct comparison between, for example, rat and human behaviours under identical simulation conditions.

Comparison to published experimental restitution data was made in Chapters 3 and 4, but is often made difficult by quite significant heterogeneity in experimental datasets (as in Figures 3.17 to 3.20 and Figures 4.12 to 4.15). Different restitution protocols are utilised by (and within) research groups, which in combination with, for example, variations in animal lines and laboratory conditions, makes it difficult and unlikely that a model will perfectly reproduce restitution curves from multiple groups. Thus, comparisons of simulated to experimental restitution curves made in this thesis are done so in open acknowledgement of this inherent difficulty.

Furthermore, models are by definition simplifications of reality, and do not capture all aspects of physiology. Simulations are, therefore, a compromise between biophysical detail and computational efficiency, particularly at the tissue and organ levels. Nevertheless, they can provide important quantitative and mechanistic insight that is otherwise experimentally intractable. Their continued refinement, development and verification is therefore pivotal for future research.

7.4 Future works

7.4.1 Developing single cell model variants

In Chapter 5, electrophysiological alterations as observed in failing rat ventricular myocytes from experiments in our laboratory were simulated, to investigate if and how they may promote pro-arrhythmic behaviour in single myocytes. However, as described earlier, experimental observations of reduced channel expression do not necessarily correlate to equal reductions in current density (i.e. a 50% reduction in I_{to} mRNA expression does not necessarily result in a 50% reduction in I_{to} density). Such reduction or attenuation of simulated channel activity is therefore likely a simplification, and potentially unphysiological. However, there exists wide variability in ion channel and Ca^{2+} handling remodelling data in the literature, so data isolated from a consistent data source are desirable if such a goal is to be achieved. Congruent data sources do exist for channel expression in heart failure (e.g. in [34, 139]), but corresponding data for current densities, for example, are not always available. Incorporating such data into a model is further complicated by the rate-dependence of certain parameters.

The ability to modulate model parameters on a simulation-by-simulation basis is an invaluable asset computational modelling provides, as it allows for immediate investigations into certain phenomena that would otherwise take hours of laboratory time at considerable financial cost (to potentially fail, or reveal nothing). Though Monte Carlo simulation methods can be useful to explore a vast range of changes to multiple model parameters, there should always exist some degree of physiological constraint so as to ensure results remain feasible and meaningful. For this reason, inclusion of descriptions for isoprenaline-induced changes or heterogeneity should ideally be validated against experimental data, and not just include arbitrary scalings for certain parameters. Likewise, the preferential expression of proteins such as I_{NaCa} and I_{CaL} to the T-tubules can be disrupted in disease states, resulting in orphaned RyRs, or patches of detubulated membrane, which can disrupt normal electrophysiological processes and promote spontaneous Ca^{2+} release events. Thus, the development of rat-specific formulations for modulating conditions (such as isoprenaline or detubulation) can provide useful insight, but would need validation to ensure outputs are physiologically feasible. Table 7.1 shows example isoprenaline or HF data that could be utilised for the future refinement of the model. Similarly, the wide-ranging effects of other drugs, such as ryanodine or thapsigargin (discussed in Chapter 6), could be incorporated into the model for future studies.

Table 7.1. Experimental data for isoprenaline (ISO) or heart failure-associated (HF) remodelling.

Parameter	Control	Remodelled	Units	Condition	Source
Systolic $[Ca^{2+}]_{i,1Hz}$	0.483±0.002	0.767±0.004	μM	ISO	[341]
Systolic $[Ca^{2+}]_{i,2Hz}$	0.774	0.293	μM	ISO	[340]
Systolic $[Ca^{2+}]_{i,3Hz}$	0.389±0.065	0.421±0.06	μM	HF	[144]
Diastolic $[Ca^{2+}]_{i,2Hz}$	0.157	0.190	μM	ISO	[340]
Diastolic $[Ca^{2+}]_{i,3Hz}$	0.383±0.023	0.303±0.04	μM	HF	[144]
Diastolic $[Ca^{2+}]_{i,4Hz}$	0.133±0.011	0.251±0.022	μM	ISO	[121]
Diastolic $[Ca^{2+}]_{i,6Hz}$	0.156±0.013	0.364±0.019	μM	ISO	[121]
Diastolic $[Ca^{2+}]_{i,8Hz}$	0.179±0.018	0.496±0.051	μM	ISO	[121]
Amplitude $[Ca^{2+}]_{i,6Hz}$	0.153±0.023	1.318±0.246	μM	ISO	[121]
Amplitude $[Ca^{2+}]_{i,8Hz}$	0.087±0.017	1.159±0.246	μM	ISO	[121]
SR $[Ca^{2+}]_{1Hz}$	79.6±8	143±9	μM	ISO	[121]
SR $[Ca^{2+}]_{3Hz}$	0.147±0.038	0.15±0.039	μM	HF	[144]
SR $[Ca^{2+}]_{4Hz}$	86.9±7	170.56±9.9	μM	ISO	[121]
SR $[Ca^{2+}]_{6Hz}$	94.1±8	171.14±11.1	μM	ISO	[121]
SR $[Ca^{2+}]_{8Hz}$	96.96±9.9	180.49±14	μM	ISO	[121]
$APD_{90,4Hz}$	66±6	72±8	ms	ISO	[121]
$APD_{90,6Hz}$	62.8±5	39.1±8	ms	ISO	[121]
$APD_{90,8Hz}$	59.1±8	25.2±6	ms	ISO	[121]

Furthermore, it is well known that transmural heterogeneities in AP morphology exist for all mammalian species, and these result from differential expression of membrane currents and proteins. The APD of endocardial myocytes, for example, is consistently reported to be longer than in epicardial cells [92], and exhibit greater rate-dependent effects [363], characteristics which are important for inotropy [59]. These heterogeneities could dictate the response of different regions of the heart to pro-arrhythmic phenomena, and in tissue settings may influence spiral wave dynamics. Thus, the development of a suite of models from different regions of the heart (epicardial, endocardial, and midmyocardial, and for other regions such asthe Purkinje fibres) could provide useful insight into differing mechanisms underlying spontaneous Ca^{2+} release or on tissue-level arrhythmia dynamics.

The framework in which the model presented in this thesis is embedded within [97] permits the integration of further cell models and model variants.

7.4.2 Tissue modelling

In this thesis, the focus has been the development of a single cell model of rat ventricular electrophysiology and calcium handling in order to understand, quantify and explore electrophysiological alterations resulting from aberrant subcellular calcium cycling. However, arrhythmias are inherently organ-scale phenomena, and so visualisation of excitation-propagation within three-dimensions is required to understand the mechanisms underlying ventricular fibrillation, and other arrhythmias. Experimental studies to date have largely been restricted to mapping surface electrical activity [152, 435] or using plunge electrodes [71, 218]. More recently, however, advances have been achieved through mapping endocardial activity in sections of ventricular tissue [449] or by using dual-excitation wavelength fluorescence techniques (such as optical mapping) to simultaneously visualise transmembrane potential and calcium concentration changes [262, 420, 422]. Depth-resolved imaging techniques have also been used with some success to explore the mechanisms underlying VF [37].

To combat these experimental challenges, tissue-scale computational models can be utilised to study the complex 3D organisation of electrical excitation waves during arrhythmias. Reaction-diffusion models of cardiac electrophysiology incorporate dynamic AP behaviour alongside myocardial architecture (from imaging modalities such as diffusion tensor MRI, or contrast-enhanced micro CT [20, 36]) and offer a powerful alternative approach to studying complex 3D excitation phenomena. By allowing the investigator to control ion current or calcium handling properties, as well as tissue structure and anisotropy, such computational approaches provide potent platforms for investigating and quantifying arrhythmia dynamics [93, 94]. Furthermore, as HF is a complex condition in which there are multiple changes to cardiac electrophysiology, as well as structural remodelling, such structural data becomes of even greater importance when investigating disease mechanisms at the tissue-scale.

Though electrophysiological variability has been a focus in most studies to date [272], such tissue-scale models also allow for the investigation into how complex geometry and structural variation can underlie arrhythmia dynamics, which are less well understood. Preliminary results suggest that cardiac microanatomy and microstructure influence the dynamics of arrhythmias, alongside specific proprerties such as filament length and lifespan. The Fenton-Karma three variable (FK3V) minimal action potential model [136] was modified to reproduce the short ventricular AP and restitution characteristics in rat, then used in tissue simulations with geometries determined from diffusion tensor imaging (DTI) [385]. Arrhythmias were simulated by reducing conduction velocity by 50% to facilitate the sustenance of re-entry. Inclusion of DTI-based microstructure increased the filament number and length for initiated scroll waves, thereby increasing the propensity for sustained arrhythmias (Figure 7.1). Thus, for future translation of computational models to a clinical setting, the integration of patient-specific electrophysiology with personalised myocardial structure is likely to be a critical step.

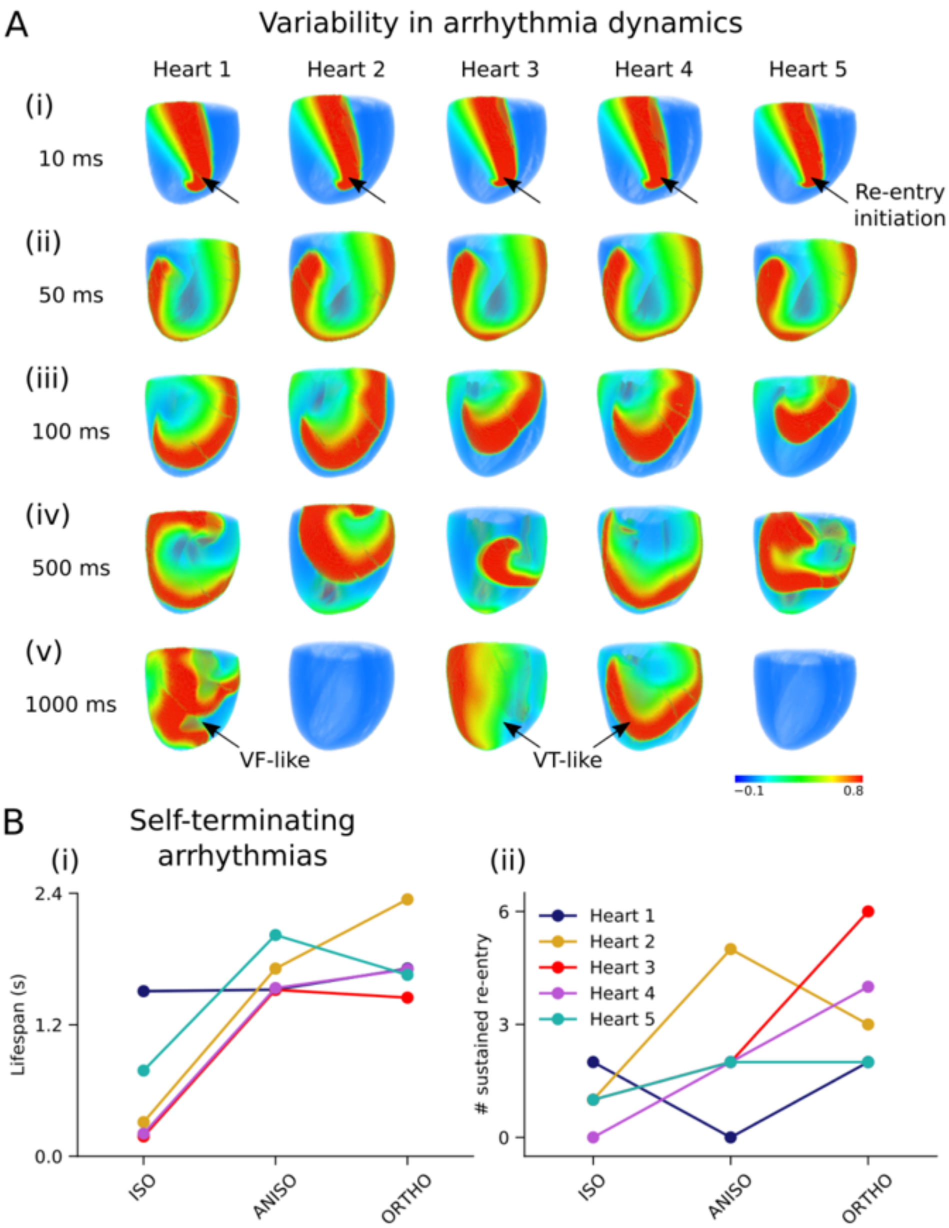

Figure 7.1. Effect of structure on arrhythmia dynamics. A: Scroll wave evolution from a prescribed location on the left ventricular wall (denoted by arrow) in 5 hearts at times t = (i) 10 ms, (ii) 50 ms, (iii) 100 ms, (iv) 500 ms, and (v) 1000 ms. Scroll waves either self-terminate, exhibit ventricular tachycardia (VT)-like behaviour, or degenerate into ventricular fibrillation (VF)-like excitations. B: Comparison between the 5 hearts of (i) lifespan of self-terminating arrhythmias under isotropic (ISO), anisotropic (ANISO), and orthotropic (ORTHO) conditions, and (ii) the number of sustained arrhythmias (lasting $>$ 5000 ms). Reproduced with permission from Dr Dominic Whittaker at the University of Nottingham (Whittaker *et al.*, unpublished).

Bibliography

[1] Abriel, H. (2010) Cardiac sodium channel Na(v)1.5 and interacting proteins: Physiology and pathophysiology. *Journal of Molecular and Cellular Cardiology*, **48**, 2–11.

[2] Abriel, H. & Kass, R. S. (2005) Regulation of the voltage-gated cardiac sodium channel Na(v)1.5 by interacting proteins. *Trends in Cardiovascular Medicine*, **15**, 35–40.

[3] Acsai, K., Kun, A., Farkas, A. S., Fulop, F., Nagy, N., Balazs, M., Szentandrassy, N., Nanasi, P. P., Papp, J. G., Varro, A. & Toth, A. (2007) Effect of partial blockade of the Na+/Ca2+-exchanger on Ca2+ handling in isolated rat ventricular inyocytes. *European Journal of Pharmacology*, **576**, 1–6.

[4] Aggarwal, R., Shorofsky, S. R., Goldman, L. & Balke, C. W. (1997) Tetrodotoxin-blockable calcium currents in rat ventricular myocytes; a third type of cardiac cell sodium current. *Journal of Physiology*, **505**, 353–369.

[5] Agus, Z. S., Dukes, I. D. & Morad, M. (1991) Divalent-cations modulate the transient outward current in rat ventricular myocytes. *American Journal of Physiology*, **261**, C310–C318.

[6] Aitman, T. J., Critser, J. K., Cuppen, E., Dominiczak, A., Fernandez-Suarez, X. M., Flint, J., Gauguier, D., Geurts, A. M., Gould, M., Harris, P. C., Holmdahl, R., Hubner, N., Izsvak, Z., Jacob, H. J., Kuramoto, T., Kwitek, A. E., Marrone, A., Mashimo, T., Moreno, C., Mullins, J., Mullins, L., Olsson, T., Pravenec, M., Riley, L., Saar, K., Serikawa, T., Shull, J. D., Szpirer, C., Twigger, S. N., Voigt, B. & Worley, K. (2008) Progress and prospects in rat genetics: a community view. *Nature Genetics*, **40**, 516–522.

[7] Alboni, P., Gianfranchi, L. & Brignole, M. (2009) Treatment of persistent sinus bradycardia with intermittent symptoms: are guidelines clear? *Europace*, **11**, 562–564.

[8] Ali, R. M., Al Kury, L. T., Yang, K. S., Qureshi, A., Rajesh, M., Galadari, S., Shuba, Y. M., Howarth, F. C. & Oz, M. (2015) Effects of cannabidiol on contractions and calcium signaling in rat ventricular myocytes. *Cell Calcium*, **57**, 290–299.

[9] Allen, D. G. & Kurihara, S. (1982) The effects of muscle length on intracellular calcium transients in mammalian cardiac-muscle. *Journal of Physiology-London*, **327**, 79–94.

[10] Allessie, M., Ausma, J. & Schotten, U. (2002) Electrical, contractile and structural remodeling during atrial fibrillation. *Cardiovascular Research*, **54**, 230–246.

[11] Alvarez, B. V., Perez, N. G., Ennis, I. L., de Hurtado, M. C. C. & Cingolani, H. E. (1999) Mechanisms underlying the increase in force and Ca2+ transient that follow stretch of cardiac muscle - A possible explanation of the Anrep effect. *Circulation Research*, **85**, 716–722.

[12] Alvarez-Collazo, J., Diaz-Garcia, C. M., Lopez-Medina, A. I., Vassort, G. & Alvarez, J. L. (2012) Zinc modulation of basal and beta-adrenergically stimulated L-type Ca2+ current in rat ventricular cardiomyocytes: consequences in cardiac diseases. *Pflugers Archiv-European Journal of Physiology*, **464**, 459–470.

[13] Amos, G. J., Abrahamsson, C., Duker, G., Hondeghem, L., Palmer, M. & Carlsson, L. (2001) Potassium and calcium current blocking properties of the novel antiarrhythmic agent H 345/52: implications for proarrhythmic potential. *Cardiovascular Research*, **49**, 351–360.

[14] Antzelevitch, C. (2000) Electrical heterogeneity, cardiac arrhythmias, and the sodium channel. *Circulation Research*, **87**, 964–965.

[15] Antzelevitch, C. (2007) Role of spatial dispersion of repolarization in inherited and acquired sudden cardiac death syndromes. *American Journal of Physiology-Heart and Circulatory Physiology*, **293**, H2024–H2038.

[16] Apkon, M. & Nerbonne, J. M. (1991) Characterization of 2 distinct depolarization-activated K+ currents in isolated adult-rat ventricular myocytes. *Journal of General Physiology*, **97**, 973–1011.

[17] Armoundas, A. A., Hohnloser, S. H., Ikeda, T. & Cohen, R. J. (2005) Can microvolt T-wave alternans testing reduce unnecessary defibrillator implantation? *Nature Clinical Practice Cardiovascular Medicine*, **2**, 522–528.

[18] Aslanidi, O. V., Boyett, M. R., Dobrzynski, H., Li, J. & Zhang, H. G. (2009) Mechanisms of Transition from Normal to Reentrant Electrical Activity in a Model of Rabbit Atrial Tissue: Interaction of Tissue Heterogeneity and Anisotropy. *Biophysical Journal*, **96**, 798–817.

[19] Aslanidi, O. V., Colman, M. A., Stott, J., Dobrzynski, H., Boyett, M. R., Holden, A. V. & Zhang, H. (2011) 3D virtual human atria: A computational platform for studying clinical atrial fibrillation. *Progress in Biophysics & Molecular Biology*, **107**, 156–68.

[20] Aslanidi, O. V., Nikolaidou, T., Zhao, J., Smaill, B. H., Gilbert, S. H., Holden, A. V., Lowe, T., Withers, P. J., Stephenson, R. S., Jarvis, J. C., Hancox, J. C., Boyett, M. R. & Zhang, H. (2013) Application of micro-computed tomography with iodine staining to cardiac imaging, segmentation, and computational model development. *IEEE Transactions on Medical Imaging*, **32**, 8–17.

[21] Babij, P., Askew, G. R., Nieuwenhuijsen, B., Su, C. M., Bridal, T. R., Jow, B., Argentieri, T. M., Kulik, J., DeGennaro, L. J., Spinelli, W. & Colatsky, T. J. (1998) Inhibition of cardiac delayed rectifier K+ current by overexpression of the long-QT syndrome HERG G628S mutation in transgenic mice. *Circulation Research*, **83**, 668–678.

[22] Baczkó, I., Giles, W. R. & Light, P. E. (2003) Resting membrane potential regulates Na+-Ca2+ exchange-mediated Ca2+ overload during hypoxia-reoxygenation in rat ventricular myocytes. *Journal of Physiology*, **550**, 889–898.

[23] Baczko, I., Jost, N., Virag, L., Bosze, Z. & Varro, A. (2016) Rabbit models as tools for preclinical cardiac electrophysiological safety testing: Importance of repolarization reserve. *Progress in Biophysics & Molecular Biology*, **121**, 157–168.

[24] Barandi, L., Harmati, G., Horvath, B., Szentandrassy, N., Magyar, J., Varro, A., Nanasi, P. P. & Banyasz, T. (2010) Drug-induced changes in action potential duration are proportional to action potential duration in rat ventricular myocardium. *General Physiology and Biophysics*, **29**, 309–313.

[25] Barr, R. C. & Plonsey, R. (2007) *Bioelectricity: A Quantitative Approach*. 3 edition. Springer.

[26] Barry, D. M. & Nerbonne, J. M. (1996) Myocardial potassium channels: Electrophysiological and molecular diversity. *Annual Review of Physiology*, **58**, 363–394.

[27] Bassani, J. W. M., Bassani, R. A. & Bers, D. M. (1994) Relaxation in rabbit and rat cardiac-cells - species-dependent differences in cellular mechanisms. *Journal of Physiology-London*, **476**, 279–293.

[28] Bassani, R. A., Bassani, J. W. M. & Bers, D. M. (1992) Mitochondrial and sarcolemmal Ca2+ transport reduce Ca2+ (I) during caffeine contractures in rabbit cardiac myocytes. *Journal of Physiology-London*, **453**, 591–608.

[29] Bassani, R. A. & Bers, D. M. (1995) Rate of diastolic Ca release rom the sarcoplasmic-reticulum of intact rabbit and rat ventricular myocytes. *Biophysical Journal*, **68**, 2015–2022.

[30] Bean, B. P., Cohen, C. J. & Tsien, R. W. (1983) Lidocaine block of cardiac sodium-channels. *Journal of General Physiology*, **81**, 613–642.

[31] Bébarová, M., Matejovič, P., Pásek, M., Ohlídalová, D., Jansová, D., Šimurdová, M. & Šimurda, J. (2010) Effect of ethanol on action potential and ionic membrane currents in rat ventricular myocytes. *Acta Physiologica*, **200**, 301–314.

[32] Beeler, G. W. & Reuter, H. (1977) Reconstruction of the action potential of ventricular myocardial fibres. *The Journal of Physiology*, **268**, 177–210.

[33] Belge, C., Massion, P. B., Pelat, M. & Balligand, J. L. (2005) Nitric oxide and the heart - Update on new paradigms. In: Sideman, S., Beyar, R. & Landesberg, A. (Editors) *Communicative Cardiac Cell*. Pages 173–182.

[34] Benoist, D., Stones, R., Drinkhill, M., Bernus, O. & White, E. (2011) Arrhythmogenic substrate in hearts of rats with monocrotaline-induced pulmonary hypertension and right ventricular hypertrophy. *American Journal of Physiology-Heart and Circulatory Physiology*, **300**, H2230–H2237.

[35] Benoist, D., Stones, R., Drinkhill, M. J., Benson, A. P., Yang, Z. K., Cassan, C., Gilbert, S. H., Saint, D. A., Cazorla, O., Steele, D. S., Bernus, O. & White,

E. (2012) Cardiac arrhythmia mechanisms in rats with heart failure induced by pulmonary hypertension. *American Journal of Physiology-Heart and Circulatory Physiology*, **302**, H2381–H2395.

[36] Benson, A. P., Aslanidi, O. V., Zhang, H. & Holden, A. V. (2008) The canine virtual ventricular wall: a platform for dissecting pharmacological effects on propagation and arrhythmogenesis. *Progress in Biophysics & Molecular Biology*, **96**, 187–208.

[37] Benson, A. P., Bernus, O., Dierckx, H., Gilbert, S. H., Greenwood, J. P., Holden, A. V., Mohee, K., Plein, S., Radjenovic, A., Ries, M. E., Smith, G. L., Sourbron, S. & Walton, R. D. (2011) Construction and validation of anisotropic and orthotropic ventricular geometries for quantitative predictive cardiac electrophysiology. *Interface Focus*, **1**, 101–16.

[38] Bers, D. M. (1989) SR Ca loading in cardiac-muscle preparations based on rapid-cooling contractures. *American Journal of Physiology*, **256**, C109–C120.

[39] Bers, D. M. (1991) Species-differences and the role of sodium-calcium exchange in cardiac-muscle relaxation. *Annals of the New York Academy of Sciences*, **639**, 375–385.

[40] Bers, D. M. (2000) Calcium fluxes involved in control of cardiac myocyte contraction. *Circulation Research*, **87**, 275–281.

[41] Bers, D. M. (2001) *Excitation-contraction coupling and cardiac contractile force*. Kluwer Academic Publishers.

[42] Bers, D. M. (2002) Cardiac excitation-contraction coupling. *Nature*, **415**, 198–205.

[43] Bers, D. M. (2014) Cardiac Sarcoplasmic Reticulum Calcium Leak: Basis and Roles in Cardiac Dysfunction. In: Julius, D. (Editor) *Annual Review of Physiology, Vol 76*. Pages 107–127.

[44] Beuckelmann, D. J., Nabauer, M. & Erdmann, E. (1993) Alterations of K+ currents in isolated human ventricular myocytes from patients with terminal heart-failure. *Circulation Research*, **73**, 379–385.

[45] Beuckelmann, D. J., Nabauer, M., Kruger, C. & Erdmann, E. (1995) Altered diastolic Ca2+ (i) handling in human ventricular myocytes from patients with terminal heart-failure. *American Heart Journal*, **129**, 684–689.

[46] Bezanilla, F. & Armstrong, C. M. (1977) Inactivation of sodium channel .1. Sodium current experiments. *Journal of General Physiology*, **70**, 549–566.

[47] Bhatnagar, P., Wickramasinghe, K., Wilkins, E. & Townsend, N. (2016) Trends in the epidemiology of cardiovascular disease in the UK. *Heart*, **102**, 1945–1952.

[48] Bhindi, R., Whiting, P. K., McMahon, A. C., Khachigian, L. M. & Lowe, H. C. (2006) Rat models of myocardial infarction - Pathogenetic insights and clinical relevance. *Thrombosis and Haemostasis*, **96**, 602–610.

[49] Biktashev, V. N. & Holden, A. V. (1998) Reentrant waves and their elimination in a model of mammalian ventricular tissue. *Chaos*, **8**, 48–56.

[50] Bilginoglu, A. & Kandilci, H. B. (2013) Intracellular levels of Na+ and TTX-sensitive Na+ channel current in diabetic rat ventricular cardiomyocytes. *Cardiovascular Toxicology*, **13**, 138–147.

[51] Blatter, L. A., Kockskamper, J., Sheehan, K. A., Zima, A. V., Huser, J. & Lipsius, S. L. (2003) Local calcium gradients during excitation-contraction coupling and alternans in atrial myocytes. *Journal of Physiology-London*, **546**, 19–31.

[52] Blatter, L. A. & Niggli, E. (1998) Confocal near-membrane detection of calcium in cardiac myocytes. *Cell Calcium*, **23**, 269–279.

[53] Blechschmidt, S., Haufe, V., Benndorf, K. & Zimmer, T. (2008) Voltage-gated Na+ channel transcript patterns in the mammalian heart are species-dependent. *Progress in Biophysics & Molecular Biology*, **98**, 309–318.

[54] Bode, E. F., Briston, S. J., Overend, C. L., O'Neill, S. C., Trafford, A. W. & Eisner, D. A. (2011) Changes of SERCA activity have only modest effects on sarcoplasmic reticulum Ca2+ content in rat ventricular myocytes. *Journal of Physiology-London*, **589**, 4723–4729.

[55] Bogeholz, N., Muszynski, A. & Pott, C. (2012) The physiology of cardiac calcium handling. *Wien Med Wochenschr*, **162**, 278–82.

[56] Bondarenko, V. E., Szigeti, G. P., Bett, G. C., Kim, S. J. & Rasmusson, R. L. (2004) Computer model of action potential of mouse ventricular myocytes. *American Journal of Physiology - Heart and Circulatory Physiology*, **287**, H1378–403.

[57] Bou-Abboud, E., Li, H. L. & Nerbonne, J. M. (2000) Molecular diversify of the repolarizing voltage-gated K+ currents in mouse atrial cells. *Journal of Physiology-London*, **529**, 345–358.

[58] Bouchard, R. A. & Bose, D. (1989) Analysis of the interval-force relationship in rat and canine ventricular myocardium. *American Journal of Physiology*, **257**, H2036–47.

[59] Bouchard, R. A., Clark, R. B. & Giles, W. R. (1995) EFfects of action-potential duration on excitation-contraction coupling in rat ventricular myocytes - action-potential voltage-clamp measurements. *Circulation Research*, **76**, 790–801.

[60] Bowditch, H. P. (1871) Über die Eigentümlichkeiten der Reizbarkeit welche die Muskelfasern des Herzens zeigen. *Arbeiten aus der Physiologischen Anstalt zu Leipzig*, 652–89.

[61] Boyett, M. R. & Fedida, D. (1987) The effect of heart rate on the membrane currents of isolated sheep Purkinje fibres. *Journal of Physiology*, **399**, 467–491.

[62] Boyle, W. A. & Nerbonne, J. M. (1991) A novel type of depolarization-activated K+ current in isolated adult-rat atrial myocytes. *American Journal of Physiology*, **260**, H1236–H1247.

[63] Brette, F., Komukai, K. & Orchard, C. H. (2002) Validation of formamide as a detubulation agent in isolated rat cardiac cells. *American Journal of Physiology-Heart and Circulatory Physiology*, **283**, H1720–H1728.

[64] Brette, F. & Orchard, C. (2003) T-tubule function in mammalian cardiac myocytes. *Circulation Research*, **92**, 1182–1192.

[65] Brette, F. & Orchard, C. H. (2006) Density and sub-cellular distribution of cardiac and neuronal sodium channel isoforms in rat ventricular myocytes. *Biochemical and Biophysical Research Communications*, **348**, 1163–1166.

[66] Brooksby, P., Levi, A. J. & Jones, J. V. (1992) Calcium handling in ventricular myocytes from the spontaneously hypertensive rat (SHR). *Journal of Molecular and Cellular Cardiology*, **24**, S46–S46.

[67] Brown, H. & Kozlowski, R. (1997) *Physiology and Pharmacology of the Heart*. 1 edition. Blackwell Science Ltd.

[68] Brunet, S., Aimond, F., Li, H. L., Guo, W. N., Eldstrom, J., Fedida, D., Yamada, K. A. & Nerbonne, J. M. (2004) Heterogeneous expression of repolarizing, voltage-gated K+ currents in adult mouse ventricles. *Journal of Physiology-London*, **559**, 103–120.

[69] Bugenhagen, S. M. & Beard, D. A. (2015) Computational analysis of the regulation of Ca2+ dynamics in rat ventricular myocytes. *Physical Biology*, **12**, 056008.

[70] Calaghan, S. & White, E. (2004) Activation of Na+-H+ exchange and stretch-activated channels underlies the slow inotropic response to stretch in myocytes and muscle from the rat heart. *Journal of Physiology-London*, **559**, 205–214.

[71] Caldwell, B. J., Trew, M. L., Sands, G. B., Hooks, D. A., LeGrice, I. J. & Smaill, B. H. (2009) Three Distinct Directions of Intramural Activation Reveal Nonuniform Side-to-Side Electrical Coupling of Ventricular Myocytes. *Circulation-Arrhythmia and Electrophysiology*, **2**, 433–440.

[72] Callewaert, G., Cleemann, L. & Morad, M. (1989) Caffeine-induced Ca2+ release activates Ca2+ extrusion via Na+-Ca2+ exchanger in cardiac myocytes. *American Journal of Physiology*, **257**, C147–C152.

[73] Campbell, S. E., Gerdes, A. M. & Smith, T. D. (1987) Comparison of regional differences in cardiac myocyte dimensions in rats, hamsters, and guinea-pigs. *Anatomical Record*, **219**, 53–59.

[74] Campos, F. O., Shiferaw, Y., Prassl, A. J., Boyle, P. M., Vigmond, E. J. & Plank, G. (2015) Stochastic spontaneous calcium release events trigger premature ventricular complexes by overcoming electrotonic load. *Cardiovascular Research*, **107**, 175–183.

[75] Cannell, M. B. & Kong, C. H. T. (2012) Local control in cardiac E-C coupling. *Journal of Molecular and Cellular Cardiology*, **52**, 298–303.

[76] Cannell, M. B., Kong, C. H. T., Imtiaz, M. S. & Laver, D. R. (2013) Control of Sarcoplasmic Reticulum Ca2+ Release by Stochastic RyR Gating within a 3D Model of the Cardiac Dyad and Importance of Induction Decay for CICR Termination. *Biophysical Journal*, **104**, 2149–2159.

[77] Carmeliet, E. (2004) Intracellular Ca(2+) concentration and rate adaptation of the cardiac action potential. *Cell Calcium*, **35**, 557–73.

[78] Casadei, B. & Sears, C. E. (2003) Nitric-oxide-mediated regulation of cardiac contractility and stretch responses. *Progress in Biophysics & Molecular Biology*, **82**, 67–80.

[79] Casimiro, M. C., Knollmann, B. C., Ebert, S. N., Vary, J. C., Greene, A. E., Franz, M. R., Grinberg, A., Huang, S. P. & Pfeifer, K. (2001) Targeted disruption of the Kcnq1 gene produces a mouse model of Jervell and Lange-Nielsen Syndrome. *Proceedings of the National Academy of Sciences of the United States of America*, **98**, 2526–2531.

[80] Cerbai, E., Barbieri, M. & Mugelli, A. (1994) Characterization of the hyperpolarization-activated current, I-f, in ventricular myocytes isolated from hypertensive rats. *Journal of Physiology-London*, **481**, 585–591.

[81] Cerbai, E., Barbieri, M. & Mugelli, A. (1996) Occurrence and properties of the hyperpolarization-activated current if in ventricular myocytes from normotensive and hypertensive rats during aging. *Circulation*, **94**, 1674–1681.

[82] Cerbai, E., Pino, R., Porciatti, F., Sani, G., Toscano, M., Maccherini, M., Giunti, G. & Mugelli, A. (1997) Characterization of the hyperpolarization-activated current, I-f, in ventricular myocytes from human failing heart. *Circulation*, **95**, 568–571.

[83] Cerbai, E., Pino, R., Sartiani, L. & Mugelli, A. (1999) Influence of postnatal-development on I-f occurrence and properties in neonatal rat ventricular myocytes. *Cardiovascular Research*, **42**, 416–423.

[84] Chen, K., Xu, X., Sun, H., Du, X., Liu, H., Yang, L., Xiao, G., Wang, Y., Jin, M. & Li, G. (2016) Distinctive property and pharmacology of voltage-gated sodium currents in rat atrial vs ventricular myocytes. *Heart Rhythm*, **13**, 762–770.

[85] Chen, P. S., Wu, T. J., Ting, C. T., Karagueuzian, H. S., Garfinkel, A., Lin, S. F. & Weiss, J. N. (2003) A tale of two fibrillations. *Circulation*, **108**, 2298–2303.

[86] Chen, X. D., Feng, Y. D., Huo, Y. L. & Tan, W. C. (2018) The Interplay of Rogue and Clustered Ryanodine Receptors Regulates Ca2+ Waves in Cardiac Myocytes. *Frontiers in Physiology*, **9**, volume.

[87] Chen, Y., Chen, Y., Chen, S. & Lin, C. (2009) Cardiac Cellular Electrophysiology, Voltage Clamp, and Patch Clamp. *Acta Cardiologica Sinica*, **25**, 59–63.

[88] Cheng, H. P. & Lederer, W. J. (2008) Calcium sparks. *Physiological Reviews*, **88**, 1491–1545.

[89] Choi, H. S., Trafford, A. W., Orchard, C. H. & Eisner, D. A. (2000) The effect of acidosis on systolic Ca2+ and sarcoplasmic reticulum calcium content in isolated rat ventricular myocytes. *Journal of Physiology-London*, **529**, 661–668.

[90] Cingolani, H. E., Chiappe, G. E., Ennis, I. L., Morgan, P. G., Alvarez, B. V., Casey, J. R., Dulce, R. A., Perez, N. G. & de Hurtado, M. C. C. (2003) Influence of Na+-independent Cl–HCO3- exchange on the slow force response to myocardial stretch. *Circulation Research*, **93**, 1082–1088.

[91] Clark, R. B., Bouchard, R. A. & Giles, W. R. (1996) Action potential duration modulates calcium influx, Na+-Ca2+ exchange, and intracellular calcium release in rat ventricular myocytes. In: Hilgemann, D. W., Philipson, K. D. & Vassort, G. (Editors) *Sodium-Calcium Exchange: Proceedings of the Third International Conference*. Pages 417–429.

[92] Clark, R. B., Bouchard, R. A., Salinasstefanon, E., Sanchezchapula, J. & Giles, W. R. (1993) Heterogeneity of action-potential wave-forms and potassium currents in rat ventricle. *Cardiovascular Research*, **27**, 1795–1799.

[93] Clayton, R. H., Bernus, O., Cherry, E. M., Dierckx, H., Fenton, F. H., Mirabella, L., Panfilov, A. V., Sachse, F. B., Seemann, G. & Zhang, H. (2011) Models of cardiac tissue electrophysiology: progress, challenges and open questions. *Progress in Biophysics & Molecular Biology*, **104**, 22–48.

[94] Clayton, R. H., Zhuchkova, E. A. & Panfilov, A. V. (2006) Phase singularities and filaments: Simplifying complexity in computational models of ventricular fibrillation. *Progress in Biophysics & Molecular Biology*, **90**, 378–398.

[95] Colatsky, T. J. & Tsien, R. W. (1979) Sodium channels in rabbit cardiac Purkinje-fibers. *Nature*, **278**, 265–268.

[96] Colinas, O., Gallego, M., Setien, R., Lopez-Lopez, J. R., Perez-Garcia, M. T. & Casis, O. (2006) Differential modulation of Kv4.2 and Kv4.3 channels by

calmodulin-dependent protein kinase II in rat cardiac myocytes. *American Journal of Physiology-Heart and Circulatory Physiology*, **291**, H1978–H1987.

[97] Colman, M. A. (2019) Arrhythmia mechanisms and spontaneous calcium release: Bi-directional coupling between re-entrant and focal excitation. *PLoS Computational Biology*, **15**.

[98] Colman, M. A., Alday, E. A. P., Holden, A. V. & Benson, A. P. (2017) Trigger vs. Substrate: Multi-Dimensional Modulation of QT-Prolongation Associated Arrhythmic Dynamics by a hERG Channel Activator. *Frontiers in Physiology*, **8**.

[99] Colman, M. A., Aslanidi, O. V., Kharche, S., Boyett, M. R., Garratt, C., Hancox, J. C. & Zhang, H. (2013) Pro-arrhythmogenic effects of atrial fibrillation-induced electrical remodelling: insights from the three-dimensional virtual human atria. *Journal of Physiology*, **591**, 4249–72.

[100] Colman, M. A., Parra-Rojas, C. & Perez-Alday, E. A. (2015) From Microscopic Calcium Sparks to the ECG: Model Reduction Approaches for Multi-scale Cardiac Simulation. *Computing in Cardiology*, **2015**, 325–328.

[101] Colman, M. A., Pinali, C., Trafford, A. W., Zhang, H. G. & Kitmotto, A. (2017) A computational model of spatio-temporal cardiac intracellular calcium handling with realistic structure and spatial flux distribution from sarcoplasmic reticulum and t-tubule reconstructions. *PLoS Computational Biology*, **13**.

[102] Cooke, R. (2004) Milestone in physiology - The sliding filament model: 1972-2004. *Journal of General Physiology*, **123**, 643–656.

[103] Cooper, J., Mirams, G. R. & Niederer, S. A. (2011) High-throughput functional curation of cellular electrophysiology models. *Progress in Biophysics & Molecular Biology*, **107**, 11–20.

[104] Cortassa, S., Aon, M. A., Marban, E., Winslow, R. L. & O'Rourke, B. (2003) An integrated model of cardiac mitochondrial energy metabolism and calcium dynamics. *Biophysical Journal*, **84**, 2734–2755.

[105] Cortassa, S., Aon, M. A., O'Rourke, B., Jacques, R., Tseng, H. J., Marban, E. & Winslow, R. L. (2006) A computational model integrating electrophysiology, contraction, and mitochondrial bioenergetics in the ventricular myocyte. *Biophysical Journal*, **91**, 1564–1589.

[106] Cox, B. (2014) Ion channel drug discovery: a historical perspective. In: Cox, B. & Gosling, M. (Editors) *Ion Channel Drug Discovery*. Royal Society of Chemistry. chapter 1, Pages 1–15.

[107] Craig, R. & Lehman, W. (2001) Crossbridge and tropomyosin positions observed in native, interacting thick and thin filaments. *Journal of Molecular Biology*, **311**, 1027–1036.

[108] Crampin, E. J. & Smith, N. P. (2006) A dynamic model of excitation-contraction coupling during acidosis in cardiac ventricular myocytes. *Biophysical Journal*, **90**, 3074–3090.

[109] Crotti, L., Celano, G., Dagradi, F. & Schwartz, P. J. (2008) Congenital long QT syndrome. *Orphanet Journal of Rare Diseases*, **3**, volume.

[110] Davies, M. R., Wang, K., Mirams, G. R., Caruso, A., Noble, D., Walz, A., Lave, T., Schuler, F., Singer, T. & Polonchuk, L. (2016) Recent developments in using mechanistic cardiac modelling for drug safety evaluation. *Drug Discovery Today*, **21**, 924–38.

[111] de Boer, T. P. & Stengl, M. (2018) Action potential contour and inter-species differences. *Europace*, **20**, 1395–1396.

[112] de Tombe, P. P. & ter Keurs, H. E. (1990) Force and velocity of sarcomere shortening in trabeculae from rat heart. Effects of temperature. *Circulation Research*, **66**, 1239–54.

[113] Delgado, C., Artiles, A., Gomez, A. M. & Vassort, G. (1999) Frequency-dependent increase in cardiac Ca2+ current is due to reduced Ca2+ release by the sarcoplasmic reticulum. *Journal of Molecular and Cellular Cardiology*, **31**, 1783–1793.

[114] Demir, S. S., Clark, J. W., Murphey, C. R. & Giles, W. R. (1994) A mathematical-model of a rabbit sinoatrial node cell. *American Journal of Physiology*, **266**, C832–C852.

[115] Despa, S. & Bers, D. M. (2003) Na/K pump current and Na (i) in rabbit ventricular myocytes: Local Na (i) depletion and Na buffering. *Biophysical Journal*, **84**, 4157–4166.

[116] Devenyi, R. A., Ortega, F. A., Groenendaal, W., Krogh-Madsen, T., Christini, D. J. & Sobie, E. A. (2017) Differential roles of two delayed rectifier potassium currents in regulation of ventricular action potential duration and arrhythmia susceptibility. *Journal of Physiology-London*, **595**, 2301–2317.

[117] Devenyi, R. A. & Sobie, E. A. (2016) There and back again: Iterating between population-based modeling and experiments reveals surprising regulation of calcium transients in rat cardiac myocytes. *Journal of Molecular and Cellular Cardiology*, **96**, 38–48.

[118] Dhalla, N. S., Dixon, I. M. C., Rupp, H. & Barwinsky, J. (1991) Experimental congestive-heart-failure due to myocardial-infarction - sarcolemmal receptors and cation transporters. *Basic Research in Cardiology*, **86**, 13–23.

[119] Dhamoon, A. S. & Jalife, J. (2005) The inward rectifier current (I-K1) controls cardiac excitability and is involved in arrhythmogenesis. *Heart Rhythm*, **2**, 316–324.

[120] Dhamoon, A. S., Pandit, S. V., Sarmast, F., Parisian, K. R., Guha, P., Li, Y., Bagwe, S., Taffet, S. M. & Anumonwo, J. M. B. (2004) Unique Kir2.x properties determine regional and species differences in the cardiac inward rectifier K+ current. *Circulation Research*, **94**, 1332–1339.

[121] Dibb, K. M., Eisner, D. A. & Trafford, A. W. (2007) Regulation of systolic Ca2+ (i) and cellular Ca2+ flux balance in rat ventricular myocytes by SR Ca2+, L-type Ca2+ current and diastolic Ca2+ (i). *Journal of Physiology-London*, **585**, 579–592.

[122] DiFrancesco, D. & Noble, D. (1985) A model of cardiac electrical-activity incorporating ionic pumps and concentration changes. *Philosophical Transactions of the Royal Society of London Series B-Biological Sciences*, **307**, 353–398.

[123] Dilly, S. G. & Lab, M. J. (1988) Electrophysiological alternans and restitution during acute regional ischaemia in myocardium of anaesthetized pig. *Journal of Physiology*, **402**, 315–33.

[124] Dorian, P. & Newman, D. (2000) Rate dependence of the effect of antiarrhythmic drugs delaying cardiac repolarization: an overview. *Europace*, **2**, 277–85.

[125] Drici, M. D., Baker, L., Plan, P., Barhanin, J., Romey, G. & Salama, G. (2002) Mice display sex differences in halothane-induced polymorphic ventricular tachycardia. *Circulation*, **106**, 497–503.

[126] Edwards, A. G., Grandi, E., Hake, J. E., Patel, S., Li, P., Miyamoto, S., Omens, J. H., Brown, J. H., Bers, D. M. & McCulloch, A. D. (2014) Nonequilibrium Reactivation of Na+ Current Drives Early Afterdepolarizations in Mouse Ventricle. *Circulation-Arrhythmia and Electrophysiology*, **7**, 1205–U366.

[127] Edwards, A. G. & Louch, W. E. (2017) Species-Dependent Mechanisms of Cardiac Arrhythmia: A Cellular Focus. *Clinical Medicine Insights-Cardiology*, **11**, volume.

[128] Edwards, J. N. & Blatter, L. A. (2014) Cardiac alternans and intracellular calcium cycling. *Clinical and Experimental Pharmacology and Physiology*, **41**, 524–32.

[129] Eisner, D., Bode, E., Venetucci, L. & Trafford, A. (2013) Calcium flux balance in the heart. *Journal of Molecular and Cellular Cardiology*, **58**, 110–117.

[130] Eisner, D. A., Kashimura, T., Venetucci, L. A. & Trafford, A. W. (2009) From the Ryanodine Receptor to Cardiac Arrhythmias. *Circulation Journal*, **73**, 1561–1567.

[131] Endoh, M. (2004) Force-frequency relationship in intact mammalian ventricular myocardium: physiological and pathophysiological relevance. *European Journal of Pharmacology*, **500**, 73–86.

[132] Fabiato, A. & Fabiato, F. (1972) Excitation-contraction coupling of isolated cardiac fibers with disrupted or closed sarcolemmas - calcium-dependent cyclic and tonic contractions. *Circulation Research*, **31**, 293–+.

[133] Fauconnier, J., Bedut, S., Le Guennec, J. Y., Babuty, D. & Richard, S. (2003) Ca2+ current-mediated regulation of action potential by pacing rate in rat ventricular myocytes. *Cardiovascular Research*, **57**, 670–680.

[134] Fauconnier, J., Lacampagne, A., Rauzier, J. M., Vassort, G. & Richard, S. (2005) Ca2+-dependent reduction of IK1 in rat ventricular cells: a novel paradigm for arrhythmia in heart failure? *Cardiovascular Research*, **68**, 204–12.

[135] Feng, J. L., Yue, L. X., Wang, Z. G. & Nattel, S. (1998) Ionic mechanisms of regional action potential heterogeneity in the canine right atrium. *Circulation Research*, **83**, 541–551.

[136] Fenton, F. & Karma, A. (1998) Vortex dynamics in three-dimensional continuous myocardium with fiber rotation: Filament instability and fibrillation. *Chaos*, **8**, 20–47.

[137] Findlay, I. (2003) Is there an A-type K+ current in guinea pig ventricular myocytes? *American Journal of Physiology-Heart and Circulatory Physiology*, **284**, H598–H604.

[138] Flister, M. J., Prokop, J. W., Lazar, J., Shimoyama, M., Dwinell, M. & Geurts, A. (2015) 2015 guidelines for establishing genetically modified rat models for cardiovascular research. *Journal of Cardiovascular Translational Research*, **8**, 269–277.

[139] Fowler, E. D., Drinkhill, M. J., Norman, R., Pervolaraki, E., Stones, R., Steer, E., Benoist, D., Steele, D. S., Calaghan, S. C. & White, E. (2018) Beta1-adrenoceptor antagonist, metoprolol attenuates cardiac myocyte Ca2+ handling dysfunction in rats with pulmonary artery hypertension. *Journal of Molecular and Cellular Cardiology*, **120**, 74–83.

[140] Fowler, M. R., Dobson, R. S., Orchard, C. H. & Harrison, S. M. (2004) Functional consequences of detubulation of isolated rat ventricular myocytes. *Cardiovascular Research*, **62**, 529–537.

[141] Frampton, J. E., Harrison, S. M., Boyett, M. R. & Orchard, C. H. (1991) Ca2+ and Na+ in rat myocytes showing different force-frequency relationships. *American Journal of Physiology*, **261**, C739–C750.

[142] Franz, M. R. (2003) The electrical restitution curve revisited: Steep or flat slope - Which is better? *Journal of Cardiovascular Electrophysiology*, **14**, S140–S147.

[143] Frisk, M., Koivumaki, J. T., Norseng, P. A., Maleckar, M. M., Sejersted, O. M. & Louch, W. E. (2014) Variable t-tubule organization and Ca2+ homeostasis across the atria. *American Journal of Physiology-Heart and Circulatory Physiology*, **307**, H609–H620.

[144] Gandhi, A., Siedlecka, U., Shah, A. P., Navaratnarajah, M., Yacoub, M. H. & Terracciano, C. M. (2013) The Effect of SN-6, a Novel Sodium-Calcium Exchange Inhibitor, on Contractility and Calcium Handling in Isolated Failing Rat Ventricular Myocytes. *Cardiovascular Therapeutics*, **31**, E115–E124.

[145] Garfinkel, A., Kim, Y. H., Voroshilovsky, O., Qu, Z. L., Kil, J. R., Lee, M. H., Karagueuzian, H. S., Weiss, J. N. & Chen, P. S. (2000) Preventing ventricular fibrillation by flattening cardiac restitution. *Proceedings of the National Academy of Sciences of the United States of America*, **97**, 6061–6066.

[146] Gattoni, S., Roe, A. T., Frisk, M., Louch, W. E., Niederer, S. A. & Smith, N. P. (2016) The calcium-frequency response in the rat ventricular myocyte: an experimental and modelling study. *Journal of Physiology-London*, **594**, 4193–4224.

[147] Gaur, N. & Rudy, Y. (2011) Multiscale Modeling of Calcium Cycling in Cardiac Ventricular Myocyte: Macroscopic Consequences of Microscopic Dyadic Function. *Biophysical Journal*, **100**, 2904–2912.

[148] Gauthier, L. D., Greenstein, J. L. & Winslow, R. L. (2012) Toward an integrative computational model of the guinea pig cardiac myocyte. *Frontiers in Physiology*, **3**, volume.

[149] Giles, W. R. & Imaizumi, Y. (1988) Comparison of potassium currents in rabbit atrial and ventricular cells. *Journal of Physiology-London*, **405**, 123–145.

[150] Gomez, A. M., Benitah, J. P., Henzel, D., Vinet, A., Lorente, P. & Delgado, C. (1997) Modulation of electrical heterogeneity by compensated hypertrophy in rat left ventricle. *American Journal of Physiology-Heart and Circulatory Physiology*, **272**, H1078–H1086.

[151] Grandi, E., Pasqualini, F. S., Puglisi, J. L. & Bers, D. M. (2009) A Novel Computational Model of the Human Ventricular Action Potential and Ca transient. *Biophysical Journal*, **96**, 664A–665A.

[152] Gray, R. A., Pertsov, A. M. & Jalife, J. (1998) Spatial and temporal organization during cardiac fibrillation. *Nature*, **392**, 75–78.

[153] Greensmith, D. J., Eisner, D. A. & Nirmalan, M. (2010) The effects of hydrogen peroxide on intracellular calcium handling and contractility in the rat ventricular myocyte. *Cell Calcium*, **48**, 341–351.

[154] Guo, A., Zhang, C. M., Wei, S., Chen, B. Y. & Song, L. S. (2013) Emerging mechanisms of T-tubule remodelling in heart failure. *Cardiovascular Research*, **98**, 204–215.

[155] Guo, D., Zhou, J., Zhao, X., Gupta, P., Kowey, P. R., Martin, J., Wu, Y., Liu, T. & Yan, G. X. (2008) L-type calcium current recovery versus ventricular repolarization: preserved membrane-stabilizing mechanism for different QT intervals across species. *Heart Rhythm*, **5**, 271–279.

[156] Guo, W. N., Xu, H. D., London, B. & Nerbonne, J. M. (1999) Molecular basis of transient outward K+ current diversity in mouse ventricular myocytes. *Journal of Physiology-London*, **521**, 587–599.

[157] Guyton, A. C. & Hall, J. E. (2000) *Texbook of Medical Physiology*. Saunders/Elsevier.

[158] Hamlin, R. L. (2007) Animal models of ventricular arrhythmias. *Pharmacology & Therapeutics*, **113**, 276–95.

[159] Hardy, M. E. L., Pervolaraki, E., Bernus, O. & White, E. (2018) Dynamic Action Potential Restitution Contributes to Mechanical Restitution in Right Ventricular Myocytes From Pulmonary Hypertensive Rats. *Frontiers in Physiology*, **9**, volume.

[160] Hedley, P. L., Jorgensen, P., Schlamowitz, S., Wangari, R., Moolman-Smook, J., Brink, P. A., Kanters, J. K., Corfield, V. A. & Christiansen, M. (2009) The genetic basis of long QT and short QT syndromes: A mutation update. *Human Mutation*, **30**, 1486–1511.

[161] Heijman, J., Voigt, N., Nattel, S. & Dobrev, D. (2014) Cellular and molecular electrophysiology of atrial fibrillation initiation, maintenance, and progression. *Circulation Research*, **114**, 1483–1499.

[162] Heinzel, F. R., Bito, V., Volders, P. G. A., Antoons, G., Mubagwa, K. & Sipido, K. R. (2002) Spatial and temporal inhomogeneities during Ca2+ release from the sarcoplasmic reticulum in pig ventricular myocytes. *Circulation Research*, **91**, 1023–1030.

[163] Herren, A. W., Bers, D. M. & Grandi, E. (2013) Post-translational modifications of the cardiac Na channel: contribution of CaMKII-dependent phosphorylation to acquired arrhythmias. *American Journal of Physiology-Heart and Circulatory Physiology*, **305**, H431–H445.

[164] Hilgemann, D. W. & Noble, D. (1987) Excitation contraction coupling and extracellular calcium transients in rabbit atrium - reconstruction of basic cellular mechanisms. *Proceedings of the Royal Society Series B-Biological Sciences*, **230**, 163–205.

[165] Hinch, R. (2004) A mathematical analysis of the generation and termination of calcium sparks. *Biophysical Journal*, **86**, 1293–1307.

[166] Hinch, R., Greenstein, J. L., Tanskanen, A. J., Xu, L. & Winslow, R. L. (2004) A simplified local control model of calcium-induced calcium release in cardiac ventricular myocytes. *Biophysical Journal*, **87**, 3723–36.

[167] Hodgkin, A. L. & Huxley, A. F. (1952) The components of membrane conductance in the giant axon of Loligo. *Journal of Physiology-London*, **116**, 473–496.

[168] Hodgkin, A. L. & Huxley, A. F. (1952) Currents carried by sodium and potassium ions through the membrane of the giant axon of Loligo. *Journal of Physiology-London*, **116**, 449–472.

[169] Hodgkin, A. L. & Huxley, A. F. (1952) The dual effect of membrane potential on sodium conductance in the giant axon of Loligo. *Journal of Physiology-London*, **116**, 497–506.

[170] Hodgkin, A. L. & Huxley, A. F. (1952) A quantitative description of membrane current and its application to conduction and excitation in nerve. *The Journal of Physiology*, **117**, 500–544.

[171] Hodgkin, A. L. & Huxley, A. F. (1952) A quantitative description of membrane current and its application to conduction and excitation in nerve. *Journal of Physiology-London*, **117**, 500–544.

[172] Hodgkin, A. L., Huxley, A. F. & Katz, B. (1952) Measurement of current-voltage relations in the membrane of the giant axon of Loligo. *Journal of Physiology-London*, **116**, 424–448.

[173] Hof, T., Simard, C., Rouet, R., Salle, L. & Guinamard, R. (2013) Implication of the TRPM4 nonselective cation channel in mammalian sinus rhythm. *Heart Rhythm*, **10**, 1683–1689.

[174] Holmes, K. C. & Geeves, M. A. (2000) The structural basis of muscle contraction. *Philosophical Transactions of the Royal Society of London Series B-Biological Sciences*, **355**, 419–431.

[175] Holzem, K. M. & Efimov, I. R. (2012) Arrhythmogenic remodelling of activation and repolarization in the failing human heart. *Europace*, **14**, 50–57.

[176] Hondeghem, L. M., Carlsson, L. & Duker, G. (2001) Instability and triangulation of the action potential predict serious proarrhythmia, but action potential duration prolongation is antiarrhythmic. *Circulation*, **103**, 2004–2013.

[177] Hondeghem, L. M., Dujardin, K. & De Clerck, F. (2001) Phase 2 prolongation, in the absence of instability and triangulation, antagonizes class III proarrhythmia. *Cardiovascular Research*, **50**, 345–353.

[178] Hood, A. R., Ai, X. & Pogwizd, S. M. (2017) Regulation of cardiac gap junctions by protein phosphatases. *Journal of Molecular and Cellular Cardiology*, **107**, 52–57.

[179] Huang, B., El-Sherif, T., Gidh-Jain, M., Qin, D. Y. & El-Sherif, N. (2001) Alterations of sodium channel kinetics and gene expression in the postinfarction remodeled myocardium. *Journal of Cardiovascular Electrophysiology*, **12**, 218–225.

[180] Huang, G., Tong, C., Kumbhani, D. S., Ashton, C., Yan, H. & Ying, Q. (2011) Beyond knockout rats: New insights into finer genome manipulation in rats. *Cell Cycle*, **10**, 1059–1066.

[181] Hund, T. J., Kucera, J. P., Otani, N. F. & Rudy, Y. (2001) Ionic charge conservation and long-term steady state in the Luo-Rudy dynamic cell model. *Biophysical Journal*, **81**, 3324–3331.

[182] Jacob, H. J. & Kwitek, A. E. (2002) Rat genetics: Attaching physiology and pharmacology to the genome. *Nature Reviews Genetics*, **3**, 33–42.

[183] Jacques, D., Bkaily, G., Jasmin, G., Menard, D. & Proschek, L. (1997) Early fetal like slow Na+ current in heart cells of cardiomyopathic hamster. *Molecular and Cellular Biochemistry*, **176**, 249–256.

[184] Jaffe, L. F. (1991) The path of calcium in cytosolic calcium oscillations - a unifying hypothesis. *Proceedings of the National Academy of Sciences of the United States of America*, **88**, 9883–9887.

[185] Jaimes, 3rd, R., Walton, R. D., Pasdois, P., Bernus, O., Efimov, I. R. & Kay, M. W. (2016) A technical review of optical mapping of intracellular calcium within myocardial tissue. *American Journal of Physiology - Heart and Circulatory Physiology*, **310**, H1388–401.

[186] Janse, M. J. (2004) Electrophysiological changes in heart failure and their relationship to arrhythmogenesis. *Cardiovascular Research*, **61**, 208–217.

[187] January, C. T. & Riddle, J. M. (1989) Early afterdepolarizations - mechanism of induction and block - a role for L-type Ca2+ current. *Circulation Research*, **64**, 977–990.

[188] Janvier, N. C., McMorn, S. O., Harrison, S. M., Taggart, P. & Boyett, M. R. (1997) The role of Na+-Ca2+ exchange current in electrical restitution in ferret ventricular cells. *Journal of Physiology-London*, **504**, 301–314.

[189] Johnson, D. M., Heijman, J., Bode, E. F., Greensmith, D. J., van der Linde, H., Abi-Gerges, N., Eisner, D. A., Trafford, A. W. & Volders, P. G. A. (2013) Diastolic Spontaneous Calcium Release From the Sarcoplasmic Reticulum Increases Beat-to-Beat Variability of Repolarization in Canine Ventricular Myocytes After beta-Adrenergic Stimulation. *Circulation Research*, **112**, 246–+.

[190] Jost, N., Virag, L., Comtois, P., Oerdoeg, B., Szuts, V., Seprenyi, G., Bitay, M., Kohajda, Z., Koncz, I., Nagy, N., Szel, T., Magyar, J., Kovacs, M., Puskas, L. G., Lengyel, C., Wettwer, E., Ravens, U., Nanasi, P. P., Papp, J. G., Varro, A. & Nattel, S. (2013) Ionic mechanisms limiting cardiac repolarization reserve in humans compared to dogs. *Journal of Physiology-London*, **591**, 4189–4206.

[191] Kääb, S., Dixon, J., Duc, J., Ashen, D., Näbauer, M., Beuckelmann, D. J., Steinbeck, G., McKinnon, D. & Tomaselli, G. F. (1998) Molecular basis of transient outward potassium current downregulation in human heart failure: a decrease in Kv4.3 mRNA correlates with a reduction in current density. *Circulation*, **98**, 1383–1393.

[192] Kaab, S., Nuss, H. B., Chiamvimonvat, N., Orourke, B., Pak, P. H., Kass, D. A., Marban, E. & Tomaselli, G. F. (1996) Ionic mechanism of action potential pro-

longation in ventricular myocytes from dogs with pacing-induced heart failure. *Circulation Research*, **78**, 262–273.

[193] Kagaya, Y., Weinberg, E. O., Ito, N., Mochizuki, T., Barry, W. H. & Lorell, B. H. (1995) Glycolytic inhibition - effects on diastolic relaxation and intracellular calcium handling in hypertrophied rat ventricular myocytes. *Journal of Clinical Investigation*, **95**, 2766–2776.

[194] Kamp, T. J. & Hell, J. W. (2000) Regulation of cardiac L-type calcium channels by protein kinase A and protein kinase C. *Circulation Research*, **87**, 1095–1102.

[195] Katsube, Y., Yokoshiki, H., Nguyen, L., Yamamoto, M. & Sperelakis, N. (1998) L-type Ca2+ currents in ventricular myocytes from neonatal and adult rats. *Canadian Journal of Physiology and Pharmacology*, **76**, 873–881.

[196] Katz, A. M. (2010) *Physioloy of the Heart*. 5 edition. Lippincott Williams and Wilkins.

[197] Keldermann, R. H., ten Tusscher, Khwj, Nash, M. P., Hren, R., Taggart, P. & Panfilov, A. V. (2008) Effect of heterogeneous APD restitution on VF organization in a model of the human ventricles. *American Journal of Physiology-Heart and Circulatory Physiology*, **294**, H764–H774.

[198] Kentish, J. C. & Wrzosek, A. (1998) Changes in force and cytosolic Ca2+ concentration after length changes in isolated rat ventricular trabeculae. *Journal of Physiology-London*, **506**, 431–444.

[199] Kiyosue, T., Spindler, A. J., Noble, S. J. & Noble, D. (1993) Background inward current in ventricular and atrial cells of the guinea-pig. *Proceedings of the Royal Society B-Biological Sciences*, **252**, 65–74.

[200] Kleiman, R. B. & Houser, S. R. (1988) Calcium currents in normal and hypertrophied isolated feline ventricular myocytes. *American Journal of Physiology*, **255**, H1434–H1442.

[201] Knollmann, B. C., Casimiro, M. C., Katchman, A. N., Sirenko, S. G., Schober, T., Rong, Q., Pfeifer, K. & Ebert, S. N. (2004) Isoproterenol exacerbates a long QT phenotype in Kcnq1-deficient neonatal mice: Possible roles for human-like Kcnq1

isoform 1 and slow delayed rectifier K+ current. *Journal of Pharmacology and Experimental Therapeutics*, **310**, 311–318.

[202] Ko, C. Y., Song, Z., Qu, Z. L. & Weiss, J. N. (2015) Multiscale Consequences of Spontaneous Calcium Release on Cardiac Delayed Afterdepolarizations. *Biophysical Journal*, **108**, 264A–264A.

[203] Koller, M. L., Riccio, M. L. & Gilmour, R. F. (1998) Dynamic restitution of action potential duration during electrical alternans and ventricular fibrillation. *American Journal of Physiology-Heart and Circulatory Physiology*, **275**, H1635–H1642.

[204] Koumi, S., Sato, R. & Hayakawa, H. (1995) Characterization of the acetylcholine-sensitive muscarinic K+ channel in isolated feline atrial and ventricular myocytes. *Journal of Membrane Biology*, **145**, 143–150.

[205] Lagadic-Gossmann, D., Buckler, K. J., Le Prigent, K. & Feuvray, D. (1996) Altered Ca2+ handling in ventricular myocytes isolated from diabetic rats. *American Journal of Physiology*, **270**, H1529–37.

[206] Lallukka, T., Millear, A., Pain, A., Cortinovis, M. & Giussani, G. (2017) Global, regional, and national life expectancy, all-cause mortality, and cause-specific mortality for 249 causes of death, 1980–2015: a systematic analysis for the Global Burden of Disease Study 2015. *Lancet*, **389**, E1–E1.

[207] Lamoureux, L., Radhakrishnan, J. & Gazmuri, R. J. (2015) A rat model of ventricular fibrillation and resuscitation by conventional closed-chest technique. *Journal of Visualized Experiments*, **98**, volume.

[208] Land, S., Park-Holohan, S. J., Smith, N. P., dos Remedios, C. G., Kentish, J. C. & Niederer, S. A. (2017) A model of cardiac contraction based on novel measurements of tension development in human cardiomyocytes. *Journal of Molecular and Cellular Cardiology*, **106**, 68–83.

[209] Lavorato, M., Huang, T. Q., Iyer, V. R., Perni, S., Meissner, G. & Franzini-Armstrong, C. (2015) Dyad content is reduced in cardiac myocytes of mice with impaired calmodulin regulation of RyR2. *Journal of Muscle Research and Cell Motility*, **36**, 205–214.

[210] Layland, J. & Kentish, J. C. (1999) Positive force- and Ca2+ (i)-frequency relationships in rat ventricular trabeculae at physiological frequencies. *American Journal of Physiology-Heart and Circulatory Physiology*, **276**, H9–H18.

[211] Lee, H. C., Lu, T., Weintraub, N. L., VanRollins, M., Spector, A. A. & Shibata, E. F. (1999) Effects of epoxyeicosatrienoic acids on the cardiac sodium channels in isolated rat ventricular myocytes. *Journal of Physiology-London*, **519**, 153–168.

[212] Leem, C. H., Lagadic-Gossmann, D. & Vaughan-Jones, R. D. (1999) Characterization of intracellular pH regulation in the guinea-pig ventricular myocyte. *Journal of Physiology-London*, **517**, 159–180.

[213] Leifert, W. R, McCurchie, E. J. & Saint, D. A. (1999) Inhibition of cardiac sodium currents in adult rat myocytes by n-3 polyunsaturated fatty acids. *Journal of Physiology*, **520**, 671–679.

[214] Lewalle, A., Niederer, S. A. & Smith, N. P. (2014) Species-dependent adaptation of the cardiac Na+/K+ pump kinetics to the intracellular Na+ concentration. *Journal of Physiology-London*, **592**, 5355–5371.

[215] Li, G. R., Eng, J. L., Wang, Z. G., Fermini, B. & Nattel, S. (1996) Adrenergic modulation of ultrarapid delayed rectifier K+ current in human atrial myocytes. *Circulation Research*, **78**, 903–915.

[216] Li, G. R., Lau, C. P., Ducharme, A., Tardif, J. C. & Nattel, S. (2002) Transmural action potential and ionic current remodeling in ventricles of failing canine hearts. *American Journal of Physiology-Heart and Circulatory Physiology*, **283**, H1031–H1041.

[217] Li, G. R., Yang, B. F., Feng, J. L., Bosch, R. F., Carrier, M. & Nattel, S. (1999) Transmembrane I-Ca contributes to rate-dependent changes of action potentials in human ventricular myocytes. *American Journal of Physiology-Heart and Circulatory Physiology*, **276**, H98–H106.

[218] Li, L., Jin, Q., Dosdall, D. J., Huang, J., Pogwizd, S. M. & Ideker, R. E. (2010) Activation becomes highly organized during long-duration ventricular fibrillation in canine hearts. *American Journal of Physiology-Heart and Circulatory Physiology*, **298**, H2046–H2053.

[219] Li, L., Niederer, S. A., Idigo, W., Zhang, Y. H., Swietach, P., Casadei, B. & Smith, N. P. (2010) A mathematical model of the murine ventricular myocyte: a data-driven biophysically based approach applied to mice overexpressing the canine NCX isoform. *American Journal of Physiology-Heart and Circulatory Physiology*, **299**, H1045–H1063.

[220] Li, X. T., Dyachenko, V., Zuzarte, M., Putzke, C., Preisig-Muller, R., Isenberg, G. & Daut, J. (2006) The stretch-activated potassium channel TREK-1 in rat cardiac ventricular muscle. *Cardiovascular Research*, **69**, 86–97.

[221] Li, Z., Dutta, S., Sheng, J., Tran, P. N., Wu, W., Chang, K., Mdluli, T., Strauss, D. G. & Colatsky, T. (2017) Improving the In Silico Assessment of Proarrhythmia Risk by Combining hERG (Human Ether-a-go-go-Related Gene) Channel-Drug Binding Kinetics and Multichannel Pharmacology. *Circulation - Arrhythmia and Electrophysiology*, **10**, e004628.

[222] Lin, M. C., Rockman, H. A. & Chien, K. R. (1995) Heart and lung-disease in engineered mice. *Nature Medicine*, **1**, 749–751.

[223] Lin, Y. Y., Wu, D. M., Liu, L., Liu, Q. H., Yan, Z. Y. & Wu, B. W. (2008) Activation of delta-opioid receptors inhibits L-type Ca(2+) current and transient outward K(+) current in rat ventricular myocytes. *Sheng Li Xue Bao*, **60**, 38–42.

[224] Liu, J. L. Y., Maniadakis, N., Gray, A. & Rayner, M. (2002) The economic burden of coronary heart disease in the UK. *Heart*, **88**, 597–603.

[225] Liu, M. B., Ko, C. Y., Song, Z., Garfinkel, A., Weiss, J. N. & Qui, Z. L. (2016) A Dynamical Threshold for Cardiac Delayed Afterdepolarization-Mediated Triggered Activity. *Biophysical Journal*, **111**, 2523–2533.

[226] Liu, Q. H., Qiao, X., Zhang, L. J., Wang, J., Zhang, L., Zhai, X. W., Ren, X. Z., Li, Y., Cao, X. N., Feng, Q. L., Cao, J. M. & Wu, B. W. (2019) I(K1) Channel Agonist Zacopride Alleviates Cardiac Hypertrophy and Failure via Alterations in Calcium Dyshomeostasis and Electrical Remodeling in Rats. *Frontiers in Pharmacology*, **10**, 929.

[227] Lodge, N. J. & Normandin, D. E. (1997) Alterations in I-to1, I-Kr and I-k1 density in the BIO TO-2 strain of syrian myopathic hamsters. *Journal of Molecular and Cellular Cardiology*, **29**, 3211–3221.

[228] Lomax, A. E., Kondo, C. S. & Giles, W. R. (2003) Comparison of time- and voltage-dependent K+ currents in myocytes from left and right atria of adult mice. *American Journal of Physiology-Heart and Circulatory Physiology*, **285**, H1837–H1848.

[229] Loose, K. O., Sadredini, M. N., Sejersted, O. M., Stokke, M. K. & Louch, W. E. (2012) Ca2+ Wave Velocity in Cardiomyocytes is Regulated by Ryanodine Receptor Ca2+ Sensitivity and SR Ca2+ Content. *Biophysical Journal*, **102**, 99A–100A.

[230] Lopatin, A. N. & Nichols, C. G. (2001) Inward rectifiers in the heart: An update on I-K1. *Journal of Molecular and Cellular Cardiology*, **33**, 625–638.

[231] Louch, W. E., Bito, V., Heinzel, F. R., Macianskiene, R., Vanhaecke, J., Flameng, W., Mubagwa, K. & Sipido, K. R. (2004) Reduced synchrony of Ca2+ release with loss of T-tubules-a comparison to Ca2+ release in human failing cardiomyocytes. *Cardiovascular Research*, **62**, 63–73.

[232] Louch, W. E., Sejersted, O. M. & Swift, F. (2010) There goes the neighbourhood: Pathological alterations in T-tubule morphology and consequences for cardiomyocyte Ca2+ handling. *Journal of Biomedicine and Biotechnology*, **2010**, 17.

[233] Louch, W. E., Stokke, M. K., Sjaastad, I., Christensen, G. & Sejersted, O. M. (2012) No Rest for the Weary: Diastolic Calcium Homeostasis in the Normal and Failing Myocardium. *Physiology*, **27**, 308–323.

[234] Luo, C. H. & Rudy, Y. (1991) A model of the ventricular cardiac action-potential - depolarization, repolarization, and their interaction. *Circulation Research*, **68**, 1501–1526.

[235] Luo, C. H. & Rudy, Y. (1994) A dynamic-model of the cardiac ventricular action-potential 1. Simulations of ionic currents and concentration changes. *Circulation Research*, **74**, 1071–1096.

[236] Luo, C. H. & Rudy, Y. (1994) A dynamic-model of the cardiac ventricular action-potential 2. Afterdepolarizations, triggered activity, and potentiation. *Circulation Research*, **74**, 1097–1113.

[237] Lyon, A. R., MacLeod, K. T., Zhang, Y. J., Garcia, E., Kanda, G. K., Lab, M. J., Korchev, Y. E., Harding, S. E. & Gorelik, J. (2009) Loss of T-tubules and other

changes to surface topography in ventricular myocytes from failing human and rat heart. *Proceedings of the National Academy of Sciences of the United States of America*, **106**, 6854–6859.

[238] MacLennan, D. H. & Kranias, E. G. (2003) Phospholamban: A crucial regulator of cardiac contractility. *Nature Reviews Molecular Cell Biology*, **4**, 566–577.

[239] Maier, L. S., Bers, D. M. & Pieske, B. (2000) Differences in Ca2+-handling and sarcoplasmic reticulum Ca2+-content in isolated rat and rabbit myocardium. *Journal of Molecular and Cellular Cardiology*, **32**, 2249–2258.

[240] Maier, L. S., Brandes, R., Pieske, B. & Bers, D. M. (1998) Effects of left ventricular hypertrophy on force and Ca2+ handling in isolated rat myocardium. *American Journal of Physiology-Heart and Circulatory Physiology*, **274**, H1361–H1370.

[241] Maltsev, V. A., Sabbah, H. N. & Undrovinas, A. I. (2002) Down-regulation of sodium current in chronic heart failure: effect of long-term therapy with carvedilol. *Cellular and Molecular Life Sciences*, **59**, 1561–1568.

[242] Maltsev, V. A., Yaniv, Y., Maltsev, A. V., Stern, M. D. & Lakatta, E. G. (2014) Modern perspectives on numerical modelling of cardiac pacemaker cell. *Journal of Pharmacological Sciences*, **125**, 6–38.

[243] Martini, H. F., Nath, J. L. & Bartholomew, E. F. (2012) *Fundamentals of Anatomy and Physiology*. 9 edition. Pearson Education.

[244] Marx, S. O., Reiken, S., Hisamatsu, Y., Jayaraman, T., Burkhoff, D., Rosemblit, N. & Marks, A. R. (2000) PKA phosphorylation dissociates FKBP12.6 from the calcium release channel (ryanodine receptor): Defective regulation in failing hearts. *Cell*, **101**, 365–376.

[245] Maughan, D. W. (2005) Kinetics and energetics of the crossbridge cycle. *Heart Failure Reviews*, **10**, 175–185.

[246] McAllister, R. E., Noble, D. & Tsien, R. W. (1975) Reconstruction of the electrical activity of cardiac Purkinje fibres. *Journal of Physiology*, **251**, 1–59.

[247] McDermott, J. S., Salmen, H. J., Cox, B. F. & Gintant, G. A. (2002) Importance of species selection in arrythmogenic models of Q-T interval prolongation. *Antimicrobial Agents and Chemotherapy*, **46**, 938–939.

[248] Mellors, L. J., Kotsanas, G. & Wendt, I. R. (1999) Effects of pyruvate on intracellular Ca2+ regulation in cardiac myocytes from normal and diabetic rats. *Clinical and Experimental Pharmacology and Physiology*, **26**, 889–97.

[249] Miake, J., Marban, E. & Nuss, H. B. (2003) Functional role of inward rectifier current in heart probed by Kir2.1 overexpression and dominant-negative suppression. *Journal of Clinical Investigation*, **111**, 1529–1536.

[250] Michele, D. E. & Metzger, J. M. (2000) Physiological consequences of tropomyosin mutations associated with cardiac and skeletal myopathies. *Journal of Molecular Medicine-Jmm*, **78**, 543–553.

[251] Miller, L., Greensmith, D. J., Sankaranarayanan, R., O'Neill, S. C. & Eisner, D. A. (2015) The effect of 2,5-di-(tert-butyl)-1,4-benzohydroquinone (TBQ) on intracellular Ca2+ handling in rat ventricular myocytes. *Cell Calcium*, **58**, 208–214.

[252] Mitchell, M. R., Powell, T., Terrar, D. A. & Twist, V. W. (1984) Ryanodine prolongs Ca-currents while suppressing contraction in rat ventricular muscle cells. *British Journal of Pharmacology*, **81**, 13–15.

[253] Mobitz, W. (1924) Über die unvollständige Störung der Erregungs-überleitung zwischen Vorhof und Kammer des menschlichen Herzens. *Zeitschrift für die gesamte experimentelle Medizin*, **41**, 180–237.

[254] Mond, H. G. & Vohra, J. (2017) The electrocardiographic footprints of Wenckebach block. *Heart Lung and Circulation*, **26**, 1252–1266.

[255] Monteiro, L. M., Vasques-Novoa, F., Ferreira, L., Pinto-do O, P. & Nascimento, D. S. (2017) Restoring heart function and electrical integrity: closing the circuit. *Regenerative Medicine*, **2**, 9.

[256] Moreno-Galindo, E. G., Sanchez-Chapula, J. A., Sachse, F. B., Alberto Rodriguez-Paredes, J., Tristani-Firouzi, M. & Navarro-Polanco, R. A. (2011) Relaxation gating of the acetylcholine-activated inward rectifier K plus current is mediated by intrinsic voltage sensitivity of the muscarinic receptor. *Journal of Physiology-London*, **589**, 1755–1767.

[257] Morita, N., Lee, J. H., Xie, Y. F., Sovari, A., Qu, Z. L., Weiss, J. N. & Karagueuzian, H. S. (2011) Suppression of Re-Entrant and Multifocal Ventricu-

lar Fibrillation by the Late Sodium Current Blocker Ranolazine. *Journal of the American College of Cardiology*, **57**, 366–375.

[258] Morotti, S. & Grandi, E. (2019) Quantitative systems models illuminate arrhythmia mechanisms in heart failure: Role of the Na+-Ca2+-Ca2+/calmodulin-dependent protein kinase II-reactive oxygen species feedback. *Wiley Interdisciplinary Reviews: Systems Biology and Medicine*, **11**, e1434.

[259] Morotti, S., McCulloch, A. D., Bers, D. M., Edwards, A. G. & Grandi, E. (2016) Atrial-selective targeting of arrhythmogenic phase-3 early afterdepolarizations in human myocytes. *Journal of Molecular and Cellular Cardiology*, **96**, 63–71.

[260] Mulla, W., Gillis, R., Murninkas, M., Klapper-Goldstein, H., Gabay, H., Mor, M., Elyagon, S., Liel-Cohen, N., Bernus, O. & Etzion, Y. (2018) Unanesthetized Rodents Demonstrate Insensitivity of QT Interval and Ventricular Refractory Period to Pacing Cycle Length. *Frontiers in Physiology*, **9**, volume.

[261] Myles, R. C., Burton, F. L., Cobbe, S. M. & Smith, G. L. (2008) The link between repolarisation alternans and ventricular arrhythmia: Does the cellular phenomenon extend to the clinical problem? *Journal of Molecular and Cellular Cardiology*, **45**, 1–10.

[262] Myles, R. C., Wang, L., Kang, C., Bers, D. M. & Ripplinger, C. M. (2012) Local beta-adrenergic stimulation overcomes source-sink mismatch to generate focal arrhythmia. *Circulation Research*, **110**, 1454–64.

[263] Nabauer, M., Beuckelmann, D. J., Uberfuhr, P. & Steinbeck, G. (1996) Regional differences in current density and rate-dependent properties of the transient outward current in subepicardial and subendocardial myocytes of human left ventricle. *Circulation*, **93**, 168–177.

[264] Naish, J., Revest, P. & Syndercombe Court, D. (2009) *Medical Sciences*. 1 edition. Saunders/Elsevier.

[265] Nanasi, P. P., Pankucsi, C., Banyasz, T., Szigligeti, P., Papp, J. G. Y. & Varro, A. (1996) Electrical restitution in rat ventricular muscle. *Acta Physiologica Scandinavica*, **158**, 143–153.

[266] Nattel, S. (2002) New ideas about atrial fibrillation 50 years on. *Nature*, **415**, 219–226.

[267] Nattel, S. (2003) Remodeling of cardiac inward-rectifier currents: an often-overlooked contributor to arrhythmogenic states. *Journal of Molecular and Cellular Cardiology*, **35**, 1395–1398.

[268] Nattel, S. & Dobrev, D. (2012) The multidimensional role of calcium in atrial fibrillation pathophysiology: mechanistic insights and therapeutic opportunities. *European Heart Journal*, **33**, 1870–+.

[269] Nerbonne, J. M. (2000) Molecular basis of functional voltage-gated K+ channel diversity in the mammalian myocardium. *Journal of Physiology-London*, **525**, 285–298.

[270] Nerbonne, J. M. & Kass, R. S. (2005) Molecular physiology of cardiac repolarization. *Physiological Reviews*, **85**, 1205–1253.

[271] Ng, G. A. (2017) Feasibility of selection of antiarrhythmic drug treatment on the basis of arrhythmogenic mechanism - Relevance of electrical restitution, wavebreak and rotors. *Pharmacology & Therapeutics*, **176**, 1–12.

[272] Ni, H. B., Morotti, S. & Grandi, E. (2018) A Heart for Diversity: Simulating Variability in Cardiac Arrhythmia Research. *Frontiers in Physiology*, **9**, volume.

[273] Nichols, C. G. & Lee, S. (2018) Polyamines and potassium channels: A 25-year romance. *Journal of Biological Chemistry*, **293**, 18779–18788.

[274] Nicoll, D. A., Longoni, S. & Philipson, K. D. (1990) Molecular-cloning and functional expression of the cardiac sarcolemmal Na+-Ca2+ exchanger. *Science*, **250**, 562–565.

[275] Niederer, S. A., Hunter, P. J. & Smith, N. P. (2006) A quantitative analysis of cardiac myocyte relaxation: A simulation study. *Biophysical Journal*, **90**, 1697–1722.

[276] Niederer, S. A. & Smith, N. P. (2007) A mathematical model of the slow force response to stretch in rat ventricular myocytes. *Biophysical Journal*, **92**, 4030–44.

[277] Nishimura, S., Yasuo, K., Toshiaki, N., Hosoya, Y., Fujita, H., Katoh, M., Yamashita, H., Nagai, R. & Sugiura, S. (2006) Membrane potential of rat ventricular myocytes responds to axial stretch in phase, amplitude and speed-dependent manners. *Cardiovascular Research*, **72**, 403–411.

[278] Nivala, M., de Lange, E., Rovetti, R. & Qu, Z. (2012) Computational modeling and numerical methods for spatiotemporal calcium cycling in ventricular myocytes. *Frontiers in Physiology*, **3**, volume.

[279] Niwa, N. & Nerbonne, J. M. (2010) Molecular determinants of cardiac transient outward potassium current (I-to) expression and regulation. *Journal of Molecular and Cellular Cardiology*, **48**, 12–25.

[280] Noble, D. (1962) A modification of the Hodgkin-Huxley equations applicable to Purkinje fibre action and pacemaker potentials. *The Journal of Physiology*, **160**, 317–352.

[281] Noble, D. (2007) From the Hodgkin-Huxley axon to the virtual heart. *Journal of Physiology*, **580**, 15–22.

[282] Noble, D., A., Garny & Noble, P. (2012) How the Hodgkin-Huxley equations inspired the Cardiac Physiome Project. *Journal of Physiology-London*, **590**, 2613–2628.

[283] Noble, D. & Tsien, R. W. (1968) The kinetics and rectifier properties of the slow potassium current in cardiac Purkinje fibres. *Journal of Physiology*, **195**, 185–214.

[284] Noble, D. & Tsien, R. W. (1969) Outward membrane currents activated in the plateau range of potentials in cardiac Purkinje fibres. *Journal of Physiology*, **200**, 205–31.

[285] Nolasco, J. B. & Dahlen, R. W. (1968) A graphic method for study of alternation in cardiac action potentials. *Journal of Applied Physiology*, **25**, 191–+.

[286] Nygren, A., Fiset, C., Firek, L., Clark, J. W., Lindblad, D. S., Clark, R. B. & Giles, W. R. (1998) Mathematical model of an adult human atrial cell - The role of K+ currents in repolarization. *Circulation Research*, **82**, 63–81.

[287] Ochala, J. (2008) Thin filament proteins mutations associated with skeletal myopathies: Defective regulation of muscle contraction. *Journal of Molecular Medicine-Jmm*, **86**, 1197–1204.

[288] Oehmen, C. (1999) *Parameter sensitivity studies of various cardiac channels*. Master's thesis, University of Tennessee, Memphis.

[289] O'Hara, T., Virág, L., Varró, A. & Rudy, Y. (2011) Simulation of the Undiseased Human Cardiac Ventricular Action Potential: Model Formulation and Experimental Validation. *PLoS Computational Biology*, **7**, volume.

[290] Olson, M. L., Kargacin, M. E., Ward, C. A. & Kargacin, G. J. (2007) Effects of phloretin and phloridzin on Ca2+ handling, the action potential, and ion currents in rat ventricular myocytes. *Journal of Pharmacology and Experimental Therapeutics*, **321**, 921–929.

[291] Ono, N., Yamaguchi, T., Ishikawa, H., Arakawa, M., Takahashi, N., Saikawa, T. & Shimada, T. (2009) Morphological varieties of the Purkinje fiber network in mammalian hearts, as revealed by light and electron microscopy. *Archives of Histology and Cytology*, **72**, 139–149.

[292] Ouadid, H., Albat, B. & Nargeot, J. (1995) Calcium currents in diseased human cardiac-cells. *Journal of Cardiovascular Pharmacology*, **25**, 282–291.

[293] Pandit, S. V., Clark, R. B., Giles, W. R. & Demir, S. S. (2001) A mathematical model of action potential heterogeneity in adult rat left ventricular myocytes. *Biophysical Journal*, **81**, 3029–51.

[294] Pandit, S. V., Giles, W. R. & Demir, S. S. (2003) A mathematical model of the electrophysiological alterations in rat ventricular myocytes in type-I diabetes. *Biophysical Journal*, **84**, 832–841.

[295] Pasek, M., Christe, G. & Simurda, J. (2003) A quantitative model of the cardiac ventricular cell incorporating the transverse-axial tubular system. *General Physiology and Biophysics*, **22**, 355–368.

[296] Pasek, M., Simurda, J. & Christe, G. (2006) The functional role of cardiac T-tubules explored in a model of rat ventricular myocytes. *Philosophical Transactions of the Royal Society A-Mathematical Physical and Engineering Sciences*, **364**, 1187–1206.

[297] Patterson, E., Scherlag, B. J. & Lazzara, R. (1997) Early afterdepolarizations produced by d,l-sotalol and clofilium. *Journal of Cardiovascular Electrophysiology*, **8**, 667–678.

[298] Pereira, L., Bare, D. J., Galice, S., Shannon, T. R. & Bers, D. M. (2017) B-adrenergic induced SR Ca2+ leak is mediated by an Epac-NOS pathway. *Journal of Molecular and Cellular Cardiology*, **108**, 8–16.

[299] Perez-Cortes, E. J., Islas, A. A., Arevalo, J. P., Mancilla, C., Monjaraz, E. & Salinas-Stefanon, E. M. (2015) Modulation of the transient outward current (I-to) in rat cardiac myocytes and human K(v)4.3 channels by mefloquine. *Toxicology and Applied Pharmacology*, **288**, 203–212.

[300] Petroff, M. G. V., Kim, S. H., Pepe, S., Dessy, C., Marban, E., Balligand, J. L. & Sollott, S. J. (2001) Endogenous nitric oxide mechanisms mediate the stretch dependence of Ca2+ release in cardiomyocytes. *Nature Cell Biology*, **3**, 867–873.

[301] Philipson, K. D., Longoni, S. & Ward, R. (1988) Purification of the cardiac Na+-Ca2+ exchange protein. *Biochimica Et Biophysica Acta*, **945**, 298–306.

[302] Philipson, K. D. & Nicoll, D. A. (2000) Sodium-calcium exchange: A molecular perspective. *Annual Review of Physiology*, **62**, 111–133.

[303] Pitt, G. S., Dun, W. & Boyden, P. A. (2006) Remodeled cardiac calcium channels. *Journal of Molecular and Cellular Cardiology*, **41**, 373–388.

[304] Pogwizd, S. M. (1995) Nonreentrant mechanisms underlying spontaneous ventricular arrhythmias in a model of nonischemic heart-failure in rabbits. *Circulation*, **92**, 1034–1048.

[305] Pogwizd, S. M. & Bers, D. M. (2004) Cellular basis of triggered arrhythmias in heart failure. *Trends in Cardiovascular Medicine*, **14**, 61–66.

[306] Portero, V., Wilders, R., Casini, S., Charpentier, F., Verkerk, A. O. & Remme, C. A. (2018) KV4.3 Expression Modulates NaV1.5 Sodium Current. *Frontiers in Physiology*, **9**.

[307] Prakosa, A., Arevalo, H. J., Deng, D. D., Boyle, P. M., Nikolov, P. P., Ashikaga, H., Blauer, J. J. E., Ghafoori, E., Park, C. J., Blake, R. C., Han, F. T., MacLeod,

R. S., Halperin, H. R., Callans, D. J., Ranjan, R., Chrispin, J., Nazarian, S. & Trayanova, N. A. (2018) Personalized virtual-heart technology for guiding the ablation of infarct-related ventricular tachycardia. *Nature Biomedical Engineering*, **2**, 732–740.

[308] Press, W. H., Teukolsky, S. A., Vetterling, W. T. & Flannery, B. P. (1992) Numerical Recipes in C. The Art of Scientific Computing. volume.

[309] Puglisi, J. L. & Bers, D. M. (2001) LabHEART: an interactive computer model of rabbit ventricular myocyte ion channels and Ca transport. *American Journal of Physiology-Cell Physiology*, **281**, C2049–C2060.

[310] Qin, D. Y., Zhang, Z. H., Caref, E. B., Boutjdir, M., Jain, P. & ElSherif, N. (1996) Cellular and ionic basis of arrhythmias in postinfarction remodeled ventricular myocardium. *Circulation Research*, **79**, 461–473.

[311] Qin, M., Liu, T., Hu, H., Wang, T., Yu, S. B. & Huang, C. X. (2013) Effect of isoprenaline chronic stimulation on APD restitution and ventricular arryhthmogenesis. *Journal of Cardiology*, **61**, 162–168.

[312] Qu, Z. L., Hu, G., Garfinkel, A. & Weiss, J. N. (2014) Nonlinear and stochastic dynamics in the heart. *Physics Reports-Review Section of Physics Letters*, **543**, 61–162.

[313] Qu, Z. L., Weiss, J. N. & Garfinkel, A. (1999) Cardiac electrical restitution properties and stability of reentrant spiral waves: a simulation study. *American Journal of Physiology-Heart and Circulatory Physiology*, **276**, H269–H283.

[314] Qu, Z. L., Xie, L. H., Olcese, R., Karagueuzian, H. S., Chen, P. S., Garfinkel, A. & Weiss, J. N. (2013) Early afterdepolarizations in cardiac myocytes: beyond reduced repolarization reserve. *Cardiovascular Research*, **99**, 6–15.

[315] Rahm, A., Lugenbiel, P., Schweizer, P. A., Katus, H. A. & Thomas, D. (2018) Role of ion channes in heart failure and channelopathies. *Biophysical Reviews*, **10**, 1097–1106.

[316] Ranu, H. K., Terracciano, C. M. N., Davia, K., Bernobich, E., Chaudhri, B., Robinson, S. E., Kang, Z. B., Hajjar, R. J., MacLeod, K. T. & Harding, S. E. (2002) Effects of Na+/Ca2+-exchanger overexpression on excitation-contraction coupling in

adult rabbit ventricular myocytes. *Journal of Molecular and Cellular Cardiology*, **34**, 389–400.

[317] Ratner, M. (2015) Heart failure gene therapy disappoints but experts keep the faith. *Nature Biotechnology*, **33**, 573–574.

[318] Reinecke, H., Studer, R., Vetter, R., Holtz, J. & Drexler, H. (1996) Cardiac Na+/Ca2+ exchange activity in patients with end-stage heart failure. *Cardiovascular Research*, **31**, 48–54.

[319] Restrepo, J. G., Weiss, J. N. & Karma, A. (2008) Calsequestrin-mediated mechanism for cellular calcium transient alternans. *Biophysical Journal*, **95**, 3767–3789.

[320] Reuter, H. (1967) The dependence of slow inward current in Purkinje fibres on the extracellular calcium-concentration. *Journal of Physiology*, **192**, 479–92.

[321] Rice, J. J., Winslow, R. L. & Hunter, W. C. (1999) Comparison of putative cooperative mechanisms in cardiac myocytes: lenth dependence and dynamic responses. *Americal Journal of Physiology-Heart and Circulatory Physiology*, **276**, H1734–H1754.

[322] Richard, S., Charnet, P. & Nerbonne, J. M. (1993) Interconversion between distinct gating pathways of the high threshold calcium-channel in rat ventricular myocytes. *Journal of Physiology-London*, **462**, 197–228.

[323] Richard, S., Perrier, E., Fauconnier, J., Perrier, R., Pereira, L., Gomez, A. M. & Benitah, J. P. (2006) 'Ca2+-induced Ca2+ entry' or how the L-type Ca2+ channel remodels its own signalling pathway in cardiac cells. *Progress in Biophysics & Molecular Biology*, **90**, 118–135.

[324] Richards, M. A., Clarke, J. D., Saravanan, P., Voigt, N., Dobrev, D., Eisner, D. A., Trafford, A. W. & Dibb, K. M. (2011) Transverse tubules are a common feature in large mammalian atrial myocytes including human. *American Journal of Physiology-Heart and Circulatory Physiology*, **301**, H1996–H2005.

[325] Riemer, T. L., Sobie, E. A. & Tung, L. (1998) Stretch-induced changes in arrhythmogenesis and excitability in experimentally based heart cell models. *American Journal of Physiology-Heart and Circulatory Physiology*, **275**, H431–H442.

[326] Robinson, R. B. & Siegelbaum, S. A. (2003) Hyperpolarization-activated cation currents: From molecules to physiological function. *Annual Review of Physiology*, **65**, 453–480.

[327] Robinson, R. B., Yu, H. G., Chang, F. & Cohen, I. S. (1997) Developmental change in the voltage-dependence of the pacemaker current, i(f), in rat ventricle cells. *Pflugers Archiv-European Journal of Physiology*, **433**, 533–535.

[328] Rocchetti, M., Freli, V., Perego, V., Altomare, C., Mostacciuolo, G. & Zaza, A. (2006) Rate dependency of beta-adrenergic modulation of repolarizing currents in the guinea-pig ventricle. *Journal of Physiology-London*, **574**, 183–193.

[329] Rudy, Y. & Silva, J. R. (2006) Computational biology in the study of cardiac ion channels and cell electrophysiology. *Quarterly Reviews of Biophysics*, **39**, 57–116.

[330] Rush, S. & Larsen, H. (1978) A practical algorithm for solving dynamic membrane equations. *IEEE Transactions on Biomedical Engineering*, **25**, 389–392.

[331] Sadredini, M., Danielsen, T. K., Aronsen, J. M., Manotheepan, R., Hougen, K., Sjaastad, I. & Stokke, M. K. (2016) Beta-adrenoceptor stimulations reveals Ca2+ waves and sarcoplasmic reticulum Ca2+ depletion in left ventricular cardiomyocytes from post-infarction rats with and without heart failure. *PLoS One*, **11**.

[332] Saint, D. A. & Tang, Y. (1998) Propofol block of cardiac sodium currents in rat isolated myocardial cells is increased at depolarized resting potentials. *Clinical and Experimental Pharmacology and Physiology*, **25**, 336–340.

[333] Sakakibara, Y., Furukawa, T., Singer, D. H., Jia, H. J., Backer, C. L., Arentzen, C. E. & Wasserstrom, J. A. (1993) Sodium current in isolated human ventricular myocytes. *American Journal of Physiology*, **265**, H1301–H1309.

[334] Sakakibara, Y., Wasserstrom, J. A., Furukawa, T., Jia, H., Arentzen, C. E., Hartz, R. S. & Singer, D. H. (1992) Characterization of the sodium current in single human atrial myocytes. *Circulation Research*, **71**, 535–46.

[335] Salama, G. & Hwang, S. M. (2009) Simultaneous optical mapping of intracellular free calcium and action potentials from Langendorff perfused hearts. *Current Protocols in Cytometry*, **Chapter 12**, Unit 12.17.

[336] Salle, L., Kharche, S., Zhang, H. & Brette, F. (2008) Mechanisms underlying adaptation of action potential duration by pacing rate in rat myocytes. *Progress in Biophysics & Molecular Biology*, **96**, 305–320.

[337] Sanguinetti, M. C. & Bennett, P. B. (2003) Antiarrhythmic drug target choices and screening. *Circulation Research*, **93**, 491–9.

[338] Sanguinetti, M. C. & Jurkiewicz, N. K. (1990) 2 components of cardiac delayed rectifier K+ current - differential sensitivity to block by class-III antiarrhythmic agents. *Journal of General Physiology*, **96**, 195–215.

[339] Sanguinetti, M. C. & Jurkiewicz, N. K. (1991) Delayed rectifier outward K+ current is composed of 2 currents in guinea-pig atrial cells. *American Journal of Physiology*, **260**, H393–H399.

[340] Sankaranarayanan, R., Kistamas, K., Greensmith, D. J., Venetucci, L. A. & Eisner, D. A. (2017) Systolic Ca2+ (i) regulates diastolic levels in rat ventricular myocytes. *Journal of Physiology-London*, **595**, 5545–5555.

[341] Sankaranarayanan, R., Li, Y. T., Greensmith, D. J., Eisner, D. A. & Venetucci, L. (2016) Biphasic decay of the Ca transient results from increased sarcoplasmic reticulum Ca leak. *Journal of Physiology-London*, **594**, 611–623.

[342] Santana, L. F., Cheng, E. P. & Lederer, W. J. (2010) How does the shape of the cardiac action potential control calcium signaling and contraction in the heart? *Journal of Molecular and Cellular Cardiology*, **49**, 901–903.

[343] Santangeli, P., Muser, D., Maeda, S., Filtz, A., Zado, E. S., Frankel, D. S., Dixit, S., Epstein, A. E., Callans, D. J. & Marchlinski, F. E. (2016) Comparative effectiveness of antiarrhythmic drugs and catheter ablation for the prevention of recurrent ventricular tachycardia in patients with implantable cardioverter-defibrillators: A systematic review and meta-analysis of randomized controlled trials. *Heart Rhythm*, **13**, 1552–1559.

[344] Sartiani, L., Cerbai, E. & Mugelli, A. (2011) The Funny Current in Cardiac Non-Pacemaker Cells: Functional Role and Pharmacological Modulation. In: Das, M. R. (Editor) *Modern Pacemakers - Present and Future*. InTech.

[345] Satoh, H., Blatter, L. A. & Bers, D. M. (1997) Effects of Ca2+ (i), SR Ca2+ load, and rest on Ca2+ spark frequency in ventricular myocytes. *American Journal of Physiology-Heart and Circulatory Physiology*, **272**, H657–H668.

[346] Satoh, H., Delbridge, L. M. D., Blatter, L. A. & Bers, D. M. (1996) Surface:volume relationship in cardiac myocytes studied with confocal microscopy and membrane capacitance measurements: Species-dependence and developmental effects. *Biophysical Journal*, **70**, 1494–1504.

[347] Saucerman, J. J., Brunton, L. L., Michailova, A. P. & McCulloch, A. D. (2003) Modeling beta-adrenergic control of cardiac myocyte contractility in silico. *Journal of Biological Chemistry*, **278**, 47997–48003.

[348] Saucerman, J. J., Healy, S. N., Belik, M. E., Puglisi, J. L. & McCulloch, A. D. (2004) Proarrhythmic consequences of a KCNQ1 AKAP-binding domain mutation - Computational models of whole cells and heterogeneous tissue. *Circulation Research*, **95**, 1216–1224.

[349] Saxon, L. A., Bristow, M. R., Boehmer, J., Krueger, S., Kass, D. A., De Marco, T., Carson, P., DiCarlo, L., Feldman, A. M., Galle, E. & Ecklund, F. (2006) Predictors of sudden cardiac death and appropriate shock in the Comparison of Medical Therapy, Pacing, and Defibrillation in Heart Failure (COMPANION) Trial. *Circulation*, **114**, 2766–2772.

[350] Schouten, V. J. & ter Keurs, H. E. (1991) Role of Ica and Na+/Ca2+ exchange in the force-frequency relationship of rat heart muscle. *Journal of Molecular and Cellular Cardiology*, **23**, 1039–50.

[351] Schreieck, J., Wang, Y., Zrenner, N., Schomig, A. & Schmitt, C. (1998) Contrasting effect of beta-adrenergic stimulation on action potential duration in the presence of of new class III antiarrhythmic agents dofetilide and chromanol 293B. *Journal of the American College of Cardiology*, **31**, 471A–471A.

[352] Schulz, D. J., Goaillard, J. M. & Marder, E. E. (2007) Quantitative expression profiling of identified neurons reveals cell-specific constraints on highly variable levels of gene expression. *Proceedings of the National Academy of Sciences of the United States of America*, **104**, 13187–13191.

[353] Scriven, D. R. L., Dan, P. & Moore, E. D. W. (2000) Distribution of proteins implicated in excitation-contraction coupling in rat ventricular myocytes. *Biophysical Journal*, **79**, 2682–2691.

[354] Selvaraj, R. J., Picton, P., Nanthakumar, K. & Chauhan, V. S. (2007) Steeper restitution slopes across right ventricular endocardium in patients with cardiomyopathy at high risk of ventricular arrhythmias. *American Journal of Physiology-Heart and Circulatory Physiology*, **292**, H1262–H1268.

[355] Sham, J. S. K., Hatem, S. N. & Morad, M. (1995) Species-differences in the activity of the Na+-Ca2+ exchanger in mammalian cardiac myocytes. *Journal of Physiology-London*, **488**, 623–631.

[356] Shannon, T. R., Wang, F., Puglisi, J., Weber, C. & Bers, D. M. (2004) A mathematical treatment of integrated Ca dynamics within the ventricular myocyte. *Biophysical Journal*, **87**, 3351–3371.

[357] Shattock, M. J. & Bers, D. M. (1989) Rat vs rabbit ventricle - Ca flux and intracellular Na assessed by ion-selective microelectrodes. *American Journal of Physiology*, **256**, C813–C822.

[358] Shaw, R. M. & Rudy, Y. (1995) The vulnerable window for unidirectional block in cardiac tissue - characterization and dependence on membrane excitability and intercellular coupling. *Journal of Cardiovascular Electrophysiology*, **6**, 115–131.

[359] Shaw, R. M. & Rudy, Y. (1997) Ionic mechanisms of propagation in cardiac tissue - Roles of the sodium and L-type calcium currents during reduced excitability and decreased gap junction coupling. *Circulation Research*, **81**, 727–741.

[360] Shiferaw, Y., Watanabe, M. A., Garfinkel, A., Weiss, J. N. & Karma, A. (2003) Model of intracellular calcium cycling in ventricular myocytes. *Biophysical Journal*, **85**, 3666–86.

[361] Shigematsu, S., Kiyosue, T., Sato, T. & Arita, M. (1997) Rate-dependent prolongation of action potential duration in isolated rat ventricular myocytes. *Basic Research in Cardiology*, **92**, 123–128.

[362] Shimoni, Y., Firek, L., Severson, D. & Giles, W. (1994) Short-term diabetes alters K+ currents in rat ventricular myocytes. *Circulation Research*, **74**, 620–628.

[363] Shimoni, Y., Severson, D. & Giles, W. (1995) Thyroid status and diabetes modulate regional differences in potassium currents in rat ventricle. *Journal of Physiology-London*, **488**, 673–688.

[364] Silva, J. & Rudy, Y. (2005) Subunit interaction determines I-Ks participation in cardiac repolarization and repolarization reserve. *Circulation*, **112**, 1384–1391.

[365] Sipido, K. R. (2006) Calcium overload, spontaneous calcium release, and ventricular arrhythmias. *Heart Rhythm*, **3**, 977–979.

[366] Smith, J. M., Clancy, E. A., Valeri, C. R., Ruskin, J. N. & Cohen, R. J. (1988) Electrical alternans and cardiac electrical instability. *Circulation*, **77**, 110–121.

[367] Soeller, C. & Cannell, M. B. (1999) Examination of the transverse tubular system in living cardiac rat myocytes by 2-photon microscopy and digital image-processing techniques. *Circulation Research*, **84**, 266–275.

[368] Song, L. S., Sobie, E. A., McCulle, S., Lederer, W. J., Balke, C. W. & Cheng, H. P. (2006) Orphaned ryanodine receptors in the failing heart. *Proceedings of the National Academy of Sciences of the United States of America*, **103**, 4305–4310.

[369] Song, Z., Ko, C. Y., Nivala, M., Weiss, J. N. & Qu, Z. (2015) Calcium-voltage coupling in the genesis of early and delayed afterdepolarizations in cardiac myocytes. *Biophysical Journal*, **108**, 1908–1921.

[370] Starmer, C. F., Biktashev, V. N., Romashko, D. N., Stepanov, M. R., Makarova, O. N. & Krinsky, V. I. (1993) Vulnerability in an excitable medium: analytical and numerical studies of initiating unidirectional propagation. *Biophysical Journal*, **65**, 1775–1787.

[371] Stern, M. D., Song, L. S., Cheng, H. P., Sham, J. S. K., Yang, H. T., Boheler, K. R. & Rios, E. (1999) Local control models of cardiac excitation-contraction coupling - A possible role for allosteric interactions between ryanodine receptors. *Journal of General Physiology*, **113**, 469–489.

[372] Stewart, J., Manmathan, G. & Wilkinson, P. (2017) Primary prevention of cardiovascular disease: A review of contemporary guidance and literature. *JRSM Cardiovascular Disease*, **6**, 1–6.

[373] Stilli, D., Sgoifo, A., Macchi, E., Zaniboni, M., De Iasio, S., Cerbai, E., Mugelli, A., Lagrasta, C., Olivetti, G. & Musso, E. (2001) Myocardial remodeling and arrhythmogenesis in moderate cardiac hypertrophy in rats. *American Journal of Physiology-Heart and Circulatory Physiology*, **280**, H142–H150.

[374] Stillitano, F., Lonardo, G., Zicha, S., Varro, A., Cerbai, E., Mugelli, A. & Nattel, S. (2008) Molecular basis of funny current (I-f) in normal and failing human heart. *Journal of Molecular and Cellular Cardiology*, **45**, 289–299.

[375] Stokke, M. K., Tovsrud, N., Louch, W. E., Oyehaug, L., Hougen, K., Sejersted, O. M., Swift, F. & Sjaastad, I. (2013) I-CaL inhibition prevents arrhythmogenic Ca2+ waves caused by abnormal Ca2+ sensitivity of RyR or SR Ca2+ accumulation. *Cardiovascular Research*, **98**, 315–325.

[376] Studer, R., Reinecke, H., Bilger, J., Eschenhagen, T., Bohm, M., Hasenfuss, G., Just, H., Holtz, J. & Drexler, H. (1994) Gene-expression of the cardiac Na+-Ca2+ exchanger in end-stage human heart-failure. *Circulation Research*, **75**, 443–453.

[377] Su, Z., Li, F. H., Spitzer, K. W., Yao, A., Ritter, M. & Barry, W. H. (2003) Comparison of sarcoplasmic reticulum Ca2(+)-ATPase function in human, dog, rabbit, and mouse ventricular myocytes. *Journal of Molecular and Cellular Cardiology*, **35**, 761–767.

[378] Sun, L., Fan, J. S., Clark, J. W. & Palade, P. T. (2000) A model of the L-type Ca2+ channel in rat ventricular myocytes: ion selectivity and inactivation mechanisms. *Journal of Physiology-London*, **529**, 139–158.

[379] Sung, R. J., Wu, S. N., Wu, J. S., Chang, H. D. & Luo, C. H. (2006) Electrophysiological mechanisms of ventricular arrhythmias in relation to Andersen-Tawil syndrome under conditions of reduced IK1: a simulation study. *American Journal of Physiology - Heart and Circulatory Physiology*, **291**, H2597–605.

[380] Sutko, J. L., Willerson, J. T., Templeton, G. H., Jones, L. R. & Besch, H. R. (1979) Ryanodine - its alterations of cat papillary-muscle contractile state and responsiveness to inotropic interventions and a suggested mechanism of action. *Journal of Pharmacology and Experimental Therapeutics*, **209**, 37–47.

[381] Swietach, P., Spitzer, K. W. & Vaughan-Jones, R. D. (2010) Modeling calcium waves in cardiac myocytes: importance of calcium diffusion. *Frontiers in Bioscience-Landmark*, **15**, 661–680.

[382] Szabo, B., Sweidan, R., Rajagopalan, C. V. & Lazzara, R. (1994) Role of Na+Ca2+ exchange current in Cs+-induced early afterdepolarizations in Purkinje-fibers. *Journal of Cardiovascular Electrophysiology*, **5**, 933–944.

[383] Tang, L., Gao, W. & Taylor, P. B. (1996) Force-frequency response in isoproterenol-induced hypertrophied rat heart. *European Journal of Pharmacology*, **318**, 349–56.

[384] Taylor, D. G., Parilak, L. D., LeWinter, M. M. & Knot, H. J. (2004) Quantification of the rat left ventricle force and Ca2+-frequency relationships: similarities to dog and human. *Cardiovascular Research*, **61**, 77–86.

[385] Teh, I., McClymont, D., Burton, R. A. B., Maguire, M. L., Whittington, H. J., Lygate, C. A., Kohl, P. & Schneider, J. E. (2016) Resolving Fine Cardiac Structures in Rats with High-Resolution Diffusion Tensor Imaging. *Scientific Reports*, **6**.

[386] Temporal, S., Lett, K. M. & Schulz, D. J. (2014) Activity-Dependent Feedback Regulates Correlated Ion Channel mRNA Levels in Single Identified Motor Neurons. *Current Biology*, **24**, 1899–1904.

[387] ten Tusscher, K. H. W. J. & Panfilov, A. V. (2006) Alternans and spiral breakup in a human ventricular tissue model. *American Journal of Physiology - Heart and Circulatory Physiology*, **291**, H1088–H1100.

[388] Terracciano, C. M. N. & MacLeod, K. T. (1997) Measurements of Ca2+ entry and sarcoplasmic reticulum Ca2+ content during the cardiac cycle in guinea pig and rat ventricular myocytes. *Biophysical Journal*, **72**, 1319–1326.

[389] Timmis, A., Townsend, N., Gale, C., Grobbee, R., Maniadakis, N., Flather, M., Wilkins, E., Wright, L., Vos, R., Bax, J., Blum, M., Pinto, F. & Vardas, P. (2018) European Society of Cardiology: Cardiovascular Disease Statistics 2017. *European Heart Journal*, **39**, 508–579.

[390] Tobin, A. E., Cruz-Bermudez, N. D., Marder, E. & Schulz, D. J. (2009) Correlations in Ion Channel mRNA in Rhythmically Active Neurons. *PLoS One*, **4**, volume.

[391] Townsend, N., Wilson, L., Bhatnagar, P., Wickramasinghe, K., Rayner, M. & Nichols, M. (2016) Cardiovascular disease in Europe: epidemiological update 2016. *European Heart Journal*, **37**, 3232–3245.

[392] Trafford, A. W., Diaz, M. E. & Eisner, D. A. (1998) Stimulation of Ca-induced Ca release only transiently increases the systolic Ca transient: measurements of Ca fluxes and sarcoplasmic reticulum Ca. *Cardiovascular Research*, **37**, 710–717.

[393] Trafford, A. W., Diaz, M. E. & Eisner, D. A. (1999) A novel, rapid and reversible method to measure Ca buffering and time-course of total sarcoplasmic reticulum Ca content in cardiac ventricular myocytes. *Pflugers Archiv-European Journal of Physiology*, **437**, 501–503.

[394] Trafford, A. W., Diaz, M. E. & Eisner, D. A. (2001) Coordinated control of cell Ca2+ loading and triggered release from the sarcoplasmic reticulum underlies the rapid inotropic response to increased L-type Ca2+ current. *Circulation Research*, **88**, 195–201.

[395] Trafford, A. W., Diaz, M. E., Oneill, S. C. & Eisner, D. A. (1995) Comparison of subsarcolemmal and bulk calcium-concentration during spontaneous calcium-release in rat ventricular myocytes. *Journal of Physiology-London*, **488**, 577–586.

[396] Trafford, A. W., Diaz, M. E., Sibbring, G. C. & Eisner, D. A. (2000) Modulation of CICR has no maintained effect on systolic Ca2+: simultaneous measurements of sarcoplasmic reticulum and sarcolemmal Ca2+ fluxes in rat ventricular myocytes. *Journal of Physiology-London*, **522**, 259–270.

[397] Trafford, A. W. & Eisner, D. A. (2003) No role for a voltage sensitive release mechanism in cardiac muscle. *Journal of Molecular and Cellular Cardiology*, **35**, 145–151.

[398] Tran, D. X., Sato, D., Yochelis, A., Weiss, J. N., Garfinkel, A. & Qu, Z. L. (2009) Bifurcation and Chaos in a Model of Cardiac Early Afterdepolarizations. *Physical Review Letters*, **102**, volume.

[399] Tristani-Firouzi, M. & Sanguinetti, M. C. (1998) Voltage-dependent inactivation of the human K+ channel KvLQT1 is eliminated by association with minimal K+ channel (minK) subunits. *Journal of Physiology-London*, **510**, 37–45.

[400] Tse, G., Wong, S. T., Tse, V. & Yeo, J. M. (2016) Restitution analysis of alternans using dynamic pacing and its comparison with S1S2 restitution in heptanol-treated, hypokalaemic Langendorff-perfused mouse hearts. *Biomedical Reports*, **4**, 673–680.

[401] Tsuji, Y., Opthof, T., Kamiya, K., Yasui, K., Liu, W. R., Lu, Z. B. & Kodama, I. (2000) Pacing-induced heart failure causes a reduction of delayed rectifier potassium currents along with decreases in calcium and transient outward currents in rabbit ventricle. *Cardiovascular Research*, **48**, 300–309.

[402] Tsuji, Y., Zicha, S., Qi, X. Y., Kodama, I. & Nattel, S. (2006) Potassium channel subunit remodeling in rabbits exposed to long-term bradycardia or tachycardia - Discrete arrhythmogenic consequences related to differential delayed-rectifier changes. *Circulation*, **113**, 345–355.

[403] Ueda, H., Nakayama, Y., Tsumura, K., Yoshimaru, K., Hayashi, T. & Yoshikawa, J. (2004) Intravenous nicorandil can reduce the occurrence of ventricular fibrillation and QT dispersion in patients with successful coronary angioplasty in acute myocardial infarction. *Canadian Journal of Cardiology*, **20**, 625–629.

[404] Undrovinas, A. I., Maltsev, V. A. & Sabbah, H. N. (1999) Repolarization abnormalities in cardiomyocytes of dogs with chronic heart failure: role of sustained inward current. *Cellular and Molecular Life Sciences*, **55**, 494–505.

[405] Valderrabano, M. (2007) Influence of anisotropic conduction properties in the propagation of the cardiac action potential. *Progress in Biophysics & Molecular Biology*, **94**, 144–168.

[406] Varro, A., Hester, S. & Papp, J. G. (1993) Caffeine-induced decreases in the inward rectifier potassium and the inward calcium currents in rat ventricular myocytes. *British Journal of Pharmacology*, **109**, 895–897.

[407] Varro, A., Hester, S. & Papp, J. G. (1993) Caffeine-induced decreases in the inward rectifier potassium and the inward calcium currents in rat ventricular myocytes. *British Journal of Pharmacology*, **109**, 895–897.

[408] Varro, A., Lathrop, D. A., Hester, S. B., Nanasi, P. P. & Papp, J. G. Y. (1993) Ionic currents and action-potentials in rabbit, rat, and guinea-pig ventricular myocytes. *Basic Research in Cardiology*, **88**, 93–102.

[409] Venetucci, L. A., Trafford, A. W., Dïaz, M. E., O'Neill, S. C. & Eisner, D. A. (2006) Reducing ryanodine receptor open probability as a means to abolish spontaneous Ca2+ release and increase Ca2+ transient amplitude in adult ventricular myocytes. *Circulation Research*, **98**, 1299–1305.

[410] Veys, K., Snyders, D. & De Schutter, E. (2013) Kv3.3b expression defines the shape of the complex spike in the Purkinje cell. *Frontiers in Cellular Neuroscience*, **13**, 205.

[411] Virag, L., Iost, N., Opincariu, M., Szolnoky, J., Szecsi, J., Bogats, G., Szenohradszky, P., Varro, A. & Papp, J. G. (2001) The slow component of the delayed rectifier potassium current in undiseased human ventricular myocytes. *Cardiovascular Research*, **49**, 790–797.

[412] Voigt, N., Heijman, J., Wang, Q. L., Chiang, D. Y., Li, N., Karck, M., Wehrens, X. H. T., Nattel, S. & Dobrev, D. (2014) Cellular and Molecular Mechanisms of Atrial Arrhythmogenesis in Patients With Paroxysmal Atrial Fibrillation. *Circulation*, **129**, 145–156.

[413] von Lewinski, D., Stumme, B., Maier, L. S., Luers, C., Bers, D. A. & Pieske, B. (2003) Stretch-dependent slow force response in isolated rabbit myocardium is Na+ dependent. *Cardiovascular Research*, **57**, 1052–1061.

[414] Wagner, J. & Keizer, J. (1994) Effects of rapid buffers on Ca2+ diffusion and Ca2+ oscillations. *Biophysical Journal*, **67**, 447–456.

[415] Wagner, M., Goltz, D., Stucke, C., Schwoerer, A. P., Ehmke, H. & Volk, T. (2007) Modulation of the transient outward K+ current by inhibition of endothelin-A receptors in normal and hypertrophied rat hearts. *Pflugers Archiv-European Journal of Physiology*, **454**, 595–604.

[416] Wagner, M., Moritz, A. & Volk, T. (2011) Interaction of gonadal steroids and the glucocorticoid corticosterone in the regulation of the L-type Ca(2+) current in rat left ventricular cardiomyocytes. *Acta Physiologica*, **202**, 629–40.

[417] Wagner, S., Hacker, E., Grandi, E., Weber, S. L., Dybkova, N., Sossalla, S., Sowa, T., Fabritz, L., Kirchhof, P., Bers, D. M. & Maier, L. S. (2009) Ca/Calmodulin Kinase II Differentially Modulates Potassium Currents. *Circulation-Arrhythmia and Electrophysiology*, **2**, 285–294.

[418] Walden, A. P., Dibb, K. M. & Trafford, A. W. (2009) Differences in intracellular calcium homeostasis between atrial and ventricular myocytes. *Journal of Molecular and Cellular Cardiology*, **46**, 463–473.

[419] Walker, S., Asaria, M., Manca, A., Palmer, S., Gale, C. P., Shah, A. D., Abrams, K. R., Crowther, M., Timmis, A., Hemingway, H. & Sculpher, M. (2016) Long-term healthcare use and costs in patients with stable coronary artery disease: a population-based cohort using linked health records (CALIBER). *European Heart Journal-Quality of Care and Clinical Outcomes*, **2**, 125–140.

[420] Walton, R. D., Benoist, D., Hyatt, C. J., Gilbert, S. H., White, E. & Bernus, O. (2010) Dual excitation wavelength epifluorescence imaging of transmural electrophysiological properties in intact hearts. *Heart Rhythm*, **7**, 1843–1849.

[421] Walweel, K., Li, J., Molenaar, P., Imtiaz, M. S., Quail, A., dos Remedios, C. G., Beard, N. A., Dulhunty, A. F., van Helden, D. F. & Laver, D. R. (2014) Differences in the regulation of RyR2 from human, sheep, and rat by Ca2+ and Mg2+ in the cytoplasm and in the lumen of the sarcoplasmic reticulum. *Journal of General Physiology*, **144**, 263–271.

[422] Wang, L. G., Myles, R. C., De Jesus, N. M., Ohlendorf, A. K. P., Bers, D. M. & Ripplinger, C. M. (2014) Optical Mapping of Sarcoplasmic Reticulum Ca2+ in the Intact Heart. *Circulation Research*, **114**, 1410–1421.

[423] Wang, X., Wang, X., Gu, Y., Wang, T. & Huang, C. (2013) Wenxin Keli attenuates ischemia-induced ventricular arrhythmias in rats: Involvement of L-type calcium and transient outward potassium currents. *Molecular Medicine Reports*, **7**, 519–524.

[424] Wang, Y. & Hill, J. A. (2010) Electrophysiological remodeling in heart failure. *Journal of Molecular and Cellular Cardiology*, **48**, 619–32.

[425] Wang, Y. G., Joyner, R. W., Wagner, M. B., Cheng, J., Lai, D. W. & Crawford, B. H. (2009) Stretch-activated channel activation promotes early afterdepolarizations in rat ventricular myocytes under oxidative stress. *American Journal of Physiology-Heart and Circulatory Physiology*, **296**, H1227–H1235.

[426] Waring, M. J., Arrowsmith, J., Leach, A. R., Leeson, P. D., Mandrell, S., Owen, R. M., Pairaudeau, G., Pennie, W. D., Pickett, S. D., Wang, J., Wallace, O. &

Weir, A. (2015) An analysis of the attrition of drug candidates from four major pharmaceutical companies. *Nature Reviews Drug Discovery*, **14**, 475–86.

[427] Wasserstrom, J. A., Shiferaw, Y., Ramakrishna, S., Patel, H., O'Toole, M. J., Pappas, A., Khan, A., Arora, R. & Aistrup, G. L. (2010) Synchronization of Spontaneous Calcium Release Waves Among Myocytes in Intact Heart Determines the Magnitude of Delayed Afterdepolarizations and Triggered Activity. *Biophysical Journal*, **98**, 104A–104A.

[428] Watanabe, T., Delbridge, L. M., Bustamante, J. O. & McDonald, T. F. (1983) Heterogeneity of the action-potential in isolated rat ventricular myocytes and tissue. *Circulation Research*, **52**, 280–290.

[429] Weber, C. R., Ginsburg, K. S., Philipson, K. D., Shannon, T. R. & Bers, D. M. (2001) Allosteric regulation of Na/Ca exchange current by cytosolic Ca in intact cardiac myocytes. *Journal of General Physiology*, **117**, 119–131.

[430] Weigand, K., Witte, R., Moukabary, T., Chinyere, I., Lancaster, J., Pierce, M. K., Goldman, S. & Juneman, E. (2017) In vivo electrophysiological study of induced ventricular tachycardia in intact rat model of chronic ischemic heart failure. *IEEE Transactions on Biomedical Engineering*, **64**, 1393–1399.

[431] Wickenden, A. D., Kaprielian, R., Parker, T. G., Jones, O. T. & Backx, P. H. (1997) Effects of development and thyroid hormone on K+ currents and K+ channel gene expression in rat ventricle. *Journal of Physiology-London*, **504**, 271–286.

[432] Wier, W. G. & Balke, C. W. (1999) Ca2+ release mechanisms, Ca2+ sparks, and local control of excitation-contraction coupling in normal heart muscle. *Circulation Research*, **85**, 770–776.

[433] Wilson, L. D. & Rosenbaum, D. S. (2007) Mechanisms of arrythmogenic cardiac alternans. *Europace*, **9**, 77–82.

[434] Winslow, R. L., Rice, J., Jafri, S., Marban, E. & O'Rourke, B. (1999) Mechanisms of altered excitation-contraction coupling in canine tachycardia-induced heart failure, II - Model studies. *Circulation Research*, **84**, 571–586.

[435] Witkowski, F. X., Leon, L. J., Penkoske, P. A., Giles, W. R., Spano, M. L., Ditto, W. L. & Winfree, A. T. (1998) Spatiotemporal evolution of ventricular fibrillation. *Nature*, **392**, 78–82.

[436] Workman, A. J., Kane, A. K. & Rankin, A. C. (2001) The contribution of ionic currents to changes in refractoriness of human atrial myocytes associated with chronic atrial fibrillation. *Cardiovascular Research*, **52**, 226–235.

[437] Wu, W. & Sanguinetti, M. C. (2016) Molecular Basis of Cardiac Delayed Rectifier Potassium Channel Function and Pharmacology. *Cardiac Electrophysiology Clinics*, **8**, 275–84.

[438] Wymore, R. S., Gintant, G. A., Wymore, R. T., Dixon, J. E., McKinnon, D. & Cohen, I. S. (1997) Tissue and species distribution of mRNA for the I-Kr-like K+ channel, erg. *Circulation Research*, **80**, 261–268.

[439] Xiao, R. P., Cheng, H. P., Lederer, W. J., Suzuki, T. & Lakatta, E. G. (1994) Dual regulation of Ca2+/calmodulin-dependent kinase-II activity by membrane voltage and by calcium influx. *Proceedings of the National Academy of Sciences of the United States of America*, **91**, 9659–9663.

[440] Xie, L.H., Chen, F., Karagueuzian, H.S. & Weiss, J.N. (2009) Oxidative Stress-Induced Afterdepolarizations and Calmodulin Kinase II Signaling. *Circulation Research*, **104**, 79–86.

[441] Xu, H. D., Guo, W. N. & Nerbonne, J. M. (1999) Four kinetically distinct depolarization-activated K+ currents in adult mouse ventricular myocytes. *Journal of General Physiology*, **113**, 661–677.

[442] Xu, L. & Meissner, G. (1998) Regulation of cardiac muscle Ca2+ release channel by sarcoplasmic reticulum lumenal Ca2+. *Biophysical Journal*, **75**, 2302–2312.

[443] Yang, Z., Pascarel, C., Steele, D. S., Kornukai, K., Brette, F. & Orchard, C. H. (2002) Na+-Ca2+ exchange activity is localized in the T-tubules of rat ventricular myocytes. *Circulation Research*, **91**, 315–322.

[444] Yao, A., Spitzer, K. W., Ito, N., Zaniboni, M., Lorell, B. H. & Barry, W. H. (1997) The restriction of diffusion of cations at the external surface of cardiac myocytes varies between species. *Cell Calcium*, **22**, 431–438.

[445] Yasui, K., Liu, W. R., Opthof, T., Kada, K., Lee, J. K., Kamiya, K. & Kodama, I. (2001) I-f current and spontaneous activity in mouse embryonic ventricular myocytes. *Circulation Research*, **88**, 536–542.

[446] Yuan, W. L., Ginsburg, K. S. & Bers, D. M. (1996) Comparison of sarcolemmal calcium channel current in rabbit and rat ventricular myocytes. *Journal of Physiology-London*, **493**, 733–746.

[447] Yuan, Y. F., Bai, X. Y., Luo, C. J., Wang, K. Q. & Zhang, H. G. (2015) The virtual heart as a platform for screening drug cardiotoxicity. *British Journal of Pharmacology*, **172**, 5531–5547.

[448] Yue, L. X., Feng, J. L., Li, G. R. & Nattel, S. (1996) Transient outward and delayed rectifier currents in canine atrium: Properties and role of isolation methods. *American Journal of Physiology-Heart and Circulatory Physiology*, **270**, H2157–H2168.

[449] Zaitsev, A. V., Berenfeld, O., Mironov, S. F., Jalife, J. & Pertsov, A. M. (2000) Distribution of excitation frequencies on the epicardial and endocardial surfaces of fibrillating ventricular wall of the sheep heart. *Circulation Research*, **86**, 408–417.

[450] Zhai, Y., Luo, Y., Wu, P. & Li, D. (2018) New insights into SERCA2a gene therapy in heart failure: pay attention to the negative effects of B-type natriuretic peptides. *Journal of Medical Genetics*, **55**, 287–296.

[451] Zhang, Z. S., Cheng, H. J., Onishi, K., Ohte, N., Wannenburg, T. & Cheng, C. P. (2005) Enhanced inhibition of L-type Ca2+ current by beta(3)-adrenergic stimulation in failing rat heart. *Journal of Pharmacology and Experimental Therapeutics*, **315**, 1203–1211.

[452] Zhou, P., Cheng, C. P., Li, T., Ferrario, C. M. & Cheng, H. (2015) Modulation of cardiac L-type Ca2+ current by angiotensin-(1-7): Normal versus heart failure. *Therapeutic Advances in Cardiovascular Disease*, **9**, 342–353.

[453] Zhou, P., Cheng, H. J., Cross, M., Little, W. C. & Chang, C. P. (2009) Modulation of Cardiac L-Type Ca2+ Current by Angiotensin-(1-7): Normal vs Heart Failure. *Circulation*, **120**, S694–S694.

[454] Zicha, S., Moss, I., Allen, B., Varro, A., Papp, J., Dumaine, R., Antzelevich, C. & Nattel, S. (2003) Molecular basis of species-specific expression of repolarizing K+ currents in the heart. *American Journal of Physiology-Heart and Circulatory Physiology*, **285**, H1641–H1649.

[455] Zima, A. V., Bovo, E., Bers, D. M. & Blatter, L. A. (2010) Ca2+ spark-dependent and -independent sarcoplasmic reticulum Ca2+ leak in normal and failing rabbit ventricular myocytes. *Journal of Physiology-London*, **588**, 4743–4757.

[456] Zimmer, T., Haufe, V. & Blechschmidt, S. (2014) Voltage-gated sodium channels in the mammalian heart. *Global Cardiology Science & Practice*, **2014**, 449–63.

[457] Zobel, C., Brixius, K., Pietsch, M., Münch, G., Bölck, B. & Schwinger, R. (1998) Unchanged sarcoplasmic reticulum Ca2+-ATPase activity, reduced Ca2+ sensitivity, and negative force-frequency relationship in transgenic rats overexpressing the mouse renin gene. *Journal of Molecular Medicine*, **76**, 533–544.

[458] Zumino, A. P., Risler, N. R., Schanne, O. F., Petrich, E. R. & Carrión, A. (1997) Magnesium: Effects on reperfusion arrhythmias and membrane potential in isolated rat hearts. *Molecular and Cellular Biochemistry*, **171**, 85–93.